The University of Sheffield

CARRIER SIGNAL INJECTION BASED SENSORLESS CONTROL OF PERMANENT MAGNET BRUSHLESS AC MACHINES

Liming Gong

A thesis submitted for the degree of Doctor of Philosophy

Department of Electronic and Electrical Engineering

University of Sheffield

Mappin Street, Sheffield, S1 3JD, UK

31 January 2012

ABSTRACT

This thesis is focused on the carrier signal injection based sensorless control of Permanent Magnet (PM) Brushless AC (BLAC) machines.

Based on the machine saliency property, carrier signal injection based sensorless techniques have been well developed in the past decade. In order to provide the insight into machine saliency information, a simplified experimental procedure is presented to obtain the machine saliency distribution in the *dq* plane, including magnetic saturation and cross-saturation effects. Based on the measured machine saliency information, Sensorless Safety Operation Area (SSOA), which accounts for quantization errors in the Analog to Digital (AD) conversion, is proposed to investigate the effectiveness of sensorless operation for practical applications. The SSOA defines a working area in *dq* plane, in which the machine can work in sensorless mode with guaranteed steady state performance for either pulsating or rotating carrier signal injection based methods.

The non-ideal characteristics of machines and drives introduce additional carrier current disturbances in carrier signal injection based sensorless control, which eventually results in the deterioration of the position estimation accuracy, the degradation of dynamic performance and even stability problems. This thesis investigates the influence of inverter nonlinearity effects on rotating carrier signal injection based methods. With the aid of theoretical analysis and experimental measurement, it is proven that the positive sequence carrier current distortion resulting from inverter nonlinearity effects can be used to compensate the influence of inverter nonlinearity on negative sequence carrier current. Hence, a new online post-compensation scheme is developed in this thesis by utilizing the measured distortion of positive sequence carrier current.

In sensorless control, great efforts are required to compensate for nonlinear effects in order to improve the accuracy of the estimated position information. Alternatively, the optimal efficiency of machines, instead of accurate position estimation, can be taken as the sensorless operation objective. In this way, the sensorless operation performance is improved by the proposed online optimal efficiency tracking without any compensation for nonlinear effects.

In addition, a robust magnetic polarity identification scheme is developed in this thesis based on *d*-axis magnetic saturation effect. The proposed scheme can be seamlessly integrated into conventional carrier signal injection based sensorless control algorithm.

ACKNOWLEDGEMENTS

I would like to express my sincere gratitude to my supervisor Prof. Z. Q. Zhu. Throughout the whole course of this research work, his professional technical guidance and constructive help are valuable and impressive.

I am very grateful to Dr. Yi Li for his technical assistance. His research work gave me a good starting point for my Ph.D. study. Many thanks go to Dr. Jintao Chen for his support and help in many ways. Discussions with Mr. Nick Leong and Dr. Xu Liu were also very helpful.

Further thanks for the support provided by the technical staff in the Electrical Machines and Drives Group at the University of Sheffield.

Finally, I am very grateful for my wife Ying Liu's love, encouragement and faith throughout my Ph.D. study. Her understanding and strong support make me dedicate great efforts on the research work. I would also like to thank my whole family for their endless care.

CONTENTS

LIST OF SYMBOLS

α	Phase angle of injected carrier voltage signal, $a = w_c t + j$
E_{ex}	Extended EMF
e_a, e_b and e_c	3-phase back-EMF
e_α and e_β	α- and β-axis back-EMF
e_d and e_q	d- and q-axis back-EMF
f_r	Rotation frequency of motor
f_c	Injected signal frequency
$f(\Delta\theta)$	Position error signal
$i_{\alpha h}$ and $i_{\beta h}$	α- and β-axis high frequency currents
i_a, i_b and i_c	3-phase currents
i_{ah}, i_{bh} and i_{ch}	3-phase high frequency currents
i_{neg}	Negative sequence carrier current
I_p and I_n	$I_p = V_c/(\omega_c L_p)$, $I_n = V_c/(\omega_c L_n)$
I_{qu}	Quantum current of ADC
i_d and i_q	d- and q-axis currents
i_d^e and i_q^e	d- and q-axis currents in estimated reference frame
i_{dh} and i_{qh}	d- and q-axis high frequency currents
i_{dh}^e and i_{qh}^e	d- and q-axis high frequency currents in estimated reference frame
$L_{\alpha h}$ and $L_{\beta h}$	Incremental self- inductances of α- and β-axes
L_a, L_b and L_c	3-phase apparent self-inductances
L_{ah}, L_{bh} and L_{ch}	3-phase incremental self-inductances
L_{sa} and L_{sd}	$L_{sa}=(L_{qh}+L_{dh})/2$, $L_{sd}=(L_{qh}-L_{dh})/2$
L_p	$L_p = (L_{dh}L_{qh} - L_{dqh}^2)/L_{sa}$,
L_n	$L_n = (L_{dh}L_{qh} - L_{dqh}^2)/\sqrt{L_{sd}^2 + L_{dqh}^2}$
L_d and L_q	Apparent self-inductances of d- and q-axes
L_{dh} and L_{qh}	Incremental self-inductances of d- and q-axes

L_{dq} and L_{qd}	Apparent mutual-inductances between *d*- and *q*-axes
L_{dqh} and L_{qdh}	Incremental mutual-inductances between *d*- and *q*-axes
L_{lm}	Boundary inductance of SSOA
L_s	Equal *dq*-axis inductance
max	Maximum operation
n_p	Number of pole pairs
N_w	Number of turns of winding
p	Derivative operation, $p=d/dt$
$P(\theta_r)$	Position vector
P_{cu}	Copper loss
P_{fe}	Iron loss
P_{str}	Stray loss
P_{dq}	Instantaneous active power in synchronous reference frame
R_c	Equivalent resistance of iron loss
R_s	Phase winding resistance
R_{xh}	Equivalent HF resistance of inverter nonlinearity effects
$T(\Delta\theta)$	Rotation matrix from actual to estimated reference frame
T_{em}	Electromagnetic torque
T_{eq}	Equivalent time constant
T_L	Load torque
$v_{\alpha h}$ and $v_{\beta h}$	α- and β-axis high frequency voltages
v_a, v_b and v_c	3-phase voltages
v_{ah}, v_{bh} and v_{ch}	3-phase high frequency voltages
v_d and v_q	*d*- and *q*-axis voltages
v_d^e and v_q^e	*d*- and *q*-axis voltages in estimated reference frame
v_{dh} and v_{qh}	*d*- and *q*-axis high frequency voltages
v_{dh}^e and v_{qh}^e	*d*- and *q*-axis high frequency voltages in estimated reference frame
v_s	Stator voltage vector
V_o	Zero sequence voltage

Δu_{xo}	Terminal voltage error due to inverter nonlinearity effects
Δu	Disturbance voltage vector due to inverter nonlinearity effects
Δu_f	Fundamental disturbance voltage due to inverter nonlinearity
Δu_h	HF disturbance voltage due to inverter nonlinearity
V_c	Amplitude of injected high frequency voltage signal
$\Delta\theta$	Error in estimated rotor position
θ_m	$q_m = \tan^{-1}(-L_{dqh} / L_{sd})$
θ_r and θ_r^e	Actual and estimated rotor position
ε_s	Quantization error of ADC, $\varepsilon_s = \pm I_{qu}/2$
ψ_α, ψ_β	α- and β-axis flux-linkages
ψ_s	Stator flux-linkage vector
ψ_{si} and ψ_{sv}	Estimated stator flux-linkages from current and voltage model
ψ_d and ψ_q	d- and q-axis flux-linkages
ψ_d^a	Active flux-linkage
ψ_m	Permanent magnet flux-linkage
ω_c	Angular speed of injected signal
ω_r	Angular speed of rotor, $\omega_r = 2\pi f_r$
ω_r^e	Estimated angular speed of rotor

LIST OF ABBREVIATIONS

AC	Alternating current
AD	Analog to digital
ADC	Analog to digital converter
BLAC	Brushless AC
BLDC	Brushless DC
CVC	Current vector control
DAC	Digital to analog converter
DC	Direct current
DSP	Digital signal processor
DSK	DSP starter kit
DTC	Direct torque control
EKF	Extended Kalman filter
EM	Extended modulation
EMF	Electromotive force
FEA	Finite element analysis
HF	High frequency
IGBT	Insulated-gate bipolar transistor
INFORM	Indirect flux detection by online reactance measurement
IPM	Interior permanent magnet
LPF	Low pass filter
MCL	Minimum copper loss
MIL	Minimum iron loss
MRAS	Model reference adaptive system
MTL	Minimum total loss
MTPA	Maximum torque per ampere
PI	Proportional integral
PID	Proportional integral derivative

PLL	Phase lock loop
PM	Permanent magnet
PTC	Predictive torque control
PWM	Pulse width modulation
RPM	Revolutions per minute
SNR	Signal to noise ratio
SRFF	Synchronous reference frame filter
SSOA	Sensorless safety operation area
ZVCD	Zero vector current derivative

CHAPTER 1

SENSORLESS CONTROL OF PERMANENT MAGNET BRUSHLESS AC MACHINES

1.1 Introduction

In the last several decades, the development of permanent magnet (PM) materials, power electronic devices and microprocessors has made a great contribution to the emergence of brushless PM synchronous machines, which have the advantages of high efficiency, high power density, easy maintenance and excellent control performance.

Brushless PM synchronous machines are characterized by having a field produced by the permanent magnet on the rotor. Fig. 1.1 illustrates the typical rotor structures for conventional inner rotor radial field brushless PM machines [LI09a]. Unlike the iron with high magnetic permeability, the rare earth PM materials have lower permeability, which is close to the value of air gap. As a consequence, there is negligible geometrical saliency for the surface mounted rotor configuration, whereas, the other three rotor configurations exhibit significant saliency effect resulting from geometrical anisotropy.

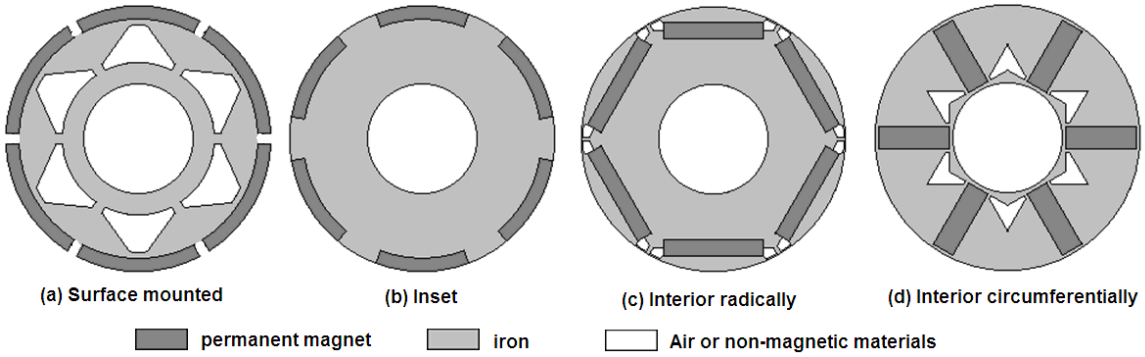

Fig. 1.1 Typical rotor structures of brushless PM synchronous machines [LI09a].

According to the type of fundamental excitation, brushless PM synchronous machines can be categorized as brushless DC (BLDC) machines driven by square wave current excitation, and brushless AC (BLAC) machines driven by sinusoidal current

excitation, as shown in Fig. 1.2. BLDC machines are usually used in relatively low cost applications, where only discrete rotor position information with low resolution is required. Whereas, BLAC machines are excited by a sinusoidal phase current, synchronizing with the permanent magnet flux, thus continuous rotor position information with high resolution is required. Therefore, the rotor position information is a critical concern for both BLDC and BLAC machines.

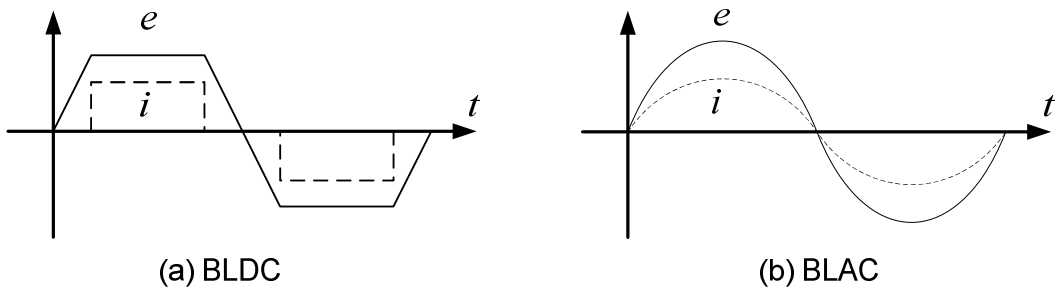

Fig. 1.2 Excitation of BLDC and BLAC machines.

However, the physical position sensor presents several disadvantages, including increased size, reduced reliability, sensitivity to noise, additional cost and increased complexity of the whole system. To overcome these drawbacks, there has been considerable interest in on-line rotor position estimation, rather than direct measurement using a physical position sensor. This kind of technique is normally referred to as sensorless, self-sensing or encoderless control. In this thesis, the term of sensorless is employed and only sensorless current vector control (CVC) for PM BLAC machines is considered.

Sensorless CVC for BLAC machines can be broadly classified as: fundamental model based methods and machine saliency based methods, as shown in Fig. 1.3. Algorithms that rely on the fundamental model have the advantages of simplicity and straightforwardness. Most critical conditions exist at low speed and standstill operation, where the signal to noise ratio (SNR) of position dependent signal is too weak to effectively extract position information. Such limitations, however, can be overcome with machine saliency based sensorless methods. Since machine saliency property is

independent on the rotor speed, and the rotor position information can be effectively estimated at low speed and even standstill condition.

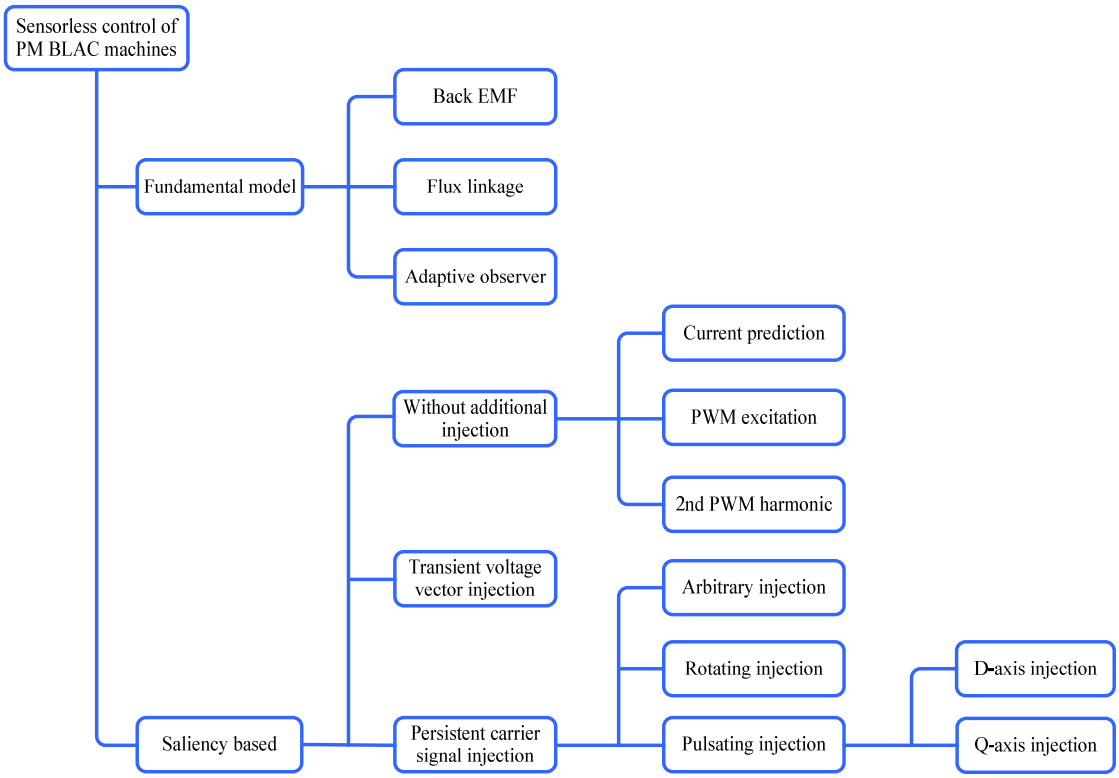

Fig. 1.3 Categories of sensorless control for PM BLAC machines.

Alternatively, direct torque control (DTC), which exhibits better dynamic performance than conventional CVC, is claimed to be inherently sensorless. However, the position information is also required at standstill and very low speed operation, since in that case, the stator flux linkage is estimated from a current model rather than voltage model [AND08]. Although more computation efforts are required compared with DTC, predictive torque control (PTC) has become attractive recently for its faster dynamic torque response and lower torque ripple than DTC [KEN10] [ROD11]. Without any additional injection, saliency based sensorless PTC is developed in [LAN10].

1.2 Fundamental Model Based Methods

The basic idea of fundamental model based sensorless methods is to estimate back electromotive force (EMF) or flux linkage according to fundamental model, in which the rotor position information is contained. Position estimation can be performed through open loop calculation or close loop observer. Additionally, the adaptive observers

including the extended Kalman filter (EKF) and model reference adaptive system (MRAS) provide other options to estimate the rotor position directly from machine fundamental model. Fundamental model based methods work well at middle and high speed ranges, whereas this kind of methods tend to fail at low speed and standstill operations due to unobserved machine model in that case. Therefore, specific starting up techniques should be employed for wide speed range operation.

1.2.1 Back-EMF based methods

The fundamental mathematical model of PM BLAC machines in the synchronous reference frame can be expressed as,

$$\begin{bmatrix} v_d \\ v_q \end{bmatrix} = \begin{bmatrix} R_s & 0 \\ 0 & R_s \end{bmatrix} \begin{bmatrix} i_d \\ i_q \end{bmatrix} + p \begin{bmatrix} y_d \\ y_q \end{bmatrix} + w_r \begin{bmatrix} -y_q \\ y_d \end{bmatrix} \tag{1. 1}$$

where p denotes the differential operator, R_s is the phase winding resistance, ω_r indicates the rotor angular speed, and Ψ_d, Ψ_q represent the d- and q-axis flux linkages respectively. Assuming ideal sinusoidal flux distribution without saturation and cross-saturation effects, the above equation can be re-written as,

$$\begin{bmatrix} v_d \\ v_q \end{bmatrix} = \begin{bmatrix} R_s + L_d p & -w_r L_q \\ w_r L_d & R_s + L_q p \end{bmatrix} \begin{bmatrix} i_d \\ i_q \end{bmatrix} + \begin{bmatrix} 0 \\ w_r y_m \end{bmatrix} \tag{1. 2}$$

where L_d and L_q are the d- and q-axis inductances, and ψ_m is the flux linkage due to PM.

For non-salient PM BLAC machines, i.e., L_d=L_q=L, it can be seen that the matrix in (1.2) becomes symmetric. For a symmetric matrix, it could keep the identical form after the rotating transformation, i.e.,

$$\begin{bmatrix} a & -b \\ b & a \end{bmatrix} = \begin{bmatrix} \cos(\Delta q) & -\sin(\Delta q) \\ \sin(\Delta q) & \cos(\Delta q) \end{bmatrix} \begin{bmatrix} a & -b \\ b & a \end{bmatrix} \begin{bmatrix} \cos(\Delta q) & \sin(\Delta q) \\ -\sin(\Delta q) & \cos(\Delta q) \end{bmatrix} \tag{1. 3}$$

In sensorless control, the real rotor position information is unknown. Using rotating transformation, the fundamental model for a non-salient PM BLAC machines in estimated synchronous reference frame is derived as [SHA98][CHE00],

$$\begin{bmatrix} v_d^e \\ v_d^e \end{bmatrix} = \begin{bmatrix} R_s + Lp & -w_r L \\ w_r L & R_s + Lp \end{bmatrix} \begin{bmatrix} i_d^e \\ i_q^e \end{bmatrix} + w_r y_m \begin{bmatrix} -\sin(\Delta q) \\ \cos(\Delta q) \end{bmatrix} \tag{1. 4}$$

where $\omega_r\psi_m$ is referred to as conventional back-EMF. The above equation shows that, for non-salient machines, only the back-EMF contains rotor position information even with position estimation error. However, for salient machines, the conventional back-EMF term would not completely contain the position information due to asymmetric matrix in (1.2).

Referring to the mathematical model for non-salient machine, the mathematical model of salient machines (1.2) can be re-written as,

$$\begin{bmatrix} v_d \\ v_q \end{bmatrix} = \begin{bmatrix} R_s + L_d p & -w_r L_q \\ w_r L_q & R_s + L_d p \end{bmatrix} \begin{bmatrix} i_d \\ i_q \end{bmatrix} + \begin{bmatrix} 0 \\ E_{ex} \end{bmatrix} \tag{1. 5}$$

where E_{ex} is designated as extended back-EMF [CHE00] [MOR02] [CHE03], defined by

$$E_{ex} = w_r y_{\ m} + w_r (L_d - L_q) i_d + (L_q - L_d) p i_q \tag{1. 6}$$

In this way, the rotor position information is expected to be fully contained in the extended back-EMF regardless of salient or non-salient machines. Therefore, it is a general form for PM BLAC machines. The extended back-EMF consists of conventional back-EMF generated by the permanent magnets, and the voltage terms related with machine saliency as well. For non-salient machines, the extended back-EMF would be reduced to conventional back-EMF. Furthermore, by accounting for cross-saturation effect between *d*- and *q*-axis, the extended back-EMF is improved in [LI07].

Extended back-EMF gains a distinct improvement over conventional back-EMF, the derivation process implies that speed estimation error under sensorless operation is assumed to be zero at all times. During transients, however, this assumption is not valid, thus the sensorless dynamic performance based on extended back-EMF would be degraded. To overcome this limitation, the concept of equivalent back-EMF is introduced in [LIU11], which is equivalent to the active flux, as will be discussed later.

It is difficult to directly measure the back-EMF of PM BLAC machines, since rapidly changing current exist in the machine windings all the time. According to the voltage equation, the back-EMF can be calculated directly from measured voltage and current in the stationary reference frame [NAI92][HOQ94][LI07]. However, any uncertainty of machine parameters will cause trouble to the rotor position estimation, which is the major problem of this kind of open-loop calculation method. Instead, the

general trend of back-EMF estimation has been concentrated on close-loop observer [MOR02] [CHE03] [CHI09].

Based on the linear control theory, a disturbance observer is used to estimate the extended back-EMF, as shown in Fig. 1.4 [CHE03]. The stability of disturbance observer can be easily guaranteed since it is based on a linear model of the machine. Meanwhile, sliding mode controller, as shown in Fig. 1.5, is an attractive choice to determine the back-EMF due to improved system robustness, immunity to parameter variations and disturbance rejection [CHI09].

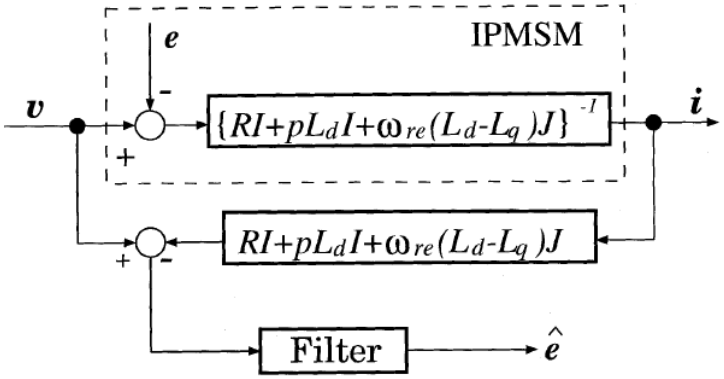

Fig. 1.4 Disturbance observer for extended back-EMF estimation [CHE03].

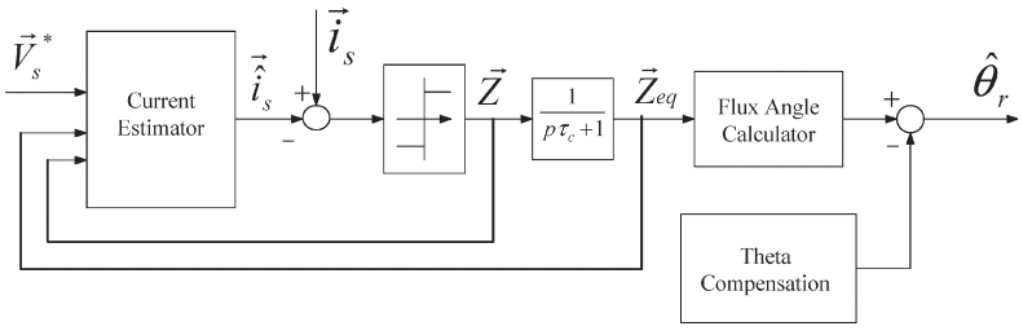

Fig. 1.5 Sliding mode controller for back-EMF estimation [CHI09]

For PM BLAC machines exhibiting a third harmonic in the phase back-EMF, discrete rotor position information can be extracted from the zero crossings of the measured third harmonic of back-EMF [MOR96] [SHE04], and then continuous rotor position information can be constructed from a phase-lock-loop (PLL) or the integration of estimated machine speed. Although third harmonic based sensorless method was

successfully implemented in flux weakening control for both PM BLDC and BLAC machines, it only applies to machines with sufficient third harmonic in back-EMF. Furthermore, the neutral point of the stator windings should be available for the measurement of the third harmonics, resulting in additional hardware complexity.

1.2.2 Flux-linkage based methods

Stator flux-linkage estimation is an important topic for DTC, and also it is a viable candidate for sensorless position estimation, since position information is contained in its phase angle. Stator flux is difficult to be measured directly, hence stator flux estimation methods should be developed.

The fundamental idea to calculate flux linkage is very simple. In stationary reference frame, the stator flux linkage can be calculated from stator voltage and current vectors, given by,

$$y_{ab} = \int (u_{ab} - R_s i_{ab}) dt \tag{1.7}$$

Although the open loop calculation from (1.7) is very straightforward, some practical issues have to be considered, such as stator resistance variations, integration drift and low SNR signal at low speed operation.

To solve the problems, close loop methods become more attractive for stator flux estimation [HU98] [AND08] [YOO09a] [BOL09] [FOO10]. Combining the voltage model estimator with current model estimator, a hybrid flux observer could estimate the stator flux in a wide speed range, as shown in Fig. 1.6. The transfer function for the combined flux observer in the stationary reference frame can be derived as [YOO09a],

$$y_s = \frac{s^2}{s^2 + 2xw_o s + w_o^2} \cdot y_{sv} + \frac{2xw_o s + w_o^2}{s^2 + 2xw_o s + w_o^2} \cdot y_{si} \tag{1.8}$$

where ψ_s is estimated stator flux linkage through the combined model, while ψ_{sv} and ψ_{si} are the estimated stator flux linkages through voltage model and current model, respectively. The voltage model is dominant at high speed, while the current model dominant at low speed. A smooth transition between them can be automatically achieved through PI compensator configuration. Another advantage of the combined flux observer is that the integration drift problem of the voltage model can be completely compensated

by using a PI compensator, due to high pass filter behavior on ψ_{sv}, as shown in (1.8). It should be noted that the rotor position information is required for the current model at low speed and standstill. With the integration of saliency based sensorless techniques, the combined flux observer exhibits good performance over wide speed range sensorless operation [SIL06] [AND08].

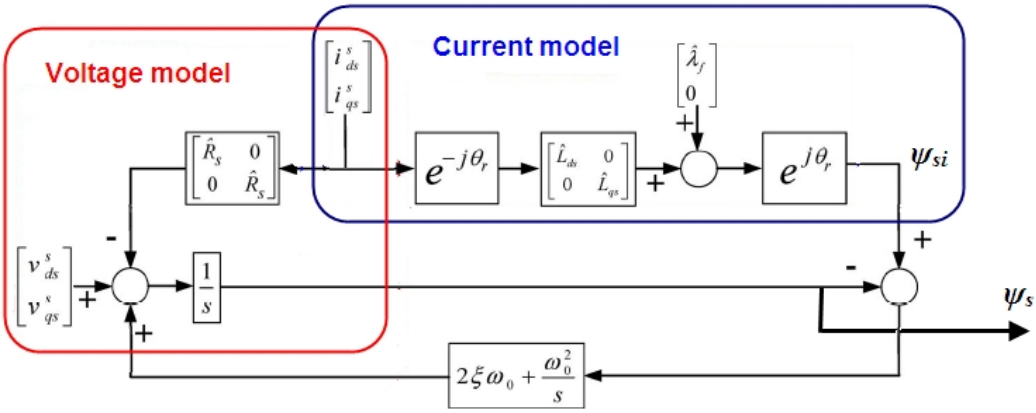

Fig. 1.6 Combined flux observer [YOO09a].

Due to armature reaction, the estimated stator flux would deviate from the permanent magnet flux, which leads to position estimation error from estimated stator flux. In [BOL08], a more general concept of active flux is proposed to unify all salient machines into fictitious non-salient machines, so that sensorless position estimation becomes simpler. The active flux is expressed as,

$$y_d^a = y_m + (L_d - L_q) i_d = y_s - L_q i_s \tag{1. 9}$$

With introduced active flux, the voltage equation for salient PM BLAC machines can be rewritten as,

$$V_s = R_s i_s + (s + jw_r) L_q i_s + (s + jw_r) y_d^a \tag{1.10}$$

In this way, the salient pole rotor machine has been transformed to a non-salient case.

For explicit explanation about this concept, the phase diagram of active flux for salient PM BLAC machines is depicted in Fig. 1.7. It clearly reveals that the active flux position is identical to the rotor position, leading to great simplification in sensorless position estimation.

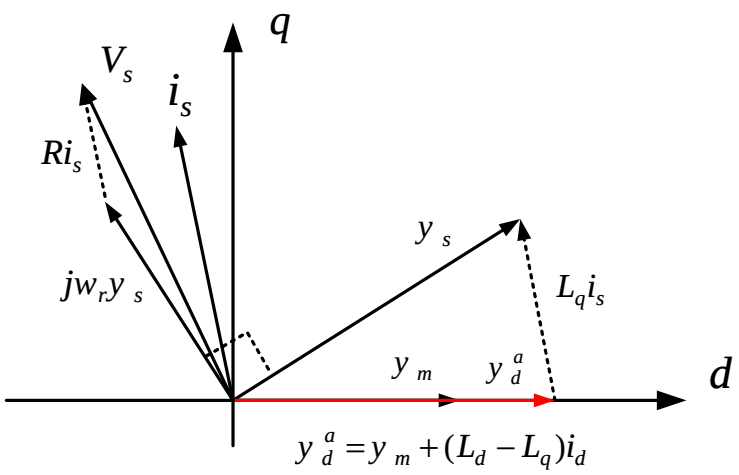

Fig. 1.7 Active flux of salient PM BLAC machines [BOL08].

1.2.3 Adaptive observer based methods

Based on the fundamental model of PM BLAC machines, adaptive observers, such as extended Kalman filter (EKF) [BOL99] and model reference adaptive system (MRAS) [PII08] [GAD10], become more and more attractive for rotor position estimation due to their robustness, quick convergence and immunity to machine parameter variation.

The Kalman filter is an optimal state observation based on least-square variance estimation for linear system with Gaussian white noise in the measurements and system states. The extended Kalman filter is an extension application of Kalman filter in a nonlinear system. It is less influenced by measured noise, and parameter inaccuracy is not as critical as in conventional fundamental estimation methods. However, a heavy computation burden makes an EKF based algorithm difficult in practical implementation for machine drives applications. To solve this problem, a reduced order EKF is presented with the assumption that some system states are free of noise. In [FUE11], the EKF technique is combined with PTC, which yields effective torque and speed control.

The MRAS scheme provides another option for sensorless position estimation [PII08] [GAD10]. The diagram of MRAS is shown in Fig. 1.8, in which the reference model represents the real machine, while the adjustable model is a fictitious machine based on the fundamental mathematical model. With the same excitation, the difference between the responses from two models yields an estimation error ε, which is input to the correction controller. Using the correction controller, the adaptive model is adjusted so as

to minimize the estimation error ε. In steady state, ε is very small, which implies that the behavior of the adaptive model is the same as that of the actual machine, hence machine states including position information can be accessed from the adaptive mathematical model. With regard to the correction controller, it can be realized by the conventional PI or nonlinear controller involving sliding mode and fuzzy logic controller [GAD10].

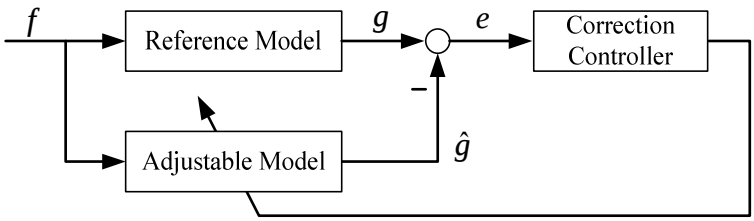

Fig. 1.8 Block diagram of MRAS.

The MRAS technique is widely employed in sensorless control due to its simple concept and low computational overhead. In conventional vector control, the output voltage of the *d*-axis current regulator can be considered as the estimation error signal ε, with PI type correction control, a simplified MRAS based sensorless vector control scheme is presented in [MAT96] [BAE03], as illustrated in Fig. 1.9. In which, the feed forward voltage term of V_{ds_ff} is calculated from machine model, hence it can be considered as the output from adaptive model; while the *d*-axis voltage command V^*_{ds} is the real voltage applied to machine, thus it can be considered as the output from reference model.

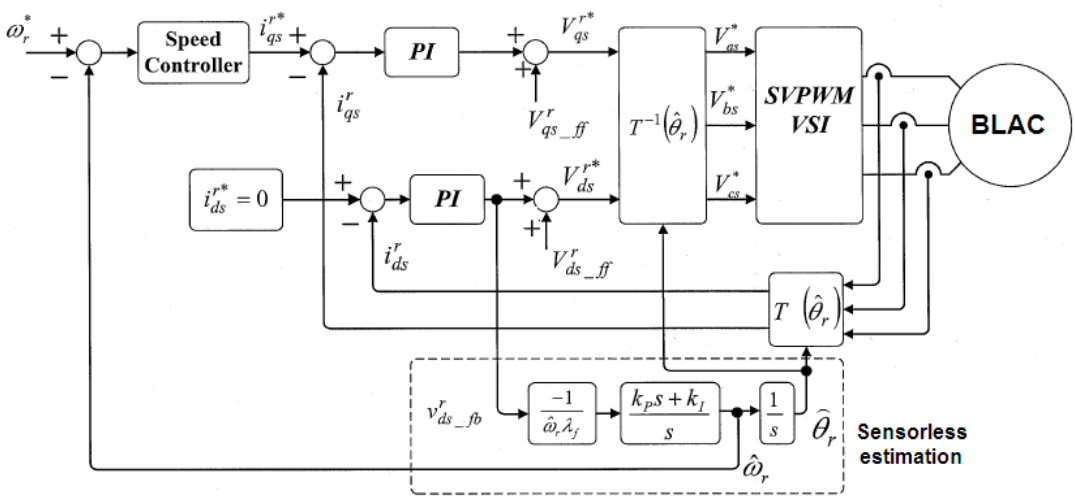

Fig. 1.9 MRAS based sensorless vector control [BAE03].

1.3 Saliency Based Methods

Alternatively, the anisotropic property of PM BLAC machines, resulting from either geometric rotor saliency, or magnetic saliency, can be exploited for sensorless position estimation. Since the machine saliency behavior is independent on the speed, the saliency based sensorless methods are expected to be reliable in the low speed range, even standstill, whereas the model based sensorless methods would fail due to lack of useful signal. In other words, the idea behind saliency based sensorless estimation can be explained that the machine winding inductance being a function of the rotor position due to saliency, and then the rotor position can be deduced from the inductance variation.

Fig. 1.10 illustrates the measured inductance variation according to electrical rotor position for salient PM BLAC machines [KAN10]. In the cross section view of the machine, the shaded rotor area is characterized by high permeability, while the white area between rotor and stator indicates the relative air gap, where the permeability is assumed to be low. It confirms that the machine inductance is modulated by the position dependent spatial saliency, however, the variation of inductance with rotor position undergoes two cycles per single electrical cycle, leading to an ambiguity of π in saliency based position estimation.

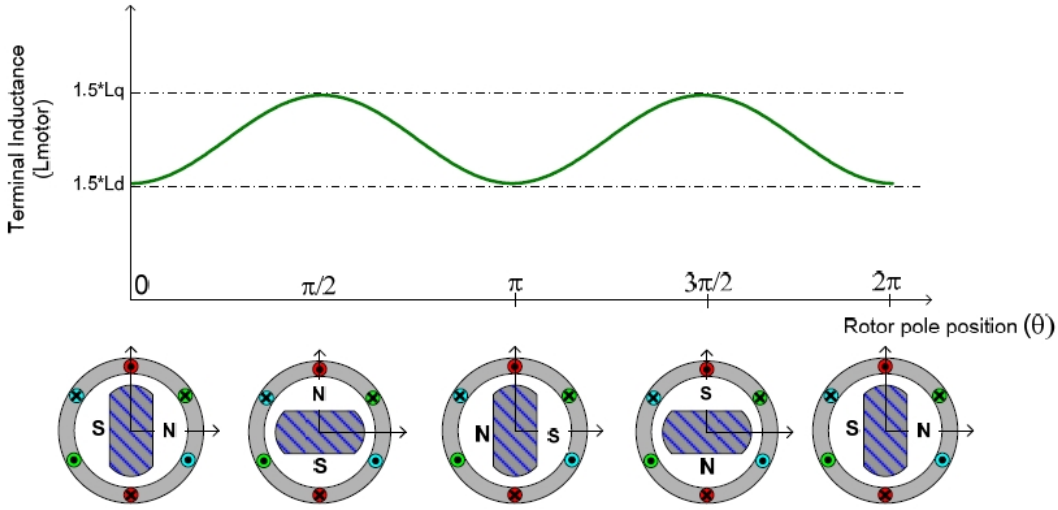

Fig. 1.10 Inductance variation according to electrical rotor position [KAN10].

In order to reveal the position information from machine saliency property, specific high frequency signal injection is necessary to evoke related position dependent response. According to the type of injected signal, the saliency based sensorless techniques can be classified into three major groups: persistent carrier signal injection, transient voltage vector injection and inherent PWM excitation without additionally injection.

1.3.1 Persistent carrier signal injection

In persistent carrier signal injection methods, a high frequency carrier signal is continuously superimposed on the fundamental excitation. The injected carrier signal interacts with the machine spatial saliency and produces rotor position dependent carrier signal response. A tracking observer can then be used to continuously extract the rotor position from the position-dependent carrier signal response.

According to the type of injected carrier signal, persistent carrier signal injection consists of a rotating sinusoidal signal injection [JAN95] [DEG98] [RAC10], a pulsating sinusoidal [COR98] [LIN02] [JAN03] [LI09b], a square wave signal injection [YOO09b] [HAM10], or arbitrary injection [PAU11].

Rotating signal injection schemes inject a balanced three phase voltage or current carrier signal (normally a voltage) in the stationary reference frame to form a rotating excitation superimposed on the fundamental excitation. The rotor position information can be deduced from the phase modulated response. For the pulsating signal injection methods, a high frequency fluctuating carrier signal (normally a voltage) is injected on the *d*- or *q*-axis in the estimated synchronous reference frame, which can be regarded as the superposition of two rotating carrier vectors with opposite rotating direction. Position is estimated through minimization of the amplitude modulated carrier frequency response signal measured along the axis orthogonal to the injection axis.

Rotating and pulsating sinusoidal carrier signal injection based sensorless methods have been well developed in the past decade, and also they are the emphasis of this thesis. Although they have simple physical principles and lower implementation cost, the limited dynamic bandwidth of system due to signal demodulation process is the major drawback.

To solve this problem, square wave signal is injected in the estimated *d*-axis [YOO09b], which eliminates the requirement of low pass filters for signal demodulation, hence sensorless dynamic performance is claimed to be remarkably enhanced with this method. In [HAM10], an effective solution with integration of pulsating square wave injection and current control loop is proposed for sensorless control of low salient surface mounted PM BLAC machines. Without use of filters, the synchronization between PWM, current control, carrier injection and demodulation provides a precise separation between the fundamental and carrier current component even under transient conditions. The proposed method allows the carrier current sampling in its maximum without any disturbance from current regulator, it is therefore very suitable for sensorless control of machines with small saliency.

The information of injected carrier signal is very important for foregoing methods, i.e., the injected carrier signal should be predefined or measured using associated sensors. Instead, an arbitrary injection with half PWM frequency square wave is presented in [PAU11]. It relies on the presence of current derivative, rather than the certain shape of injected signal. The current progression can be predicted using an isotropic machine model, meanwhile, it can also be calculated from two consecutive current measurement. From the difference between them, the saliency position information can be directly extracted. The major advantages of this scheme are higher dynamic bandwidth, and the independence of machine parameters.

1.3.2 Transient voltage vector injection

Different from the carrier signal injection based saliency tracking, the saliency position information can also be obtained through current transient response when an impulse voltage vector is applied to a salient machine. Essentially, the induced current transient response is connected with the stator inductance, which is modulated by the rotor position. Therefore, it is possible to extract the position information from the measurement of current derivative (di/dt) in response to the transient voltage vector.

The Indirect Flux Detection by On-line Reactance Measurement (INFORM) method [SCH96] [ROB04] is a typical transient injection based technique. Additional impulse

voltage vectors are superimposed during zero vector dwelling for standard PWM. Meanwhile, the current derivative is measured synchronized to the test voltage vectors.

For a standard two level voltage source inverter, the basic voltage vectors generated by the inverter are depicted in Fig. 1.11, where u_1~u_6 are active vectors, while u_0 and u_7 are zero vectors. The six active vectors can be grouped into three pairs, i.e., (u_1, u_4), (u_2, u_5), (u_3, u_6), the two vectors in the same group have identical amplitude and opposite direction, as shown in Fig. 1.11.

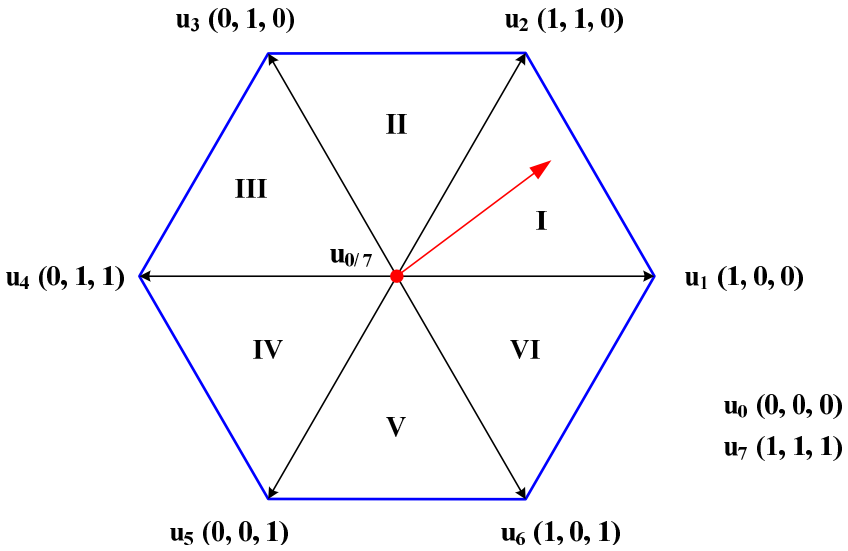

Fig. 1.11 Voltage space vectors.

In order to minimize the negative effect of additional impulse voltage vectors, the standard INFORM method applies three pairs of voltage vectors (u_1, u_4), (u_2, u_5), (u_3, u_6) in sequence to the machine during zero vector period on three successive PWM cycles, as shown in Fig. 1.12. Based on the measured current derivative (S_{u1}~S_{u6}), a position dependent position vector p can be constructed as,

$$p(q_r) = f(S_{u1}, S_{u2}, S_{u3}, S_{u4}, S_{u5}, S_{u6}) \tag{1.11}$$

From the position vector, the saliency position information can be extracted using proper position observer.

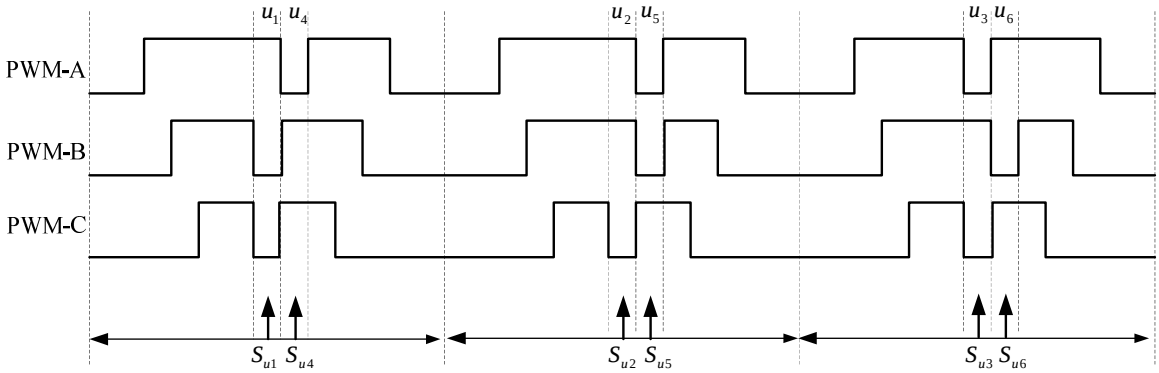

Fig. 1.12 Transient voltage vector injection for INFORM method.

Due to a minimum duration being required for the transient impulse vectors, it is difficult to obtain all *di/dt* sampling for position vector construction in one PWM cycle. Hence, three sets of test signals, each of which consisting of a pair of opposite voltage vectors, are applied on successive three PWM cycles. As a result, the position estimation would take three PWM cycles.

The major problem for the standard INFORM method is the introduced current disturbance due to addition transient voltage vectors. Furthermore, the rotor position is assumed to be constant during the successive three PWM cycles, which is reasonable for standstill and low speed operation. However, the position change could not be neglected at higher speed. To solve these problems, a compensation mechanism using double transient injection is proposed in [ROB04]. Experimental results on industrial drives verify the performance improvement with modified INFORM method.

On the other hand, with additional transient voltage vectors applied to the salient machine, the resultant zero sequence voltage for star-connection and zero sequence current derivatives for delta-connection would contain saliency position information, which also can be exploited for sensorless position estimation [HOL98] [STA06].

1.3.3 PWM excitation without additional injection

The voltage vectors used in transient voltage vector injection methods also exist in standard PWM for normal operation. Therefore, it should be possible to measure the current transient response introduced by the inherent PWM, so as to extract the saliency position information. Similar to the INFORM technique, the basic idea of PWM

excitation is also based on the saliency position modulated reactance, which can be reflected in the phase current derivative. The major advantage of PWM excitation is no requirement of additional transient voltage vector injection, which is used in the transient injection approach, and causes some problems, including additional current ripple, higher switching loss, and limited dwelling time of zero voltage vector.

The zero vector current derivative (ZVCD) method may be the simplest candidate among PWM excitation based techniques [RAU07], which does not make any change on the standard PWM. Assuming $i_d^e=0$, the current derivative on the estimated d-axis can be derived as,

$$\left.\frac{di_d^e}{dt}\right|_{u0/u7} = -\frac{R}{2}\left(\frac{1}{L_q}-\frac{1}{L_d}\right)i_q^e \sin(2\Delta q) - \frac{w j_m}{L_q}\sin(\Delta q) \tag{1.12}$$

It shows that di_d^e/dt goes to zero if the position estimation error is zero, hence it can be considered as the position error signal $f(\Delta\theta)$, which is directly fed into position observer to extract the rotor position information. The current derivative measurement is shown in Fig. 1.13.

The ZVCD scheme provides a hybrid technique, which utilizes both saliency and back-EMF for sensorless estimation. However, the condition of $i_d^e=0$ is a trade-off, in addition, the duration of zero vector should be long enough for current derivative measurement.

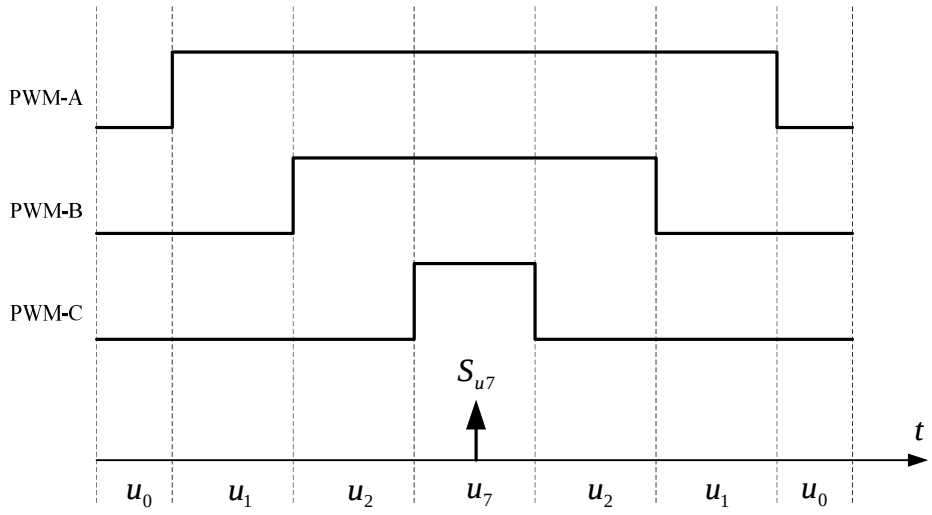

Fig. 1.13 Sampling instance for ZVCD scheme [RAU07].

Different combinations of measured current derivative in response to specific voltage vectors can be used to construct the position vector $P(\theta_r)$, from which, the saliency position information can be obtained [HOL05] [GAO07] [HUA11] [BOL11].

In [HOL05], an extended modulation (EM) scheme is presented to obtain saliency position using the current transient response introduced by modifying the PWM excitation without any additional injection. With EM technique, the voltage vector space is divided into four overlapping 120^o sectors. Referring to Fig. 1.11, sectors I and II are designated as sector I_{EM}, and sectors II and III are designated as sector II_{EM}, and so forth. In this way, the reference voltage vector lying at sector I_{EM} can be realized by active voltage vectors of u_1, u_3 and zero vectors, as shown in Fig. 1.14. The current derivative is measured under u_1, u_3, and then the position vector p can be constructed as,

$$p(q_r)_{HOL} = f(S_{u1}, S_{u3}) \tag{1.13}$$

Therefore, the position information can be instantaneously estimated in one PWM cycle. Compared with standard PWM, however, extra switching transitions can be observed on one phase, which would increase the switching loss of power devices and common mode current in the machine as well.

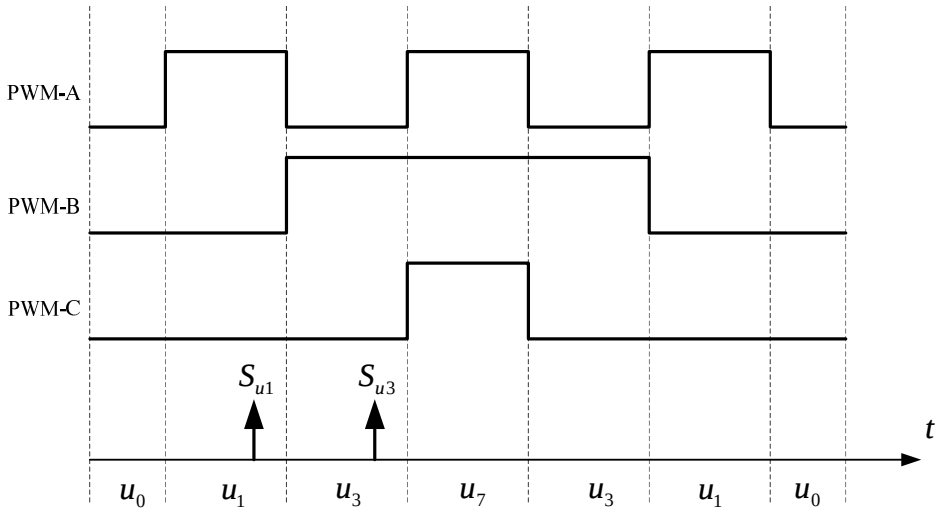

Fig. 1.14 Sampling instance for EM method [HOL05].

Compared with EM techniques, the standard PWM can also be exploited for saliency based position estimation [GAO07] [HUA11] [BOL11]. The current derivative sampling

instance for GAO's and BOL's methods is shown in Fig. 1.15 and Fig. 1.16, respectively. And the related position vectors for position estimation can be constructed as

$$p(q_r)_{GAO} = f(S_{u0}, S_{u1}, S_{u2}) \tag{1.14}$$

$$p(q_r)_{BOL} = f(S_{u0}, S_{u1}, S_{u7}, S_{u2}) \tag{1.15}$$

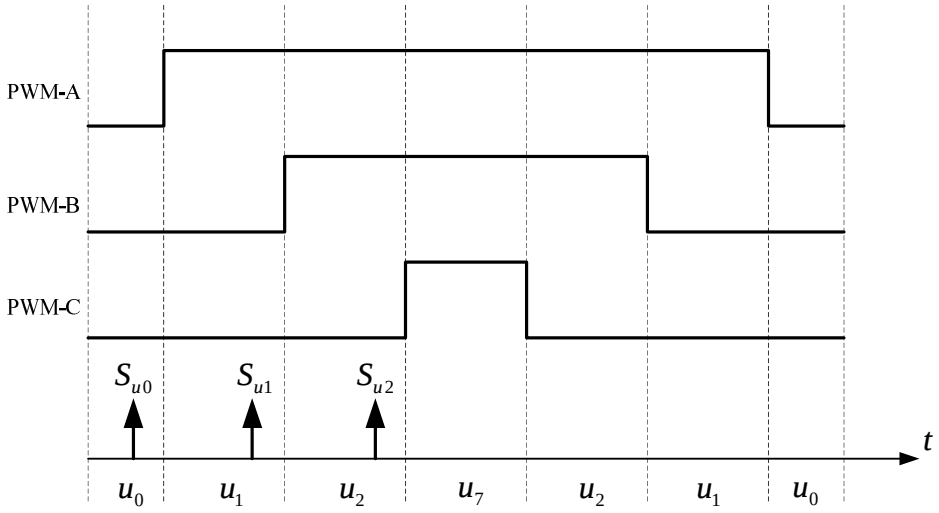

Fig. 1.15 Sampling instance for GAO's method [GAO07] [HUA11].

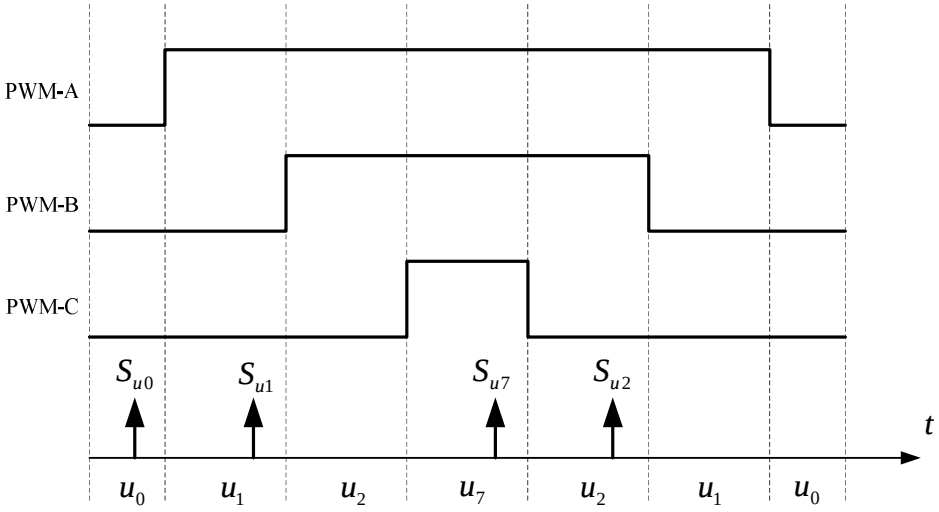

Fig. 1.16 Sampling instance for BOL's method [BOL11].

Regardless of standard or modified fundamental PWM excitation, a minimum required duration of voltage vector for current derivative measurement is a critical problem. Once a new voltage vector is applied to a machine winding, a sampling delay is required to avoid the current ringing due to parasitic effects within the drive system.

Hence, the current derivative measurement is not activated until the current oscillations settle down. Obviously, the minimum duration of voltage vector should be longer than the sampling delay, which typically varies from 5 to 25μs [GAO07].

For standard PWM excitation, the minimum duration of voltage vector could not be guaranteed at all time, since the duty cycle of the PWM is dependent on the fundamental voltage reference. To solve this problem, i.e., guarantee enough duration for specific voltage vectors, some techniques such as edge-shifting [GAO07] [HUA11] [BOL11] and extended modulation [HOL05] are presented. The basic idea is to impose the minimum duration for the required voltage vector in one half cycle of PWM, and then to apply an opposite voltage vector in the next half cycle for compensation, to keep the effective duration unchanged.

Alternatively, some different methods utilizing inherent PWM excitation for saliency based position estimation are reported in [RAU10] [LEI11].

In [RAU10], it is found that the 2nd PWM harmonic has the largest amplitude, which can be considered as a pulsating vector, rotating approximately synchronously with the fundamental voltage vector. Therefore, the resultant 2nd PWM current harmonic together with the inherent 2nd PWM voltage harmonic can be used to calculate the position dependent machine impedance. And then the position information can be extracted from position modulated impedance. The current derivative measurement is not required, however, as the amplitude and phase of the "injected" carrier voltage are determined by the fundamental operation, instead of predefined, additional voltage measurement is desirable to obtain the information of the "injected" carrier voltage. Furthermore, in order to isolate the 2nd PWM harmonics from fundamental component, high sampling frequency and a powerful microprocessor are essential to realize this kind of technique.

The zero sequence excitation introduced by standard PWM is also proven to be effective for saliency based position estimation [LEI11]. With standard PWM, zero sequence voltage would be generated, which has the same frequency as PWM. In order to make the zero sequence voltage acting on the machine, a filter is employed to connect the neutral point of star-connected machine with dc link middle point, as shown in Fig. 1.17. The filter should be properly designed to only allow high frequency zero sequence

current to pass through. From the measured current derivative at zero vector duration, the position information can be calculated using the four-quadrant arctangent function. Although higher SNR can be achieved, the requirement of additional hardware *LC* filter is a major drawback constraining the application of this technique.

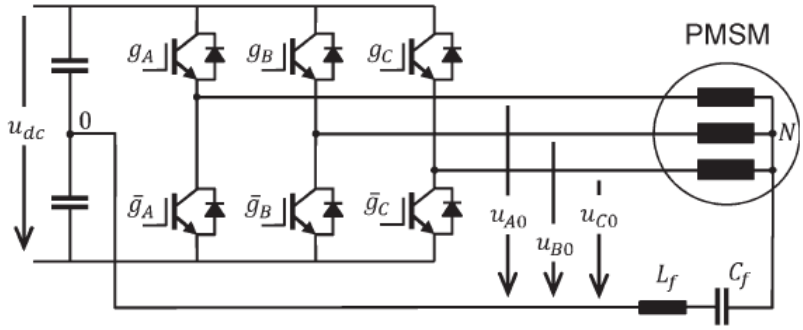

Fig. 1.17 LC filter for zero sequence injection introduced by standard PWM [LEI11].

Without additional signal injection, the inherent PWM excitation based sensorless methods are suitable for wider speed range operation. Furthermore, they have the advantage of faster dynamic performance due to high frequency PWM. However, the requirement of current derivative synchronous measurement is an obstacle to their practical applications. The PWM excitation based sensorless methods are compared in Table 1.1.

Table 1.1 Comparison of PWM excitation based sensorless methods.

Methods	**Principle**	**Current Derivative measurement**	**Voltage Measurement**	**Additional Hardware**
[RAU07] (ZVCD)	Back-EMF + Saliency	√	X	X
[HOL05]	Reactance measurement	√	X	X
[GAO07] [HUA11]	Reactance measurement	√	X	X
[BOL11]	Reactance measurement	√	X	X
[RAU10]	2nd PWM harmonic	X	√	X
[LEI11]	Zero sequence injection	√	X	√

√: required X: no requirement.

1.3.4 Current derivative measurement

From previous discussion, current derivative measurement is important for instantaneous reactance measurement based sensorless methods, regardless of whether they have or didn't have additional transient injection.

The simplest approach is using derivative calculation from two consecutive current measurements in a short time [RAU07]. Although no additional sensor is required, this method demands a high performance AD converter for current measurement to suppress the noise disturbance. In [OGA98], two 8-bit AD converters with a channel multiplexer were used to directly measure the current derivative. It is cost effective in terms of AD conversion, however, the hardware configuration is very complex.

The Rogowski coil is widely accepted in current derivative measurement due to its high bandwidth, wide measurement range, low power consumption and insensitive to temperature variation [BOL11]. However, it is criticized for high parasitic oscillations at changes of current derivative, additionally, the behavior of Rogowski coils is significantly influenced by the coil geometry [HOL05] [HUA09].

For comparison, an air-cored mutual inductor is proven to be a better solution for current derivative measurement [HOL05] [HUA09], since the highly coupled design of mutual inductor gives rise to lower parasitic inductance and capacitance, and so lower parasitic oscillations. Two examples of air-cored mutual inductor are shown in Fig. 1.18.

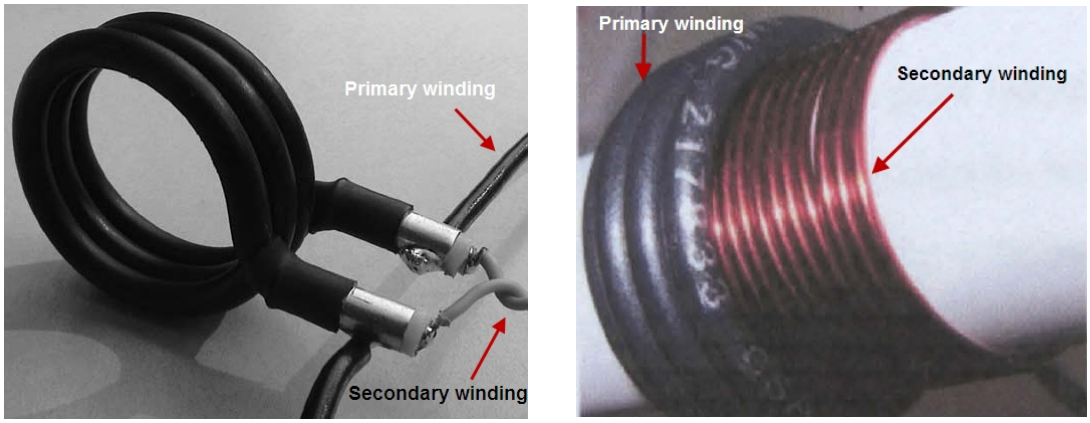

(a) [HOL05] (b) [HUA09]

Fig. 1.18 Air-cored mutual inductor for current derivative measurement

1.3.5 Comparison of saliency based sensorless methods

Three types of saliency based sensorless techniques are reviewed in this section (persistent carrier signal injection, transient voltage vector injection and PWM excitation without any injection), the comparison between them are illustrated in Fig. 1.19.

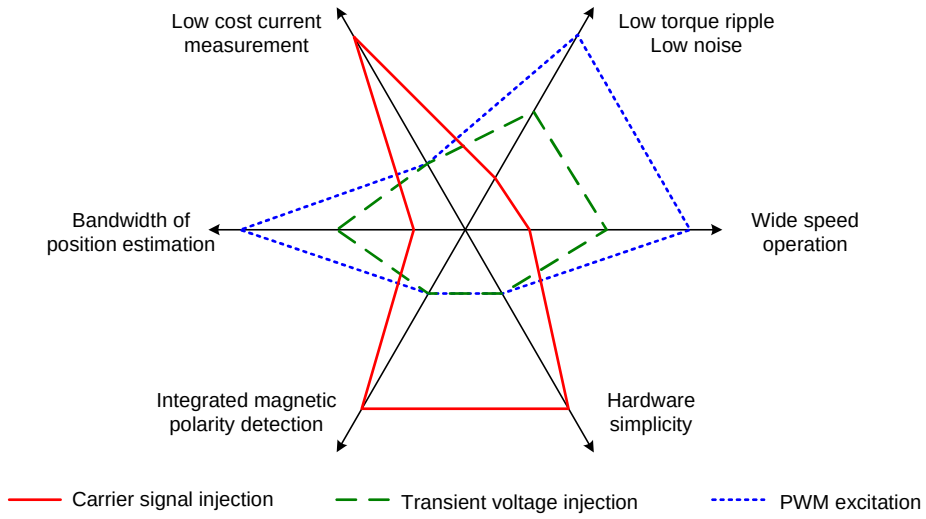

Fig. 1.19 Comparison of saliency based sensorless methods.

1.4 Direct Torque Control and Sensorless Predictive Torque Control

DTC is an inherently sensorless technique. The basic principle of DTC is to select stator voltage vectors according to the differences between the reference and actual torque and flux linkage. DTC is implemented in the stationary reference frame without coordinate transformation, hence the rotor position is not required for this purpose. Flux estimation is a critical concern in DTC, which is normally obtained by the combined flux observer, as shown in Fig. 1.6. In which, the voltage model, which is dominant at middle and high speed, does not need the position information; however, the current model requires the position information to estimate the flux at low speed and standstill. Consequently, position information is also required in DTC for standstill and very low speed operation. The integration of saliency based sensorless technique and DTC provides a significant enhancement of torque response for PM BLAC machines wide speed operation [SIL06] [AND08].

As an alternative to CVC and DTC, sensorless PTC scheme is presented in [LAN10]. According to the measured current $i_s[k]$, the current in next step $i_s[k+1]$ can be exactly predicted from applied voltage vector and time duration for an isotropic machine. For a salient machine, however, the predicted current would deviate from the real one due to additional position dependent part. Hence, the difference between predicted and measured $i_s[k+1]$, which contains the position information, can be used to extract the rotor position, as shown in Fig. 1.20.

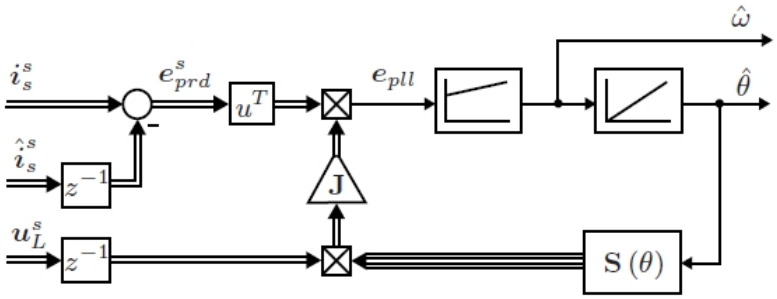

Fig. 1.20 Sensorless position estimation using current prediction [LAN10].

With this scheme, the position information can be estimated without any additional voltage injection. Compared with PWM excitation methods, current derivation measurement is not required. However, accurate machine parameters are required in this method for current prediction.

1.5 Outline and Contributions of the Thesis

Sensorless control methods for PM BLAC machines have been broadly reviewed in this chapter, while the saliency based persistent carrier signal injection method is the emphasis of this thesis.

The thesis is organized in the following chapters:

Chapter 2 gives a detailed description about the experimental setup, including hardware platform and software implementation of sensored current vector control.

Chapter 3 describes the rotating and pulsating carrier signal injection based sensorless techniques in detail, and the comparative study between them is given. In

addition, some practical issues in sensorless implementation, involving compensation of cross-saturation effect and position tracking observer, are discussed in this chapter. Finally, a robust magnetic polarity detection scheme is developed, and integrated into conventional carrier signal injection based sensorless methods.

Chapter 4 focuses on the investigation of machine saliency information for saliency based sensorless techniques. An experimental procedure is presented to measure the saliency circle, which visually reveals the machine saliency information, including magnetic saturation and cross-saturation effects.

Chapter 5 proves that inverter nonlinearity effects, especially the deadtime and parasitic capacitance, are the critical issues for carrier signal injection based sensorless control. Utilizing the distortion of positive sequence carrier current due to inverter nonlinearity effects, a novel on-line post-compensation scheme is developed for rotating carrier signal injection based sensorless techniques.

Chapter 6 improves the sensorless operation performance from the optimal efficiency point of view. With on-line continuous searching of current working point in steady state, the optimal machine efficiency can be tracked in sensorless operation.

Chapter 7 summarizes this research work and gives some discussions about future work.

The major contributions of this thesis are:

- Based on magnetic saturation effect, a robust magnetic polarity detection scheme is proposed and successfully integrated into conventional carrier signal injection based sensorless methods with slight increase of computational load.
- A pure experimental method is presented to measure machine saliency circle, which visually reveals the machine saliency information without any requirement of machine parameters. Based on the measurement results, Sensorless Safety Operation Area (SSOA) is introduced to investigate the effectiveness of sensorless operation for practical applications.

- Inverter nonlinearity effects are studied from the respects of theoretical analysis and experimental measurement. Utilizing the distortion of positive sequence carrier current due to inverter nonlinearity effects, a novel on-line compensation scheme is developed for rotating carrier signal injection based sensorless methods.
- From the efficiency point of view, on-line continuous searching algorithm is employed in sensorless operation to improve the machine efficiency without any requirements of compensation methods on nonlinear effects.

The publications originating from this Ph.D. research work are listed in Appendix 7.

CHAPTER 2

EXPERIMENTAL SYSTEM

2.1 Introduction

The experimental system is constructed based on a TMS320C31-50 digital signal processor (DSP), which is a 32-bit, floating-point processor manufactured in 0.6 mm triple-level-metal CMOS technology. Since TMS320C31-50 is a pure DSP with limited peripheral functions, additional interface boards are built to fulfill the whole system. The block diagram of whole experimental rig is shown in Fig. 2.1. The test rig is built by former Ph.D. students in the Electrical Machines and Drives Group of University of Sheffield.

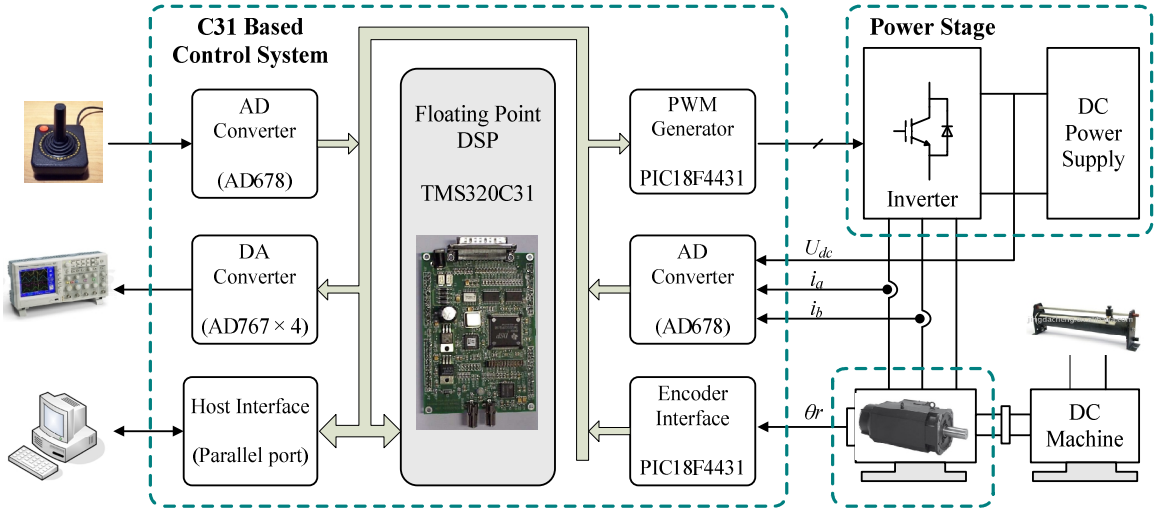

Fig. 2.1 Setup of experimental system.

2.2 Control System

2.2.1 DSP starter kit

The heart of control system is the TMS320C3x DSP Starter Kit (DSK), which is populated with a TMS320C31-50 floating point DSP running with a 50MHz external oscillator. The digital-signal-processing instruction sets have the speed of 25 Million Instructions per second. The DSK board communicates with host PC through parallel

printer port. Upon reset, the host PC downloads a communications kernel to the DSP using the bootloader. This communications kernel provides a set of low-level routines that allow the host PC and the DSP to exchange information and perform debugging functions.

It should be noted that only assembly language source program is supported by the development software. Hence, the software programming is a time consuming work compared with C or Matlab based code generation. The C31 DSP only has 2k bytes on-chip memory, which is another limitation for some applications.

Around the DSK board, several interface boards including analog to digital conversion, encoder interface, PWM generation and digital to analog conversion can be accessed by the DSP through an external memory interface.

2.2.2 Analog to digital conversion

The machine phase current is measured by the current transducers, LEM LA25-NP. Using analog conditioning circuits, the current output from transducers is transformed to a bipolar voltage signal. After that, the bipolar voltage signal is converted to a digital signal by a 12 bits AD converter (AD678). The ratio between the machine phase current and analog conditioning circuit output voltage is designed to be 5V/12.5A. The input to the AD converter has a full-scale range of -5V to 5V. In order to obtain the real current value for C31 DSP, a scale of k_i is required in software, which should satisfy,

$$i_x = i_x \cdot \frac{5V}{12.5A} \cdot \frac{4096}{10V} \cdot k_i \qquad (2.1)$$

Then k_i can be derived, as $k_i \approx 0.0061$.

In order to measure the DC bus voltage, a voltage transducer LV 25-P is used. With the voltage transducer and analog conditioning circuits, the DC link voltage of 300V is converted to a +5V voltage signal, which is the input of the AD converter (AD678). In the same way, the software scale for voltage measurement can be derived as,

$$k_v = \frac{5V}{2048} \cdot \frac{300V}{5V} \approx 0.1465 \qquad (2.2)$$

Considering the tolerance of components in practice, it is strongly recommended to fine adjust the scale by experimentation. The fine tuned scales through experiment are k_i≈0.0056 and k_v≈0.1538, which are slightly different from the designed values.

2.2.3 Encoder interface and position alignment

To verify the accuracy of sensorless position estimation, a dedicated rotor position detection board based on PIC18F4431 MCU is included to supply the DSP with the real rotor position from an optical encoder with the resolution of 2048PPR.

Before the sensorless algorithm development, it is desirable to implement the sensored current vector control, in which the position information from the encoder is used for forward and inverse park transformation. It is necessary to align the zero position of position sensor to the magnet axis (*d*-axis), as shown in Fig. 2.2. Typically, the 3-phase back electromagnetic force (EMF) is a good reference for initial position alignment.

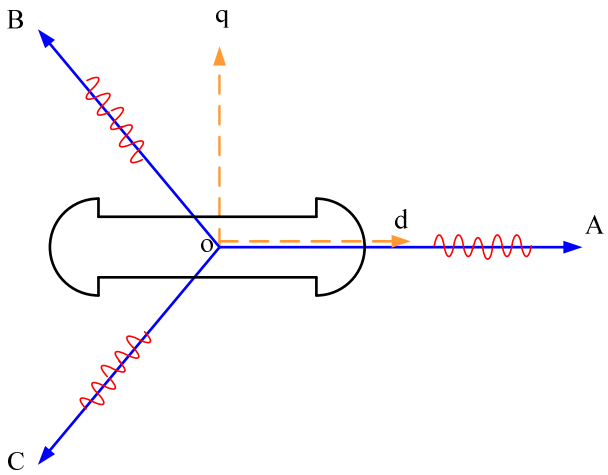

Fig. 2.2 Rotor position alignment.

Spun by load machine, the 3-phase back-EMF of PM BLAC machine can be measured from the machine winding terminals. For the case where a machine neutral point could not be accessed, the phase back-EMF can be calculated from the measured line back-EMF. Take phase-A back-EMF as an example,

$$e_a = \frac{1}{3}(e_{ab} - e_{ca}) \tag{2. 3}$$

It should be noted that the calculated phase back-EMF from measured line back-EMF would cancel the 3rd harmonic component.

Without consideration of harmonic components, the back-EMF in synchronous reference frame can be expressed as,

$$\begin{bmatrix} e_d \\ e_q \end{bmatrix} = \begin{bmatrix} 0 \\ w_r y_m \end{bmatrix} \tag{2. 4}$$

where ψ_m is the flux linkage due to permanent magnet. Transforming to stationary reference frame, it yields,

$$\begin{bmatrix} e_a \\ e_b \\ e_c \end{bmatrix} = \begin{bmatrix} \cos q_r & -\sin q_r \\ \cos(q_r - 2p/3) & -\sin(q_r - 2p/3) \\ \cos(q_r + 2p/3) & -\sin(q_r + 2p/3) \end{bmatrix} \begin{bmatrix} e_d \\ e_q \end{bmatrix} = \begin{bmatrix} -\sin q_r \\ -\sin(q_r - 2p/3) \\ -\sin(q_r + 2p/3) \end{bmatrix} w_r y_m \tag{2. 5}$$

The above equation shows that with positive rotation, the fundamental phase-A back-EMF should cross zero in the negative direction when the electrical rotor position is zero. By way of example, the position information can been well aligned for the prototype machine, as shown in Fig. 2.3.

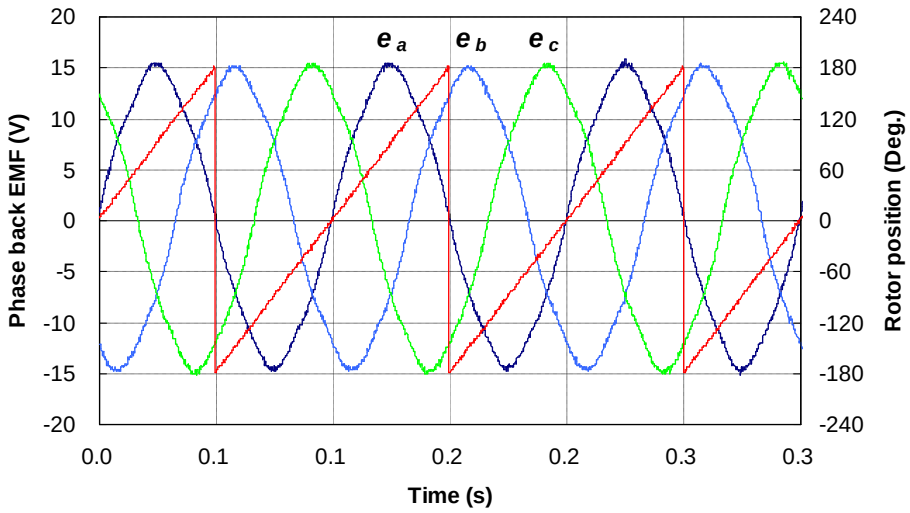

Fig. 2.3 Aligned rotor position information against phase back-EMF.

2.2.4 PWM generator

Due to lack of PWM generator within the C31 DSP, a PC18F4431 MCU is employed to receive the duty cycle from DSP, and then output PWM signals to the power stage.

Although space vector PWM (SVPWM) has become an industrial standard, the required computation effort is a big challenge for the C31 DSP. In this work, the zero sequence signal injection based method is utilized to generate the modulation wave, since it is computationally less intensive than SVPWM while keeping symmetrical placement of zero vectors [HAV98].

For 3-phase reference signals shown in Fig. 2.4(a), a zero sequence signal can be defined as,

$$V_o = -\frac{1}{2}\{\max(V_a, V_b, V_c)\} + \min(V_a, V_b, V_c)\} \tag{2. 6}$$

and then, the modulator signals can be generated as,

$$\begin{cases} V_a' = V_a + V_o \\ V_a' = V_a + V_o \\ V_a' = V_a + V_o \end{cases} \tag{2. 7}$$

Compared with the SVPWM strategy, the modulator reference signals have similar shape, as shown in Fig. 2.4(b). More detailed explanation about this modulation scheme is presented in [HAV98].

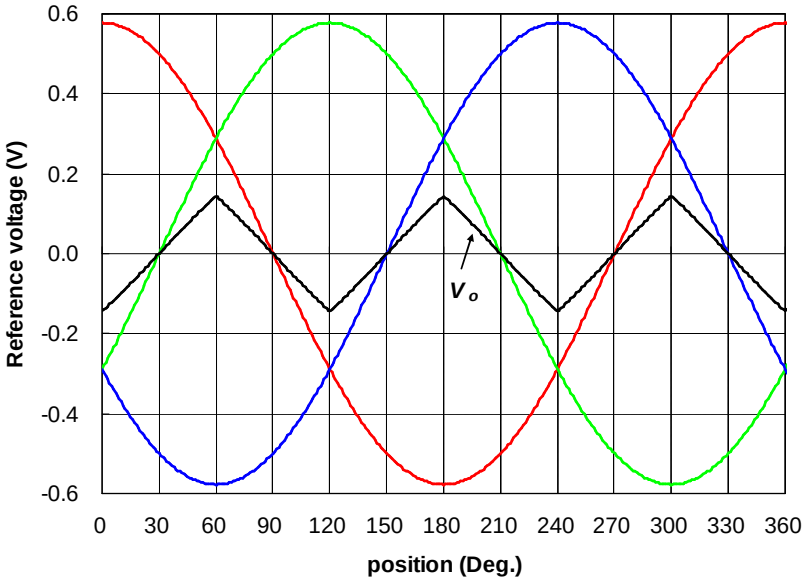

(a) 3-phase reference voltage

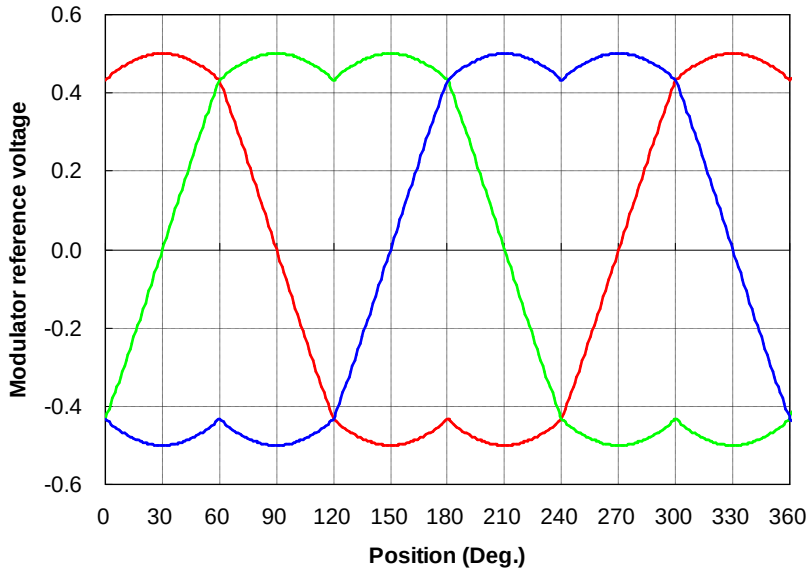

(b) Modulator signal

Fig. 2.4 Zero sequence signal injection based modulation strategy.

2.2.5 Digital to analog conversion

Four 12-bit digital to analog (DA) converters (AD767) convert the digital variables in the C31 DSP to analogue voltage signal. Therefore, digital variables inside the DSP can be monitored and recorded via an oscilloscope in real time. All the DA converters are working in bipolar mode, i.e., the input digital signal 0 to 4095 will be converted to an analogue signal from –5 to +5 volt.

2.3 Power Stage

The power stage is constructed based on a PS21255, an intelligent power module from Mitsubishi. It integrates a 600V, 20A, 3-phase IGBT inverter bridge with gate drive and related protection functions. This integration structure significantly simplifies the external circuits, and increases overall reliability of the drive system. For galvanic isolation between control system and power stage, the opto-coupler, HCPL-4506, is used to pass the gate drive signals from the PWM generator to the power stage. Meanwhile, two transformers with four channels of isolated DC voltage output (+15V) provide power supply for the gate drive circuits. Fig. 2.5 shows the picture of power stage.

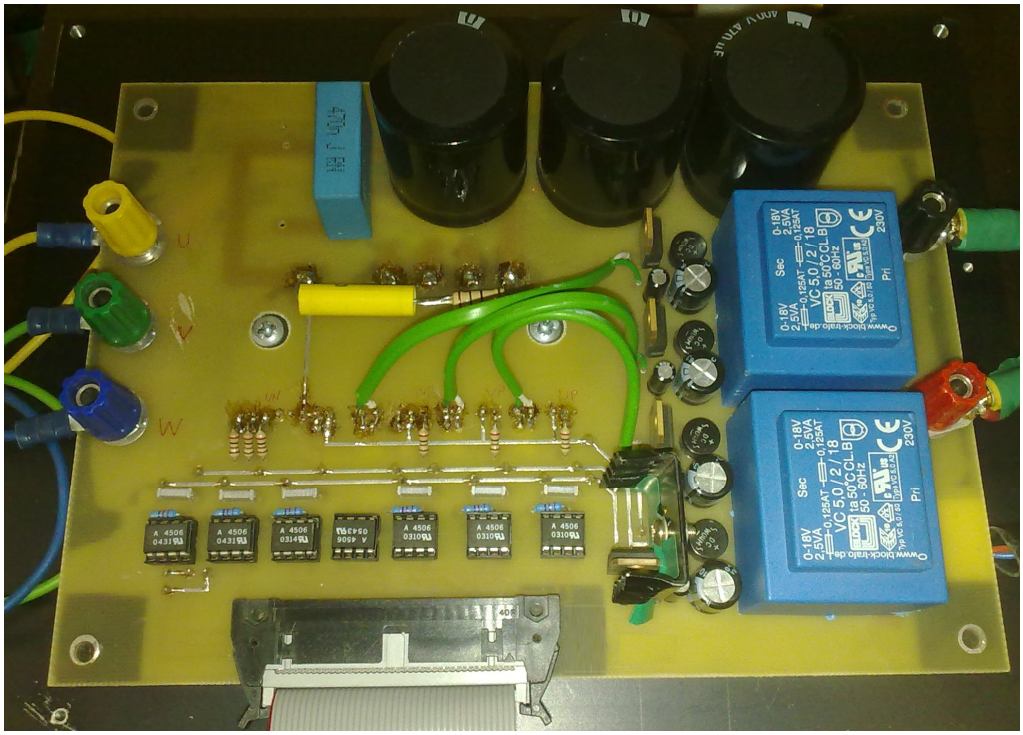

Fig. 2.5 Photograph of power stage [LI09a].

2.4 Prototype Machine

The prototype machine is a 3-phase PM BLAC machine with interior circumferential rotor configuration. The machine is made by Control Techniques Ltd., while the rotor is re-designed by the Electrical Machines and Drives Group of University of Sheffield [CHE99]. The major parameters of the prototype machine are shown in Table 2.1. And the detailed machine parameters are listed in Appendix 1.

Table 2.1 Parameters of prototype BLAC machine.

Rated voltage (peak)	158V
Rated current (peak)	4.0A
Rated power	0.6kW
Rated speed	1000rpm
Rated torque	4.0Nm
Pole numbers	6
Stator resistance (R_s)	6.0Ω

The cross-section of prototype machine is shown in Fig. 2.6. The stator is skewed by 20° mechanical degrees for reducing the cogging torque and sinusoidal back-EMF.

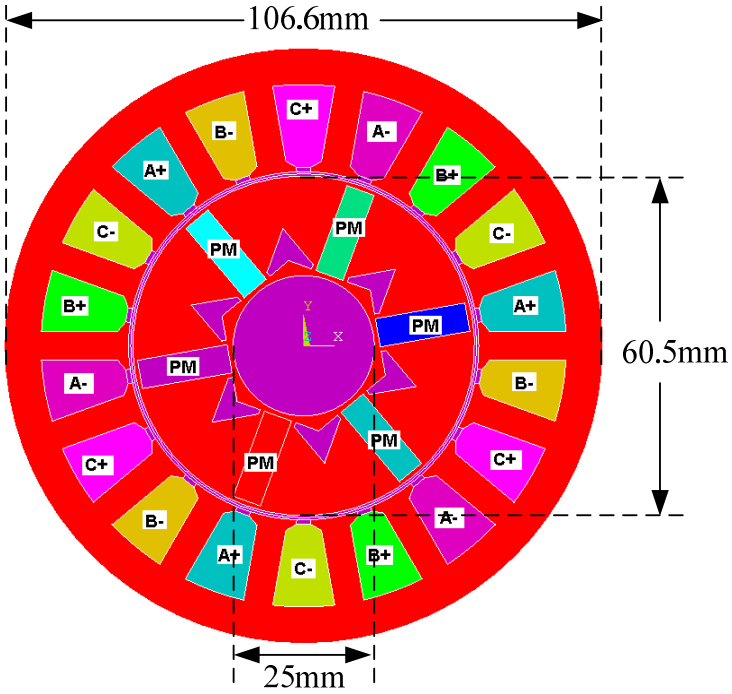

Fig. 2.6 Cross-section of prototype machine [LI09a].

Fig. 2.7 shows the calculated phase back-EMF from measured line back-EMF of the prototype machine at the speed of 200RPM (*f=10Hz*), in which the rotor position information comes from the aligned position sensor. From the measured back-EMF vector, it can be seen that some harmonics, especially the 5th harmonic, exist in the prototype machine due to a non-sinusoidal flux distribution. Using spectral analysis, the dominant 5th harmonic can be confirmed in Fig. 2.8. The amplitude ratio of 5th harmonic to fundamental component can be calculated as 3.0%.

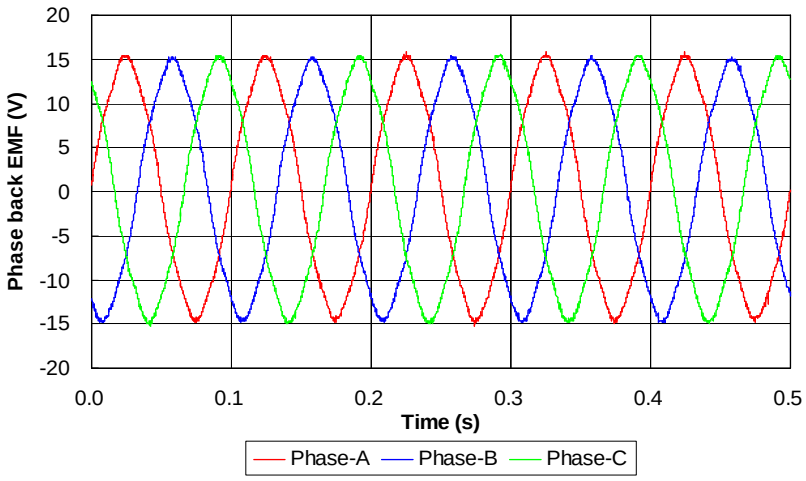

(a) Back-EMF in time domain

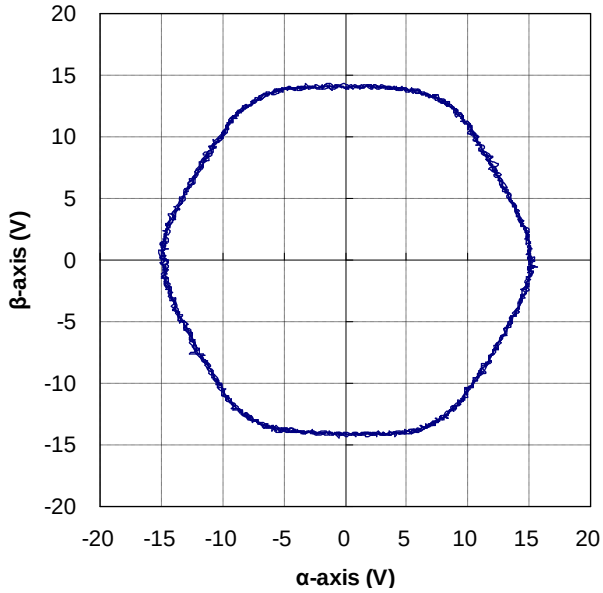

(b) Back-EMF in stationary reference frame

Fig. 2.7 Phase back-EMF for prototype machine (*f=10Hz*).

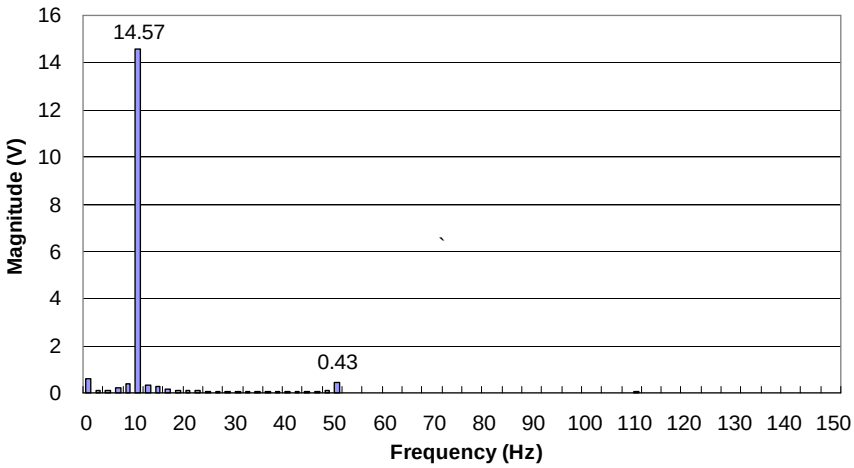

Fig. 2.8 Spectrum of phase A back-EMF (*f=10Hz*).

2.5 Load Machine

A DC generator, Table 2.2, is directly coupled to the BLAC machine as a mechanical load. A power resistor is used to dissipate the generated power from the generator. The magnet field of the DC generator is externally excited by a DC power supply. Therefore, the load condition can be adjusted by changing the field excitation current or the power resistance.

Table 2.2 Parameters of DC generator.

Rated voltage	220V
Rated current	8.0A
Maximum speed	3000rpm

According to the operation principle of DC machine, the load torque generated by the DC machine can be expressed as,

$$T_L = \frac{k i_f^2 w_m}{R_a + R_L} \tag{2. 8}$$

where k is constant, i_f is the excitation current of field winding, ω_m is the mechanical angular speed of machine shaft. R_a and R_L is machine armature resistance and load resistance, respectively. For given field current i_f and load resistance R_L, it can be seen that the generated load torque is proportional to the shaft speed. Then, equation (2.8) can be simplified as,

$$T_L = B_L w_m \tag{2. 9}$$

where $B_L = k i_f^2/(R_a+R_L)$, it is constant for given i_f and R_L. Hence, the generated load torque by the DC generator is speed dependent.

2.6 Current Vector Control

Fig. 2.9 illustrates the block diagram of current vector control for PM BLAC machine with maximum torque per ampere (MTPA) algorithm. Although the LPFs in *dq*-axis current feedback path should be avoided in terms of higher dynamic bandwidth (BW) of current loop, they are essential for filtering the carrier current components when a persistent carrier voltage signal is injected into the machine for saliency based sensorless position tracking. For commonly used *d*-axis pulsating injection technique, the LPF for *q*-axis current can be omitted since the majority of carrier current stays at *d*-axis if the position estimation error is small.

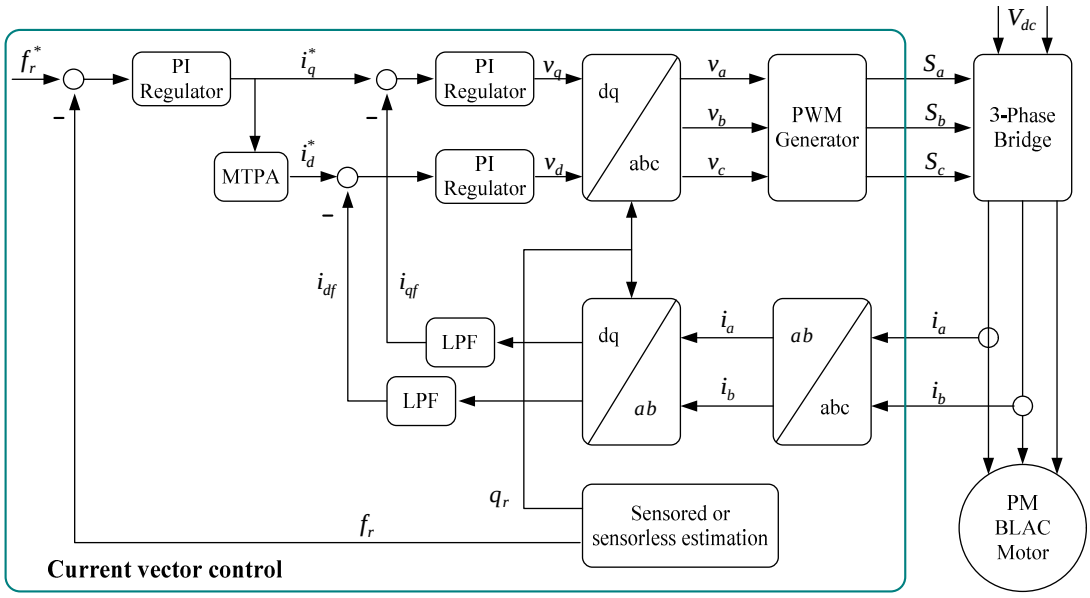

Fig. 2.9 Current vector control for PM BLAC machine.

2.6.1 Design of current regulator

As the inner loop in the current vector control system, the design of *dq*-axis current regulators is very important. With proportional integral (PI) current regulator, the block diagram of *dq*-axis current control loops accounting for practical time delay can be expressed as Fig. 2.10 [BLA98].

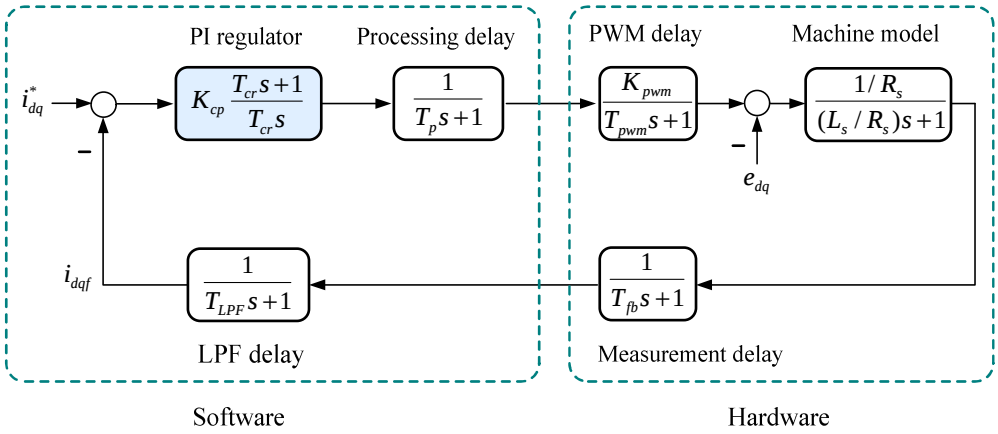

Fig. 2.10 Block diagram of current control loop [BLA98].

Accounting for the time delay including processor computation delay T_p, pulse width modulation (PWM) delay T_{pwm}, current measurement delay T_{fb} and low pass filter (LPF) delay T_{LPF}, the open loop transfer function for current loop can be expressed as,

$$G_{oi}(s)=\frac{K_pK_{pwm}(T_{cr}s+1)/R_s}{T_{cr}s(T_is+1)(T_ps+1)(T_{pwm}s+1)(T_{fb}s+1)(T_{LPF}s+1)} \tag{2.10}$$

where T_{cr} is the configurable time constant of current regulator, $T_{cr}=K_p/K_i$. T_i is the electrical time constant of machine, $T_i=L_s/R_s$. Typically, T_i is dominant compared with other time delay. In order to simplify the transfer function, an equivalent time constant T_{eq} can be defined as,

$$T_{eq}=T_p+T_{pwm}+T_{fb}+T_{LPF} \tag{2.11}$$

and then (2.10) can be re-written as,

$$G_{oi}(s)=\frac{K_pK_{pwm}(T_{cr}s+1)/R_s}{T_{cr}s(T_is+1)(T_{eq}s+1)} \tag{2.12}$$

Referring to the standard second order system, the parameters of PI current regulator is configured with a damping factor of 0.707,

$$\begin{cases} T_{cr}=T_i \\ K_p=\dfrac{R_sT_i}{2K_{pwm}T_{eq}} \end{cases} \tag{2.13}$$

Therefore, the open loop transfer function for current loop can be simplified to be,

$$G_{oi}(s)=\frac{1/(2T_{eq}^2)}{s^2+s/T_{eq}} \tag{2.14}$$

In this way, the close loop transfer function for the current loop has a standard form of second order system,

$$G_{ci}(s)=\frac{1/(\sqrt{2}T_{eq})^2}{s^2+s/T_{eq}+1/(\sqrt{2}T_{eq})^2} \tag{2.15}$$

For this kind of close loop system, the bandwidth defined by -3dB amplitude response would be substantially higher than the bandwidth defined by -45 degrees phase fall [BLA98], therefore, the latter definition is normally set as close loop bandwidth f_{cb} of current loop,

$$f_{cb}=\frac{\sqrt{3}-1}{4pT_{eq}}\approx\frac{1`}{17.17T_{eq}} \tag{2.16}$$

It clearly shows that the dynamic performance of current loop is determined by the equivalent time constant T_{eq}. For double current sampling and PWM double update

system without LPF in current feedback path, $T_{eq} \approx 0.75/f_s$, then the related current controller bandwidth can be calculated as $f_s/12.9$, which is the upper limitation of current control bandwidth for a DSP-based current vector control [WAN10]. Similarly, for single current sampling and a PWM single update system without LPF in the current feedback path, the theoretical maximal bandwidth is $f_s/25.8$.

2.6.2 Test of current regulator

In this work, single current sampling and PWM single update are employed with a current sampling frequency of 5kHz, then the equivalent time constant for the *q*-axis current loop without LPF is $T_{eq} \approx 0.3ms$, and the theoretical maximal bandwidth of current controller can be derived, to be around 194Hz. However, for the *d*-axis current loop, a software LPF is essential to remove the carrier current component in the synchronous reference frame, which would inevitably degrade the bandwidth of current controller. Here, two 1st-order LPFs with time constant of 0.8ms in series are used in the *d*-axis to filter out the carrier current ripple. With fine tuned current PI regulators, the measured *dq*-axis current step responses are shown in Fig. 2.11. It can be seen that the *q*-axis current has a rise time of 2.6ms, while the *d*-axis current has a longer rise time of 6.0ms. Using the 1st-order LPF fitting the curve of current response [WAL06], then the bandwidth of *dq*-axis current control loop can be approximated as 135Hz and 58Hz, respectively.

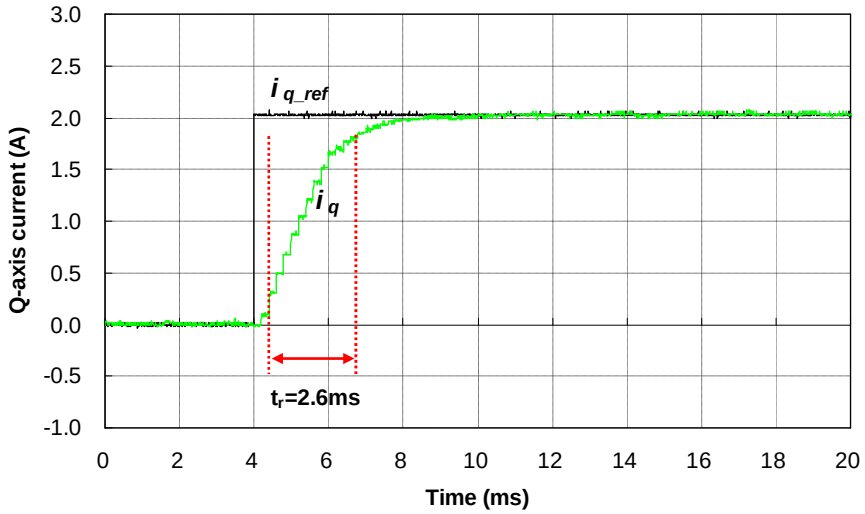

(a) *q*-axis current step response

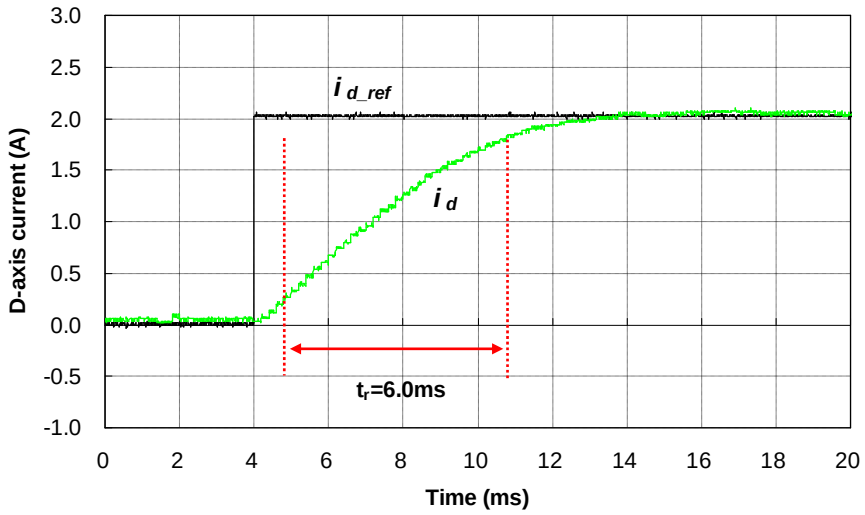

(b) *d*-axis current step response

Fig. 2.11 Current step responses.

In order to check if the designed current regulator is acceptable for carrier signal injection based sensorless control, it is necessary to make sure the carrier voltage distortion introduced by the current regulator is as little as possible. For this purpose, a pulsating carrier voltage with amplitude of 35V and frequency of 330Hz is injected along the *d*-axis during sensored operation mode, and the output signals of the *dq*-axis current regulator are recorded, as shown in Fig. 2.12. Carrier current ripple can be observed on the *d*-axis, instead of the *q*-axis. Regarding to the output signal of the current regulator, it can be found that the carrier frequency voltage ripple occurs at the output *d*-axis voltage. Considering the limited ripple amplitude (1.2V), this can be neglected when compared with the amplitude of the injected carrier voltage (*1.2/35≈3%*). Consequently, the designed current regulators are acceptable for d-axis pulsating injection based sensorless control. However, when the rotating carrier voltage signal injection based sensorless method is used, a LPF should be utilized in the *q*-axis current feedback, since carrier current ripple exists even when the estimated position error is zero. Inevitably, the introduced time delay due to the LPF would degrade the systems dynamic performance.

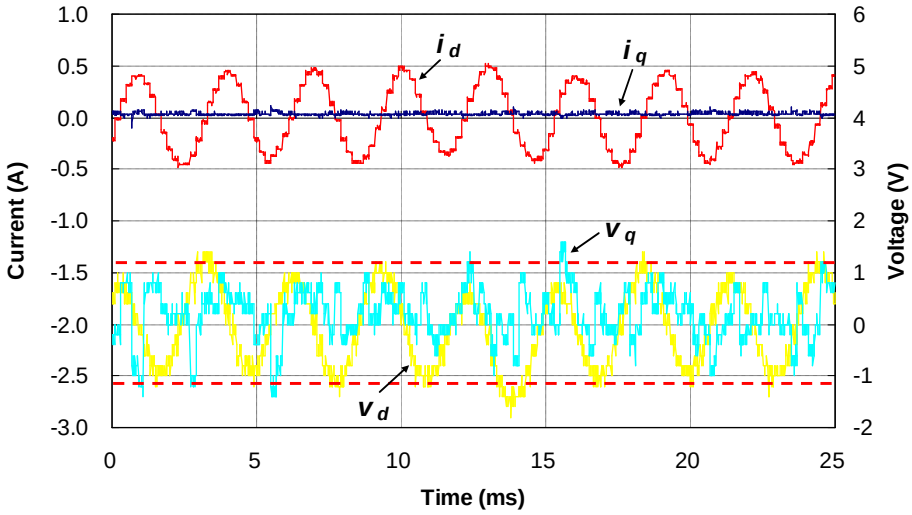

Fig. 2.12 Carrier current and output of current regulator

2.6.3 Speed regulator

The mechanical systems dynamic performance is governed by the mechanical equation,

$$J\frac{dw_m}{dt} = T_{em} - T_L - B_o w_m \tag{2.17}$$

where J is the total inertia of the shaft, T_{em} is the electromagnetic torque generated by the prototype machine, T_L is the load torque applied to the shaft by the DC generator, and B_o is viscous friction coefficient. Substituting (2.9) into (2.17) yields,

$$w_m = \frac{T_{em}}{sJ + (B_o + B_L)} = \frac{T_{em}/(B_o + B_L)}{sJ/(B_o + B_L) + 1} = \frac{T_{em}/(B_o + B_L)}{t_m s + 1} \tag{2.18}$$

where the mechanical time constant τ_m, defined by $J/(B_o+B_L)$, is an important parameter in the design of speed regulator. Equation (2.18) shows that the relationship between mechanical speed and electromagnetic torque has the behavior of standard 1st-order low pass filter, and the time constant is τ_m. Typically, compared with the electrical time constant of machine, the mechanical time constant τ_m is dominant in the control loop. Hence, the machine mechanical model can be simplified as,

$$G_m(s) = \frac{f_r}{i_q^*} = \frac{K_t}{t_m s + 1} \tag{2.19}$$

where f_r is the electrical frequency, and k_t is torque constant. With a PI-type speed regulator, the block diagram of speed control loop can be depicted as Fig. 2.13.

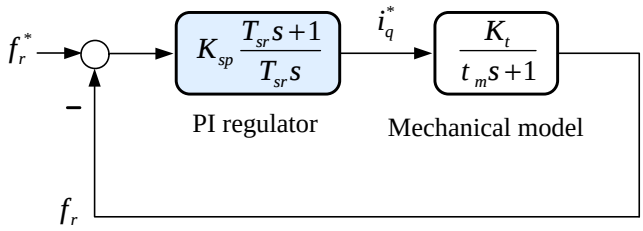

Fig. 2.13 Block diagram of speed control loop.

In order to obtain the machine mechanical model parameters, the machine run out test is employed, which does not require a torque transducer. With a given i_f and R_L for the load machine, the fundamental excitation of (i_d=0A, i_q=2A) is applied to the prototype BLAC machine, then the machine would spin at a specific speed. At steady state, cutting off the fundamental excitation for the prototype machine, the system runs out until zero speed is achieved due to friction loss. The speed response during this process can be measured, as shown in Fig. 2.14.

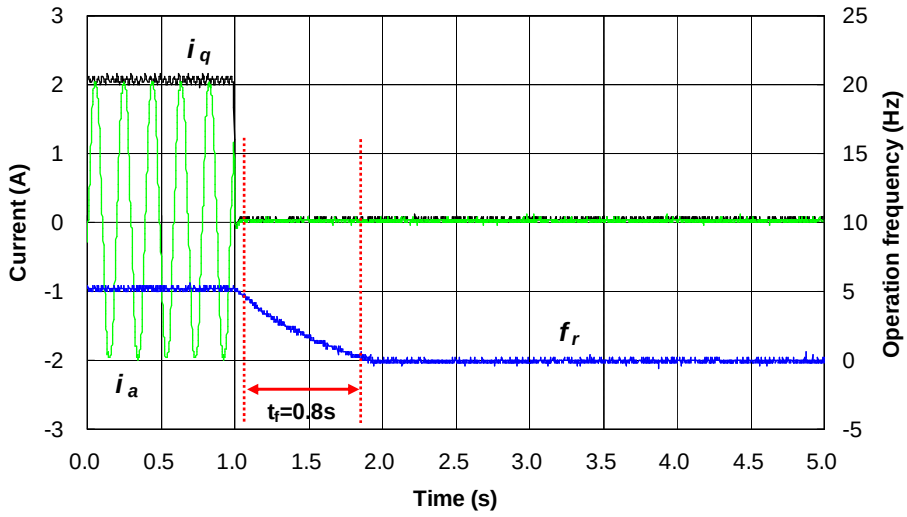

Fig. 2.14 Measurement of machine mechanical model.

From the steady state frequency, the torque constant can be calculated as k_t=2.5/A. From the measured speed response, the fall time t_f from 90% to 10% can be easily obtained, as indicated in Fig. 2.14. According to the characteristic of 1st-order low pass filter, the time constant should satisfy,

$$t_m \approx \frac{t_f}{2.2} \tag{2.20}$$

Consequently, the machine mechanical model can be obtained from the experiment,

$$G_m(s) = \frac{f_r}{i_q^*} = \frac{2.5}{0.364s + 1} \tag{2. 21}$$

Although the dynamic performance of the speed control loop can be adjusted by the speed regulator in theory, the maximum rate of speed change is limited by the inertia and the maximum electromagnetic torque. For the prototype machine with a current limit of 4.0A, coupled with a high inertial DC generator, the speed step response with well tuned speed regulator is shown in Fig. 2.15.

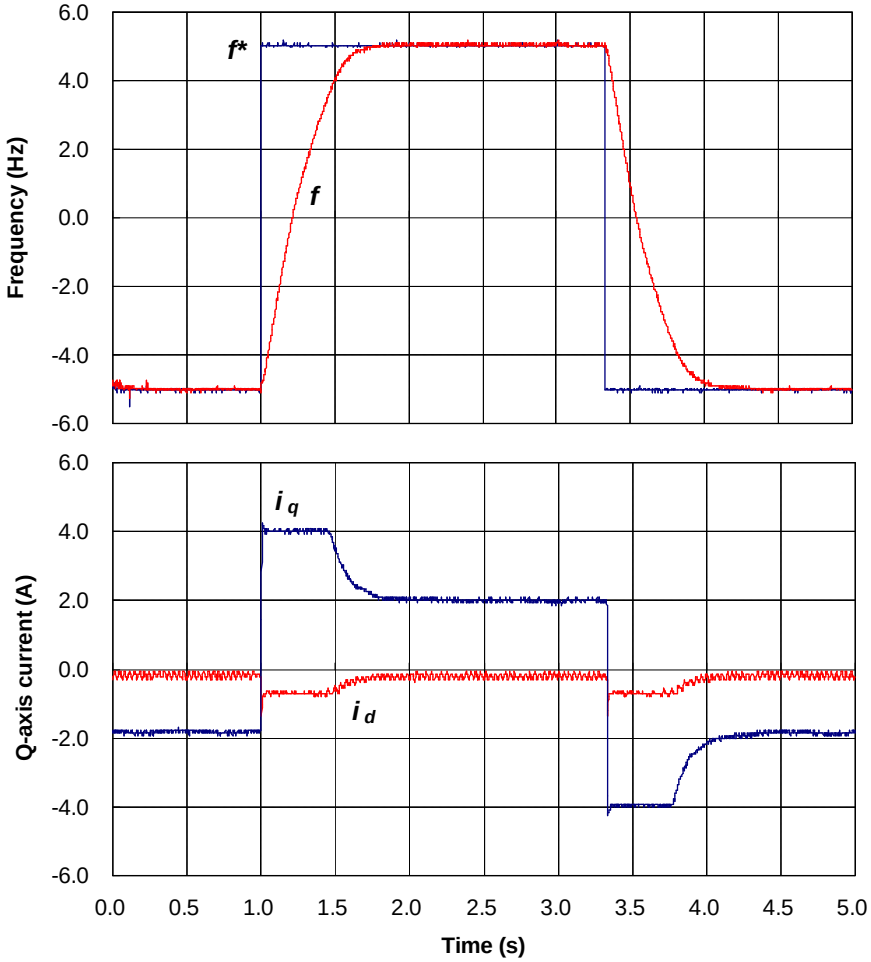

Fig. 2.15 Speed step response (-100RPM → 100RPM → -100RPM).

2.7 Conclusions

This chapter gives a detailed description about the experimental setup, including the hardware platform and software implementation of a sensored current vector control.

Although the C31 DSP based system is out of date, the modular concept of the experimental system is very popular even today.

Control Loop design is important in the current vector control system. In sensorless control, the bandwidth of position tracking observer is limited by the bandwidth of current and speed control loop. As the inner loop, the current loop, should be designed with higher bandwidth. However, the digital sampling frequency and update mode of the PWM duty cycle gives rise to the upper limit. Even worse, for carrier current injection based sensorless control methods, LPFs are necessary to filter out the carrier current ripple on the *dq*-axis current feedback, which further decrease the dynamic performance of current control loop. For the speed loop, its dynamic behavior is limited by the system inertia and the maximum electromagnetic torque of machine.

CHAPTER 3

CARRIER SIGNAL INJECTION BASED SENSORLESS CONTROL

3.1 Introduction

Carrier signal injection based sensorless control methods are well developed due to the effectiveness at low speed and at standstill. A high frequency carrier voltage signal (pulsating or rotating) is persistently superimposed on the fundamental excitation, and then the position-dependant carrier current response, which results from the interaction between the injected carrier voltage signal and the machine saliency, can be used to extract rotor position information.

Alternatively, it is possible to inject a high frequency carrier current signal to the salient machine, and extract rotor position information from the carrier voltage response. However, carrier current injection requires the current regulator to have sufficiently high bandwidth to guarantee the injected high frequency carrier current follows the reference command. Another drawback is that an additional voltage sensor should be provided to measure the carrier voltage response. For carrier voltage injection, although the injected carrier voltage signal may be disturbed by the current regulator and inverter nonlinearity effect, it is acceptable to use the carrier voltage reference signal in the control algorithm, with appropriate compensation techniques. Furthermore, the current sensors which are already present for current vector control can be used for the carrier current measurement, which would simplify the hardware design and decrease the system cost. Consequently, carrier voltage signal injection is preferred.

This chapter gives a detailed discussion about commonly used d-axis pulsating and rotating carrier signal injection based sensorless control techniques. In order to guarantee sufficient signal to noise ratio (SNR) of the resultant carrier current response, the default

carrier voltage signal with a magnitude of 35V, and frequency of 330Hz, is selected for the prototype machine used in this thesis.

Since the machine saliency undergoes two cycles in a single electrical period, the estimated position information from the machine saliency behavior contains an angular ambiguity of π. Therefore, magnetic polarity identification is required to obtain the correct rotor position for an initial start. Utilizing the variation of carrier current amplitude with respect to the *d*-axis fundamental current level, a robust polarity detection scheme is developed in this chapter, which can be seamlessly integrated with a conventional carrier signal injection based sensorless control algorithm.

3.2 High Frequency Model of PM BLAC Machines Accounting for Cross-saturation Effect

In carrier voltage signal injection based sensorless control methods, the position dependent carrier current response is subject to the impedance of the machine, hence the high frequency model of a PM BLAC machine needs to be analyzed first.

3.2.1 Model in synchronous reference frame

The voltage equation of a PM BLAC machine in the synchronous reference frame is given as below.

$$\begin{bmatrix} V_d \\ V_q \end{bmatrix} = \begin{bmatrix} R & 0 \\ 0 & R \end{bmatrix} \cdot \begin{bmatrix} i_d \\ i_q \end{bmatrix} + p \begin{bmatrix} \psi_d \\ \psi_q \end{bmatrix} + \begin{bmatrix} -w_r \psi_q \\ w_r \psi_d \end{bmatrix} \quad (3.1)$$

where p denotes the differential operator, and Ψ_d, Ψ_q represent the *d*- and *q*-axis flux linkages respectively. Assuming the machine reluctance has pure sinusoidal spatial distribution along the rotor circumference, then they are only determined by load condition (i_d, i_q), rather than rotor position.

$$\begin{cases} \psi_d = \psi_d(i_d, i_q) \\ \psi_q = \psi_q(i_d, i_q) \end{cases} \quad (3.2)$$

If the carrier frequency is sufficiently higher than the fundamental frequency (normally the case at standstill and low speed operation), back-EMF and resistive voltage drop are negligible, then the machine behaves as a purely inductive load [RAC08a]. Only

the high frequency components are considered, and the high frequency voltage equation can be derived as,

$$\begin{bmatrix} v_{dh} \\ v_{qh} \end{bmatrix} = p\begin{bmatrix} y_{\,d}(i_d, i_q) \\ y_{\,q}(i_d, i_q) \end{bmatrix} = \begin{bmatrix} \dfrac{\partial y_{\,d}}{\partial i_d} \cdot \dfrac{di_d}{dt} + \dfrac{\partial y_{\,d}}{\partial i_q} \cdot \dfrac{di_q}{dt} \\ \dfrac{\partial y_{\,q}}{\partial i_d} \cdot \dfrac{di_d}{dt} + \dfrac{\partial y_{\,q}}{\partial i_q} \cdot \dfrac{di_q}{dt} \end{bmatrix} \tag{3. 3}$$

With the aid of definition of incremental (also called differential or tangential) self- and mutual inductance, given by:

$$\begin{cases} L_{dh}(i_d, i_q) = \partial y_{\,d} / \partial i_d \approx [y_{\,d}(i_d + \Delta i_d, i_q) - y_{\,d}(i_d, i_q)] / \Delta i_d \\ L_{qh}(i_d, i_q) = \partial y_{\,q} / \partial i_q \approx [y_{\,q}(i_d, i_q + \Delta i_q) - y_{\,q}(i_d, i_q)] / \Delta i_q \\ L_{dqh}(i_d, i_q) = \partial y_{\,d} / \partial i_q \approx [y_{\,d}(i_d, i_q + \Delta i_q) - y_{\,d}(i_d, i_q)] / \Delta i_q \\ L_{qdh}(i_d, i_q) = \partial y_{\,q} / \partial i_d \approx [y_{\,q}(i_d + \Delta i_d, i_q) - y_{\,q}(i_d, i_q)] / \Delta i_d \end{cases} \tag{3. 4}$$

Then the high frequency voltage equation can be simplified as,

$$\begin{bmatrix} v_{dh} \\ v_{qh} \end{bmatrix} = \begin{bmatrix} L_{dh} & L_{dqh} \\ L_{qdh} & L_{qh} \end{bmatrix} \cdot p\begin{bmatrix} i_{dh} \\ i_{qh} \end{bmatrix} \tag{3. 5}$$

Although a slightly nonreciprocal cross-saturation coupling exists between *d*- and *q*-axis, i.e. $L_{dqh} \neq L_{qdh}$ [STU03]. In most practical applications [GUG06] [LI09b] [REI08], L_{dqh} is considered equal to L_{qdh} for simplifying the analysis, which is adopted in this work. Consequently, the high frequency voltage model of a PM BLAC machine in the synchronous reference frame can be simplified as below,

$$\begin{bmatrix} v_{dh} \\ v_{qh} \end{bmatrix} = \begin{bmatrix} L_{dh} & L_{dqh} \\ L_{dqh} & L_{qh} \end{bmatrix} \cdot p\begin{bmatrix} i_{dh} \\ i_{qh} \end{bmatrix} \tag{3. 6}$$

From the above equation, it can be seen that only incremental inductances are contained in the high frequency voltage model. Due to magnetic saturation, L_{dh}, L_{qh} and L_{dqh} vary with fundamental excitation.

The incremental self and mutual inductances can be measured by injecting the high frequency signal into the *d*- and *q*-axis, respectively [LI09a]. The high frequency signal, $v_c = V_c \cos(\omega_c t)$, is injected into the *d*-axis to obtain the relevant *dq*-axis high frequency currents (i_{dh1} and i_{qh1}), and then it is applied to the *q*-axis to record i_{dh2} and i_{qh2}. The high frequency voltages and currents, v_c, i_{dh1}, i_{qh1}, i_{dh2} and i_{qh2}, are applied to (3.6) as follows:

$$\begin{bmatrix} v_s & 0 \\ 0 & v_s \end{bmatrix} = \begin{bmatrix} L_{dh} & L_{dqh} \\ L_{qdh} & L_{qh} \end{bmatrix} \cdot p \begin{bmatrix} i_{dh1} & i_{dh2} \\ i_{qh1} & i_{qh2} \end{bmatrix} \tag{3. 7}$$

Both sides of (3.7) are multiplied by $2\cos(\omega_c t)$ and applied to a low pass filter to give:

$$\begin{bmatrix} V_c & 0 \\ 0 & V_c \end{bmatrix} = w_c \begin{bmatrix} L_{dh} & L_{dqh} \\ L_{qdh} & L_{qh} \end{bmatrix} \cdot \begin{bmatrix} I_{dh1} & I_{dh2} \\ I_{qh1} & I_{qh2} \end{bmatrix} \tag{3. 8}$$

where I_{dh1}, I_{qh1}, I_{dh2} and I_{qh2} are the amplitude of corresponding high frequency currents, and they can be measured by multiplying the relevant currents with $2\sin(\omega_c t)$ and low pass filtered to give:

$$\begin{cases} I_{dh1} = LPF(2 i_{dh1} \sin(w_c t)) \\ I_{qh1} = LPF(2 i_{qh1} \sin(w_c t)) \\ I_{dh2} = LPF(2 i_{dh2} \sin(w_c t)) \\ I_{qh2} = LPF(2 i_{qh2} \sin(w_c t)) \end{cases} \tag{3. 9}$$

The incremental self- and mutual-inductances of *dq*-axis are obtained by solving (3.9) as:

$$\begin{bmatrix} L_{dh} & L_{dqh} \\ L_{qdh} & L_{qh} \end{bmatrix} = \frac{1}{w_c} \begin{bmatrix} V_c & 0 \\ 0 & V_c \end{bmatrix} \begin{bmatrix} I_{dh1} & I_{dh2} \\ I_{qh1} & I_{qh2} \end{bmatrix}^{-1} \tag{3. 10}$$

For the prototype machine used in this work, the measured data of incremental self- and mutual-inductances are shown in Appendix 4, which can be plotted in Fig. 3.1 and Fig. 3.2 [LI09a].

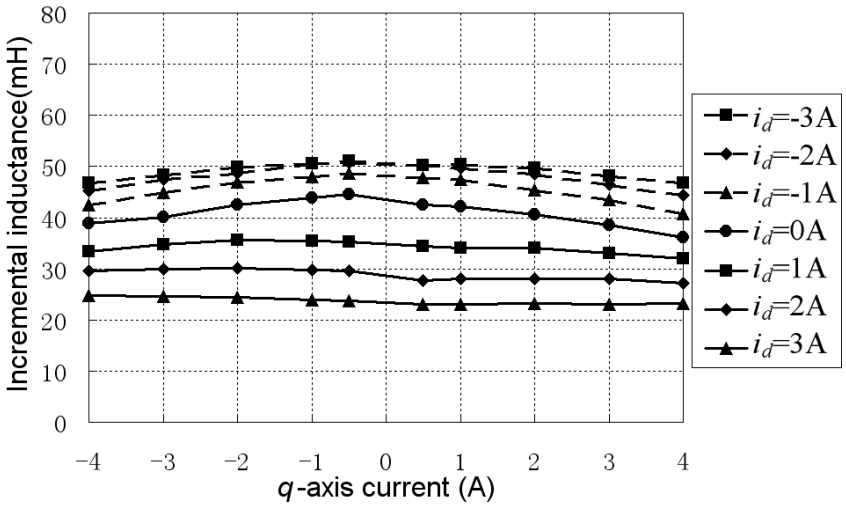

(a) *d*-axis Incremental self inductance L_{dh}

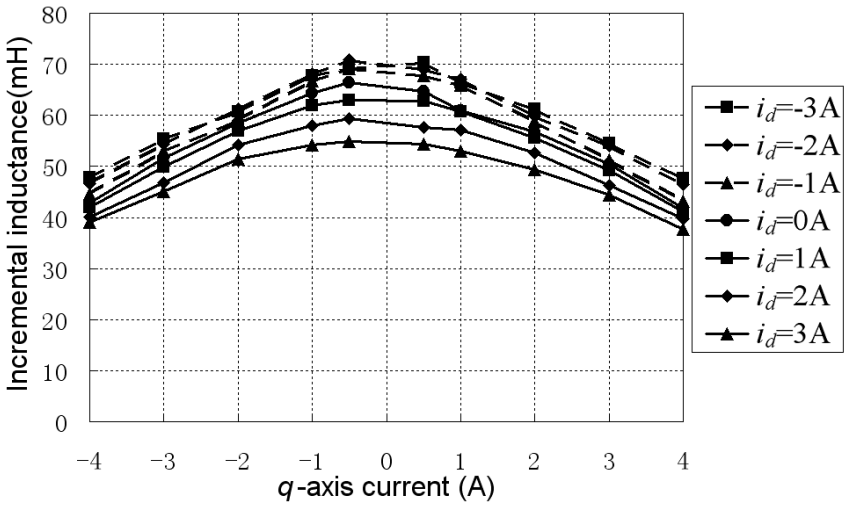

(b) *q*-axis Incremental self inductance L_{qh}

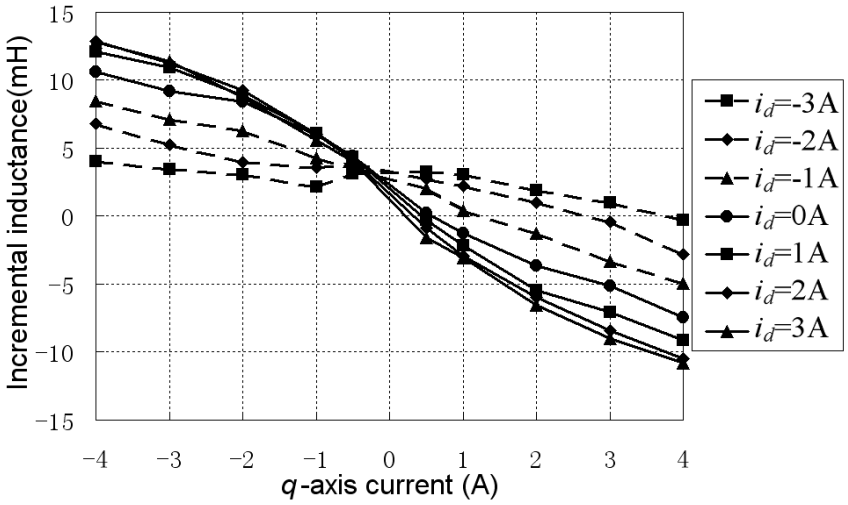

(c) Incremental mutual inductance L_{dqh}

Fig. 3.1 2D-graph of the measured incremental inductances for the prototype machine [LI09a].

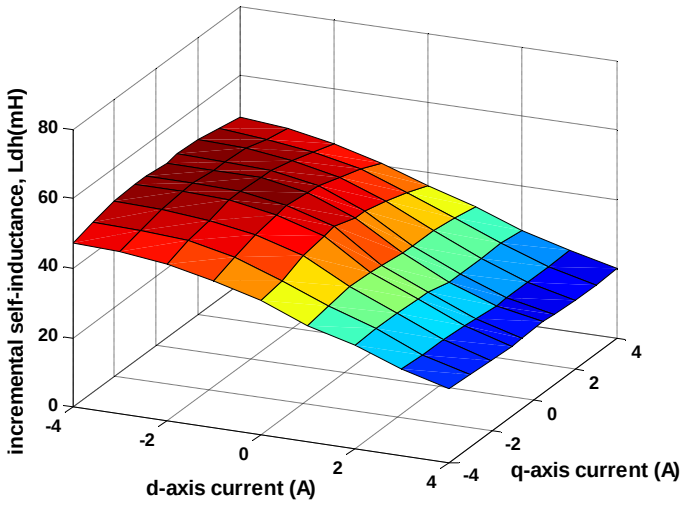

(a) *d*-axis Incremental self inductance L_{dh}

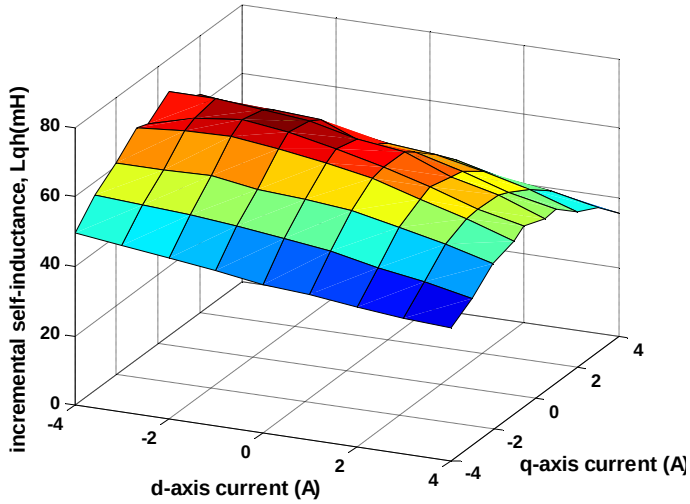

(b) *q*-axis Incremental self inductance L_{qh}

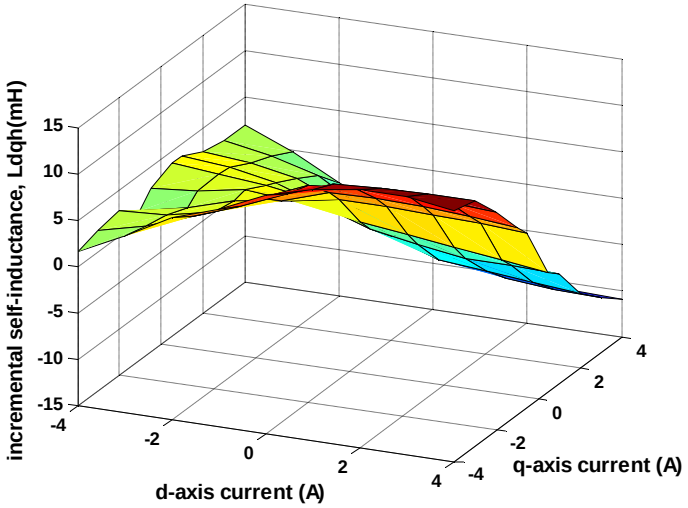

(c) Incremental mutual inductance L_{dqh}

Fig. 3.2 3D-graph of the measured incremental inductances for the prototype machine [LI09a].

3.2.2 Model in estimated synchronous reference frame

In sensorless operation, since the accurate rotor position is unknown, the estimated rotor position is used in the control algorithm. Hence, (3.6) can be transformed to the estimated synchronous reference frame (θ_r^e) from the accurate synchronous reference frame (θ_r) by the transformation matrix, $T(\Delta\theta)$, as given below,

$$T(\Delta q) = \begin{bmatrix} \cos(\Delta q) & -\sin(\Delta q) \\ \sin(\Delta q) & \cos(\Delta q) \end{bmatrix} \tag{3. 11}$$

where $\Delta\theta$ is the estimated position error, $\Delta\theta = \theta_r - \theta_r^e$, as shown in Fig. 3.3.

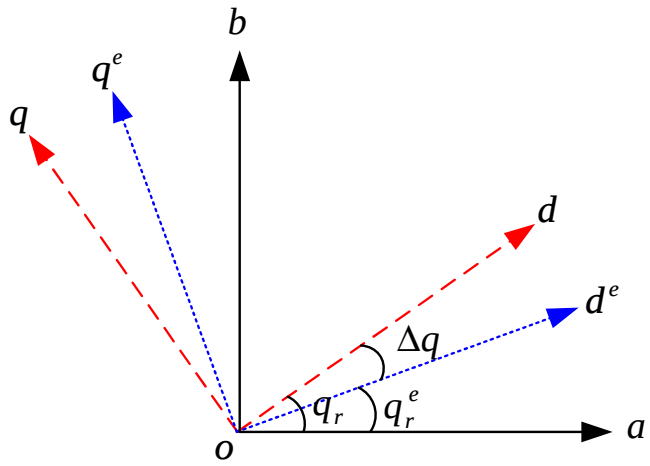

Fig. 3.3 Estimated and accurate synchronous reference frame

In the estimated synchronous reference frame, the high frequency voltage model of the PM BLAC machine can be expressed as,

$$\begin{bmatrix} v_{dh}^e \\ v_{qh}^e \end{bmatrix} = T(\Delta q)\begin{bmatrix} L_{dh} & L_{dqh} \\ L_{dqh} & L_{qh} \end{bmatrix} T^{-1}(\Delta q)\cdot p\begin{bmatrix} i_{dh}^e \\ i_{qh}^e \end{bmatrix}$$

$$= \begin{bmatrix} \cos\Delta q & -\sin\Delta q \\ \sin\Delta q & \cos\Delta q \end{bmatrix}\cdot\begin{bmatrix} L_{dh} & L_{dqh} \\ L_{dqh} & L_{qh} \end{bmatrix}\cdot\begin{bmatrix} \cos\Delta q & \sin\Delta q \\ -\sin\Delta q & \cos\Delta q \end{bmatrix}\cdot p\begin{bmatrix} i_{dh}^e \\ i_{qh}^e \end{bmatrix}$$

$$= \begin{bmatrix} L_{dh}\cos^2\Delta q + L_{qh}\sin^2\Delta q - L_{dqh}\sin 2\Delta q & (L_{dh}-L_{qh})\sin\Delta q\cos\Delta q + L_{dqh}\cos 2\Delta q \\ (L_{dh}-L_{qh})\sin\Delta q\cos\Delta q + L_{dqh}\cos 2\Delta q & L_{dh}\sin^2\Delta q + L_{qh}\cos^2\Delta q + L_{dqh}\sin 2\Delta q \end{bmatrix}\cdot p\begin{bmatrix} i_{dh}^e \\ i_{qh}^e \end{bmatrix}$$

$$= \begin{bmatrix} L_{sa} - L_{sd}\cos 2\Delta q - L_{dqh}\sin 2\Delta q & -L_{sd}\sin 2\Delta q + L_{dqh}\cos 2\Delta q \\ -L_{sd}\sin 2\Delta q + L_{dqh}\cos 2\Delta q & L_{sa} + L_{sd}\cos 2\Delta q + L_{dqh}\sin 2\Delta q \end{bmatrix}\cdot p\begin{bmatrix} i_{dh}^e \\ i_{qh}^e \end{bmatrix} \quad (3.12a)$$

where L_{sa} and L_{sd} are the average and difference of d- and q-axis incremental inductances, defined by:

$$\begin{cases} L_{sa} = (L_{qh} + L_{dh})/2 \\ L_{sd} = (L_{qh} - L_{dh})/2 \end{cases} \quad (3.12b)$$

Equation (3.12) is solved to calculate the differential of the high frequency carrier current response in the estimated synchronous reference frame,

$$
\begin{aligned}
p\begin{bmatrix} i_{dh}^e \\ i_{qh}^e \end{bmatrix} &= \begin{bmatrix} \dfrac{L_{sa}+L_{sd}\cos 2\Delta q + L_{dqh}\sin 2\Delta q}{L_{sa}^2 - L_{sd}^2 - L_{dqh}^2} & \dfrac{L_{sd}\sin 2\Delta q - L_{dqh}\cos 2\Delta q}{L_{sa}^2 - L_{sd}^2 - L_{dqh}^2} \\ \dfrac{L_{sd}\sin 2\Delta q - L_{dqh}\cos 2\Delta q}{L_{sa}^2 - L_{sd}^2 - L_{dqh}^2} & \dfrac{L_{sa}-L_{sd}\cos 2\Delta q - L_{dqh}\sin 2\Delta q}{L_{sa}^2 - L_{sd}^2 - L_{dqh}^2} \end{bmatrix} \cdot \begin{bmatrix} v_{dh}^e \\ v_{qh}^e \end{bmatrix} \\
&= \begin{bmatrix} \dfrac{L_{sa}+\sqrt{L_{sd}^2+L_{dqh}^2}\cos(2\Delta q + q_m)}{L_{dh}L_{qh} - L_{dqh}^2} & \dfrac{\sqrt{L_{sd}^2+L_{dqh}^2}\sin(2\Delta q + q_m)}{L_{dh}L_{qh} - L_{dqh}^2} \\ \dfrac{\sqrt{L_{sd}^2+L_{dqh}^2}\sin(2\Delta q + q_m)}{L_{dh}L_{qh} - L_{dqh}^2} & \dfrac{L_{sa}-\sqrt{L_{sd}^2+L_{dqh}^2}\cos(2\Delta q + q_m)}{L_{dh}L_{qh} - L_{dqh}^2} \end{bmatrix} \cdot \begin{bmatrix} v_{dh}^e \\ v_{qh}^e \end{bmatrix} \\
&= \begin{bmatrix} \dfrac{1}{L_p} + \dfrac{1}{L_n}\cos(2\Delta q + q_m) & \dfrac{1}{L_n}\sin(2\Delta q + q_m) \\ \dfrac{1}{L_n}\sin(2\Delta q + q_m) & \dfrac{1}{L_p} - \dfrac{1}{L_n}\cos(2\Delta q + q_m) \end{bmatrix} \cdot \begin{bmatrix} v_{dh}^e \\ v_{qh}^e \end{bmatrix}
\end{aligned}
\tag{3. 13a}
$$

where θ_m is referred to as the cross-saturation angle.

$$
q_m = \tan^{-1}\left(\frac{-L_{dqh}}{L_{sd}}\right), \quad L_p = \frac{L_{dh}L_{qh} - L_{dqh}^2}{L_{sa}}, \quad L_n = \frac{L_{dh}L_{qh} - L_{dqh}^2}{\sqrt{L_{sd}^2 + L_{dqh}^2}} \tag{3. 13b}
$$

normally, $L_p << L_n$.

3.2.3 Model in stationary reference frame

From Fig. 3.3, with the aid of transformation matrix $T(\theta_r)$, the high frequency voltage model of a PM BLAC machine in the stationary reference frame can also be derived from (3.6), as shown below.

$$
T(q_r) = \begin{bmatrix} \cos(q_r) & -\sin(q_r) \\ \sin(q_r) & \cos(q_r) \end{bmatrix} \tag{3.14}
$$

$$
\begin{aligned}
\begin{bmatrix} v_{ah} \\ v_{bh} \end{bmatrix} &= T(q_r)\begin{bmatrix} L_{dh} & L_{dqh} \\ L_{dqh} & L_{qh} \end{bmatrix} T^{-1}(q_r) \cdot p\begin{bmatrix} i_{ah} \\ i_{bh} \end{bmatrix} \\
&= \begin{bmatrix} L_{sa} - L_{sd}\cos 2q_r - L_{dqh}\sin 2q_r & -L_{sd}\sin 2q_r + L_{dqh}\cos 2q_r \\ -L_{sd}\sin 2q_r + L_{dqh}\cos 2q_r & L_{sa} + L_{sd}\cos 2q_r + L_{dqh}\sin 2q_r \end{bmatrix} \cdot p\begin{bmatrix} i_{ah} \\ i_{bh} \end{bmatrix}
\end{aligned}
\tag{3.15}
$$

In the similar way, the differential of the high frequency carrier current response in the stationary reference frame can be obtained as,

$$p\begin{bmatrix} i_{ah} \\ i_{bh} \end{bmatrix} = \begin{bmatrix} \frac{1}{L_p} + \frac{1}{L_n}\cos(2q_r + q_m) & \frac{1}{L_n}\sin(2q_r + q_m) \\ \frac{1}{L_n}\sin(2q_r + q_m) & \frac{1}{L_p} - \frac{1}{L_n}\cos(2q_r + q_m) \end{bmatrix} \cdot \begin{bmatrix} v_{ah} \\ v_{bh} \end{bmatrix} \tag{3.16}$$

3.3 Pulsating Carrier Signal Injection

Pulsating carrier signal injection based sensorless methods have been well developed due to their inherent advantages, such as being less computational intensive, having a faster dynamic response, and a intrinsic cancellation of the filter lags during signal processing [RAC10].

There are two kinds of algorithms in pulsating carrier signal injection:

- D-axis injection [LIN02] [HA03] [JAN03a] [LI09b]: a high frequency carrier voltage signal is injected on the estimated *d*-axis, and the carrier current response on the estimated *q*-axis is used to estimate the rotor position.
- Q-axis injection [COR98] [LIN03] [YAN11]: a high frequency carrier voltage is injected on the estimated *q*-axis, and the carrier current response on the estimated *d*-axis is used to estimate the rotor position.

3.3.1 D-axis injection

For *d*-axis pulsating carrier signal injection, the high frequency pulsating carrier voltage vector (3.17) is injected on the estimated *d*-axis.

$$\begin{bmatrix} v_{dh}^e \\ v_{qh}^e \end{bmatrix} = V_c \begin{bmatrix} \cos a \\ 0 \end{bmatrix}, \qquad a = w_c t + j \tag{3.17}$$

where V_c, ω_c and φ are the amplitude, angular speed and initial phase angle of the injected carrier voltage.

From (3.13), the differential of the carrier current in the estimated synchronous reference frame can be expressed as:

$$p\begin{bmatrix} i_{dh}^e \\ i_{qh}^e \end{bmatrix} = \begin{bmatrix} \frac{1}{L_p} + \frac{1}{L_n}\cos(2\Delta q + q_m) & \frac{1}{L_n}\sin(2\Delta q + q_m) \\ \frac{1}{L_n}\sin(2\Delta q + q_m) & \frac{1}{L_p} - \frac{1}{L_n}\cos(2\Delta q + q_m) \end{bmatrix} \cdot V_c \begin{bmatrix} \cos a \\ 0 \end{bmatrix} \tag{3.18}$$

And then, the resultant carrier current response in the estimated synchronous reference frame can be derived as:

$$\begin{bmatrix} i_{dh}^e \\ i_{qh}^e \end{bmatrix} = \begin{bmatrix} \frac{V_c}{w_c L_p} + \frac{V_c}{w_c L_n}\cos(2\Delta q + q_m) \\ \frac{V_c}{w_c L_n}\sin(2\Delta q + q_m) \end{bmatrix} \cdot \sin a = \begin{bmatrix} I_p + I_n \cos(2\Delta q + q_m) \\ I_n \sin(2\Delta q + q_m) \end{bmatrix} \cdot \sin a \qquad (3.19a)$$

where

$$I_p = \frac{V_c}{w_c L_p}, \quad I_n = \frac{V_c}{w_c L_n} \qquad (3.19b)$$

From (3.19a), it is clearly shown that the carrier current response is amplitude modulated by the rotor position information (for given load condition, cross-saturation angle θ_m is constant). When the estimated position error $\Delta\theta$ is sufficiently small, i^e_{qh} becomes very small, therefore, the q-axis carrier current response (i^e_{qh}) is usually used to extract the rotor position information. Since the introduced current ripple on the q-axis is limited, less torque ripple would be generated.

Using the form of a complex vector, the injected carrier voltage signal and carrier current response in the estimated synchronous reference frame can be expressed as,

$$v^e_{dqh} = \frac{V_c}{2}(e^{ja} + e^{-ja}), \qquad a = w_c t + j \qquad (3.20a)$$

$$i^e_{dqh} = \frac{I_p + I_n e^{j(2\Delta q + q_m)}}{2}(e^{j(a - p/2)} + e^{j(-a + p/2)}) \qquad (3.20b)$$

From the foregoing discussion, some conclusions can be drawn, as listed below:

1. From (3.20a), it can be noticed that the injected carrier signal can be regarded as the superposition of two rotating carrier vectors, one is rotating at a positive speed and the other one is rotating at a negative speed.
2. The resulting carrier current response (3.20b) in the estimated synchronous reference frame consists of two components: the positive and negative sequence components. The positive sequence component, rotating at the frequency of ω_c, has the same magnitude as the negative sequence component. The spectrum components for pulsating voltage injection method are therefore symmetrical.

3. The phase of the positive and negative sequence components do not have any position related information, whereas their magnitude is modulated by the position estimation error and can therefore be used to estimate the rotor position.

3.3.2 Q-axis injection

For *q*-axis pulsating carrier signal injection, a high frequency pulsating carrier voltage vector (3.21) is injected on the estimated *q*-axis.

$$\begin{bmatrix} v_{dh}^{e} \\ v_{qh}^{e} \end{bmatrix} = V_c \begin{bmatrix} 0 \\ \cos a \end{bmatrix}, \qquad a = w_c t + j \tag{3.21}$$

And then the resultant carrier current response in the estimated synchronous reference frame can be derived as:

$$\begin{bmatrix} i_{dh}^{e} \\ i_{qh}^{e} \end{bmatrix} = \begin{bmatrix} \dfrac{V_c}{w_c L_n} \sin(2\Delta q + q_m) \\ \dfrac{V_c}{w_c L_p} - \dfrac{V_c}{w_c L_n} \cos(2\Delta q + q_m) \end{bmatrix} \cdot \sin a = \begin{bmatrix} I_n \sin(2\Delta q + q_m) \\ I_p - I_n \cos(2\Delta q + q_m) \end{bmatrix} \cdot \sin a \tag{3.22}$$

Similar to the *d*-axis injection, the carrier current response is amplitude modulated by the rotor position information. However, the *d*-axis carrier current response (i^{e}_{dh}) is usually used to extract the rotor position information.

Q-axis injection is a good choice for zero *d*-axis current vector control ($i_d=0$) [LIN03] [YAN11], since it is less sensitive to the inverter nonlinearity effect. In this case, the magnitude of carrier current would be zero when the fundamental phase current crosses zero, as shown in Fig. 3.4. Hence, the carrier voltage distortion due to inverter nonlinearity can be minimized. Further detailed information about inverter nonlinearity effect is given in Chapter 5.

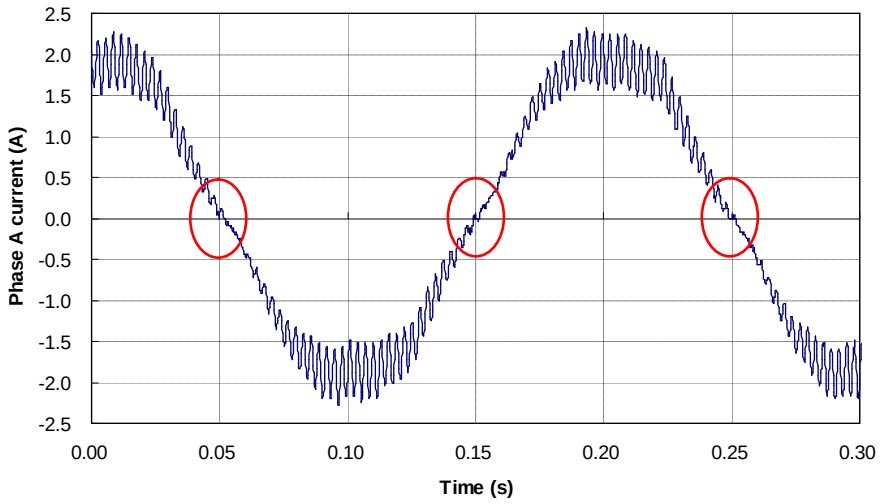

Fig. 3.4 Phase current for q-axis injection at sensored operation mode.

Compared with d-axis injection, however, more current ripple on the *q*-axis can be observed, as shown in Fig. 3.5. It would generate substantial torque ripple even the position estimation error is zero. Consequently, injection of pulsating carrier voltage along the d-axis is preferred in terms of torque ripple.

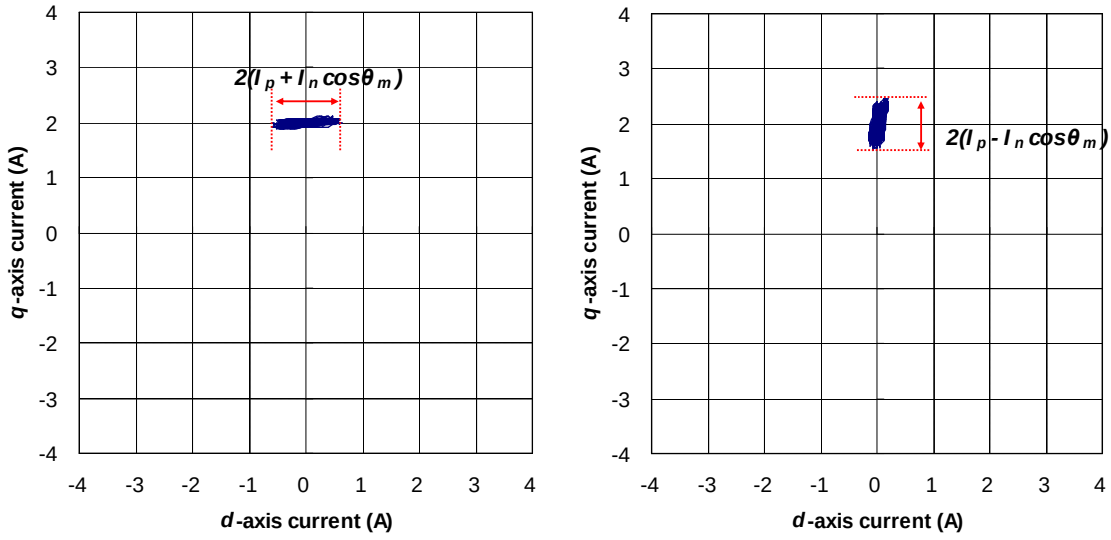

(a) d-axis pulsating injection (b) q-axis pulsating injection

Fig. 3.5 Measured current in *dq* reference frame at sensored operation mode (i_d=0A, i_q=2A).

3.3.3 Carrier signal demodulation

It is well known that the carrier current response in the estimated synchronous reference frame is amplitude modulated by rotor position information. In order to

demodulate the position dependent amplitude from total carrier current response, the synchronous detection technique is normally used [MAD95] [LI09a] [RAC10].

Assuming the current signal has the form of

$$i(t) = I_o + I_1 \sin(w_1 t) + I_2 \sin(w_2 t) \tag{3.23}$$

Both sides of (3.23) are multiplied by $2\sin(\omega_1 t+\delta)$, where δ is a constant angular offset.

$$i(t) \cdot 2\sin(w_1 t + d) = 2I_o \sin(w_1 t + d) + I_1 \cos d - I_1 \cos(2w_1 t + d) + 2I_2 \sin(w_2 t)\sin(w_1 t + d) \tag{3.24}$$

Applying this signal to a low pass filter, the output can be derived as

$$I_1 \cos d = LPF\left[i(t) \cdot 2\sin(w_1 t + d)\right] \tag{3.25}$$

It should be noted that, once $\delta=0$, the output of low pass filter is exactly the amplitude of frequency component of interest, otherwise, a gain of $\cos\delta$ is introduced. This kind of frequency isolation scheme is referred to as synchronous detection [MAD95].

With the synchronous detection technique, the amplitude of the carrier current response can be obtained with noise suppression, given by

$$\left|i^e_{dqh}\right| = \begin{bmatrix} \left|i^e_{dh}\right| \\ \left|i^e_{qh}\right| \end{bmatrix} = LPF\left(\begin{bmatrix} i^e_{dh} \\ i^e_{qh} \end{bmatrix} \cdot 2\sin a\right) = \begin{bmatrix} I_p + I_n \cos(2\Delta q + q_m) \\ I_n \sin(2\Delta q + q_m) \end{bmatrix} \tag{3.26}$$

The whole procedure of carrier signal demodulation for pulsating injection is described in Fig. 3.6.

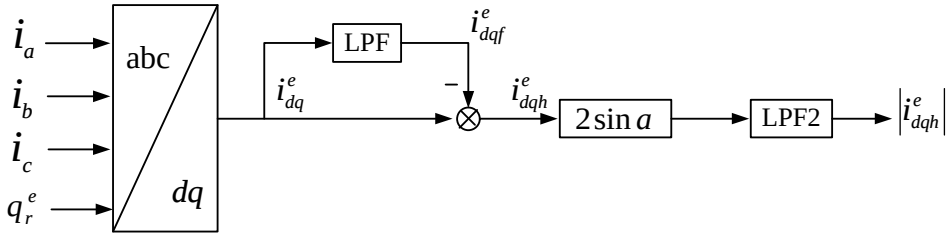

Fig. 3.6 Carrier signal demodulation for Pulsating injection.

In conventional *d*-axis pulsating injection based sensorless methods, the amplitude of *q*-axis carrier current is regarded to be the signal input to the position observer,

$$f(\Delta q) = \left|i^e_{qh}\right| = I_n \sin(2\Delta q + q_m) \tag{3.27}$$

In steady state, $f(\Delta\theta)$ is forced to be zero due to the position observer,

$$f(\Delta q) = I_n \sin(2\Delta q + q_m) = 0 \tag{3.28}$$

When the cross-saturation effect is negligible, i.e., $\theta_m \approx 0$, the rotor position information can be estimated accurately ($\Delta\theta = 0$). Accounting for the cross saturation effect, however, a position estimation error would be generated,

$$\Delta q = -q_m / 2 \tag{3.29}$$

The introduced position estimation error due to the cross-saturation effect is a critical issue, which results in reduced torque capability and even stability problem.

3.3.4 Compensation of cross-saturation effect

In order to compensate the estimated position error resulting from cross-saturation effect, either proper machine design [BIA07] or compensation control can be employed. Many efforts have been made on the control aspect. Due to its nonlinear behavior, the compensation methods depend considerably on the machine parameters, which can be acquired from finite element calculation, off-line self-commissioning, or on-line parameter identification. A relatively straightforward method is used in [ZHU07] [KOC09]. Here, the angular error is obtained from either finite element calculation or experimental measurement in sensored operation, after that, it can be directly used to compensate the estimated position error on-line. A self-commissioning procedure was presented in [TES00] to obtain the harmonics information due to cross-saturation, which can be used for on-line compensation. A more adaptive compensation method based on parameter identification is developed in [REI08], although it is more computationally intensive. Alternatively, the neural network structure is used for cross-saturation compensation [GAR07b], which is declared to have the advantages of scalability, reduced complexity and reduced commissioning time in comparison with the conventional parameter-based methods.

In this work, the compensation method proposed in [LI09b] is employed. When the rotor position estimation error $\Delta\theta$ is sufficiently small, (3.26) can be further derived as,

$$\begin{bmatrix} |i_{dh}^e| \\ |i_{qh}^e| \end{bmatrix} = \begin{bmatrix} I_p + I_n \cos(2\Delta q + q_m) \\ I_n \sin(2\Delta q + q_m) \end{bmatrix} \approx \begin{bmatrix} I_p + I_n \cos q_m \\ 2I_n \cos q_m \cdot \Delta q + I_n \sin q_m \end{bmatrix} \tag{3.30}$$

defining a coupling factor $\lambda=L_{dqh}/L_{qh}$, and then the signal input to the position observer can be re-defined as,

$$f(\Delta q)=\left|i_{qh}^{e}\right|+l\cdot\left|i_{dh}^{e}\right|\approx 2I_{n}\cos q_{m}\cdot\Delta q \tag{3.31}$$

In steady state, $f(\Delta\theta)$ is forced to be zero by the position observer. Obviously, in this way no position estimation error would be generated by the cross-saturation effect. The block diagram of d-axis pulsating carrier voltage injection based sensorless control with cross-saturation effect compensation is shown in Fig. 3.7.

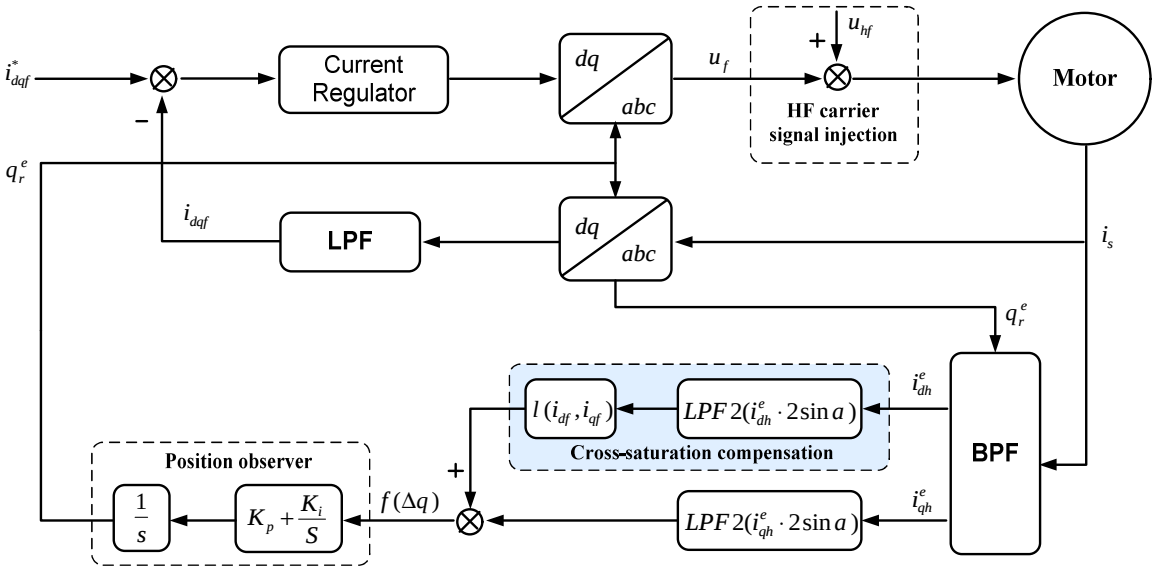

Fig. 3.7 Block diagram of *d*-axis pulsating injection based sensorless control [LI09b].

In a practical implementation, the digital system delay (measurement and sampling delay) are inevitable, especially for the high frequency carrier current response. Previous discussion about the synchronous detection technique shows that a constant gain of $\cos\delta$ would be introduced on $f(\Delta\theta)$ if a constant delay is considered. Fortunately, it does not generate an additional estimation error. Consequently, the improved compensation method has an important advantage of less sensitivity to digital system delay.

3.4 Rotating Carrier Signal Injection

When a rotating carrier voltage signal is injected into a salient machine, two types of signal response can be used to estimate the saliency position: negative sequence carrier current and zero sequence carrier signal (zero sequence carrier voltage for a

wye-connected machine and zero sequence carrier current for a delta-connected machine) [GAR07a]. Although it is claimed that zero sequence component based estimation has the advantage of increased accuracy in the estimated position, and larger estimation bandwidth due to its insensitivity to the distortion of injected carrier voltage [BRI04] [GAR07a], it is rarely used since one additional sensor is required to measure the zero sequence response. Only negative sequence carrier current based sensorless estimation is discussed here.

3.4.1 Carrier current response

For rotating carrier signal injection, a balanced rotating carrier voltage vector (3.32) is injected in the stationary reference frame,

$$\begin{bmatrix} v_{ah} \\ v_{bh} \end{bmatrix} = V_c \begin{bmatrix} \cos a \\ \sin a \end{bmatrix}, \qquad a = w_c t + j \tag{3.32}$$

where V_c, ω_c and φ is the amplitude, angular speed and initial phase angle of the injected carrier voltage.

From (3.16), the differential of carrier current in the stationary reference frame can be expressed as:

$$p\begin{bmatrix} i_{ah} \\ i_{bh} \end{bmatrix} = \begin{bmatrix} \frac{1}{L_p} + \frac{1}{L_n}\cos(2q_r + q_m) & \frac{1}{L_n}\sin(2q_r + q_m) \\ \frac{1}{L_n}\sin(2q_r + q_m) & \frac{1}{L_p} - \frac{1}{L_n}\cos(2q_r + q_m) \end{bmatrix} \cdot V_c \begin{bmatrix} \cos a \\ \sin a \end{bmatrix} \tag{3.33}$$

And then, the resultant carrier current response in the stationary reference frame can be derived as:

$$\begin{aligned} \begin{bmatrix} i_{ah} \\ i_{bh} \end{bmatrix} &= \frac{V_c}{w_c} \begin{bmatrix} \frac{1}{L_p} + \frac{1}{L_n}\cos(2q_r + q_m) & \frac{1}{L_n}\sin(2q_r + q_m) \\ \frac{1}{L_n}\sin(2q_r + q_m) & \frac{1}{L_p} - \frac{1}{L_n}\cos(2q_r + q_m) \end{bmatrix} \cdot \begin{bmatrix} \sin a \\ -\cos a \end{bmatrix} \\ &= \begin{bmatrix} I_p \cos(a - \frac{p}{2}) \\ I_p \sin(a - \frac{p}{2}) \end{bmatrix} + \begin{bmatrix} I_n \cos(-a + 2q_r + q_m + \frac{p}{2}) \\ I_n \sin(-a + 2q_r + q_m + \frac{p}{2}) \end{bmatrix} \end{aligned} \tag{3.34}$$

where I_p and I_n has the same definition as (3.19b).

Using the form of a complex vector, the injected carrier voltage signal and carrier current response in the stationary reference frame can be expressed as,

$$v_{abh} = V_c \cdot e^{ja}, \qquad a = w_c t + j \tag{3.35a}$$

$$i_{abh} = I_p \cdot e^{j(a-p/2)} + I_n \cdot e^{j(-a+2q_r+q_m+p/2)} \tag{3.35b}$$

From the carrier current response (3.35b), some conclusions can be drawn, as listed below:

1. The carrier current response consists of two components [RAC08a]. The first term is a positive sequence component, which has the same rotating speed as the injected carrier voltage vector; the second term is referred to as the negative sequence component, which contains the rotor position information in its phase angle. Consequently, the negative sequence component can be used to track the rotor position.
2. The magnitude I_p and I_n are machine parameter-dependent and proportional to the ratio of (V_c/ω_c). Unlike the symmetrical spectrum for pulsating injection, the spectrum components of positive and negative sequence carrier current are asymmetrical.
3. With regard to the negative sequence carrier current component, its phase angle is modulated by both rotor position θ_r and cross-saturation angle θ_m. Hence, a load-dependent estimated position error would be generated due to cross-saturation effect.

3.4.2 Carrier signal demodulation

In order to extract the position dependent negative sequence carrier current from the total current response, a synchronous reference frame filter (SRFF) is the typical solution [DEG98] [RAC10].

SRFF uses the frame transformation to center spectral component of interest at DC (*0Hz*). With the aid of a low pass filter, this DC component can be easily obtained without phase lag. Conversely, a high pass filter can be used to eliminate this DC component.

Assuming a current signal can be expressed as a complex vector in the stationary reference frame,

$$i_{abh} = i_1 + i_2 = I_1 e^{j(w_1 t)} + I_2 e^{j(w_2 t)} \tag{3.36}$$

In order to extract the component of i_1, the current signal is transformed to the synchronous reference frame, which has the phase angle of ($\omega_1 t+\delta$), where δ is a constant angular offset.

$$\begin{aligned} i_{abh} \cdot e^{j(-w_1 t-d)} &= I_1 e^{j(w_1 t)} \cdot e^{j(-w_1 t-d)} + I_2 e^{j(w_2 t)} \cdot e^{j(-w_1 t-d)} \\ &= I_1 \cdot e^{j(-d)} + I_2 \cdot e^{j(w_2 t - w_1 t-d)} \end{aligned} \tag{3.37}$$

Applying a low pass filter, and then transforming it back to the stationary reference frame, the interested component can be obtained without any phase lag,

$$i_1 = LPF(i_{abh} \cdot e^{j(-w_1 t-d)}) \cdot e^{j(w_1 t+d)} = I_1 e^{j(-d)} \cdot e^{j(w_1 t+d)} = I_1 e^{j(w_1 t)} \tag{3.38}$$

Considering the low amplitude of the negative sequence carrier current, the fundamental and positive sequence carrier current components should be filtered out from the total current response using a SRFF, and then the negative sequence carrier current can be obtained from the remaining components using SRFF. The signal demodulation process is shown below,

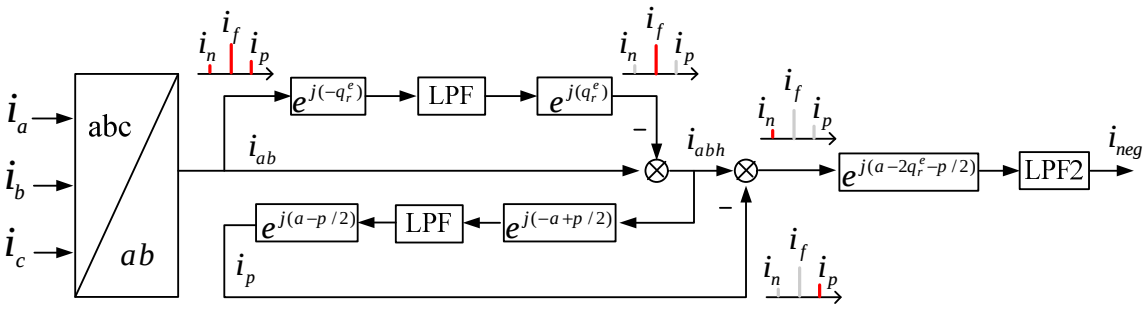

Fig. 3.8 Carrier signal demodulation for rotating injection.

The obtained negative sequence carrier current, in the reference frame synchronous with estimated negative sequence carrier frequency, can be expressed as,

$$\begin{bmatrix} g \\ e \end{bmatrix} = LPF\left\{ \begin{bmatrix} \cos(-a + 2q_r^e + \frac{p}{2}) & \sin(-a + 2q_r^e + \frac{p}{2}) \\ -\sin(-a + 2q_r^e + \frac{p}{2}) & \cos(-a + 2q_r^e + \frac{p}{2}) \end{bmatrix} \cdot \begin{bmatrix} I_n \cos(-a + 2q_r + q_m + \frac{p}{2}) \\ I_n \sin(-a + 2q_r + q_m + \frac{p}{2}) \end{bmatrix} \right\}$$
$$= \begin{bmatrix} I_n \cos(2\Delta q + q_m) \\ I_n \sin(2\Delta q + q_m) \end{bmatrix}$$
$$= \begin{bmatrix} I_n \cos q_{neg} \\ I_n \sin q_{neg} \end{bmatrix} \tag{3.39a}$$

i.e.,

$$i_{neg} = I_n \cdot e^{j(2\Delta q + q_m)} = I_n \cdot e^{jq_{neg}} \tag{3.39b}$$

where θ_{neg} is the angular offset of negative sequence carrier current, $\theta_{neg}=2\Delta\theta+\theta_m$. γ and ε refer to the *d*- and *q*-axis components of i_{neg}, respectively.

Normally, the *q*-axis component ε is regarded as the error signal $f(\Delta\theta)$ input to the position observer [JAN95] [DEG98], i.e.,

$$f(\Delta q) = e = I_n \sin(2\Delta q + q_m) \tag{3.40}$$

It is identical to (3.27) for conventional *d*-axis pulsating injection. Therefore, it is expected that the same position estimation error ($-\theta_m/2$) due to cross-saturation effect would be introduced for rotating injection.

3.4.3 Compensation of cross saturation effect

Although the introduced position estimation error due to cross saturation effect can be directly compensated by adding the load-dependent phase shift ($-\theta_m/2$) to the estimated position information [ZHU07] [KOC09], an improved method through modifying the phase angle of injected carrier signal is developed here.

Equation (3.35) shows that the negative sequence carrier current response is phase-modulated by both rotor position θ_r and cross-saturation angle θ_m. To compensate the position error resulting from cross-saturation effect, the phase angle of injected carrier voltage can be modified with the cross-saturation angle θ_m. In this way, the negative sequence carrier current response will only be phase-modulated by the rotor position.

In the proposed method, the phase angle of injected carrier voltage is modified by:

$$a' = a + q_m \tag{3.41}$$

Where, α' is the updated phase angle, then the carrier current response can be derived as:

$$i_{abh} = I_p \cdot e^{j(a+q_m-p/2)} + I_n \cdot e^{j(-a+2q_r+p/2)} \tag{3.42}$$

In comparison with (3.35), it can be seen that the cross-saturation angle θ_m has been transferred from the negative sequence carrier current to the positive sequence carrier current. The positive sequence carrier current has no use for rotor position detection. Therefore, the rotor position is expected to be accurately estimated from the negative sequence carrier current.

With modified rotating injection, (3.39) can be re-written as,

$$\begin{bmatrix} g \\ e \end{bmatrix} = \begin{bmatrix} I_n \cos(2\Delta q) \\ I_n \sin(2\Delta q) \end{bmatrix} \tag{3.43a}$$

i.e.,

$$i_{neg} = I_n \cdot e^{j(2\Delta q)} = I_n \cdot e^{jq_{neg}} \tag{3.43b}$$

where $\theta_{neg}=2\Delta\theta$. Therefore, $f(\Delta\theta)$ is updated as,

$$f(\Delta q) = e = I_n \sin(2\Delta q) \approx 2I_n \cdot \Delta q \tag{3.44}$$

With cross-saturation effect compensation, the block diagram of rotating carrier voltage injection based sensorless control is shown in Fig. 3.9.

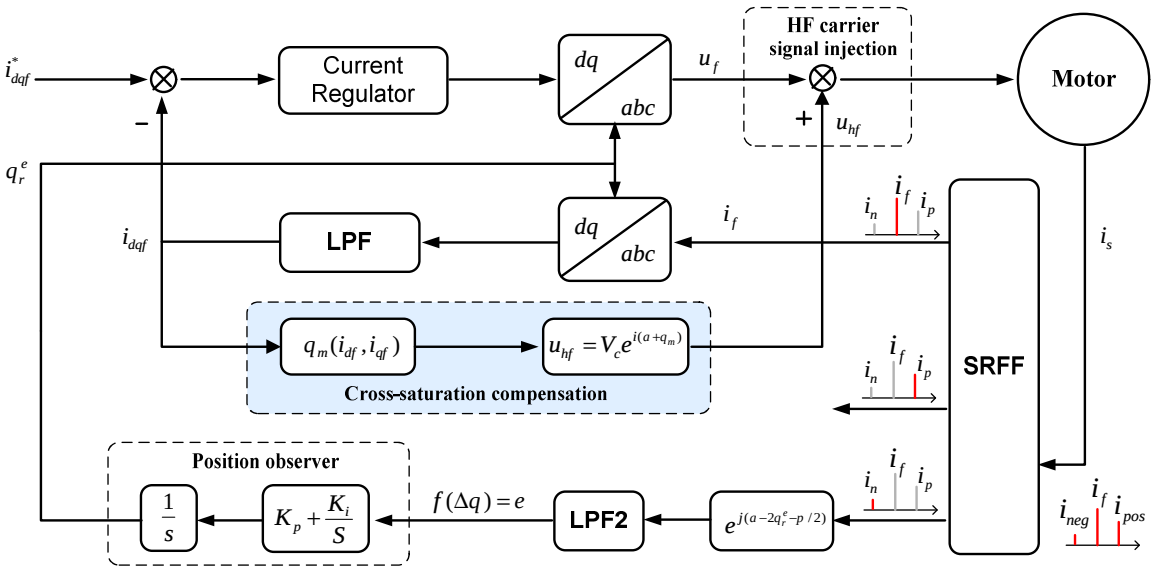

Fig. 3.9 Block diagram of rotating injection based sensorless control.

Fig. 3.10 shows the measured θ_{neg} in sensored operation mode for conventional and modified rotating carrier signal injection, respectively. By driving the machine with the real rotor position information from position sensor ($\Delta\theta=0$), it can be observed that θ_{neg} changes with load variation for a conventional signal injection method. However, θ_{neg} remains to be near zero with load variation for the proposed modified injection. From the experimental results, it clearly reveals that the cross-saturation effect has been compensated for with the proposed compensation method.

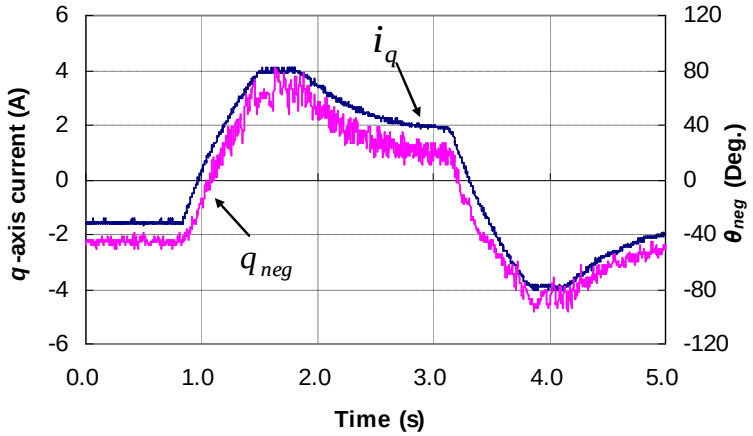

(a) Conventional rotating injection

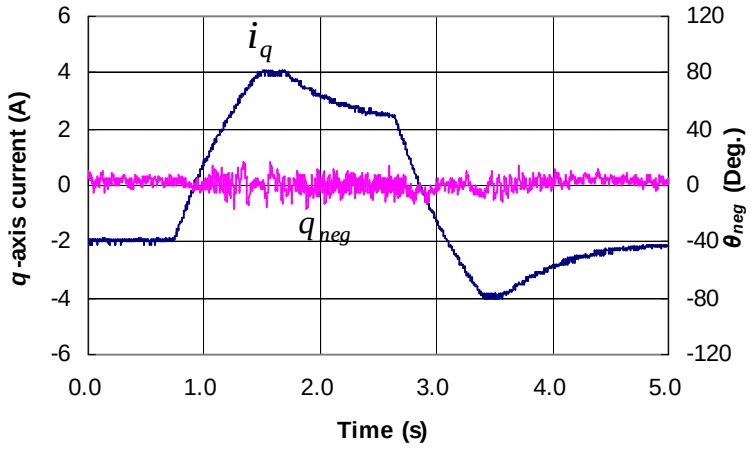

(b) Modified rotating injection

Fig. 3.10 Comparison between conventional and modified rotating injection in sensored operation.

For the proposed compensation method, the knowledge of cross-saturation angle θ_m is a critical concern. According to the measured incremental inductances shown in Fig. 3.2, θ_m can be directly predicted using the definition in (3.13b), as plotted in Fig. 3.11. It

can be observed that the load-dependent cross-saturation angle is quite nonlinear. Alternatively, θ_m can be directly measured from experiment, which is much more convenient for the practical implementation. From (3.39b), when the conventional carrier signal is injected and the machine is driven by the real rotor position from an encoder ($\Delta\theta=0$), θ_m can be directly measured by $\theta_m=\theta_{neg}$. When the specified MTPA control locus is considered, the load-dependent cross-saturation angle θ_m obtained from experiment is shown in Fig. 3.12. Using a 2nd-order polynomial to fit the measured data, the fitted curve is highlighted in red in Fig. 3.12. Plotting the predicted and measured θ_m in Fig. 3.13, the comparison shows that the measured values are in a good agreement with the predicted results.

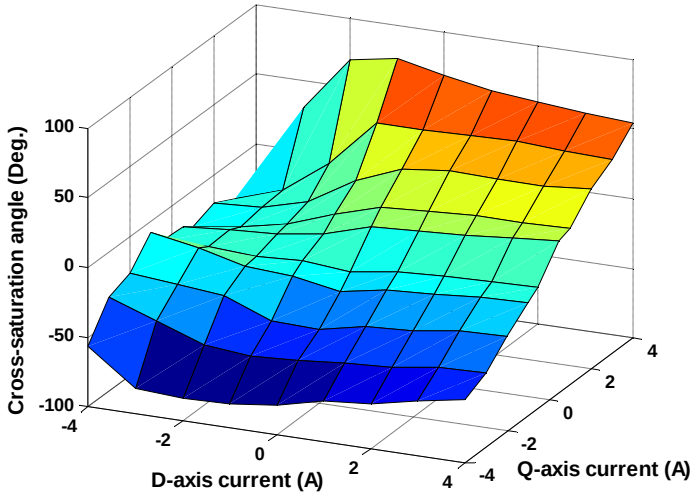

Fig. 3.11 Predicted cross-saturation angle for the prototype machine.

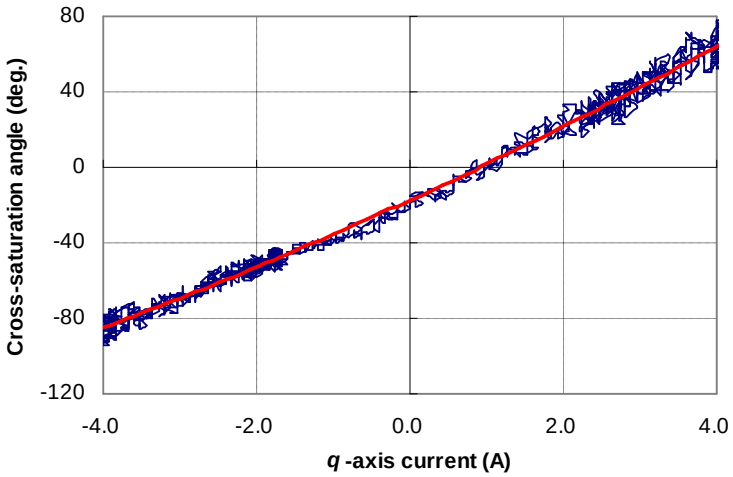

Fig. 3.12 Measured cross-saturation angle.

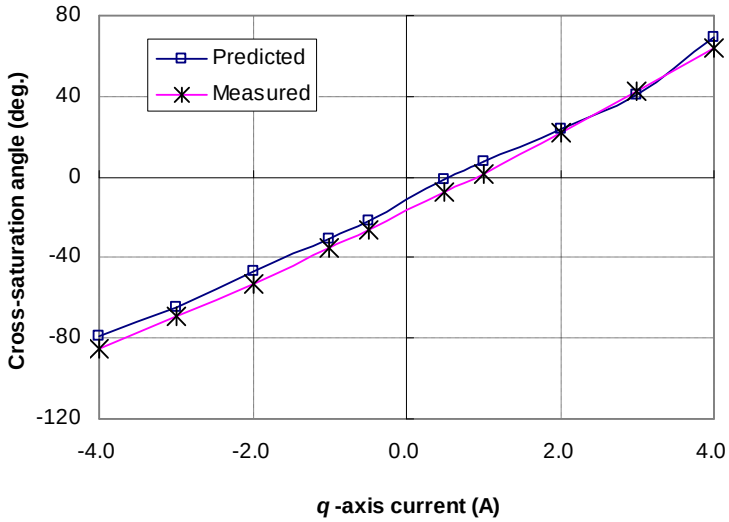

Fig. 3.13 Comparison of predicted and measured cross-saturation angle.

Fig. 3.14 and Fig. 3.15 show the experimental comparison between the conventional and proposed rotating carrier voltage injection methods in sensorless control operation. The current loci are configured to be operating along the MTPA curve. And the machine speed is configured to be changed from -200RPM to 200RPM. Without compensation of cross-saturation effect, Fig. 3.14, the estimated position error would reach up to around 30 electrical degrees at full load condition. When the proposed compensation method is employed, Fig. 3.15, the estimated position error can be constrained within ±8 electrical degrees in the whole operation range. From the experiment results, it can be concluded that the developed method is quite effective to decouple the position error resulting from cross-saturation effect.

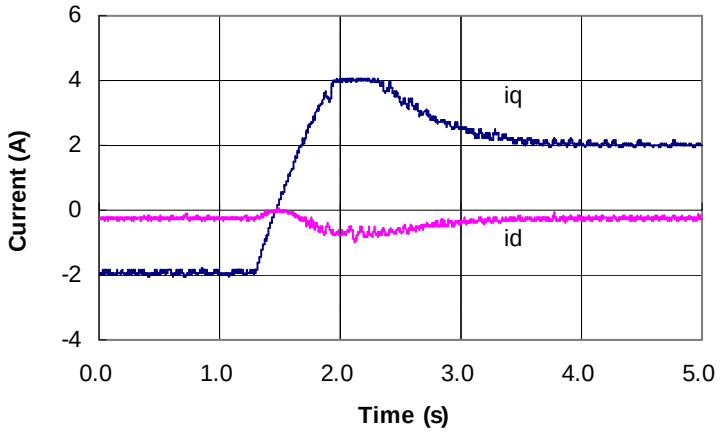

(a) Current response during speed step change

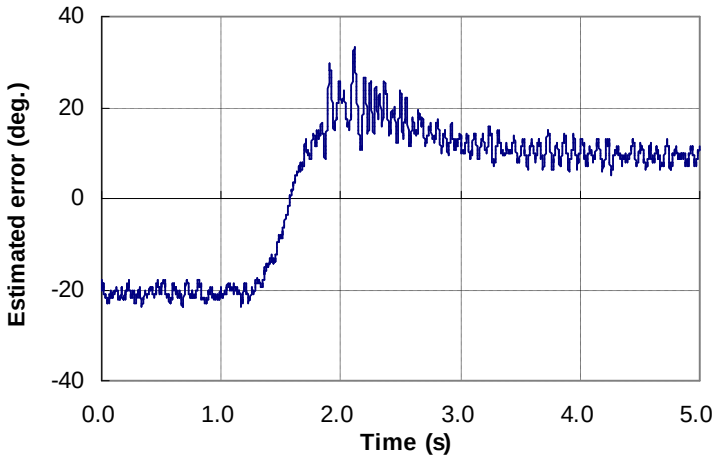

(b) Estimated position error

Fig. 3.14 Measured step speed response (without compensation).

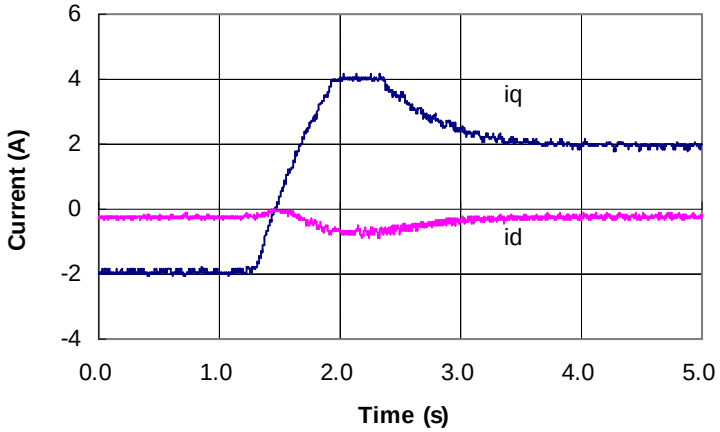

(a) Current response during speed step change

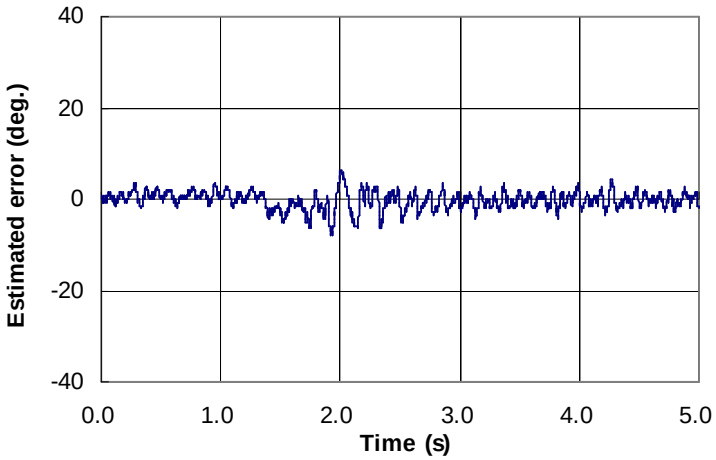

(b) Estimated position error

Fig. 3.15 Measured step speed response (with compensation).

3.5 Position Tracking Observer

For rotating carrier signal injection based sensorless methods, the arc-tangent function ($\tan^{-1}$) can be used to calculate the rotor position information from (3.43a) [TES03]. The principle is quite straightforward, however, the noise on the signal input to arc-tangent function has great contribution to the disturbance of estimated position.

Alternatively, a position tracking observer is much more popular in sensorless position estimation. Appropriate design of the position observer gives good immunity to disturbance harmonics while keeping the dynamic performance of position tracking. Although some nonlinear controllers such as bang-bang controllers can be used in position observer to enhance the dynamic characteristics [JAN04], they have the disadvantage of giving an unclear steady state response. Therefore, linear PI controllers prevail in sensorless position observer [HAR00] [CUP10], which are also employed in this work.

Considering the signal $f(\Delta\theta)$ input to the position observer for conventional pulsating and rotating injection, the block diagram of position observer including PI regulator is shown in Fig. 3.16.

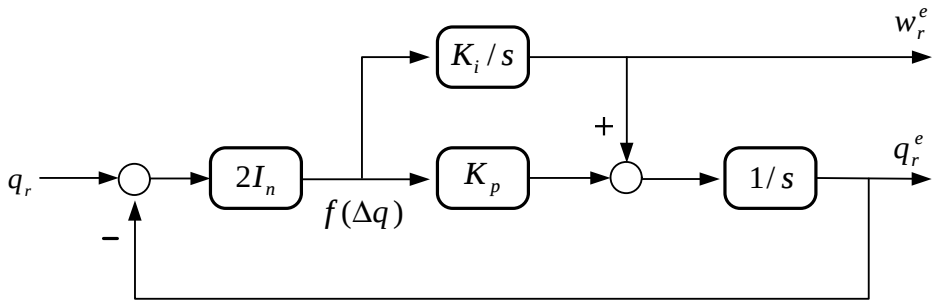

Fig. 3.16 Block diagram of position tracking observer.

According to the diagram, the close loop transfer function between the actual rotor position information and the estimated one can be expressed as,

$$\frac{q_r^e}{q_r} = \frac{2I_n k_p \cdot s + 2I_n k_i}{s^2 + 2I_n k_p \cdot s + 2I_n k_i} \tag{3.45}$$

Further analysis of the machine saliency in Chapter 4 shows that the value of I_n is load dependent, hence the parameters of k_p and k_i for position observer should be on-line

varied with I_n to maintain a constant bandwidth. For simplicity in practical implementation, however, the parameters of k_p and k_i can be selected based on the typical value of I_n at no load condition. A few papers address the criteria of selecting the parameters for a position observer [HAR00] [SEO06] [CHE10], alternatively, numerical simulation provides a quick solution for tuning of the position observer.

Although the bandwidth of the position observer can be adjusted freely based on (3.45), it has an upper limitation in a practical design due to the filters used in current measurement and the carrier signal demodulation process [CUP10]. Accounting for the time lag effect of filters, the equivalent model of a position observer for practical applications can be depicted in Fig. 3.17. It is difficult to accurately predict the time lag of the low pass filter, since it is significantly dependent on the demodulation process. It should be noted that, Fig. 3.17 is only valid when the position estimation error is very small, since great position estimation error would break the validity of (3.44).

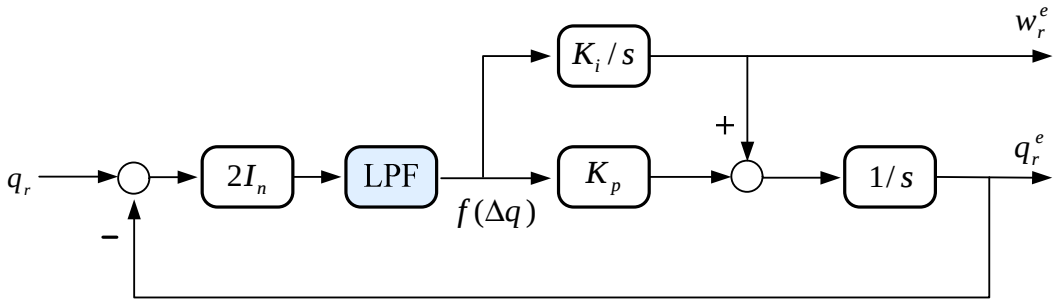

Fig. 3.17 Block diagram of position observer including low pass filter.

For the prototype system, the typical value of I_n is considered as I_n=70*mA*, the sampling frequency is configured to be 5kHz. The parameters of position observer are selected based on the optimal 2nd-order property of ideal close loop (K_p=*137*, K_i=*1250*). Without considering low pass filters, the unit step response and Bode plot of the position observer can be drawn by Matlab, as shown in Fig. 3.18. It can be seen that the designed position observer has the rise time of around 17.8ms in unit step response and loop bandwidth of around 19Hz, which satisfies the criteria present in [SEO06] [WAL06], i.e., *Bandwidth(speed) << Bandwidth(position) << Bandwidth(current).*

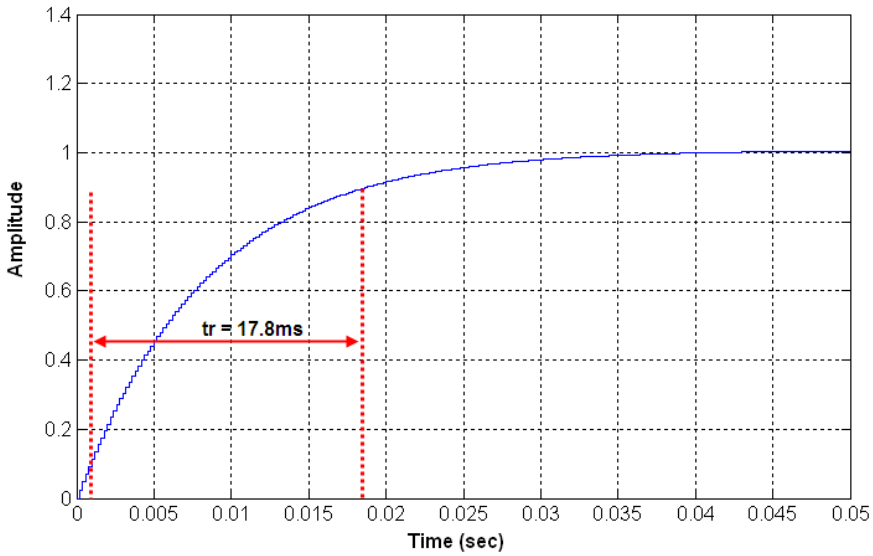

(a) Unit step response.

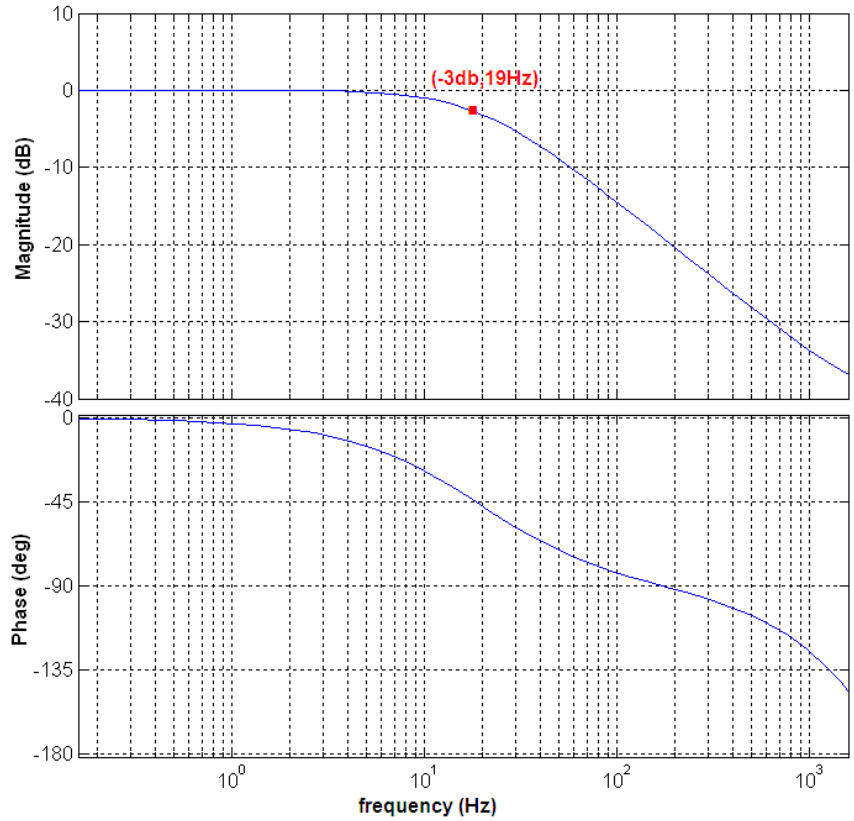

(b) Bode plot.

Fig. 3.18 Simulated dynamic performance of designed position observer.

To evaluate the effect of low pass filters on the dynamic behavior of position observer, Fig. 3.19 shows the experimentally measured step response of position tracking observer, in which LPF2 (Fig. 3.7 and Fig. 3.9) with different cut-off frequency is used to remove the carrier frequency ripple on $f(\Delta\theta)$. Without fundamental excitation, the

prototype machine stays at standstill. With the aid of optical encoder, manually rotate the rotor to the position of around -110 degrees, and then invoke the position tracking. It can be seen that, when the cut-frequency of LPF2 is much higher than designed bandwidth of position observer (*80Hz>>19Hz*), the designed position observer has similar dynamic behavior as theoretical simulation. The estimated rotor position could steadily track the real rotor position with the rise time of 19ms, similar to the predicted value of 17.8ms (Fig. 3.18a). A decrease in cut-frequency of LPF2 would lead to the dynamic performance of position observer being degraded, as shown in Fig. 3.19(b) and Fig. 3.19(c).

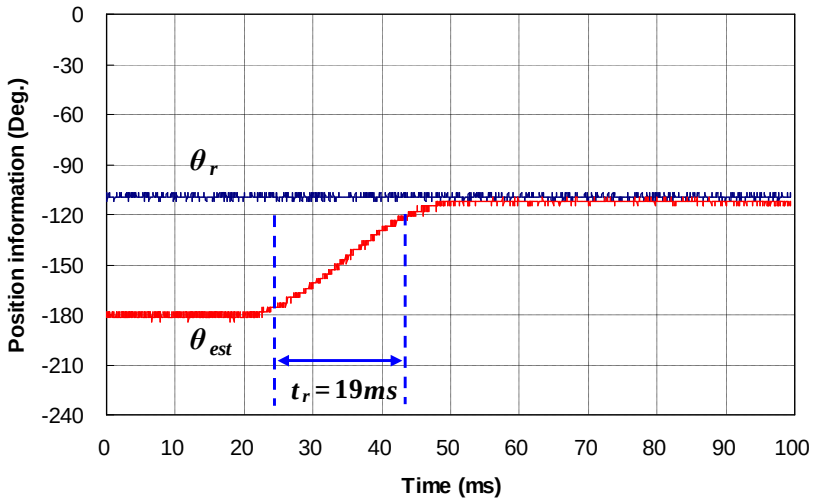

(a) f_c = *80Hz*

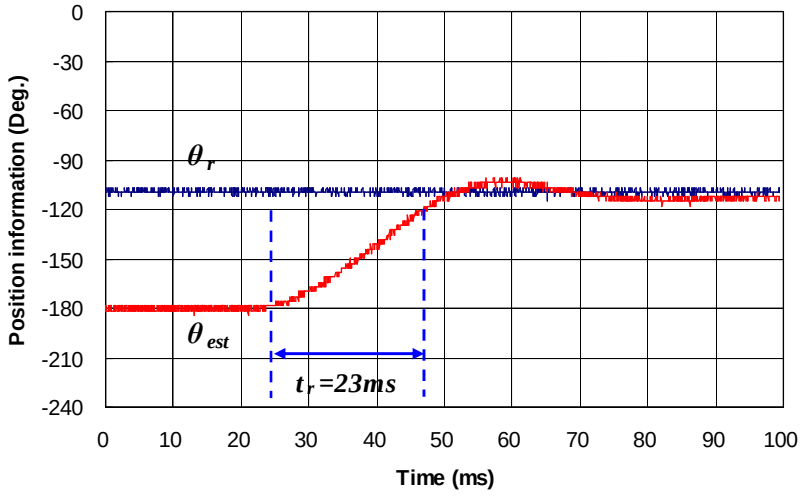

(b) f_c = *40Hz*

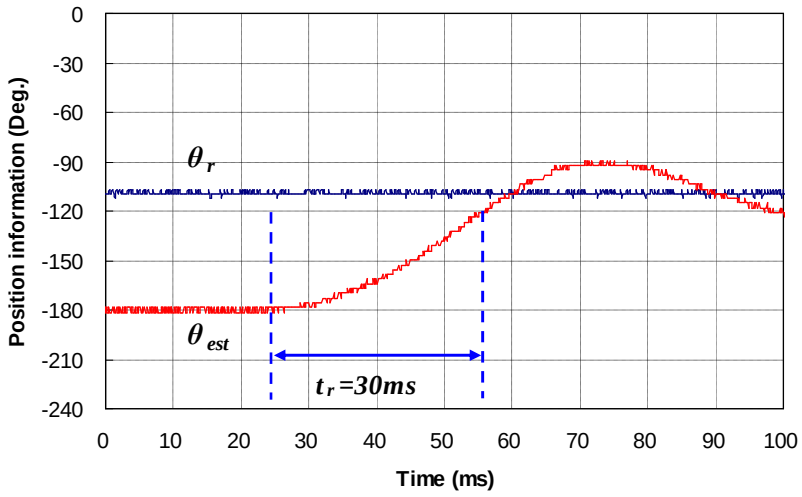

(c) f_c = *20Hz*

Fig. 3.19 Position step response with different cut frequency of LPF2.

3.6 Comparison between Pulsating and Rotating Injection Techniques

Although a similar principle is exploited to estimate the rotor position information for both pulsating and rotating carrier signal injection based sensorless techniques, they have different characteristics due to different carrier signal injection and demodulation processes. The comparative results between them are shown in Table 3.1.

Table 3.1 Comparison between *d*-axis pulsating injection and rotating injection.

	***d*-axis pulsating injection**	**rotating injection**
Based reference frame	estimated synchronous	stationary
Carrier voltage injection	pulsating carrier voltage	rotating carrier voltage vector
Carrier current response	amplitude-modulated	phase-modulated
Carrier current spectrum	symmetrical	asymmetrical
Current ripple in *q*-axis (with accurate position)	$I_n \sin q_m$	$\frac{I_p^2 - 2I_pI_n\cos q_m + I_n^2}{I_p - I_n\cos q_m}$
Torque ripple	Small	Large
Estimation error due to cross-saturation effect	$-q_m/2$	$-q_m/2$

$f(\Delta\theta)$ (without compensation)	$I_n \sin(2\Delta q + q_m)$	$I_n \sin(2\Delta q + q_m)$
Signal demodulation process	simple	complex
Sensitivity to inverter nonlinearity effect	++	++
Dynamic performance	good	medium

3.6.1 Carrier current response in time domain

When the prototype machine operates in sensored mode ($\Delta\theta=0$), the measured current response in time domain for *d*-axis injection technique can be drawn in stationary and synchronous reference frame respectively, as shown in Fig. 3.20. It can be seen that *d*-axis carrier voltage injection generates oscillating *d*-axis current, but limited current ripple on *q*-axis. Ideally, if the position estimation error is zero, (3.19) shows that *d*-axis current ripple has the amplitude of ($I_p+I_n cos\theta_m$), while *q*-axis current ripple has the amplitude of ($I_n sin\theta_m$).

By comparison, the measured current response for rotating injection technique is shown in Fig. 3.21. The carrier current locus on synchronous reference frame is of elliptic form, obviously, more torque ripple would be generated for rotating injection due to more current ripple on *q*-axis. From (3.34), the carrier current in synchronous reference frame can be derived by coordinate transformation,

$$\begin{aligned}
\begin{bmatrix} i_{dh} \\ i_{qh} \end{bmatrix} &= \begin{bmatrix} \cos q_r & \sin q_r \\ -\sin q_r & \cos q_r \end{bmatrix} \begin{bmatrix} i_{ah} \\ i_{bh} \end{bmatrix} \\
&= \begin{bmatrix} \cos q_r & \sin q_r \\ -\sin q_r & \cos q_r \end{bmatrix} \begin{bmatrix} I_p \cos(a - p/2) + I_n \cos(-a + 2q_r + q_m + p/2) \\ I_p \sin(a - p/2) + I_n \sin(-a + 2q_r + q_m + p/2) \end{bmatrix} \\
&= \begin{bmatrix} I_p \cos(a - q_r - p/2) + I_n \cos(-a + q_r + q_m + p/2) \\ I_p \sin(a - q_r - p/2) + I_n \sin(-a + q_r + q_m + p/2) \end{bmatrix} \\
&= \begin{bmatrix} \cos(q_m/2) & -\sin(q_m/2) \\ \sin(q_m/2) & \cos(q_m/2) \end{bmatrix} \begin{bmatrix} (I_p + I_n)\cos(a - q_r - q_m/2 - p/2) \\ (I_p - I_n)\sin(a - q_r - q_m/2 - p/2) \end{bmatrix}
\end{aligned} \tag{3.46}$$

The theoretical analysis implies that the carrier current trajectory in the synchronous reference frame is of elliptic form, which has a semi-major axis of (I_p+I_n) and a

semi-minor axis of (I_p-I_n). The most important point is that the elliptic current trajectory has a major axis leading the *d*-axis by an angle of $\theta_m/2$ due to cross-saturation effect.

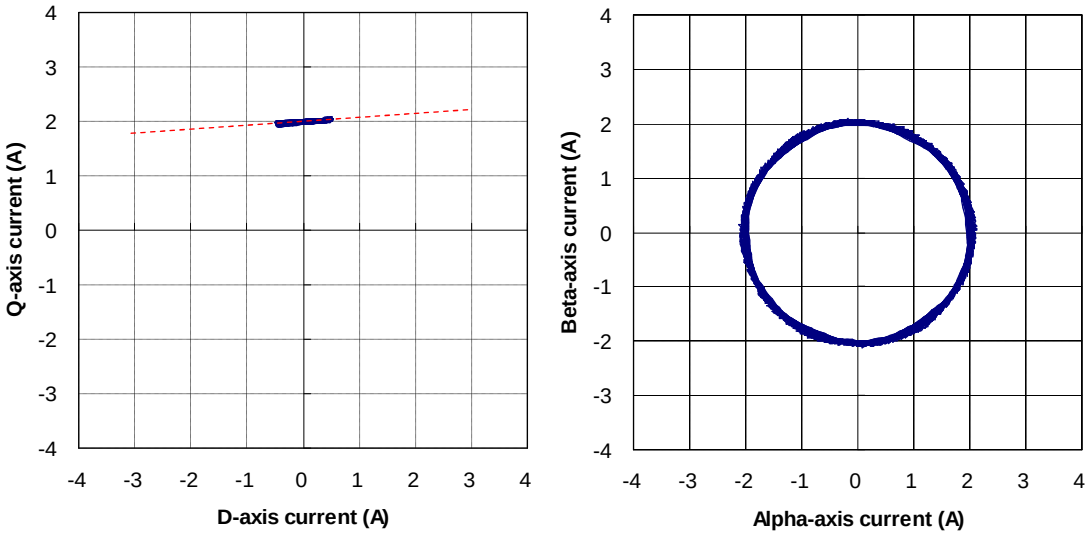

(a) Synchronous reference frame (b) Stationary reference frame

Fig. 3.20 Carrier current response for d-axis pulsating injection (i_d=0A, i_q=2A, *f*=4Hz).

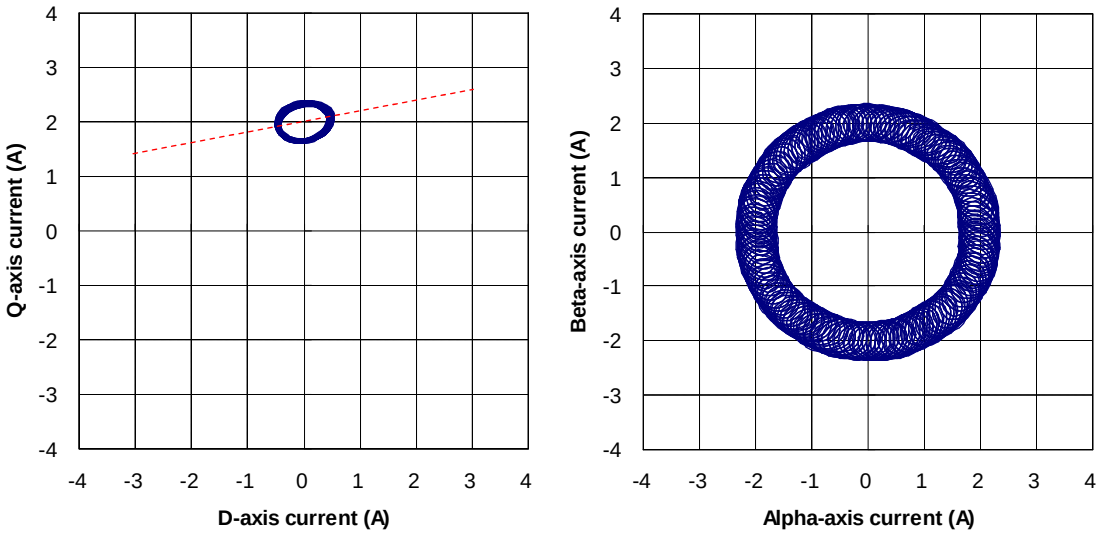

(a) Synchronous reference frame (b) Stationary reference frame

Fig. 3.21 Carrier current response for rotating injection (i_d=0A, i_q=2A, *f*=4Hz).

3.6.2 Carrier current spectral distribution

For pulsating injection, frequency domain analysis shows that spectral components of carrier current in synchronous reference frame have a symmetrical distribution, as

shown in Fig. 3.22. While an asymmetrical spectrum for rotating vector injection in the stationary reference frame can be observed in Fig. 3.23. The different spectral distributions should be due to different types of the injection signal. Essentially, the rotating vector injection method is characterized by asymmetrical injection with a rotating vector in one direction. The pulsating vector injection method, however, is equivalent to using two symmetrical rotating vectors, one is rotating in positive direction and the other one is rotating in negative direction. Furthermore, some harmonic components exist in the negative sequence range for both pulsating and rotating injection techniques, which can be explained by multiple saliency effects, and inverter nonlinearity effect as well.

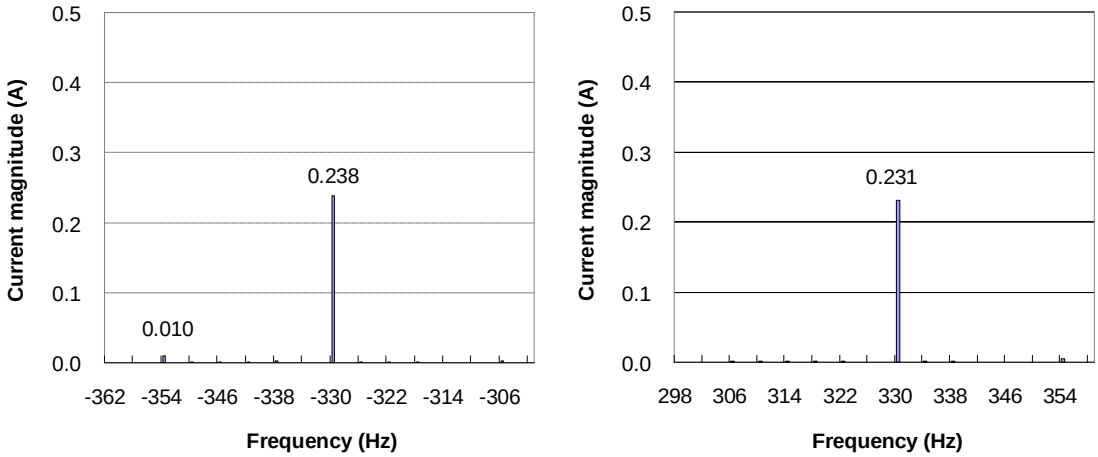

(a) Negative sequence components (b) Positive sequence components

Fig. 3.22 Carrier current spectrum for pulsating injection (i_d=0A, i_q=2A, f=4Hz).

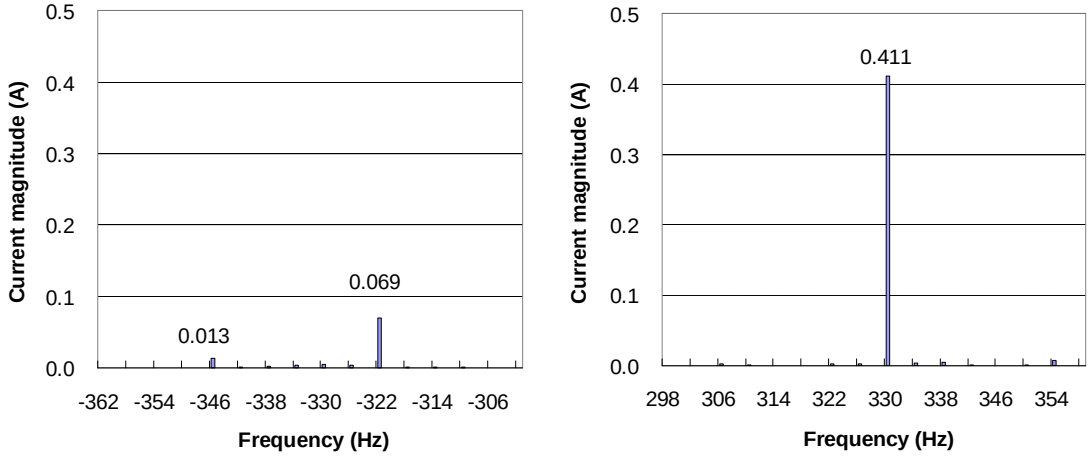

(a) Negative sequence components (b) Positive sequence components

Fig. 3.23 Carrier current spectrum for rotating injection (i_d=0A, i_q=2A, f=4Hz).

3.6.3 Cross-saturation effect

The influence of cross-saturation effect on saliency based sensorless control has been well documented by previous studies. The most critical issue resulting from cross-saturation effects is that a load-dependent position estimation error would be generated for both pulsating and rotating injection techniques. The introduced estimation error ($\theta_m/2$) is identical for both forms of injection. Fortunately, the estimation error is constant for given load condition, hence it can be easily compensated on-line based on off-line measured or simulated cross-saturation angle (θ_m).

With regard to the *q*-axis current ripple, which results in torque ripple, cross-saturation effect makes it worse even when the position estimation error is zero. For *d*-axis pulsating injection, the cross-saturation effect increases the *q*-axis current ripple up to ($I_n sin\theta_m$). For rotating injection, the cross-saturation effect rotates the major axis of elliptic current locus, which leads to more current ripple on the *q*-axis. From (3.46), the current ripple in *q*-axis can be derived as,

$$I_{ripple} = \frac{I_p^2 - 2I_p I_n \cos q_m + I_n^2}{I_p - I_n \cos q_m} \tag{3.47}$$

On the other hand, (3.13b) shows that the value of L_n decreases with cross-saturation effect (L_{dqh}), which gives rise to the increase in I_n. The increase of I_n has a positive contribution to improve the SNR for sensorless estimation. Therefore, the cross-saturation effect is expected to be helpful to extend the operation range for effective sensorless control, as will be confirmed and further discussed in detail in Chapter 4.

3.6.4 Carrier signal demodulation

The comparison between Fig. 3.6 and Fig. 3.8 shows that, the carrier signal demodulation process for pulsating injection is pretty simple and less computational intensive. Actually, the synchronous detection scheme employed in pulsating injection is not a full frame transformation [RAC10].

For the case of pulsating carrier signal injection, a gain of less than one ($\cos\delta$) would be introduced in the magnitude of the carrier current component due to the digital system delay. Although it slightly decreases the SNR of the signal, no estimation error would be

introduced in steady state. For the case of rotating carrier signal injection however, digital system delay would introduce additional phase lag in the demodulated negative sequence carrier current component, hence it should be compensated along with other lags.

Regardless of pulsating or rotating carrier signal injection, the fundamental excitation should be isolated from total current response using SRFF techniques. For *d*-axis pulsating signal injection, the LPF for a *q*-axis current regulator can be neglected since dominant carrier current exists on the *d*-axis if position estimation error is sufficiently small. For rotating signal injection however, a LPF is essential for both *dq*-axis current regulators. There is no doubt that the dynamic performance of rotating carrier signal injection based sensorless methods would be deteriorated due to the phase lag in the LPF.

3.6.5 Inverter nonlinearity effect

Inverter nonlinearity effect is one of the major sources generating carrier voltage distortion. In [LIN03] [YAN11], *q*-axis pulsating injection is proven to be insensitive to inverter nonlinearity effect, since the magnitude of carrier current is zero when the fundamental phase current crosses zero. For commonly used *d*-axis pulsating and rotating injection, the phase current response under the same load condition and fundamental frequency are measured, as shown in Fig. 3.24. There is no clear evidence to show which one is better in terms of sensitivity to inverter nonlinearity effect [RAC10].

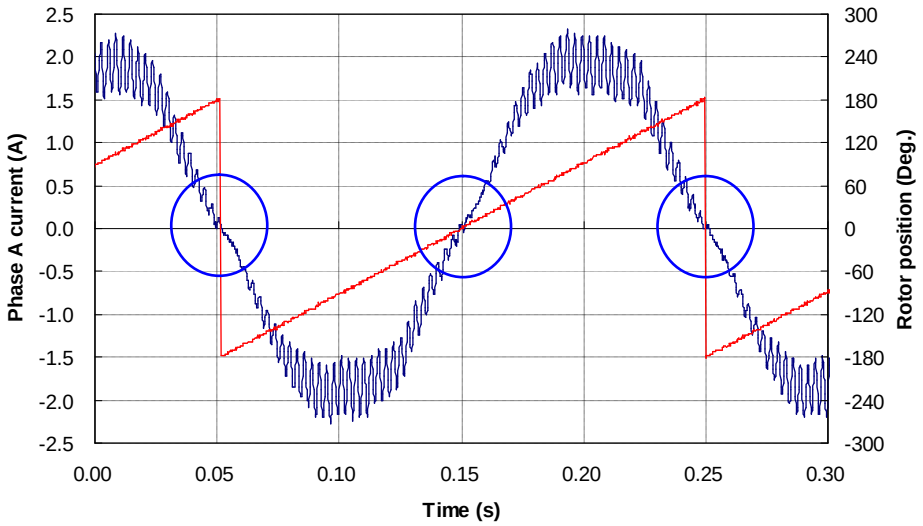

(a) Phase A current for *q*-axis pulsating injection

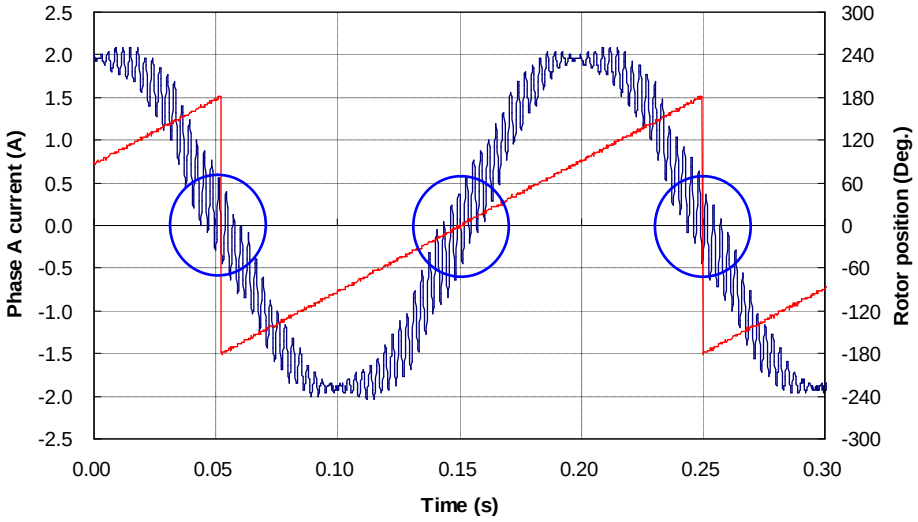

(b) Phase A current for *d*-axis pulsating injection

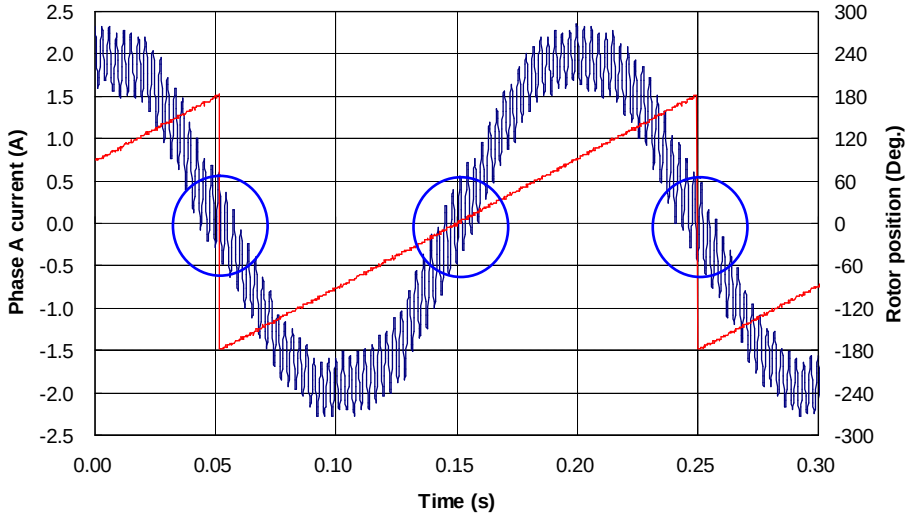

(c) Phase A current for rotating injection

Fig. 3.24 Comparison of phase current (i_d=0A, i_q=2A, f=4Hz).

3.7 Magnetic Polarity Detection

In sensorless control, it is necessary to identify the initial rotor position prior to energizing the machine for smooth start-up. The information of initial rotor position consists of two types of knowledge [NOG98]: the first one is the rotor direction, which indicates an angle between the reference axis (the winding axis of phase A) and either N or S pole; the second one is the information of magnetic polarity, which indicates either the direction of N or S pole is closer to the reference axis.

Since the machine saliency varies periodically as a second spatial harmonic, the estimated position information based on machine saliency is rotor direction without magnetic polarity information, which has an angle ambiguity of π. If the estimated rotor direction, which is aligned at the south magnetic pole position, is regarded as the rotor position, the sign of output torque will be changed and the system will be unstable. Therefore, it is important to identify the magnetic polarity before the drive is put into operation. Once the polarity information before start-up is obtained, it can be latched and the estimated initial rotor direction from carrier current response can be used to calculate the initial rotor position.

The basic principle for magnetic polarity identification is utilizing the saturation effect of the machine. A positive *d*-axis current increases the stator iron saturation, resulting in a decreased *d*-axis inductance. It should be noted that the saturation effect in *q*-axis is not available for magnetic polarity detection for the reason that the *q*-axis flux linkage is an odd function of the *q*-axis current and has no even-order terms to detect the magnetic polarity [JEO05]. Based on finite elemental analysis (FEA), the *dq*-axis flux linkages for the prototype machine are shown in Fig. 3.25. The magnetic saturation effect can be clearly observed on the *d*-axis flux linkage when positive *d*-axis current is applied to the machine.

Considering the effect of magnetic saturation in the stator core, some methods utilize the inductance measurement by monitoring the *di/dt* of winding current to obtain the initial rotor position information including magnetic polarity information [NAK00] [BOU05]. Consequently, there is no requirement for separate magnet polarity detection process. However, these kinds of methods require dedicated voltage generation and current measurement, which are quite different from the conventional one used in high frequency carrier signal injection based methods. Consequently, it is not popular for carrier signal injection based sensorless techniques.

In conventional carrier signal injection based sensorless control methods, the rotor direction can be estimated from the position dependent carrier current response, while the magnetic polarity information is absent. The magnetic polarity information can be obtained based on transient short pulses injection [AIH99] [NOG98] [HAQ03] [HOL08]

or secondary harmonics due to magnetic saturation effect [HA03] [KIM04a] [JEO05] [HAR05] [RAC08b] [LI09a].

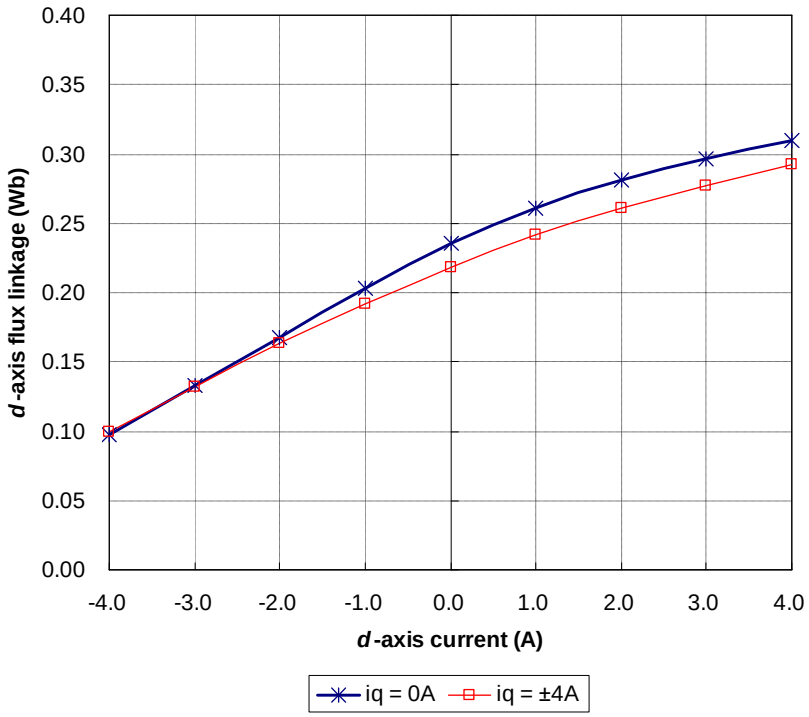

(a) *d*-axis flux linkage

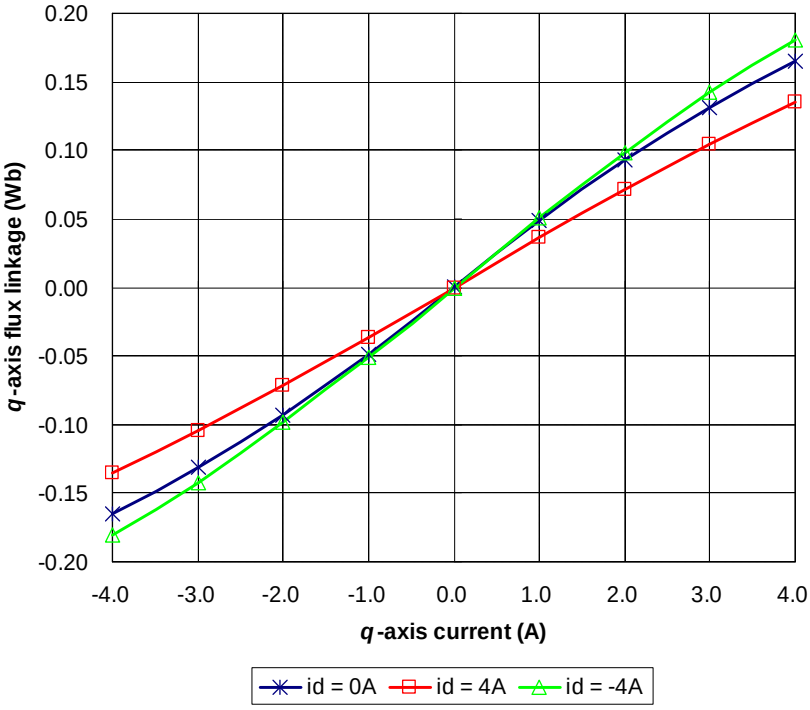

(b) *q*-axis flux linkage

Fig. 3.25 FEA simulated flux linkage for the prototype machine.

3.7.1 Short pulses injection

After the rotor direction information is obtained from conventional carrier signal injection based techniques, separate magnetic polarity detection can be performed by injecting the specified transient pulse signal, which gives rise to stator iron saturation. Different transient signals can be injected along the estimated rotor direction to examine the effect of magnet saturation, such as an AC current [NOG98], dual short voltage pulses [AIH99] [HOL08], and a rectangular AC voltage [HAQ03].

Among them, dual voltage pulses injection proposed in [AIH99] is the simplest. One of the pulses aligns with the positive direction of the magnet flux, thus increasing the magnetization of the stator iron and driving the *d*-axis incremental inductance into deeper saturation and lower value. The other pulse, aligning with the negative direction of the magnet flux, tends to de-saturate the stator iron and leads to increasing *d*-axis incremental inductance. The injected short voltage pulses have identical volt-second values, hence the amplitude of the current response differs as the respective inductance values differ, i.e., the current pulse having higher magnitude indicates the positive direction of *d*-axis. The basic principle is shown in Fig. 3.26. The electromagnetic torque which occurs with the pulse voltage injected into the machine is very small, which hardly moves the rotor.

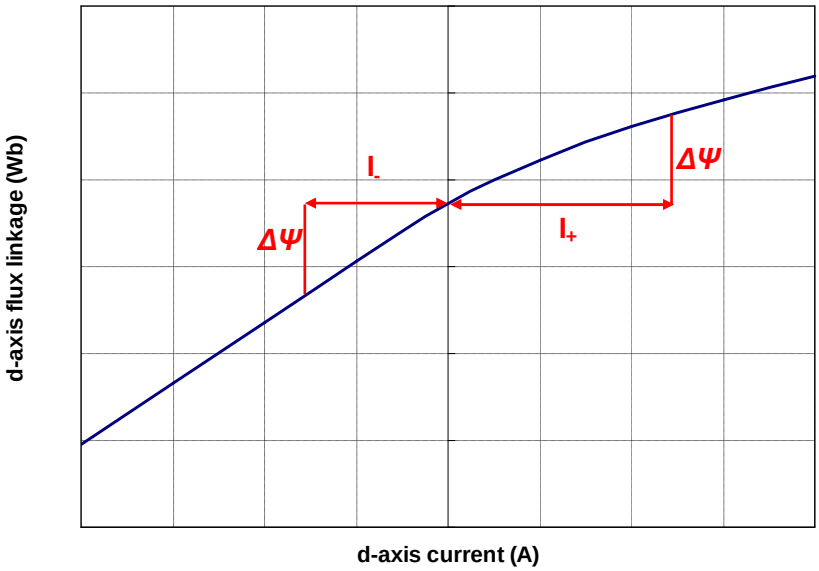

Fig. 3.26 Magnetic polarity detection using discrete voltage pulses injection.

Fig. 3.27 and Fig. 3.28 show the magnetic polarity detection for the prototype machine with dual voltage pulses method. If initially estimated rotor direction from machine saliency property is equal to the real rotor position ($\Delta\theta=0°$), the applied positive *d*-axis voltage pulse would result in higher d-axis current pulse, as shown in Fig. 3.27. On the other hand, lower amplitude current response to the positive *d*-axis voltage pulse suggests that the estimated rotor direction has an angle shift of π with respect to the real rotor position information, as shown in Fig. 3.28.

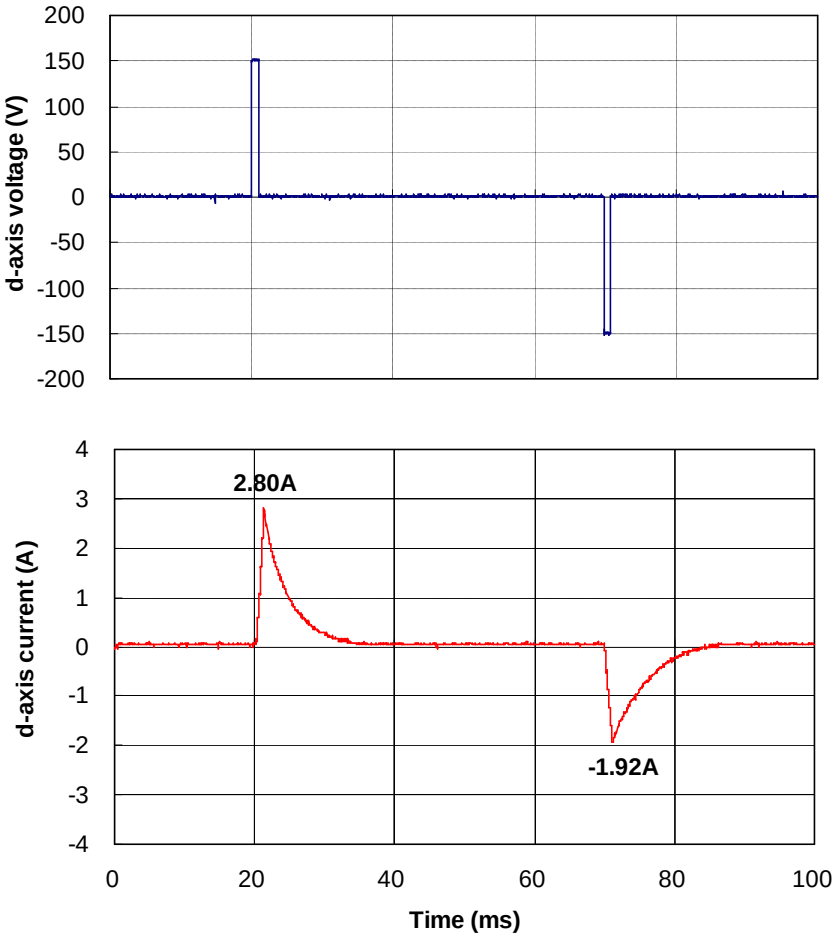

Fig. 3.27 Magnetic polarity detection with dual voltage pulses ($\Delta\theta=0°$).

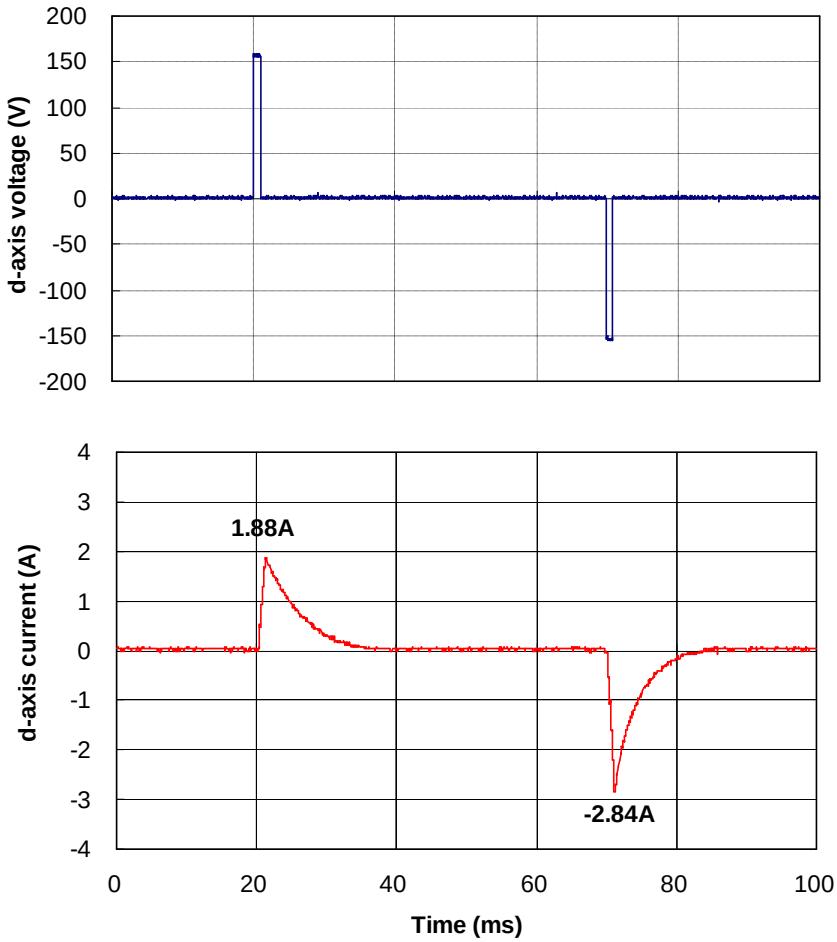

Fig. 3.28 Magnetic polarity detection with dual voltage pulses ($\Delta\theta=180°$).

Although the short pulses injection method has robust and reliable identification performance due to good SNR, it suffers from a little bit slow convergence time [HOL08]. Even worse, the magnetic polarity identification should be performed as an independent process, which is difficult to integrate with the sensorless algorithm, thus giving rise to computational complexity.

3.7.2 Secondary harmonics based method

According to the basic machine model presented before, magnetic polarity information can not be extracted from the carrier current response; however, the actual machine is subject to saturation and cross-saturation effect, and the carrier current response should contain the related information. When the machine saturation property is considered in the machine model, the resultant carrier current response to the *d*-axis pulsating carrier signal injection can be simplified as [JEO05],

$$\begin{bmatrix} i_{dh}^e \\ i_{qh}^e \end{bmatrix} = \begin{bmatrix} I_p + I_n \cos(2\Delta q + q_m) \\ I_n \sin(2\Delta q + q_m) \end{bmatrix} \cdot \sin a + \begin{bmatrix} I_{sat} \cos^2 \Delta q \cos \Delta q \\ I_{sat} \cos^2 \Delta q \sin \Delta q \end{bmatrix} \cdot \sin^2 a \qquad (3.48)$$

where $I_{sat} = \frac{V_c^2}{2w_c^2} \frac{d^2 i_d}{dy_d^2} y_m > 0$.

Compared with (3.19), it can be seen that the secondary carrier current component ($\sin^2\alpha$) resulting from the interaction between the injected carrier voltage and the saturation saliency, is effective to identify the magnetic polarity information [HA03] [KIM04a] [HAR05] [JEO05] [RAC08b] [LI09a]. From (3.48), the signals related to magnetic polarity detection can be calculated as follows,

$$\begin{cases} I_{d\sin 2a} = LPF(i_{dh}^e \cdot \sin 2a) = 0 \\ I_{d\cos 2a} = LPF(i_{dh}^e \cdot \cos 2a) = -\frac{1}{4} I_{sat} \cos^2 \Delta q \cos \Delta q \end{cases} \qquad (3.49)$$

Obviously, the magnetic polarity information can be detected from the sign of $I_{dcos2\alpha}$. In this way, the carrier current component due to primary spatial saliency ($\sin\alpha$) is used to estimate the rotor direction information, while the additional carrier current component due to magnetic saturation ($\sin^2\alpha$) is used to detect the magnetic polarity information.

Although this kind of method has the advantage of quick convergence (25~50ms) [HAR05], the major problem is that the magnitude of the secondary carrier current component for magnetic polarity detection is very low, which gives rise to limited robustness on the magnetic polarity identification. To solve this problem, some suggestions are given, which include increasing the magnitude of the injected signal, or decreasing the carrier frequency during the magnetic polarity detection process for higher SNR of the carrier current response [JEO05] [LI09a]. An alternative to this is to employ a hysteresis controller in polarity detection for noise attenuation [RAC08b].

For the prototype machine, the frequency of the injected carrier voltage signal is decreased down to 100Hz (35V/100Hz) for effective magnetic polarity detection. The measured *d*-axis carrier current and calculated secondary harmonic components are shown in Fig. 3.29 and Fig. 3.30. With correct polarity alignment, $I_{dcos2\alpha}$ is negative, Fig. 3.29; if $I_{dcos2\alpha}$ is positive, the estimated rotor direction should be compensated by π to obtain the real rotor position information, Fig. 3.30.

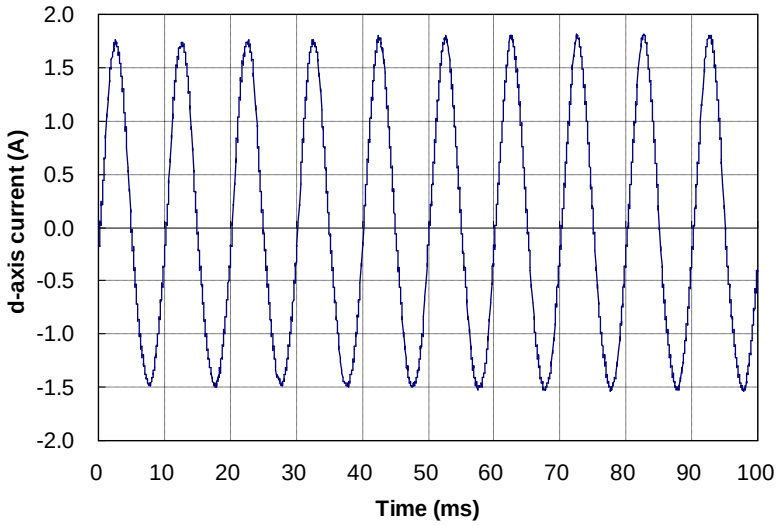

(a) Measured d-axis carrier current

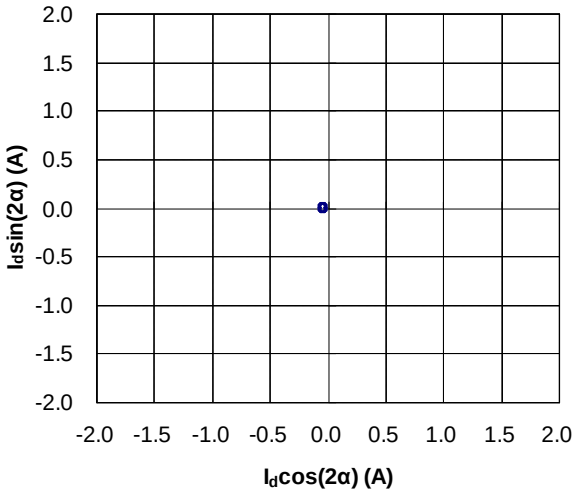

(b) Secondary harmonic components

Fig. 3.29 Magnetic polarity detection based on secondary harmonics ($\Delta\theta=0°$).

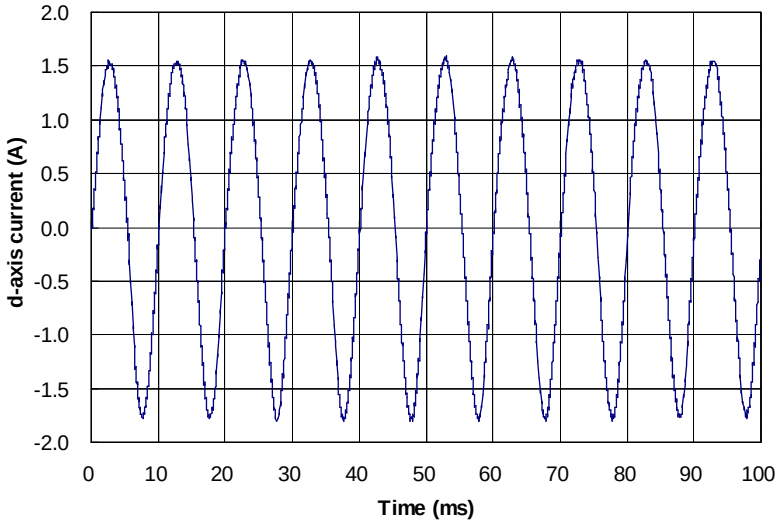

(a) Measured d-axis carrier current

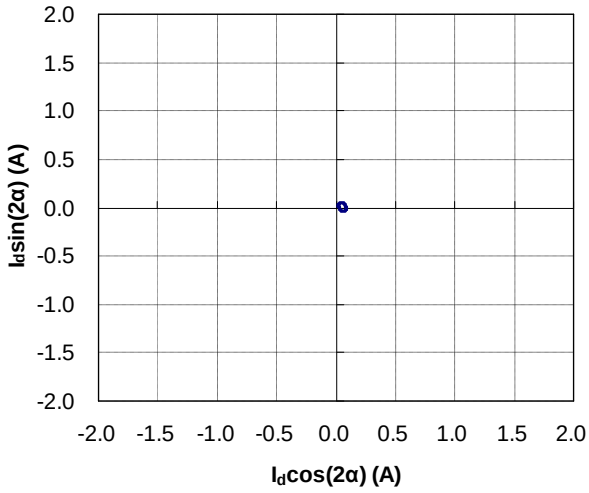

(b) Secondary harmonic components

Fig. 3.30 Magnetic polarity detection based on secondary harmonics (*Δθ=180°*).

3.7.3 Proposed method

Considering the limitation of presented methods, this thesis develops a robust scheme to identify the magnetic polarity for initial rotor position estimation, which can be easily integrated with the conventional carrier signal injection based sensorless algorithm.

In the conventional *d*-axis pulsating carrier signal injection based method, the amplitude of *q*-axis carrier current is used to extract the rotor direction information, while the amplitude of *d*-axis carrier current has not been used in control algorithm. However, it is proven to be very useful in magnetic polarity detection here, providing position estimation error is sufficient small, the amplitude of *d*-axis carrier current in the estimated synchronous reference frame can be derived from (3.26), as shown below.

$$\left|i_{dh}^{e}\right| = I_p + I_n \cos(2\Delta q + q_m) \approx I_p + I_n \cos q_m \tag{3.50}$$

Substituting (3.13b) and (3.19b) into above equation, it can be derived that,

$$\left|i_{dh}^{e}\right| \approx \frac{V_c}{w_c} \cdot \frac{L_{qh}}{L_{dh}L_{qh} - L_{dqh}^2} \tag{3.51}$$

Considering the mutual inductance is very small, i.e,. $L^2_{dqh} << L_{dh}L_{qh}$. Therefore, (3.51) can be simplified as,

$$\left|i_{dh}^{e}\right| \approx \frac{V_c}{w_c} \cdot \frac{1}{L_{dh}} \tag{3. 52}$$

For a given injected carrier voltage signal (V_c/ω_c), the above equation indicates that the amplitude of the *d*-axis carrier current is only determined by L_{dh}. Due to magnetic saturation, L_{dh} is significantly dependant on *d*-axis fundamental current, as shown in Fig. 3.31 for the prototype machine. Consequently, it is possible to identify the magnetic polarity from the variation of $|i^e_{dh}|$ against *d*-axis fundamental current.

With the aid of accurate rotor position information from the encoder, the *d*-axis current can be measured at different fundamental excitations, as shown in Fig. 3.32. From the experimental results, it can be concluded that the magnetic polarity can be reliably detected based on the comparison of $|i_{dh}|$ at different *d*-axis fundamental current levels. It is also interesting to note that the *d*-axis carrier current oscillates asymmetrically around the fundamental current reference, the ripple magnitude along the positive *d*-axis being a little bit higher. This can be explained by the fact that the magnetic saturation effect becomes more severe along the positive *d*-axis, as shown in Fig. 3.26. In order to improve the SNR, the proposed method enlarges the saturation effect through applying different *d*-axis fundamental current. Consequently, higher reliability of magnetic polarity detection can be achieved by the proposed method.

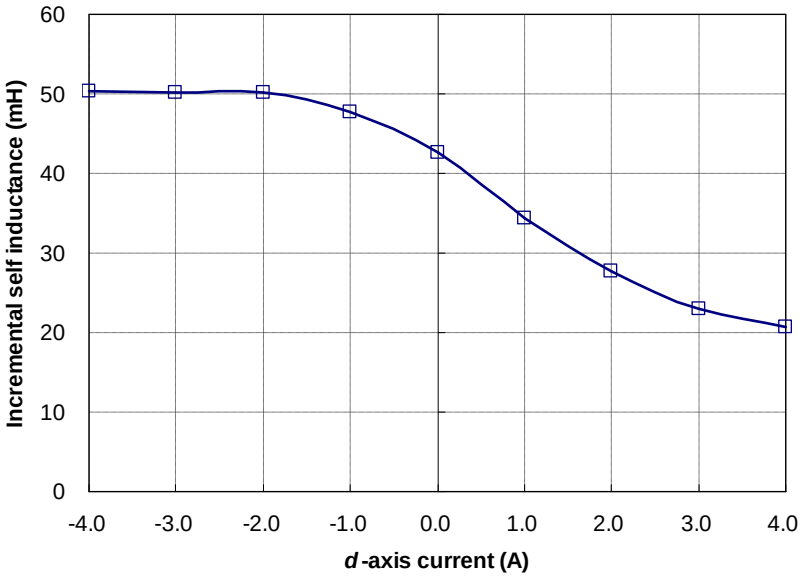

Fig. 3.31 *d*-axis incremental self-inductance for the prototype machine (L_{dh}).

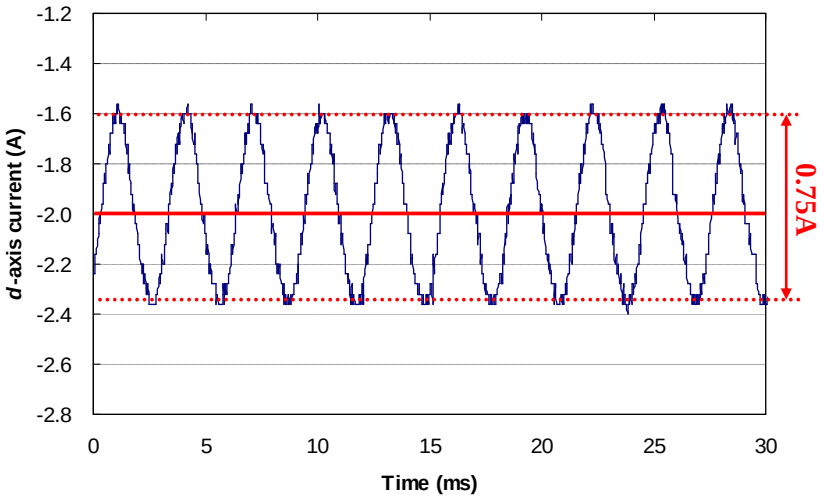

(a) i_{df} = -2A, i_{qf} = 0A

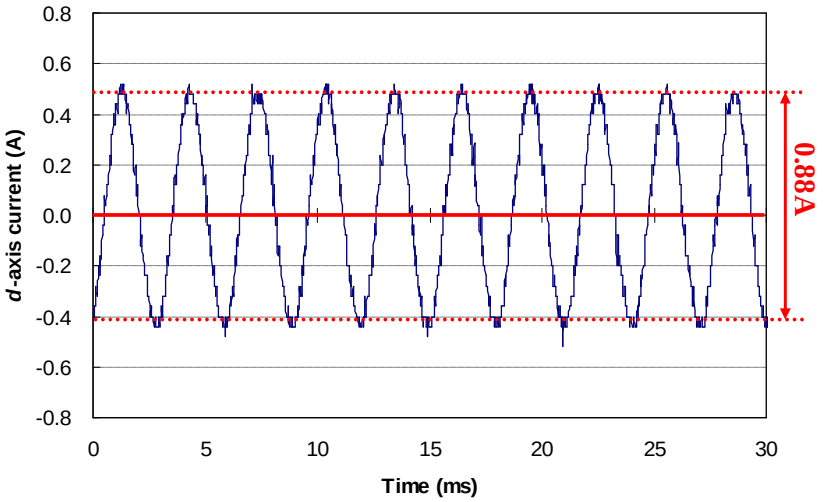

(b) i_{df} = 0A, i_{qf} = 0A

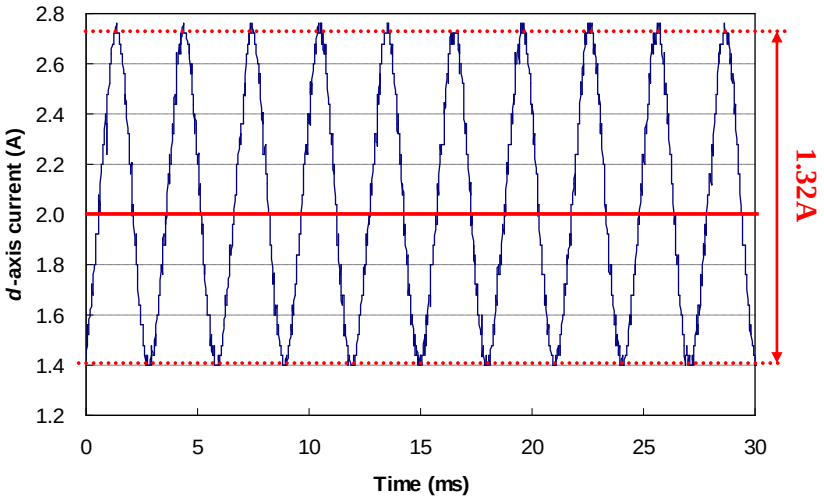

(c) i_{df} = 2A, i_{qf} = 0A

Fig. 3.32 Measured *d*-axis current in sensored operation mode.

The proposed magnetic polarity detection method can be seamlessly integrated into the *d*-axis pulsating carrier signal injection based sensorless control technique, as depicted in Fig. 3.33. The detailed description about magnetic polarity detection is shown in Fig. 3.34. It should be noted that no electromagnetic torque must be applied to the machine during the detection process (i_{qf}=*0A*). Before the drive is initially started, the rotor direction information can be obtained from conventional sensorless algorithm without fundamental excitation (i_{df}=*0A*, i_{qf}=*0A*), meanwhile, the amplitude of *d*-axis carrier current at this condition is recorded (Step 1). The estimated rotor direction either indicates the correct rotor position, or is shifted by π from the correct rotor position. Referring to the estimated rotor direction, a given *d*-axis fundament current reference is applied to the machine. The fundament current reference of (i_{df}=*2A*, i_{qf}=*0A*) is selected for the prototype machine. At the same time, the amplitude of *d*-axis carrier current at this load condition is also stored into processor memory (Step 2). After that, the fundament current reference is set back to (i_{df}=*0A*, i_{qf}=*0A*) (Step 3). Finally, the amplitude of *d*-axis carrier current at a different load condition is compared. The increase of amplitude indicates the estimated rotor direction is at the correct rotor position, otherwise, the phase shift of π should be added.

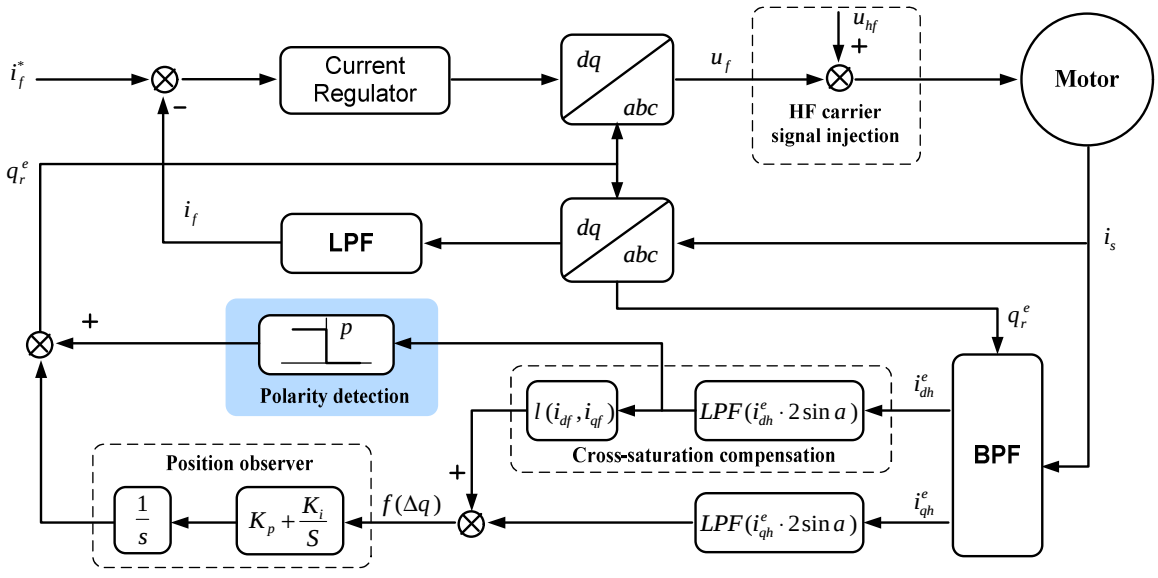

Fig. 3.33 Proposed magnetic polarity detection for pulsating carrier signal injection.

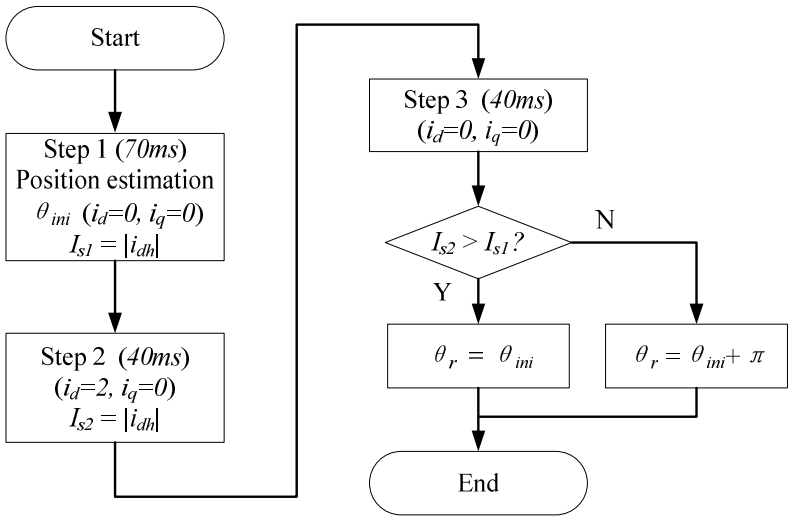

Fig. 3.34 Flow chart of proposed magnetic polarity detection.

The experimental results shown in Fig. 3.35 and Fig. 3.36 confirm the effectiveness of proposed detection method. It can be found that the initial rotor position including magnetic polarity detection can be successfully estimated within 150ms. In Fig. 3.35 and Fig. 3.36, the estimation process is activated at the time of 50ms. During step 1, the rotor position without magnetic polarity information is obtained at the fundamental excitation of (i_{df}*=0A,* i_{qf}*=0A*). At step 2, the prototype machine is excited with the fundamental reference of (i_{df}*=2A,* i_{qf}*=0A*). Finally, the fundamental excitation is reset to (i_{df}*=0A,* i_{qf}*=0A*) at step 3. During the whole process, the amplitude of the *d*-axis carrier current is recorded. At the end of step 3, the magnetic polarity information can be obtained from the amplitude variation of the *d*-axis carrier current with the change of the *d*-axis fundamental current from 0A (step 1) to 2A (step 2). The amplitude increase of the *d*-axis carrier current suggests that the estimated rotor position at step 1 is correct, Fig. 3.36, otherwise, a phase shift of π should be added, Fig. 3.35.

The proposed polarity detection method is also applicable to rotating carrier signal injection based sensorless technique. The difference is that the comparable parameter turns out to be the amplitude of the positive sequence carrier current, instead of the amplitude of the *d*-axis carrier current for pulsating injection.

Based on the *d*-axis magnetic saturation effect, the proposed magnetic polarity identification scheme can be easily integrated with conventional carrier signal injection

based sensorless technique with slight increase of computational efforts. Compared with secondary harmonics based methods, the proposed one has the advantage of robust detection due to higher SNR and less computational intensity. The convergence time of this method can be further shorted by increasing the bandwidth of *d*-axis current regulator. However, it is not encouraged to do so since more carrier voltage distortion may be introduced by the current regulator with higher bandwidth. Different kinds of magnetic polarity detection methods are compared in Fig. 3.37.

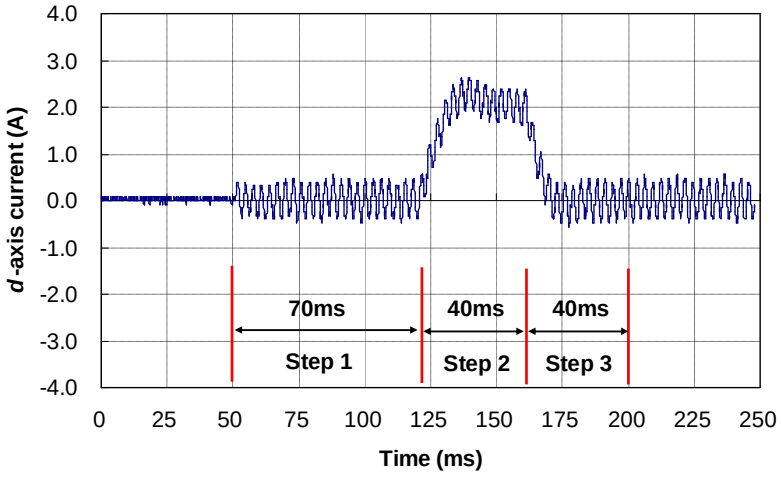

(a) *d*-axis instantaneous current

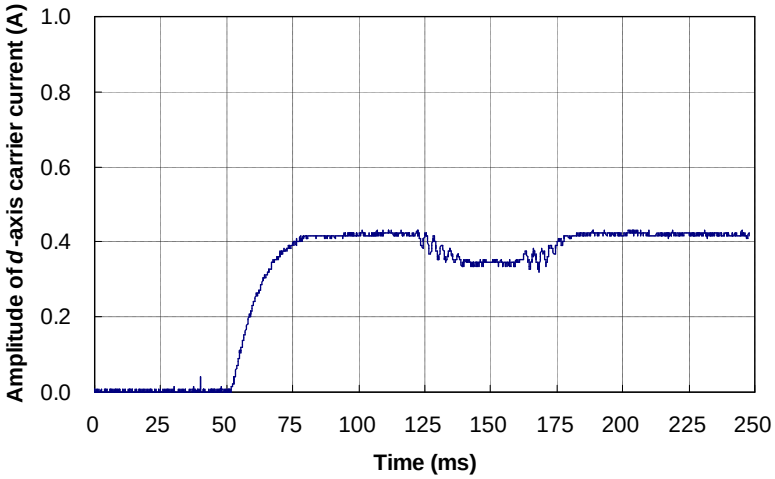

(b) Magnitude of *d*-axis carrier current

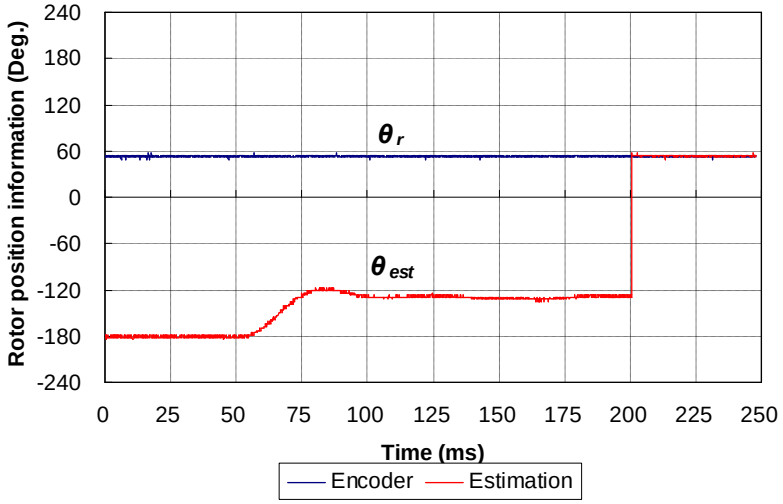

(c) Estimated rotor position information

Fig. 3.35 Initial rotor position estimation (Real rotor position: 58degrees).

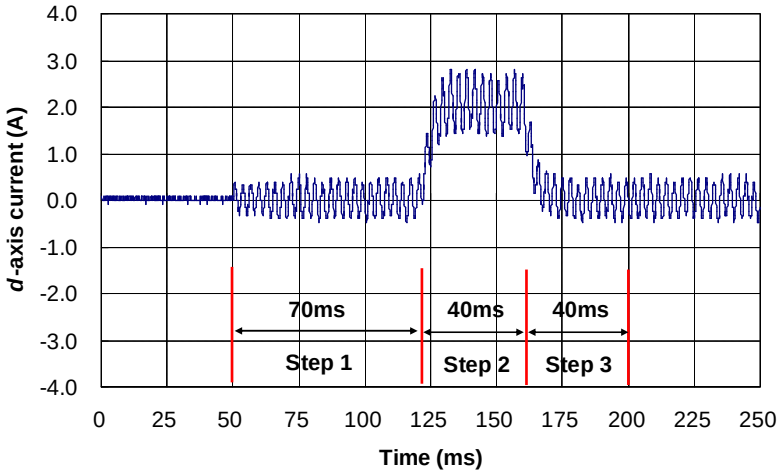

(a) *d*-axis instantaneous current

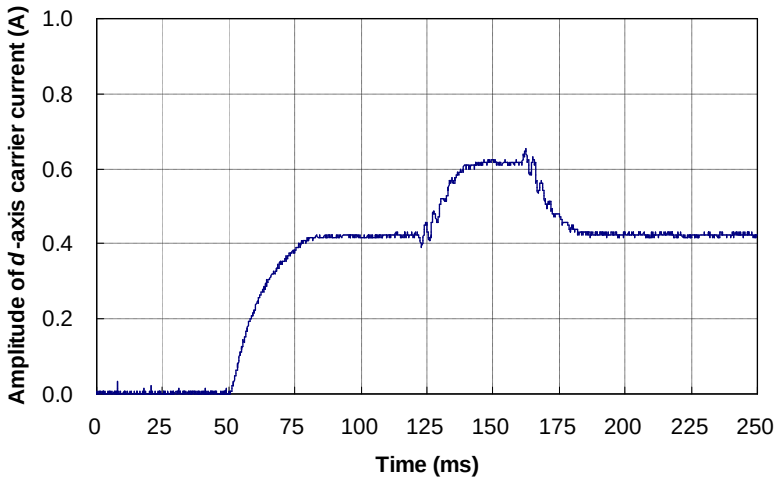

(b) Magnitude of *d*-axis carrier current

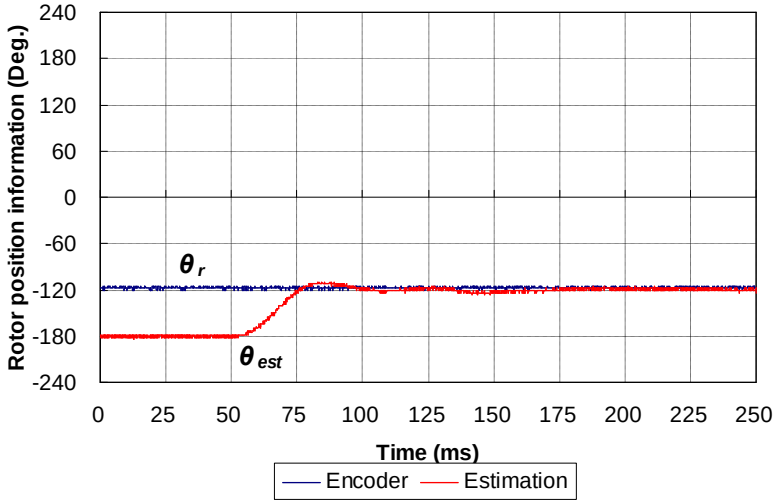

(c) Estimated rotor position information

Fig. 3.36 Initial rotor position estimation (Real rotor position: -120 degrees).

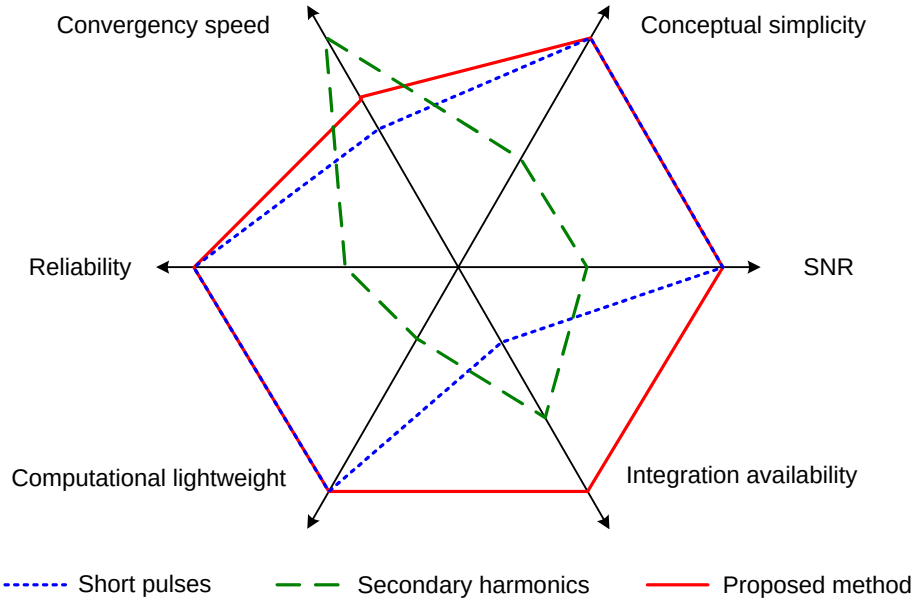

Fig. 3.37 Comparison between different kinds of magnetic polarity detection methods.

3.8 Conclusions

Carrier signal injection based sensorless methods have the similar principle to a position resolver. However, unlike the dedicate resolver with the injection frequency of 5 to 10kHz, carrier signal injection based sensorless methods superimpose the carrier signal on the fundamental excitation, with a standard voltage source inverter, which limits the carrier frequency and thus the bandwidth of whole system.

This chapter gives a detailed discussion about pulsating and rotating carrier signal injection based sensorless control methods, including machine high frequency models,

the signal demodulation process, the position tracking observer and so on. Compared with rotating carrier signal injection, the *d*-axis pulsating injection method prevails in terms of torque ripple, dynamic performance, signal demodulation process, and implementation complexity. Regarding the sensitivity to inverter nonlinearity effect, further investigation is needed to provide insight.

Actually, cross-saturation effect generates the same spatial harmonic order as the primary saliency (overlapped spectrum), hence the introduced position estimation error is critical for both pulsating and rotating carrier signal injection. Fortunately, the load dependant position estimation error is constant for a given load condition, it can be easily compensated for with the method presented in this chapter. In addition, the study on carrier current shows that more current ripple would be introduced on the *q*-axis due to cross-saturation effect, thus leading to more oscillating torque. However, the increase of I_n due to cross-saturation effect has a positive contribution to improve the SNR for sensorless estimation.

Magnetic polarity identification is another problem for saliency based sensorless techniques, since the machine saliency undergoes two cycles in single electrical period. Based on *d*-axis magnetic saturation effect, this thesis proposes a robust detection scheme, which can be easily integrated with conventional sensorless estimation algorithm.

CHAPTER 4

INVESTIGATION OF MACHINE SALIENCY AND SENSORLESS SAFETY OPERATION AREA

4.1 Introduction

Machine saliency is essential for saliency-based sensorless control of permanent magnet BLAC machines. It is well known that the machine saliency property results from physical geometric saliency and magnetic saturation as well. The saturation saliency is closely related to machine load condition, therefore, it is desirable to evaluate the machine saliency information within the whole operating range before saliency-based sensorless control is employed.

In practice, machine saliency behavior becomes very complicated due to the existence of multiple saliency effects. In saliency based sensorless position estimation, the saliency, which is exploited to extract position information, is known as primary spatial saliency; all other saliency components, acting as disturbances in position estimation, are referred as secondary saliency [RAC08b]. Consequently, higher primary spatial saliency and lower secondary saliency would make good attributes for saliency based sensorless control.

Normally, the primary spatial saliency for interior PM BLAC machines undergoes two cycles per single electrical cycle; while secondary saliency has a higher harmonic number. In order to evaluate the primary spatial saliency level, some terms such as anisotropy ratio [GUG06], saliency ratio [YAN11], and feasible region [BIA07a] [BIA07b], have been introduced. However, high-frequency parameters of machines under different load conditions are required for them. Although high-frequency impedance measurement [JAN04] [YAN11] is claimed to be a good method to investigate machine saliency property, the impedance calculation from injected carrier voltage and measured carrier current response is computational intensive. Therefore, one of the purposes of this

chapter is to develop simplified experimental procedures, from which machine saliency information can be fully obtained.

Although saliency based sensorless control methods estimate the position information from machine saliency behavior, they fulfill this task indirectly from the measured carrier current response by injection of a carrier voltage signal. Therefore, the measurement error of the carrier current response would degrade the effectiveness of sensorless detection. With accounting for carrier current measurement error due to quantization error in the AD conversion, the Sensorless Safety Operation Area (SSOA) is defined in this chapter, which provides a practical solution to investigate sensorless effectiveness.

4.2 Machine Saliency Investigation

4.2.1 Commonly used methods

Feasible region [BIA07a] [BIA07b], saliency ratio [YAN11], and anisotropy ratio [GUG06] are usually used to describe the machine saliency level.

The feasible region is used to evaluate the feasibility of sensorless operation, and is defined as the region bounded by the curve of ($L_{sd}=0$) and the current limitation circle in *dq* plane, so as to have $L_{sd}>0$ [BIA07a]. In [YAN11], the saliency ratio, which is defined as L_{sd}/L_{sa}, is used to compare the saliency based sensorless performance for different machine designs. Meanwhile, the anisotropy ratio with consideration of cross-saturation effect is introduced in [GUG06], and is defined as $(L_n+L_p)/(L_n-L_p)$. Obviously, a large anisotropy ratio means higher saliency level.

Although the foregoing presented terms are convenient to investigate machine saliency information, all of them require the machine parameters (incremental inductances). Hence, they are appropriate in theoretical analysis, instead of practical application. To avoid the requirement of machine parameters, high-frequency impedance measurements are utilized in [JAN03a] [YAN11] for machine saliency evaluation.

The basic principle for impedance measurement can be explained using complex vector. The machine impedance is represented by

$$Z = R + jX = |Z|e^{jjz} \tag{4. 1}$$

The injected carrier voltage and carrier current response are denoted by

$$V = |V|e^{jjv}, \quad I = |I|e^{jji} \tag{4. 2}$$

Substituting them into Ohm's law,

$$V = ZI = |Z||I|e^{j(jz+ji)} = |V|e^{jjv} \tag{4. 3}$$

Therefore, the machine impedance can be derived as

$$\begin{cases} R = \dfrac{V \cdot I}{I \cdot I} = \dfrac{|V||I|\cos(jv - ji)}{|I||I|} = |Z|\cos jz \\ X = |V - RI|/|I| \end{cases} \tag{4. 4}$$

where • denotes the dot product operator.

Based on injected carrier voltage and measured carrier current response, the machine impedance at different rotor positions and load conditions can be calculated according to (4.4). The machine impedance measurement provides an experimental method to investigate the machine saliency property, without any machine parameter requirement. However, the complexity of the impedance calculation leads to more computational load on the processor.

4.2.2 Experimental evaluation of machine saliency

Considering the limitation of existing methods for machine saliency investigation, it is desirable to develop a simplified experimental method to evaluate the machine saliency information before the development of saliency based sensorless control. An experimental test was presented in [KIM04b] [KOC09] for machine saliency investigation. This method is extended here to construct a saliency circle, from which the full machine saliency information including cross-saturation effect can be revealed.

With the aid of a position sensor, the rotor is locked at zero position (θ_r=0). And then, a pulsating carrier voltage signal with the form of (4.5) is injected in the virtual dq axes ($d^v q^v$), which rotates at a fixed speed ($2Hz$) in clockwise direction, as shown in Fig. 4.1. For the prototype machine shown in Appendix A, the injected carrier voltage for machine saliency evaluation has amplitude of $35V$ and frequency of $330Hz$. Meanwhile, the carrier current response in the virtual dq reference frame can be derived as (4.6).

$$\begin{bmatrix} v_{dh}^{v} \\ v_{qh}^{v} \end{bmatrix} = V_c \begin{bmatrix} \cos a \\ 0 \end{bmatrix}, \quad a = w_c t + j \tag{4. 5}$$

$$\begin{bmatrix} i_{dh}^{v} \\ i_{qh}^{v} \end{bmatrix} = \begin{bmatrix} I_p + I_n \cos(2\Delta q + q_m) \\ I_n \sin(2\Delta q + q_m) \end{bmatrix} \cdot \sin a \tag{4. 6}$$

where $\Delta q = q_r - q_r^v = -q_r^v$.

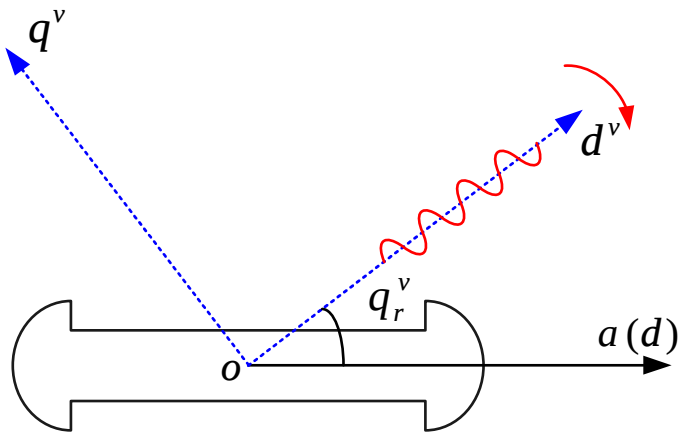

Fig. 4.1 Machine saliency evaluation.

Without fundamental excitation, the carrier current response in virtual *dq* reference frame is measured, as shown in Fig. 4.2. The experimental results are in good agreement with foregoing theoretical analysis, which clearly shows that high frequency *d*- and *q*-axis carrier current responses have the same phase angle with different amplitude, and the amplitude of carrier current is modulated by the position difference $\Delta\theta$ between virtual and real *dq* reference frame. In addition, it can be clearly observed that the *d*-axis carrier current amplitude is always greater than zero.

Utilizing synchronous detection techniques, the position dependent amplitude of carrier current can be obtained, as given by,

$$\begin{bmatrix} \left|i_{dh}^{v}\right| \\ \left|i_{qh}^{v}\right| \end{bmatrix} = LPF\left(\begin{bmatrix} i_{dh}^{v} \\ i_{qh}^{v} \end{bmatrix} \cdot 2\sin a\right) = \begin{bmatrix} I_p + I_n \cos(2\Delta q + q_m) \\ I_n \sin(2\Delta q + q_m) \end{bmatrix} \tag{4. 7}$$

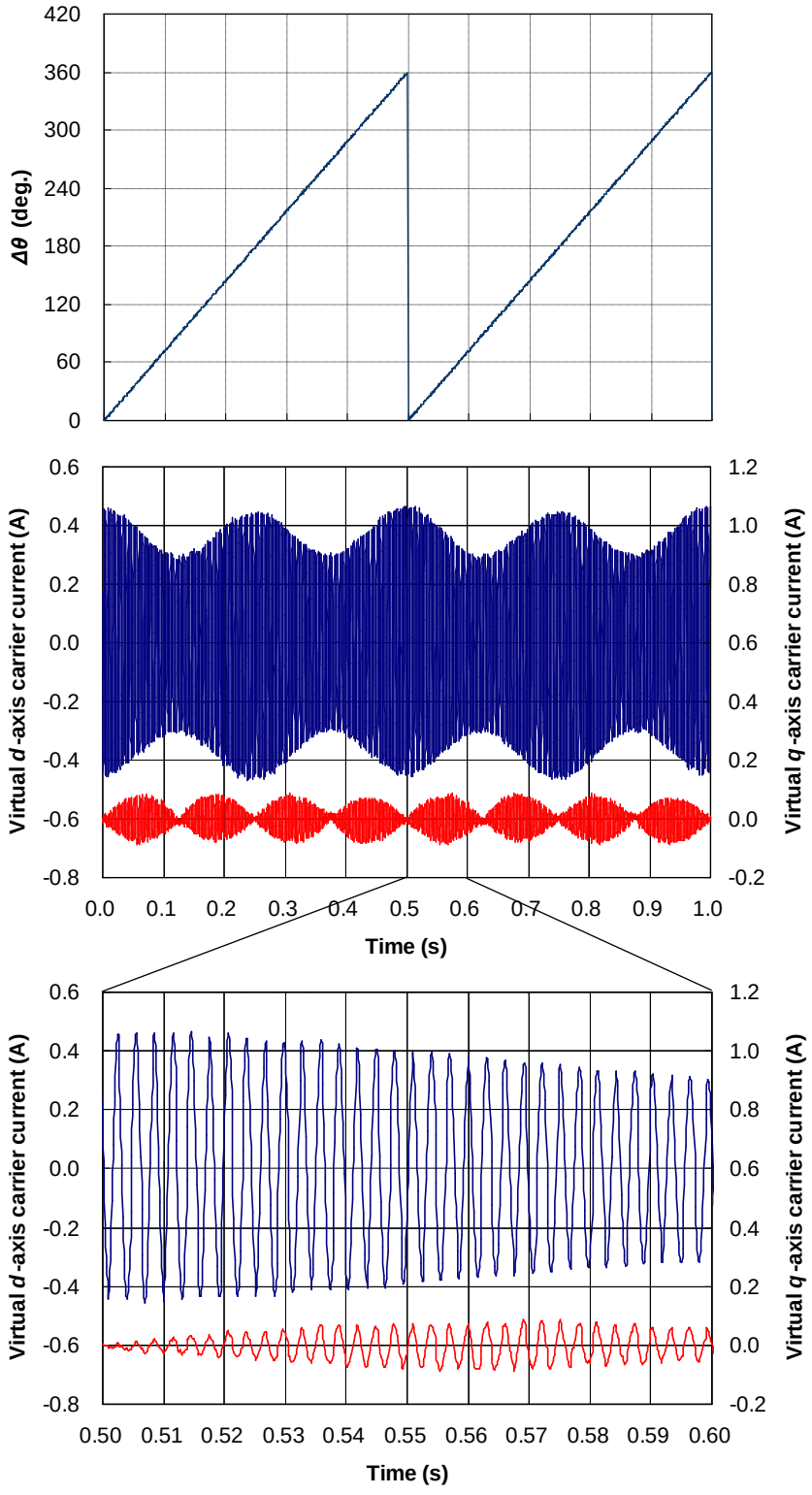

Fig. 4.2 Measured carrier current responses in virtual *dq* reference frame (i_d=0A, i_q=0A).

Fig. 4.3 shows the measured carrier current amplitude using synchronous detection techniques. When the position difference is 0^o or 180^o, i.e., the virtual *d*-axis for carrier

signal injection is aligned with real *d*-axis, the *d*-axis current amplitude reaches the maximum value, while *q*-axis current amplitude is close to zero. According to (4.7), it can be concluded that the cross-saturation angle θ_m is nearly zero, i.e., the cross-saturation effect is negligible without fundamental excitation. Furthermore, the amplitude modulation of carrier current undergoes two cycles per single electrical cycle of position, which reveals the angle ambiguity of π in sensorless position estimation.

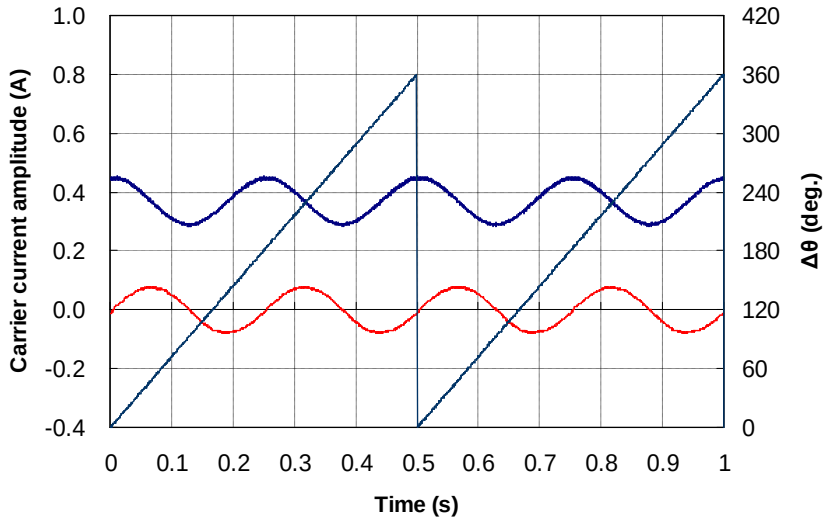

Fig. 4.3 Measured variation of carrier current amplitude with position (i_d=0A, i_q=0A).

4.2.3 Machine saliency circle

When the carrier current amplitude variations are combined together in Fig. 4.4, the formed circle is designated as machine saliency circle, which clearly shows the machine saliency information. Corresponding to (4.7), the center location of the machine saliency circle is determined by the value of I_p, while the radius of saliency circle is dependent on the value of I_n. According to the definition of I_p and I_n (3.19b), for a given injected carrier voltage signal (V_c/ω_c), the location and radius of saliency circle are only decided by the machine parameters L_p and L_n, respectively. Therefore, the scale of the saliency circle indicates the machine saliency level. The longer the radius of the saliency circles, the higher the saliency level, and vice versa.

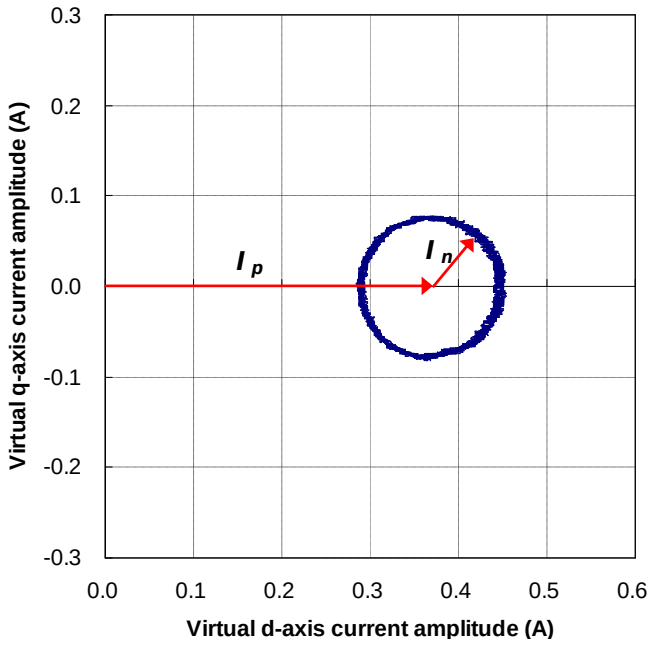

Fig. 4.4 Measured machine saliency circle (i_d=0A, i_q=0A).

In order to investigate the machine saliency information at different load conditions, a specific fundamental excitation can be applied to the machine. In the same way, the machine saliency information under different load conditions can be measured, as shown in Fig. 4.5 - Fig. 4.8. The measured saliency circles for the prototype machine under different load conditions are summarized in Fig. 4.9.

The experimental results indicate that:

1. The radius of the saliency circle changes significantly with *d*-axis current, which reveals that *d*-axis current makes more contributions to the machine saliency level for the prototype machine. Positive *d*-axis current gives rise to higher saliency level, which is beneficial for saliency based sensorless control.
2. The value of I_p shows a trend of monotonic variation with i_d when $i_q=0A$, it increases significantly with i_d variation along the positive *d*-axis. This characteristic can be utilized in magnetic polarity detection, which has been discussed in Chapter 3.
3. When $i_q=0A$, cross-saturation angle θ_m is close to zero within the current limitation circle, which means the cross-saturation effect is negligible if $i_q=0A$.
4. The measured cross-saturation angle θ_m shows that cross-saturation effect is mostly connected with *q*-axis current, rather than *d*-axis current.

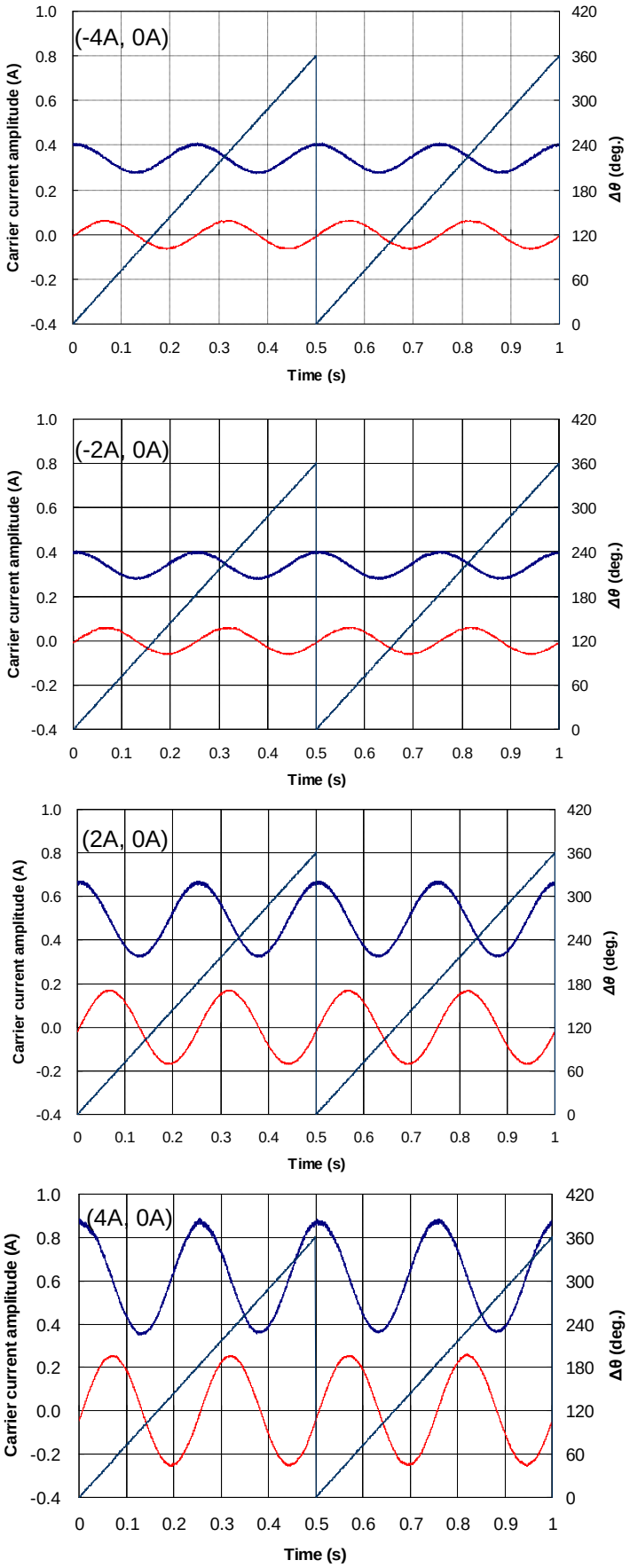

Fig. 4.5 Measured variation of carrier current amplitude against $\Delta\theta$ at different i_d (i_q=0).

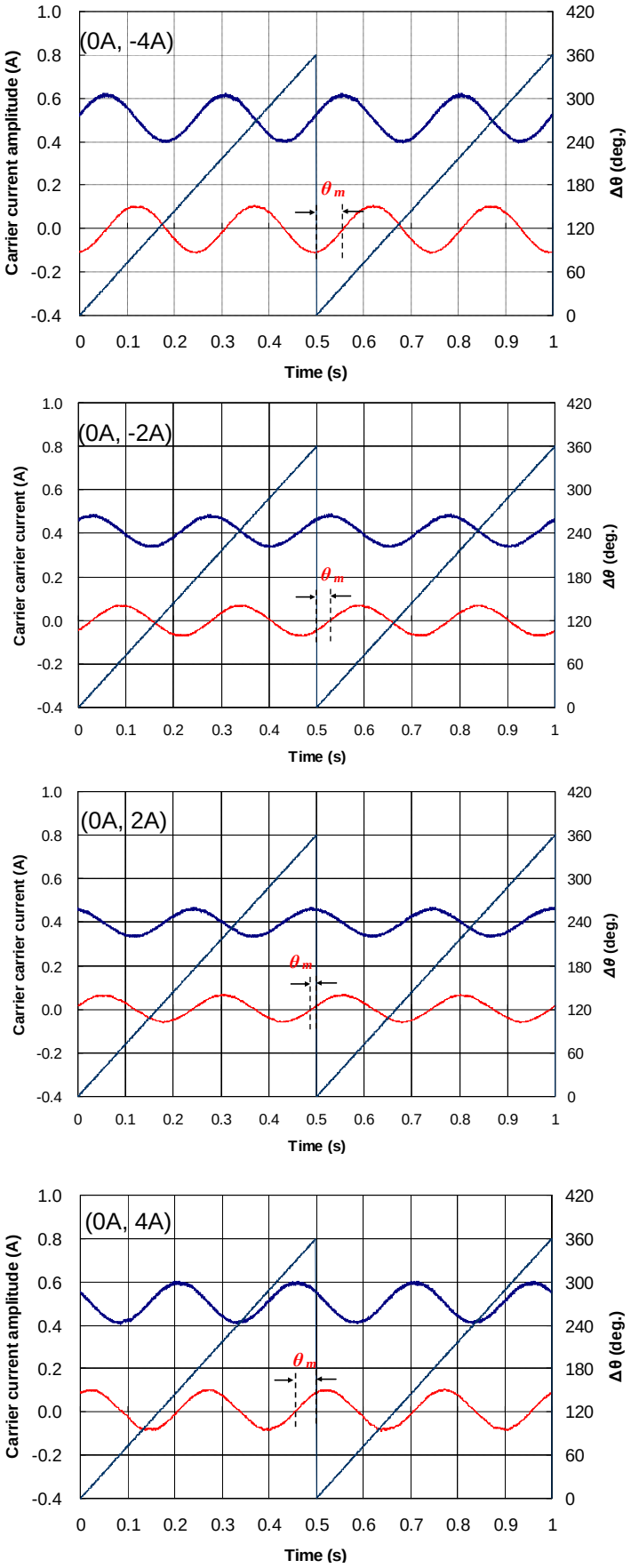

Fig. 4.6 Measured variation of carrier current amplitude against $\Delta\theta$ at different i_q (i_d=0).

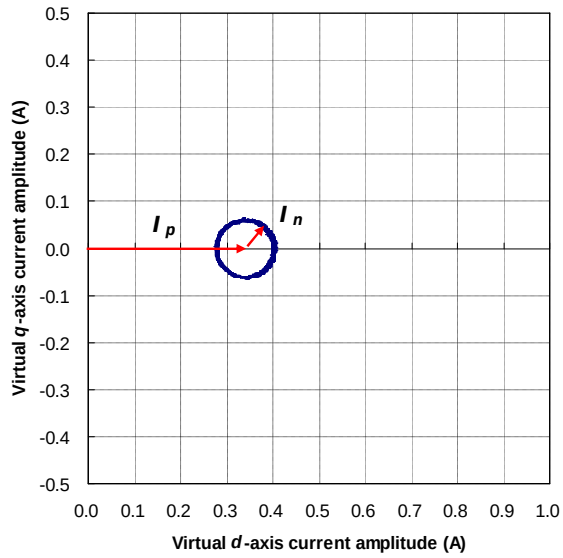

(a) (i_d=-4A)

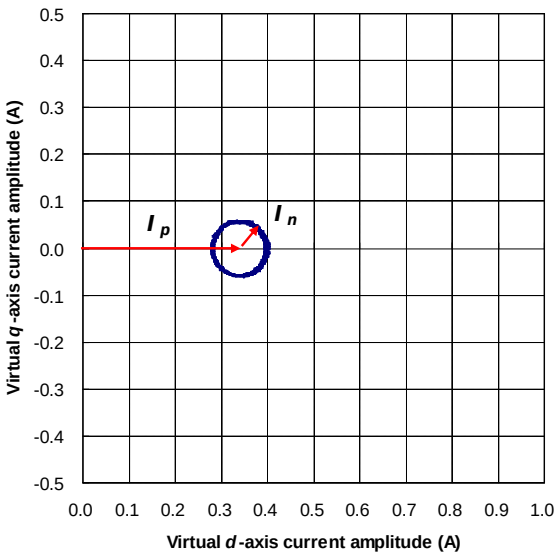

(b) (i_d=-2A)

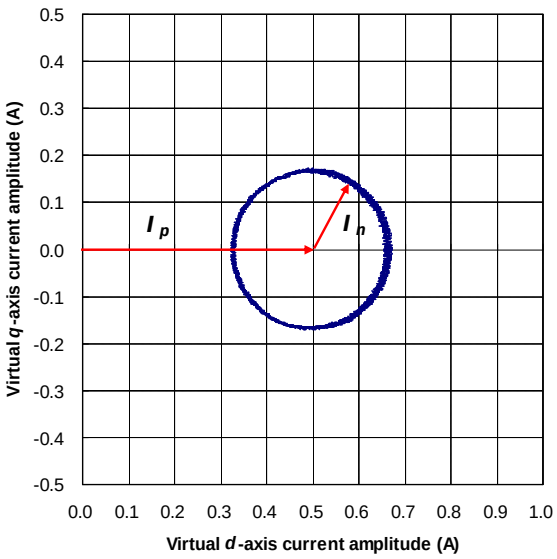

(c) (i_d=2A)

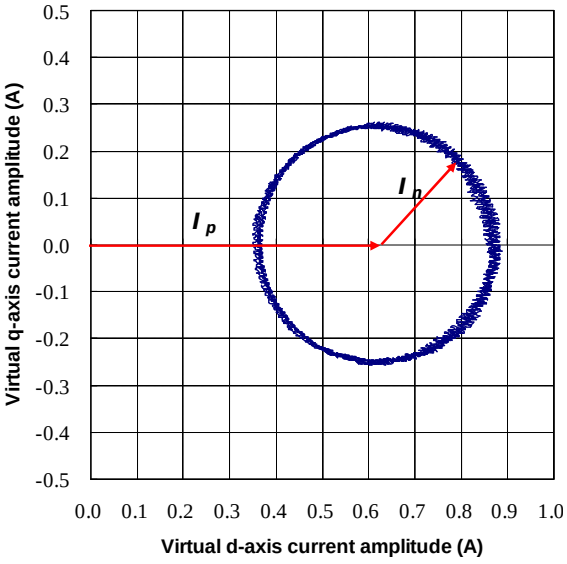

(d) (i_d=4A)

Fig. 4.7 Measured machine saliency circle (i_q=*0*).

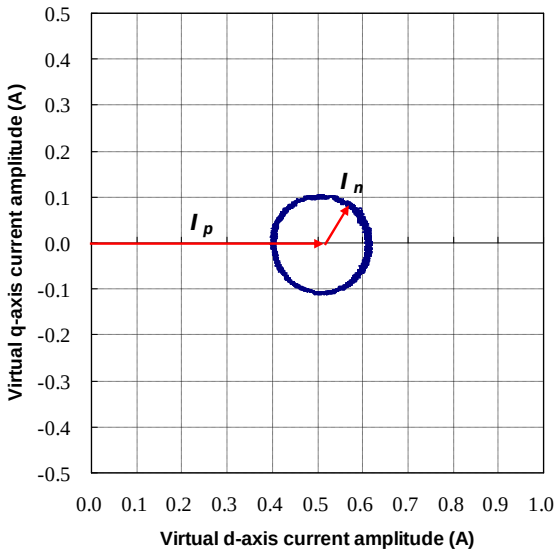

(a) (i_q=-4A)

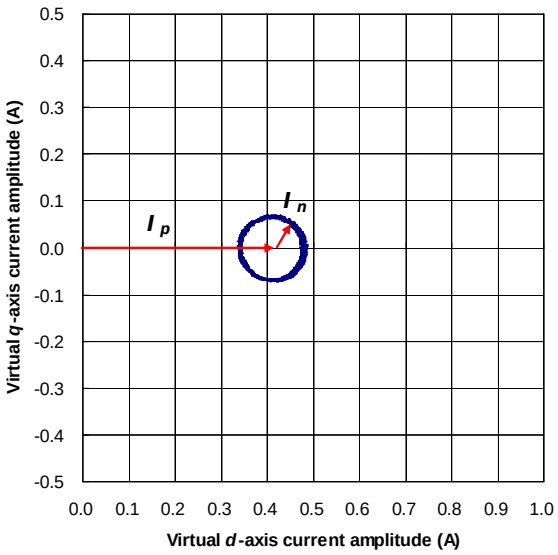

(b) (i_q=-2A)

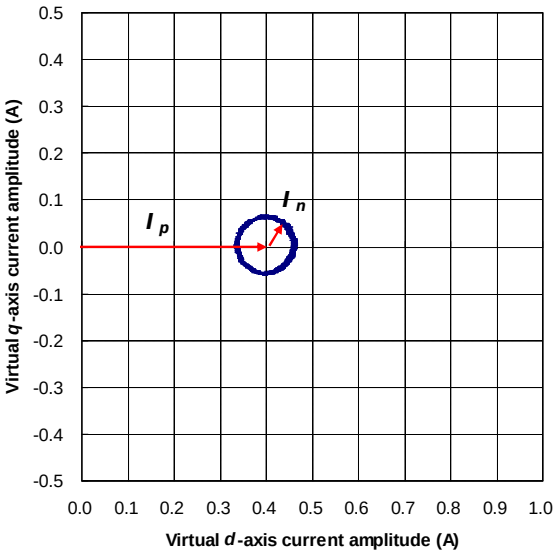

(c) (i_q=2A)

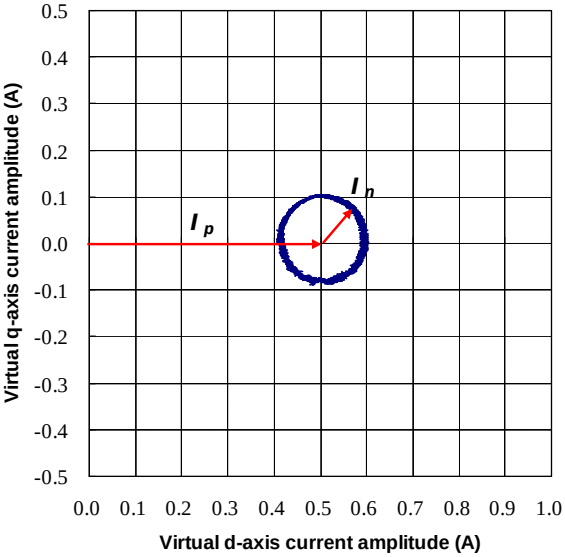

(d) (i_q=4A)

Fig. 4.8 Measured machine saliency circle (i_d=*0*).

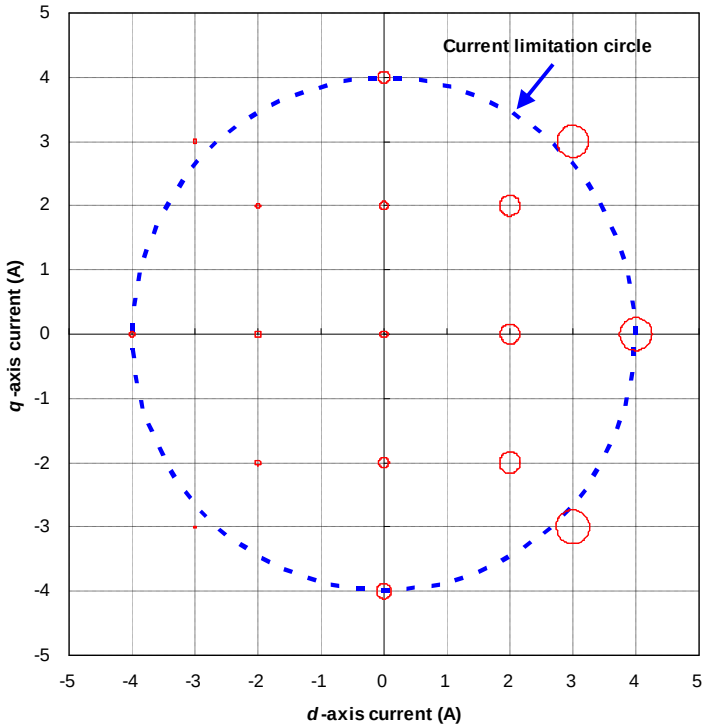

Fig. 4.9 Summary of measured saliency circles for the prototype machine.

4.3 Multiple Saliency Effect

The machine saliency investigation presented before only reveals the existence of a single spatial saliency, i.e., L_{dh} and L_{qh} are constant for a given load condition, and independent on the rotor position. However, non-sinusoidal spatial distribution of the reluctance normally exists in a real machine due to the practical design. Hence, L_{dh} and L_{qh} are associated with rotor position in practice, which can be modeled as a spatial Fourier series. The spatial saliency for sensorless position tracking is denoted as primary saliency, while other harmonic components are referred to as secondary saliency [DEG98] [RAC08a]. The summation of primary and secondary saliency is known as the multiple saliency effect. Due to the existence of secondary saliency, additional carrier current would be introduced when a high frequency carrier voltage signal is injected into the machine, which inevitably affects the bandwidth of the position observer, the accuracy of estimated position information, and even the sensorless operation stability.

Unlike the cross-saturation effect, which introduces constant error in the estimated position information for a given load condition, the introduced estimation error due to multiple saliency varies with rotor position. Although it is claimed that the multiple

saliency effect can be compensated for by a multiple saliency tracking observer [DEG98] or a structured neural network [GAR07b] [REI08], it is very computationally intensive due to its nonlinear and position-dependent behavior. Therefore, it is preferred to solve this problem through appropriate machine design. On the other hand, from the view of machine control, it is desirable to check the multiple saliency effect before sensorless algorithm development.

In [KOC09], a useful test procedure is presented to evaluate the multiple saliency effect. With the aid of a position sensor, a high frequency carrier voltage signal is injected into the accurate *d*-axis ($\Delta\theta=0$), while the test machine is slowly spun manually or by a load machine. At the same time, the amplitude of the *dq*-axis carrier currents can be calculated based on the measured currents. Without the multiple saliency effect, the amplitudes of *dq*-axis carrier currents can be derived from (3.26),

$$\begin{bmatrix} |i_{dh}^e| \\ |i_{qh}^e| \end{bmatrix} = \begin{bmatrix} I_p + I_n \cos(2\Delta q + q_m) \\ I_n \sin(2\Delta q + q_m) \end{bmatrix} = \begin{bmatrix} I_p + I_n \cos(q_m) \\ I_n \sin(q_m) \end{bmatrix} \tag{4. 8}$$

In this case, the amplitudes of the *dq*-axis carrier currents are independent on the rotor position. When a dominant secondary saliency is considered, (4.8) can be updated as [RAC10],

$$\begin{bmatrix} |i_{dh}^e| \\ |i_{qh}^e| \end{bmatrix} = \begin{bmatrix} I_p + I_n \cos(q_m) + I_{n2} \cos[(2-h)q_r - \Delta j\ ] \\ I_n \sin(q_m) + I_{n2} \sin[(2-h)q_r - \Delta j\ ] \end{bmatrix} \tag{4. 9}$$

where the component with I_{n2} is the position dependent disturbance due to secondary saliency, h is the harmonic order of dominant secondary saliency ($h\neq2$), and $\Delta\varphi$ is the initial phase difference between primary and secondary saliency. It should be noted that the cross-saturation angle θ_m is constant for a given load condition, and isn't affected by the rotor position information. From (4.9), it can be predicted that the unwanted ripple component would be generated by the multiple saliency effect.

Experiment result for the prototype machine is shown in Fig. 4.10, in which the green line indicates the measured rotor position information from an encoder. Since the rotor is spun manually, the rotor speed is not constant. It clearly reveals the existence of multiple saliency even at the no load condition. The variation of carrier current amplitude at different load conditions can be depicted against the rotor position, as shown in Fig.

4.11. The ripple term has the frequency of 6 times to fundamental frequency, which reveals that -4th or/and 8th harmonics are dominant. From (4.9), the dc component of q-axis carrier current amplitude is determined by ($I_n sin\theta_m$). Hence, the positive value indicates positive θ_m, and vice versa. Fig. 4.11 shows θ_m has a near zero value at the condition of (i_d=0A,i_q=0A), while a positive value at i_q=2A and a negative value at i_q=-2A. It is in a good agreement with the experimental result shown in Fig. 4.6. From Fig. 4.11, different ripple amplitude can be observed at different load conditions, which reveals that the multiple saliency effect is also connected with load condition.

Further analysis should be made to check how much the multiple saliency effect would affect the sensorless position estimation. With considering the multiple saliency effect, the maximum error of position estimation can be predicted as in [RAC08a],

$$\Delta q = \frac{1}{2}\sin^{-1}\left(\frac{I_{n2}}{I_n}\right) \tag{4.10}$$

The value of I_{n2} can be directly measured from the ripple component on i_{qh} in Fig. 4.11. Regarding to I_n, previous experimental results show that it is quite nonlinear for different load conditions for the prototype machine. Taking the load condition of (i_d=0A, i_q=2A) as an example, in this case, $I_n \approx 64mA$, $I_{n2} \approx 8mA$, and then, the maximum error due to multiple saliency effects can be calculated from (4.10), as given by,

$$\Delta q = \frac{1}{2}\sin^{-1}\left(\frac{I_{n2}}{I_n}\right) \approx \frac{1}{2}\sin^{-1}\left(\frac{8}{64}\right) \approx 3.6^o \tag{4.11}$$

Consequently, although the multiple saliency effect does exist in the prototype machine, it can be neglected in this work due to limited estimation error.

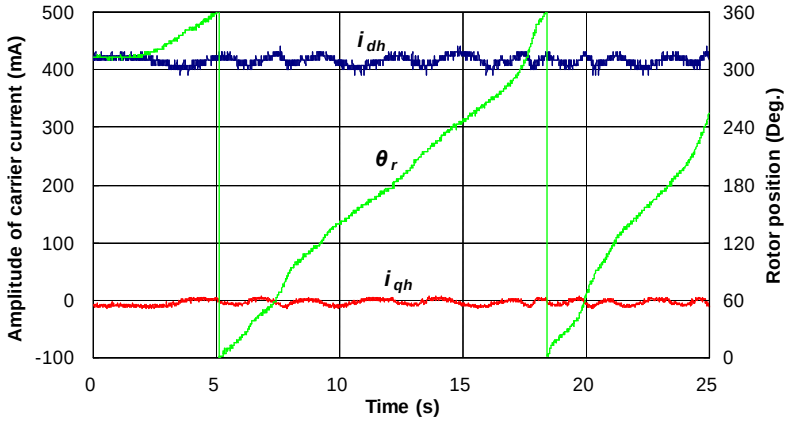

Fig. 4.10 Position dependent anisotropy (i_d=0A, i_q=0A).

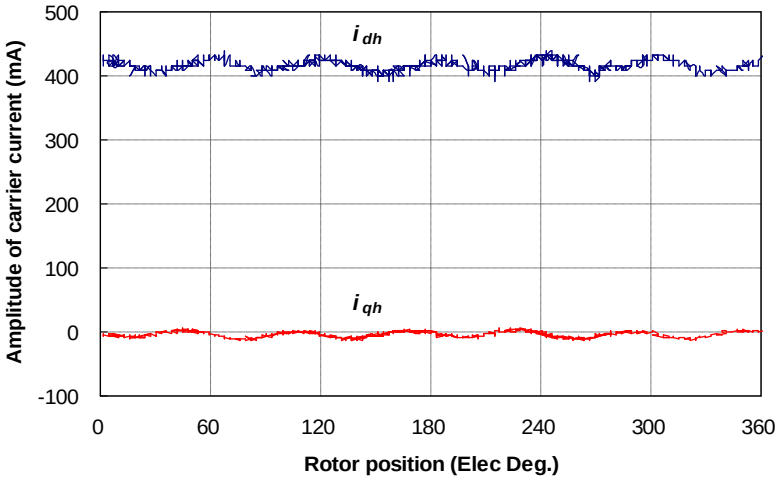

(a) (i_d=0A, i_q=0A)

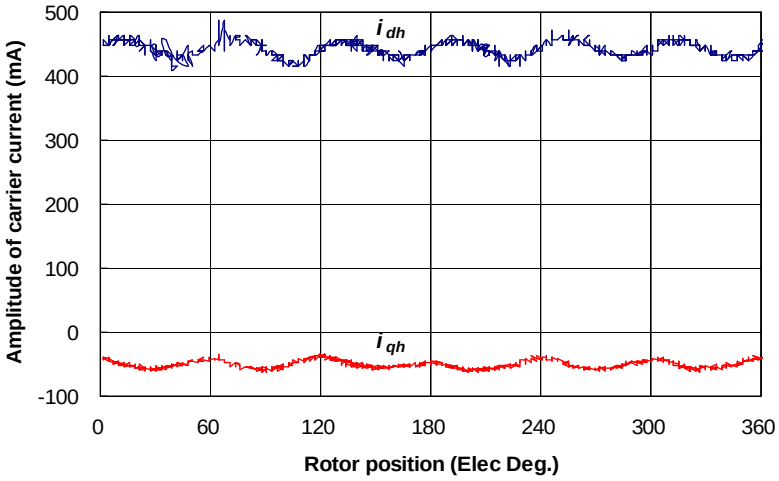

(b) (i_d=0A, i_q=-2A)

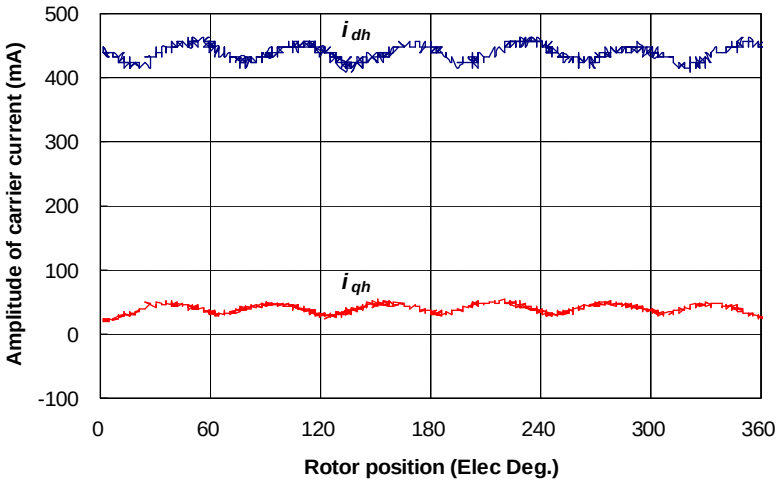

(c) (i_d=0A, i_q=2A)

Fig. 4.11 Multiple saliency evaluation for the prototype machine.

4.4 Sensorless Safety Operation Area

It is well known that, the higher the machine saliency level, the better the saliency based sensorless operation performance. Nevertheless, there is no univocal definition about the requirement of saliency level for practical sensorless operation.

Feasible region gives a theoretical analysis on the sensorless feasibility [BIA07a] [BIA07b]. It can be interpreted as the area, in which $L_{sd} \neq 0$, i.e., $I_n > 0$. For the prototype machine used in this work, the contour map of L_{sd} can be drawn in Fig. 4.12. According to the definition, the feasible region is the whole current limitation circle (shaded area), which is independent of the characteristics of the injected carrier signal. However, the real effective area for sensorless operation is significantly smaller than the feasible region, for the reason that I_n should be high enough to avoid the influence of carrier current measurement error [JAN03b] [GAR07a], especially the quantization error from the AD converter. Consequently, the Sensorless Safety Operation Area (SSOA), which accounts for the carrier current measurement error due to quantization error in the AD conversion, is introduced here to investigate the effectiveness of sensorless operation.

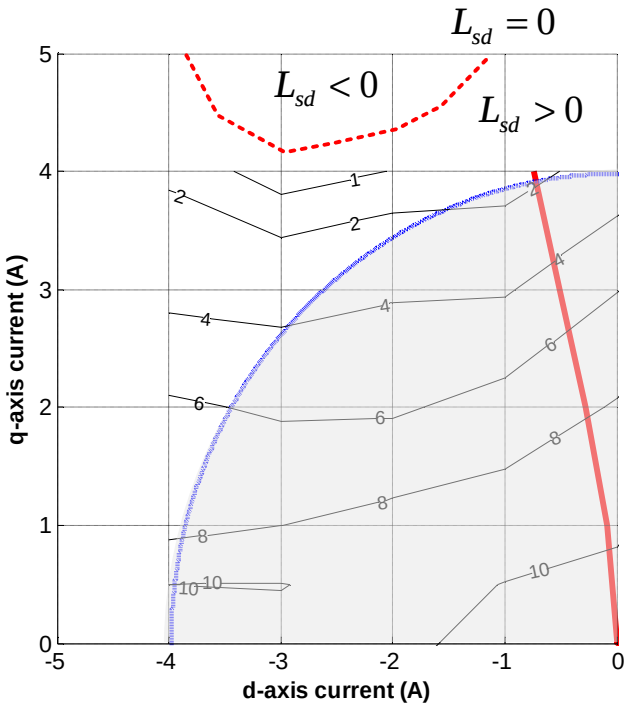

Fig. 4.12 Feasible region for the prototype machine.

4.4.1 Quantization error in AD conversion

Before defining the SSOA, it is useful to discuss the effect of quantization error in AD conversion. In general, the current sensors designed for fundamental current measurement are also used to measure the carrier current in order to reduce the system cost. Therefore, the resolution of the measured carrier current component is under the worst condition. The effect of quantization error due to AD conversion in the pulsating injection-based method has been discussed in [JAN03b]. In a similar way, the same conclusion can be drawn for the rotating injection-based method.

As shown in Fig. 4.13, it is assumed that the current value of $2I_p$ is scaled to be the full range of the AD converter with the resolution of N bits. Then, a parameter of quantum current can be defined as:

$$I_{qu} = 2I_p / 2^N \tag{4.12}$$

Therefore, the phase current measurement error due to the quantization error in AD conversion can be expressed as:

$$e_s = \pm \frac{I_{qu}}{2} \tag{4.13}$$

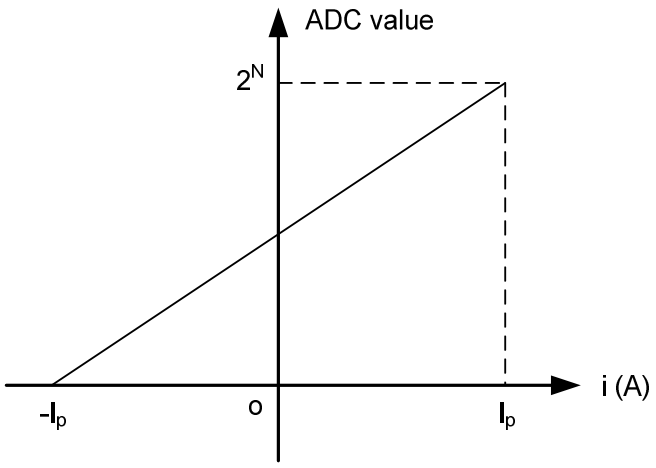

Fig. 4.13 Limited resolution of AD conversion.

Based on the definition of space vector theory, the disturbance current vector due to current measurement error can be expressed as:

$$I_{AD\_error} = \frac{2}{3}[e_s + e_s e^{j2p/3} + e_s e^{j4p/3}) \tag{4.14}$$

It indicates eight vectors (including two zero vectors) in the stationary reference frame, as shown in Fig. 4.14. The non-zero disturbance current vectors have identical magnitude of $2I_{qu}/3$. Due to its random frequency, the estimation error resulting from AD quantization is difficult to be compensated for. Under the worst case condition, the disturbance current vector lies on the *q*-axis in the estimated synchronous reference frame for pulsating injection, or the *q*-axis in the reference frame which is synchronous with the estimated negative sequence carrier frequency for rotating injection, and in turn the resultant position estimation error is the maximum, given by

$$I_n \sin(2\Delta q_{AD}) = 2I_{qu}/3 \tag{4.15}$$

Then the max position estimation error is derived as

$$\Delta q_{AD} = \pm\frac{1}{2}\sin^{-1}[(\frac{2I_{qu}}{3})/I_n] \tag{4.16}$$

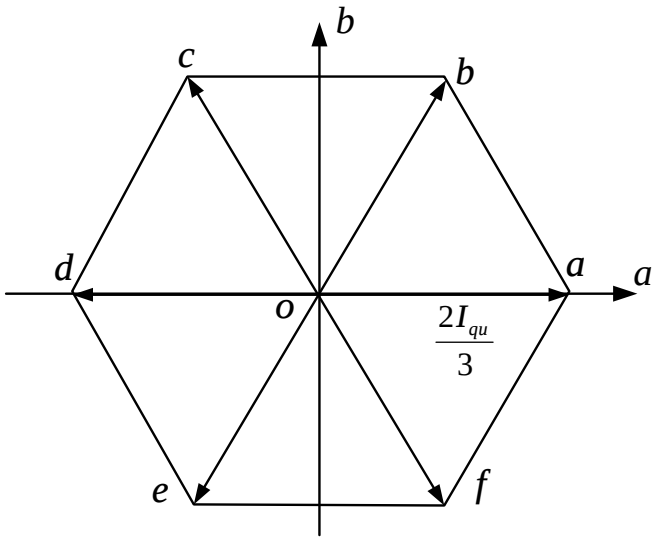

Fig. 4.14 Disturbance current vector due to quantization error.

From (4.16), the relationship between $\Delta\theta$ and I_n can be depicted in Fig. 4.15, in which I_n is expressed as a per-unit value with reference to I_{qu}. It can be observed that the position estimation error due to AD quantization decreased considerably with the increase of I_n when I_n is small. However, the estimation error tends to saturation for higher I_n.

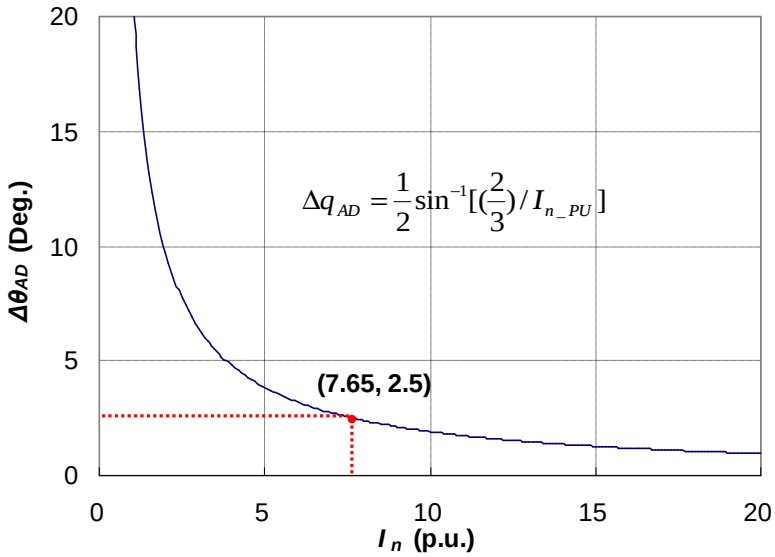

Fig. 4.15 Estimated position error due to ADC quantization error.

4.4.2 Sensorless safety operation area

Providing the position estimation error due to AD quantization should be constrained within ±2.5 electric degrees, then from (4.16) the requirement of I_n can be derived as (4.17), which is highlighted in Fig. 4.15.

$$I_n = (\frac{2I_{qu}}{3}) / \sin(2\Delta q) \geq 7.65 I_{qu} \tag{4.17}$$

With the definition of I_n (3.19b), (4.17) has an alternative form, as given by:

$$L_n \leq V_c / (7.65 w_c I_{qu}) = L_{lm} \tag{4.18}$$

where, L_{lm} is designated as the boundary inductance.

The SSOA in *dq* plane for effective sensorless operation can be defined as the area in current limitation circle, in which $L_n \leq L_{lm}$. Meanwhile, the SSOA can be interpreted as the area, in which $I_n \geq 7.65 I_{qu}$, instead of $I_n > 0$ for the feasible region. As a result, the SSOA is determined by the machine saliency level (L_n), injected carrier voltage signal (V_c/ω_c), and the resolution of current measurement (I_{qu}).

Since the value of L_n is load-dependent, it is useful to plot its contour map in the *dq* plane, as shown in Fig. 4.16. In which, the current locus of the MTPA control is indicated by the solid red line, while the current limitation circle is shown by the dashed blue line.

In this work, the current value of 23A (-11.5A to +11.5A) is scaled to the full range of the 12 bit AD converter. From the foregoing analysis, it can be obtained that:

$$\begin{cases} I_{qu} = 2\times 11.5\times 10^3 / 2^{12} = 5.62(mA) \\ I_n \geq 7.65 I_{qu} = 43.0(mA) \\ L_n \leq V_c /(7.65 w_c I_{qu}) = 395(mH) \end{cases} \tag{4.19}$$

In Fig. 4.16(a) and Fig. 4.16(b), the grey areas inside the current limitation circle, in which $L_n \leq 395mH$, is the predicted SSOA for the prototype machine with the injected signal of $V_c=35V$ and $f_c=330Hz$. Fig. 4.16(a) and Fig. 4.16(b) show the contour map of L_n without/with consideration of the cross-saturation effect. According to the definition of L_n (3.13b), the cross-saturation effect decreases the value of L_n, which results in the extension of SSOA to some extent. With the aid of cross-saturation effect, it can be seen from Fig. 4.16(b) that the whole MTPA trajectory is inside the SSOA. In the same way, the predicted SSOA for different injection signals can be summarized in Table 4.1. It clearly indicates that the SSOA shrinks with the decrease of carrier voltage amplitude, as shown in Fig. 4.16(c) and Fig. 4.16(d). It is worth noting that the SSOA is not completely symmetrical with respect to the line of zero q-axis current, which implies that the estimated rotor position in the case of negative q-axis current is slightly more accurate.

Table 4.1 Predicted SSOA for the Prototype Machine.

Injected signals	$I_n\,(mA)$	$L_n\,(mH)$	Boundary point at $i_q=2A$
V_c=35V / f_c=330Hz	≥ 43	≤ 395	i_d = -1.0A
V_c=20V / f_c=330Hz	≥ 43	≤ 226	i_d = 0.3A
V_c=10V / f_c=330Hz	≥ 43	≤ 113	i_d = 1.8A

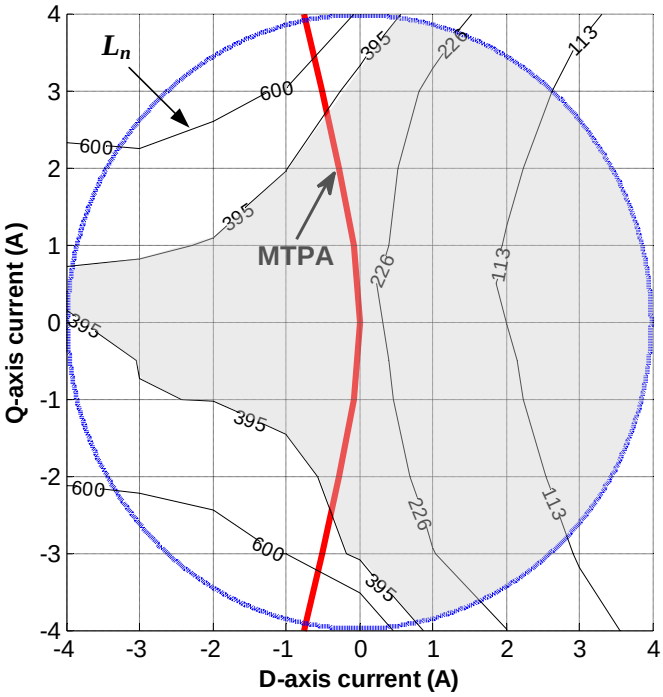

(a) Without consideration of cross-saturation effect (V_c / f_c = *35V/330Hz*)

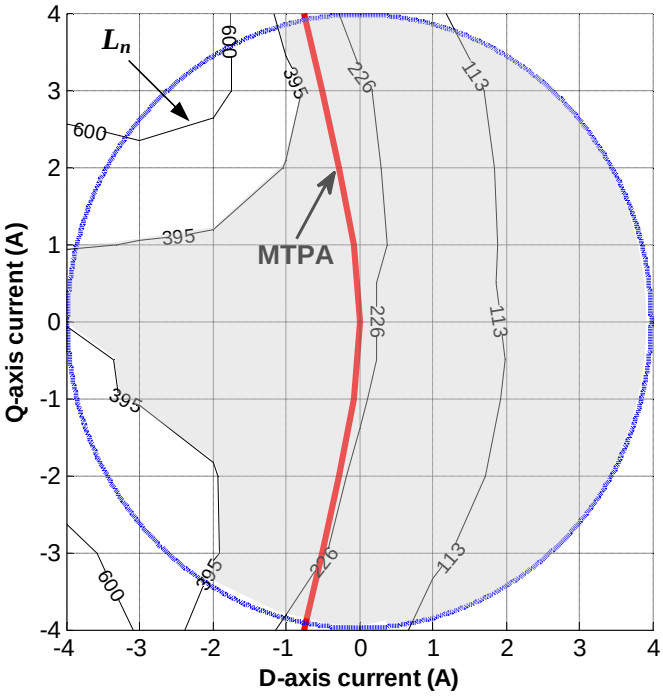

(b) With consideration of cross-saturation effect (V_c / f_c = *35V/330Hz*)

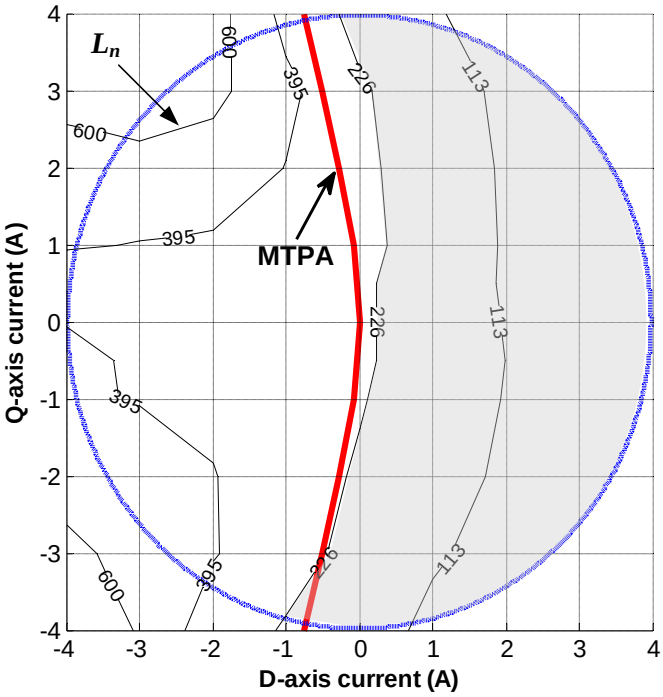

(c) With consideration of cross-saturation effect (V_c / f_c = *20V/330Hz*)

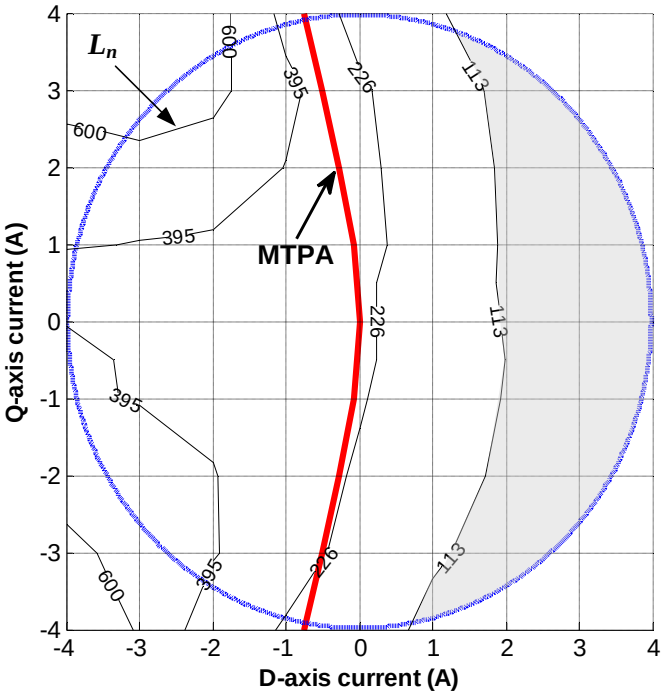

(d) With consideration of cross-saturation effect (V_c / f_c = *10V/330Hz*)

Fig. 4.16 Predicted SSOA for the prototype machine.

4.4.3 Experimental validation of SSOA

To validate the SSOA for rotating and pulsating carrier signal injection based techniques, the prototype machine operates in sensored mode, and the *q*-axis current is fixed to 2A, while the *d*-axis current is changed from -3.5A to 3.5A (inside the current limitation circle). The cross-saturation effect has been compensated using the methods proposed in Chapter 3. Hence, the remaining estimated position error can be attributed to the quantization error in the AD conversion.

In Fig. 4.17 - Fig. 4.19, the amplitude of injected carrier voltage is different, while the carrier frequency is identical, being fixed to 330Hz. The solid red lines indicate the boundary of SSOA defined by ($I_n \geq 43mA$), in Fig. 4.17, the boundary point of SSOA for ($V_c=35V$, $f_c=330Hz$) lies at ($i_d=-1.0A$, $i_q=2A$), the same as the calculated point shown in Table 4.1. The same conclusion can be drawn from Fig. 4.18 and Fig. 4.19. Regardless of the amplitude of injected carrier voltage, it can be observed that I_n increases nonlinearly with an increase of i_d for a constant *q*-axis current ($i_q=2A$), which is in accordance with the decrease of L_n along the line of $i_q=2A$, Fig. 4.16(b). Meanwhile, it can be observed that the estimated position errors reduce with the increase of I_n for both rotating and pulsating injection-based techniques, which results in the fact that the resultant position error is connected with I_n due to quantization error in the AD conversion. On the boundary of SSOA, the estimated position errors for pulsating injection reach nearly the same level of around ±2.5 electric degrees for different injection signals, which is in accordance with previous analysis. However, the estimated position errors on the boundary of SSOA for rotating injection seem to be a little higher, which may be caused by different signal demodulation processes. Finally, the experimental results show that the SSOA shrinks significantly with the decrease of V_c, as indicated in Fig. 4.16.

It is worthwhile to point out that it does not mean that the machine could not perform with sensorless operation outside the SSOA. Actually, the SSOA for sensorless operation defines a working area in the *dq* plane, in which the machine can work in sensorless mode with a guaranteed performance in steady state, i.e. the position estimation error in steady state due to quantization error can be limited to a narrow range. Besides the

machine saliency level (L_n), the definition of SSOA also considers the characteristics of injected signal (V_c/ω_c), and the resolution of current measurement (I_{qu}). Consequently, for the specific prototype machine and given current measurement resolution, the proper injected carrier signal should be selected carefully to make sure that the whole working trajectory is inside the SSOA.

4.4.4 Sensorless operation performance

Fig. 4.20 shows the dynamic performance of experimental system in sensored operation mode. The reference speed is changed from zero to 100rpm to -100 rpm. Fig. 4.21 and Fig. 4.22 show the same process of rotating injection based sensorless scheme with cross-saturation compensation for different magnitudes of injected carrier voltage.

From Fig. 4.16, it depends on the injected carrier voltage signal whether the MTPA trajectory locates inside the SSOA. In the experiments shown in Fig. 4.21, a rotating carrier voltage with magnitude of 35V and frequency of 330Hz is applied. In this case, the whole MTPA trajectory is within the SSOA, as shown in Fig. 4.16(b). Hence, the sensorless performance is guaranteed in both transient and steady state. Although the maximal estimated position error reaches up to ±10 deg during the whole process, the estimated position error in steady state can be limited to ±5 deg. In addition, the speed tracking behavior in Fig. 4.21 is as good as the one of sensored operation in Fig. 4.20.

As shown in Fig. 4.22, when the amplitude of injected carrier voltage decreases to 10V, the boundary curve for SSOA is $L_n \leq 113mH$. Fig. 4.16(d) shows that the MTPA trajectory lies outside of the SSOA entirely for this case. However, as mentioned before, it does not mean that the machine could not perform with sensorless operation outside the SSOA. Actually, the sensorless estimator may still track the rotor position in steady state with relative large position error and deteriorated performance, although it is more likely to fail to do so in the transient state. By way of example, the experimental result in Fig. 4.22 shows that the estimated position error in steady state rises up to ±10 deg. for the decreased voltage magnitude of injected carrier signal.

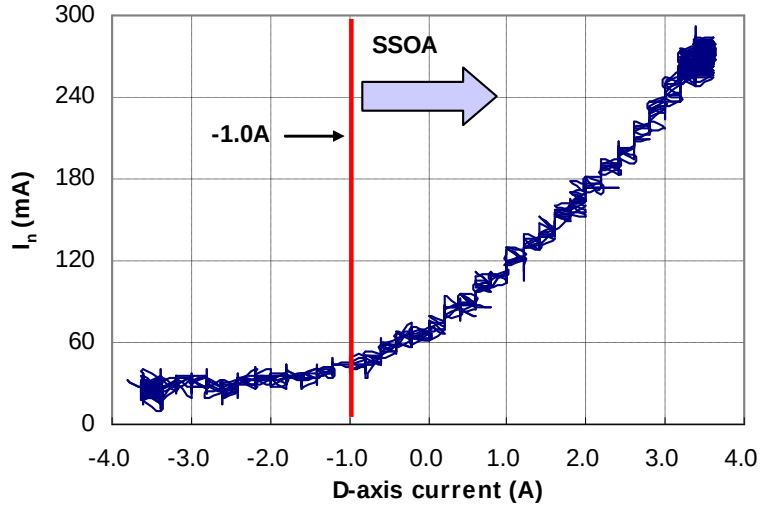

(a) Measured I_n.

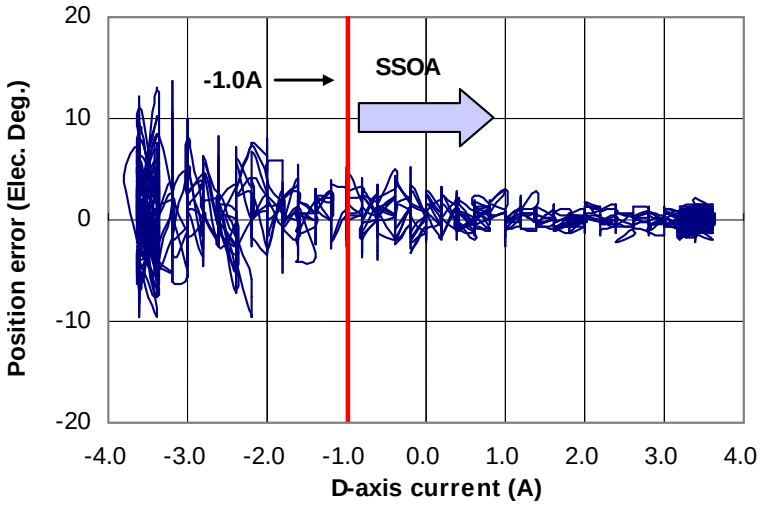

(b) Estimated position error for rotating injection.

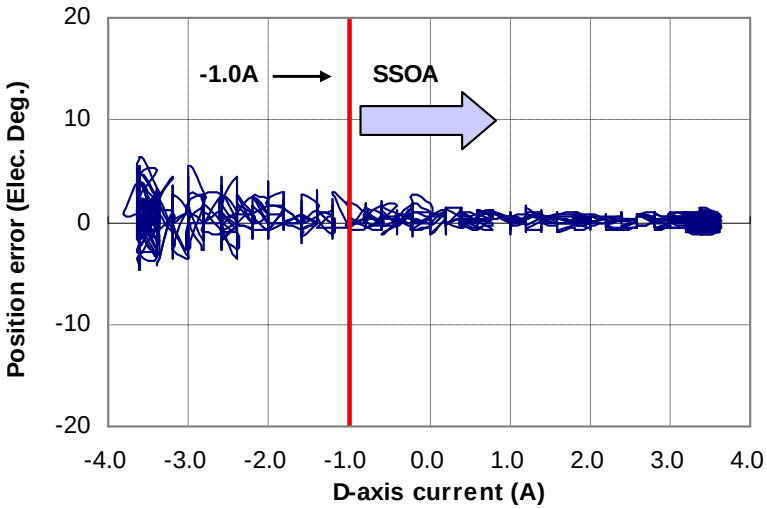

(c) Estimated position error for pulsating injection.

Fig. 4.17 Measured SSOA (Vc=35V, fc=330Hz).

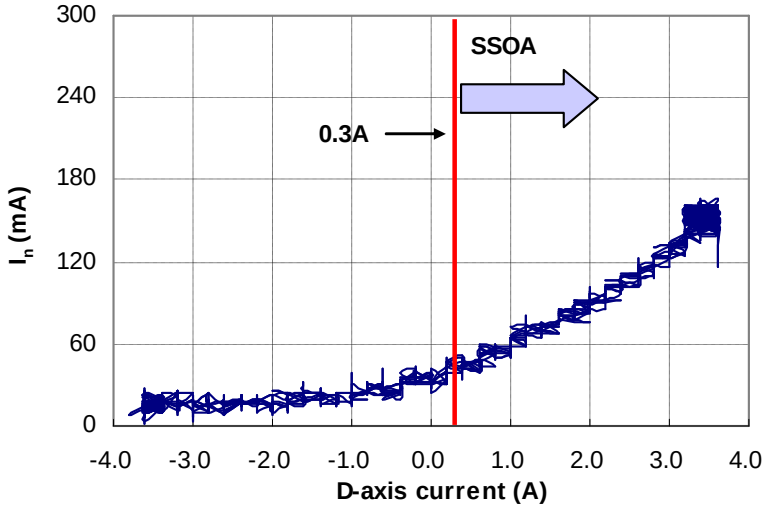

(a) Measured I_n.

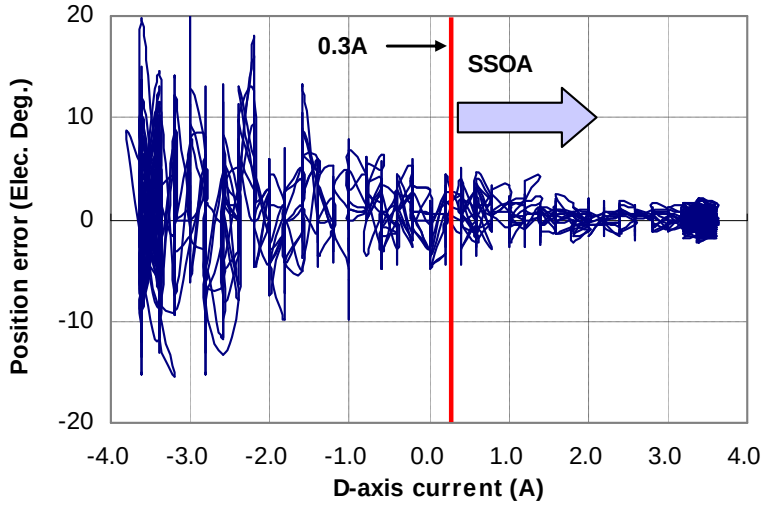

(b) Estimated position error for rotating injection.

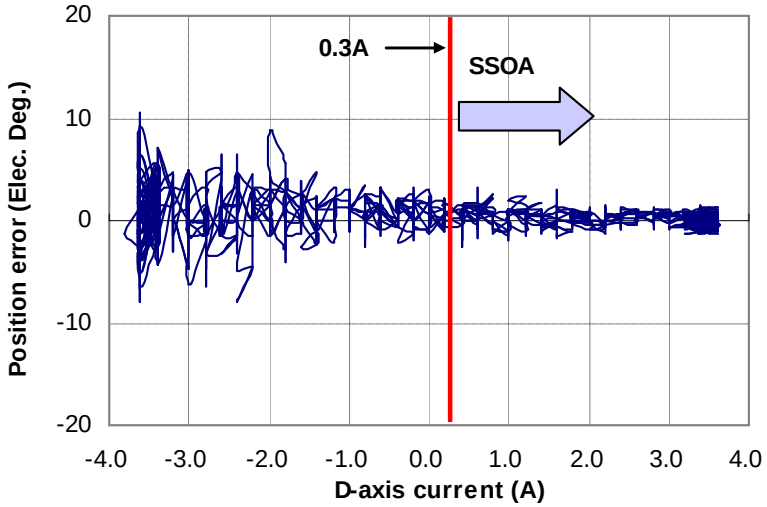

(c) Estimated position error for pulsating injection.

Fig. 4.18 Measured SSOA (Vc=20V, fc=330Hz).

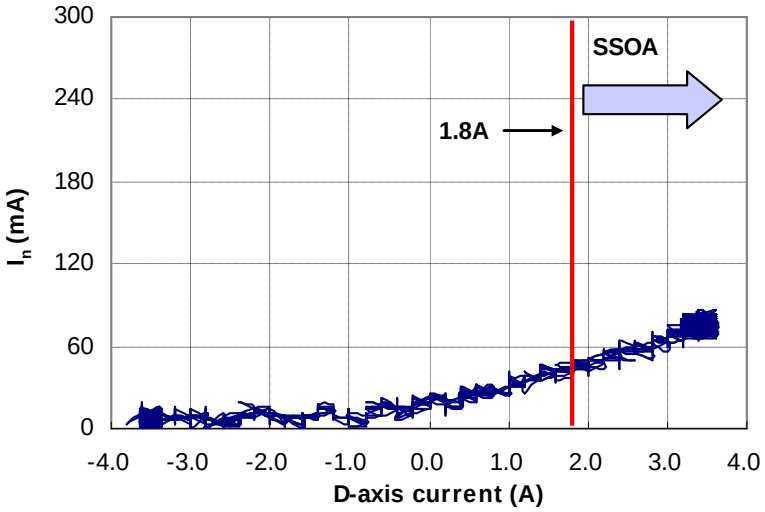

(a) Measured I_n.

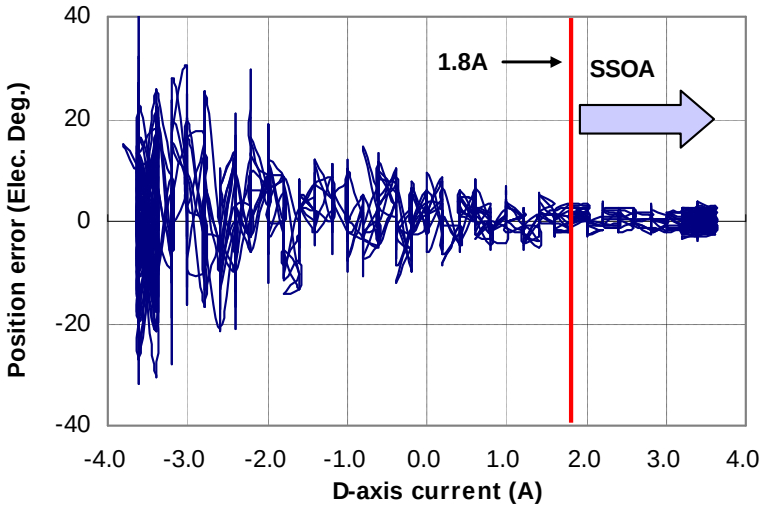

(b) Estimated position error for rotating injection.

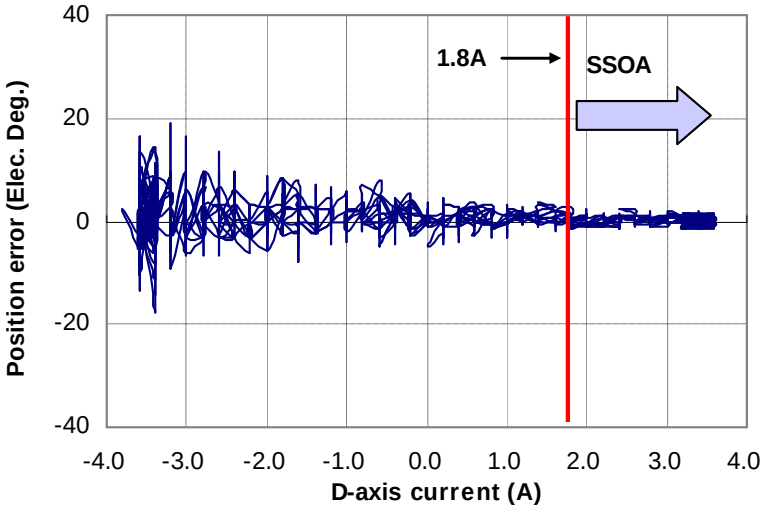

(c) Estimated position error for pulsating injection.

Fig. 4.19 Measured SSOA (Vc=10V, fc=330Hz).

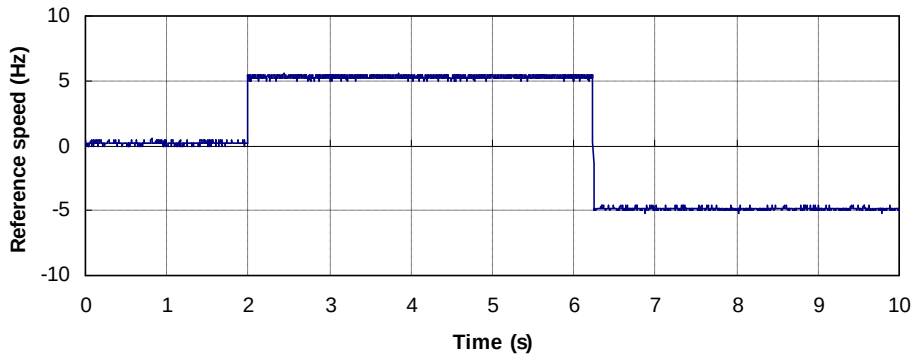

(a) Speed reference.

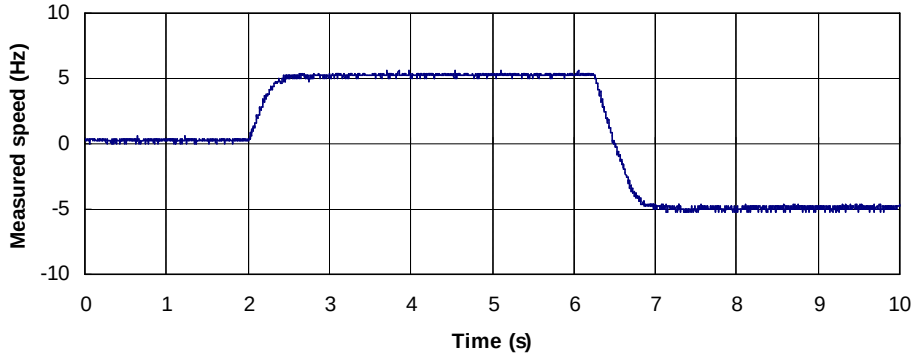

(b) Speed response.

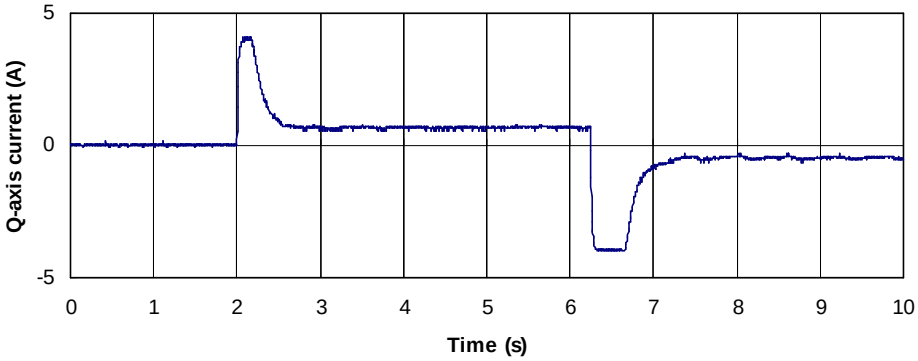

(c) *q*-axis current response.

Fig. 4.20 Measured step speed response for sensored operation.

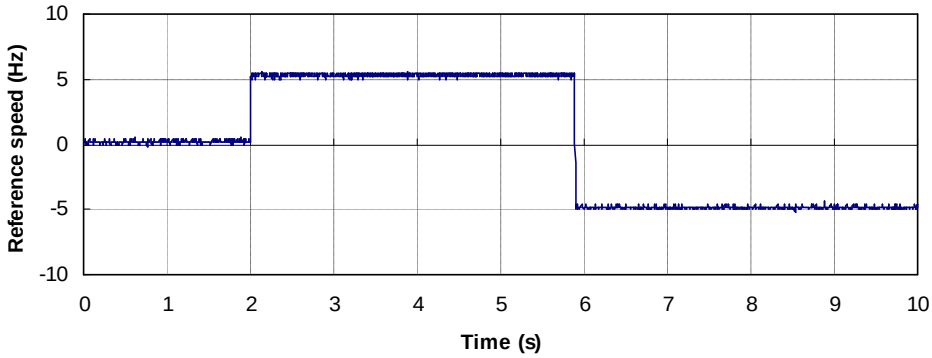

(a) Speed reference.

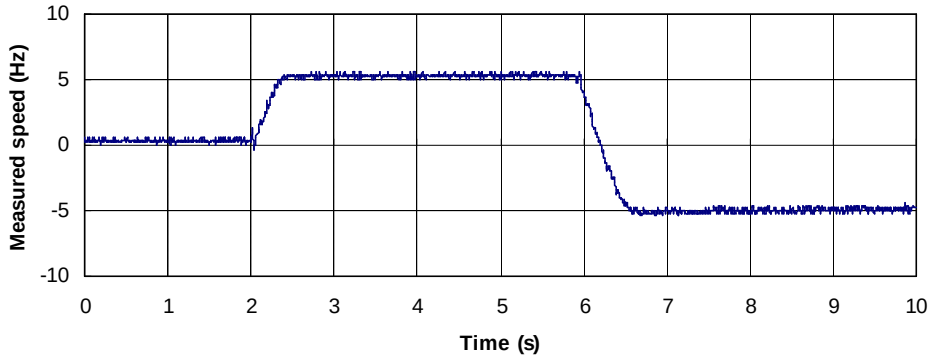

(b) Speed response.

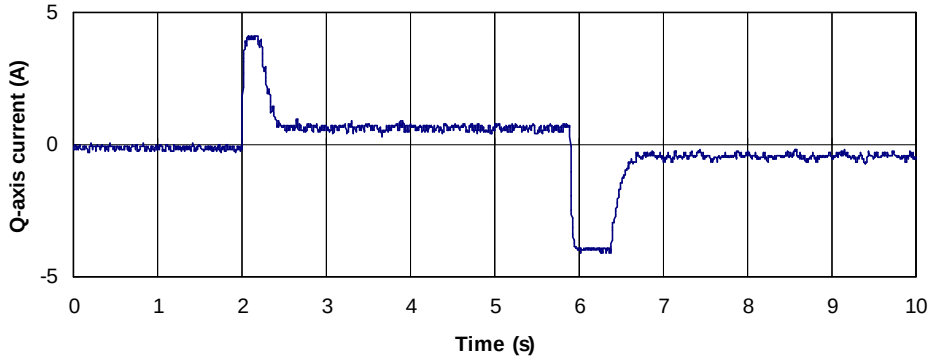

(c) *q*-axis current response.

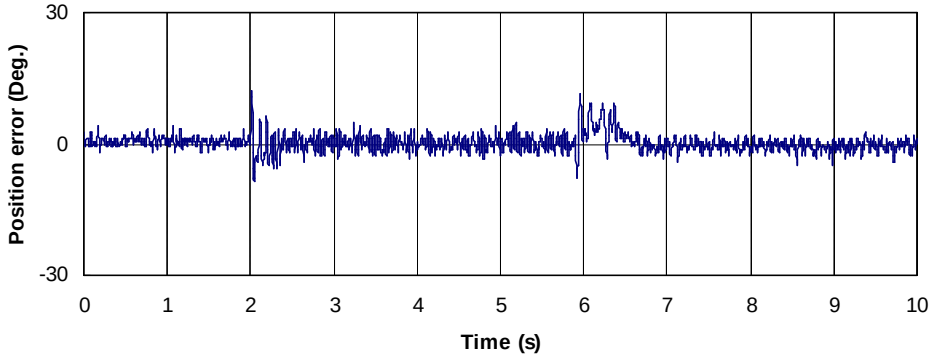

(d) Position estimation error.

Fig. 4.21 Measured step speed response for sensorless operation (35V, 330Hz).

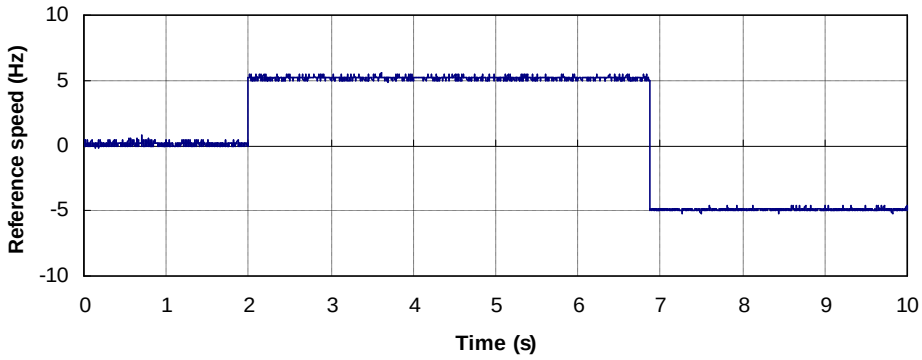

(a) Speed reference.

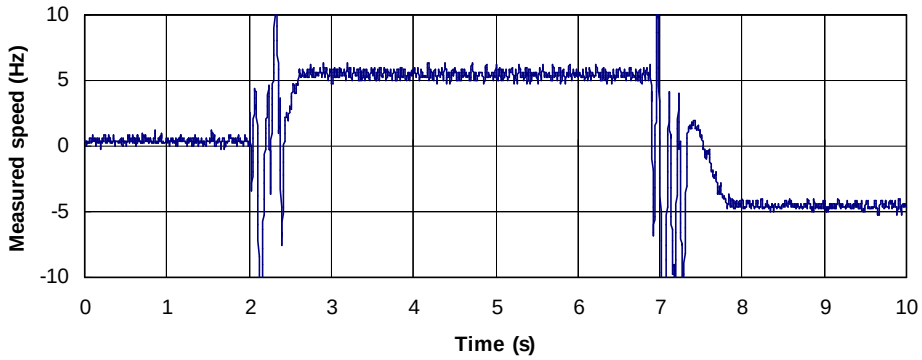

(b) Speed response.

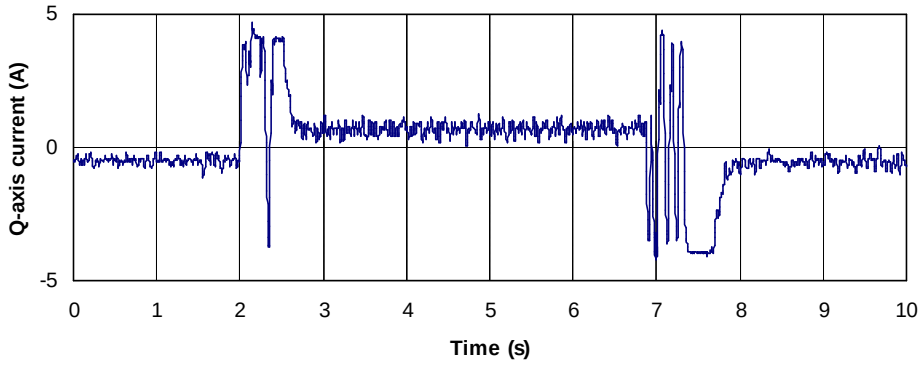

(c) *q*-axis current response.

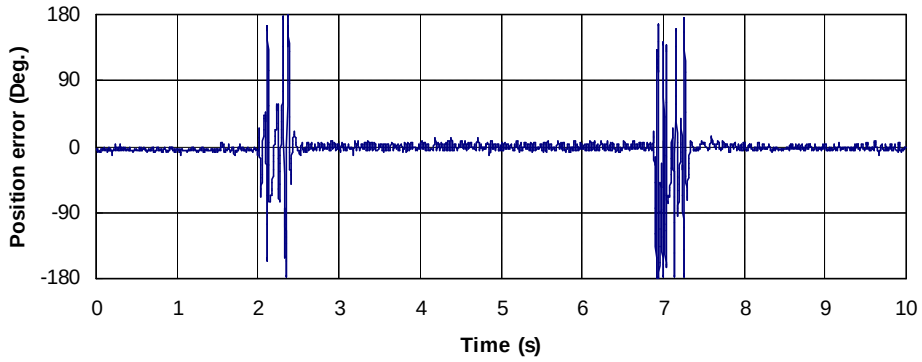

(d) Position estimation error.

Fig. 4.22 Measured step speed response for sensorless operation (10V, 330Hz).

4.5 Conclusions

The machine saliency property is vital for saliency based sensorless control techniques. After reviewing the existing methods for machine saliency investigation, this chapter presents a simplified experimental procedure to evaluate the machine saliency information, including magnetic saturation, cross-saturation and multiple saliency effects.

Unlike the cross-saturation effect, multiple saliency effect generates harmonic component in the vicinity of the primary saliency component (adjacent spectrum), which eventually introduces position dependent estimation error in the sensorless control. Although some compensation method is claimed to be effective to compensate multiple saliency effect, it is very computationally intensive due to the load-dependent and position-dependent behavior of the multiple saliency effects. Therefore, it is suggested that a better try to suppress multiple saliency effect through appropriate machine design.

Machine saliency behavior is an important factor for the feasibility of sensorless operation. However, it is proven that the sensorless effectiveness is also associated with the characteristics of the injected signal (V_c/ω_c), and the resolution of current measurement (I_{qu}). With accounting for the quantization error in AD conversion, the chapter defines the SSOA for sensorless effectiveness investigation based on L_n or I_n. With consideration of the machine saliency level, the characteristics of injected carrier voltage signal and current measurement resolution, the SSOA defines a working area in dq plane, in which the machine can perform sensorless operation with guaranteed performance in steady state. According to the definition of SSOA, a proper injected carrier signal can be selected for the specific prototype machine and current measurement resolution.

CHAPTER 5

COMPENSATION OF INVERTER NONLINEARITY EFFECTS IN ROTATING CARRIER SIGNAL INJECTION BASED SENSORLESS CONTROL

5.1 Introduction

For carrier voltage signal injection based sensorless control, the carrier current response is the major concern for position estimation. In a practical implementation, however, many nonlinear effects of both the machines and drives exert negative impacts on the carrier current response, eventually deteriorating the sensorless performance. In order to improve the accuracy of estimated rotor position, it is desirable to understand the sources of noise that distort the carrier current response. These disturbance factors can be classified into three categories [GAR07]: 1) distortion of injected carrier voltage, 2) additional carrier current components resulting from cross-saturation and multiple saliencies, 3) errors in the carrier current measurement. Regarding the distortion of injected carrier voltage, the reaction of the current regulator to the carrier current components is one of the sources of distortion. By use of a LPF and the appropriate configuration of the current regulator, the voltage distortion coming from current regulator can be effectively suppressed, which is mentioned in Chapter 2. On the other hand, inverter nonlinear behavior plays a significant role in the distortion of injected carrier voltage [GUE05].

Inverter nonlinearity effects consist of several factors: deadtime, gate drive circuit delays, switching on and switching off delay, parasitic capacitance effect, voltage drop in semiconductors, zero current clamping effect, short pulse suppression and so on. In summary, inverter nonlinearity effects can be viewed as a disturbance voltage generator, as shown in Fig. 5.1. The voltage distortion introduced by inverter nonlinear properties consists of fundamental and high-frequency components. The fundamental disturbance

voltage, which leads to fundamental current distortion, has been well documented in previous research work [CHO96] [HOL94] [HWA10]. For carrier signal injection based sensorless techniques, however, the introduced high frequency disturbance voltage is the more important factor, which results in additional carrier current components, eventually giving rise to significant position estimation error [GUE05].

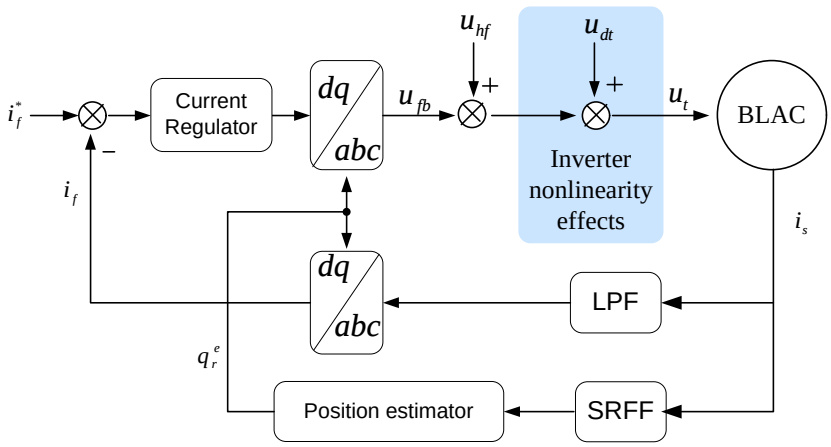

Fig. 5.1 Voltage distortion generated by inverter nonlinearity effects.

In order to suppress the negative effects of inverter nonlinearity on sensorless control, some efforts have been made to compensate for them. Compared with voltage source inverters, the matrix converter is claimed to be a good candidate for its nearly linear characteristic on voltage generation [ARI06]. For standard voltage source inverters, the common methods for solving this problem include,

1) Pre-compensation. The introduced HF disturbance voltage can be estimated on-line based on the distortion factor [CHO07], the physical characteristics of inverters [YUA09] or a closed-loop voltage disturbance observer [YUA09], and then the inverter nonlinearity can be pre-compensated by adding the estimated disturbance voltage to the voltage command. However, the requirement of instantaneous carrier current makes these methods very sensitive to the carrier current measurement error.
2) Post-compensation. A compensation strategy termed as space modulation profiling, which identifies the carrier current distortion using a 2-dimensional lookup table, is claimed to be effective in suppression of inverter nonlinearity [TES03]. Nevertheless, it is very time intensive to construct the lookup table.

3) Suppression of inverter nonlinearity. For pulsating injection based sensorless control, the *q*-axis pulsating injection scheme can prevent the origin of HF voltage distortion by making the HF current magnitude zero at every fundamental zero-crossing point [LIN03] [CHO08]. Unfortunately, this scheme is not applicable to the rotating injection based sensorless method.

This chapter is focused on the investigation and compensation of inverter nonlinearity effects in rotating injection based sensorless control methods. As will be shown by theoretical analysis and experimental measurement, the positive sequence carrier current distortion resulting from the inverter nonlinearity effects is proven to be helpful to compensate for the influence of inverter nonlinearity on position estimation. Hence, utilizing the distortion of the positive sequence carrier current to compensate for the distortion of negative sequence carrier current, a post-compensation scheme is developed. The proposed method can be easily implemented on a standard voltage source inverter without any off-line commissioning process or hardware modification. Experimental results confirm the effectiveness of the proposed method in suppressing the influence of the inverter nonlinearity effects on the position estimation.

5.2 Inverter Nonlinearity effects

Although the deadtime effect [CHO96] [HOL05] [HWA10] has been widely reported as the important factor in inverter nonlinearity, it is worth emphasizing that the inverter nonlinearity is also associated with the inherent characteristics of power devices, including the switching on and switching off delays, gate drive circuits delay, voltage drop in the power devices [CHO96], parasitic capacitance effects [QIA95] [GUE05], zero-current clamping effect [CHO95] [GUE05] and so on. In carrier signal injection based sensorless techniques, the deadtime and parasitic capacitance of semiconductors have been proven to be the major source causing carrier voltage distortion [GUE05].

5.2.1 Switching on and switching off delay

Due to the inherent characteristics of power devices, a time delay exists from when the power device is commanded to switch, to its effective fulfillment. The switching on

time t_{on}, means the time delay from the turn-on gate drive signal of the power device to the fully conducting state. The switching off time t_{off} can be defined in a similar way. In general, the switching on and switching off times are constrained within several hundred ns; however, the switching off time is considerably determined by the parasitic capacitance of power devices when the machine phase current is below a specific level, which will be discussed later.

5.2.2 Gate drive circuits delay

In general, a gate drive is required to amplify the PWM control signals to drive the power devices as soon as possible. Inevitably, some additional time delay would be introduced, especially when opto-couplers are employed in gate drive design. Combining the inherent switching on and switching off times, the power devices turn-on delay t_{du} and turn-off delay t_{dd}, are nearly constant and independent of the motor phase current under normal circumstances.

5.2.3 Deadtime

Considering the inherent turn-off delay of power devices, the deadtime is essential to avoid a shoot-through fault. When the two power devices in one phase leg are switched, the deadtime t_{dt} must be inserted to guarantee the device commanded to turn off has been switched off effectively, before the counterpart is commanded to turn on. Together with turn-on and turn-off delay, an error voltage pulse would be generated due to the unwanted time delays, as shown in Fig. 5.2 and Fig. 5.3. It should be noted that the sign of the error voltage pulse is opposite to the current polarity. The introduced terminal voltage error can be averaged in one PWM period, as given by,

$$V_{dt} = V_{ao} - V_{ao}^{*} = -sign(i_s) \cdot U_{dc} \frac{t_{dt} + t_{du} - t_{dd}}{T_s} = -sign(i_s) \cdot \Delta U \qquad (5.1)$$

where i_s is the phase current, U_{dc} is the DC bus voltage, and T_s is the PWM period. Obviously, since ΔU is constant for given DC bus voltage and PWM frequency, the average terminal voltage error is only determined by the related phase current polarity, instead of current amplitude.

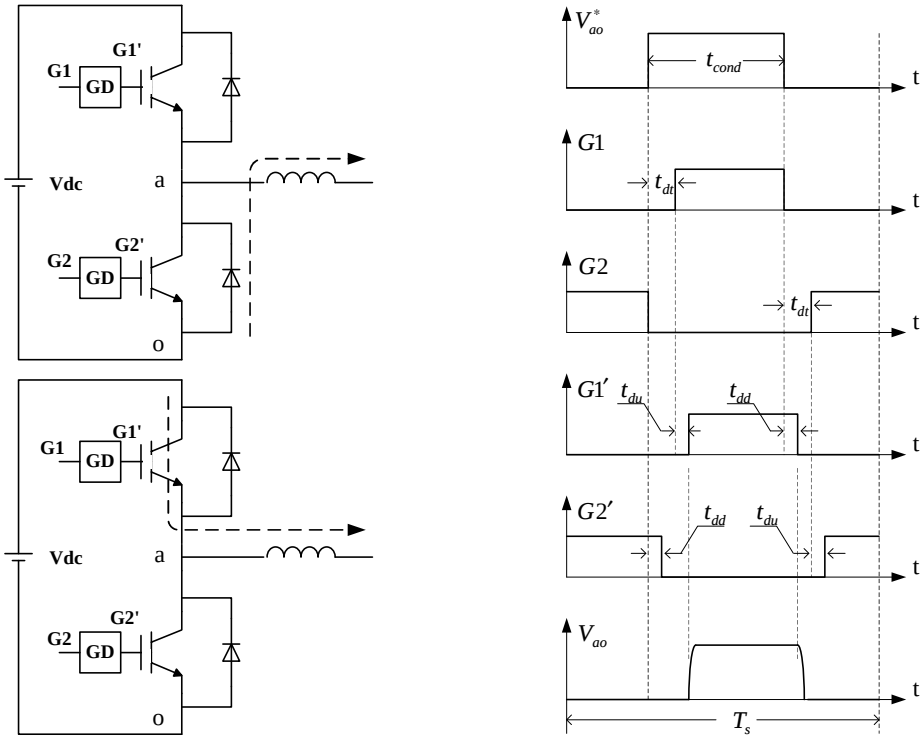

(a) Switching pattern (b) Terminal voltage error

Fig. 5.2 Deadtime effects ($i_s>0$)

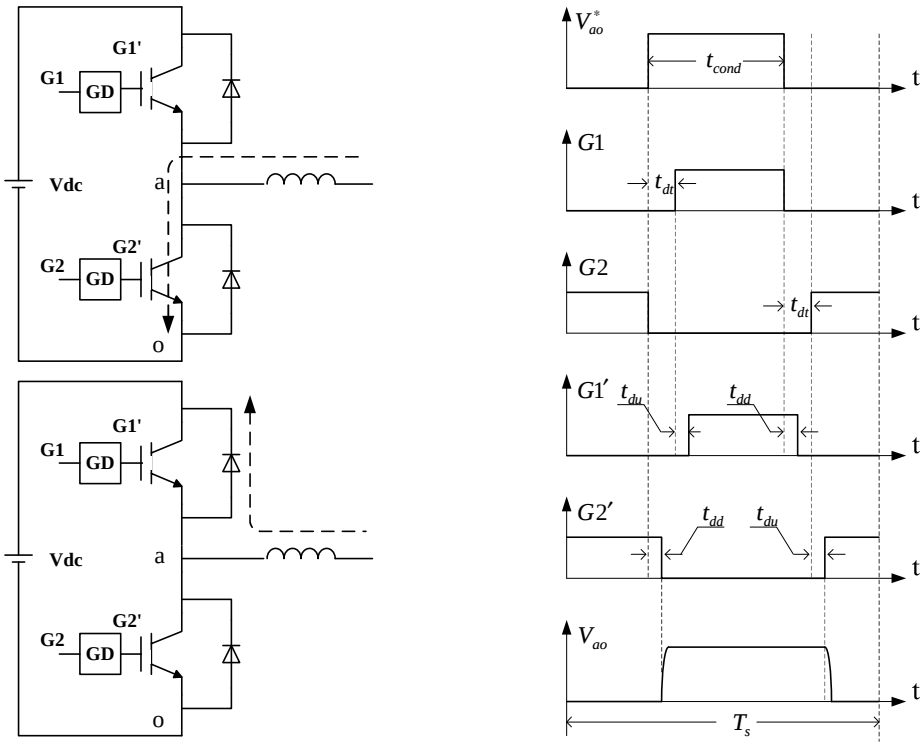

(a) Switching pattern (b) Terminal voltage error

Fig. 5.3 Deadtime effects ($i_s<0$)

5.2.4 Voltage drop in semiconductors

There exists voltage drop in the semiconductors when the motor current flows through it. Generally, the voltage drop in the active switch and freewheel diode can be modeled as,

$$\begin{cases} V_{ce} = V_{ceo} + R_{ce} \cdot i_s \\ V_d = V_{do} + R_d \cdot i_s \end{cases} \tag{5. 2}$$

Where, V_{ceo} and V_{do} are the threshold voltage of active switch and freewheel diode, R_{ce} and R_d is the equivalent on-state resistance of the active switch and freewheel diode.

Approximately, the average voltage error induced by the voltage drop in semiconductors can be expressed as [CHO96],

$$V_{drop} \approx -sign(i_s) \cdot \frac{V_{ce0} + V_{d0}}{2} - \frac{R_{ce} + R_d}{2} \cdot i_s \tag{5. 3}$$

The above equation shows that the voltage drop in semiconductors comprises two terms: the first term has the same property as deadtime effect, and the second term acts as a stator resistor. Therefore, the second term can be used to construct an equivalent stator resistance which includes actual stator resistance and equivalent resistance of power devices.

5.2.5 Zero-current clamping effects

For the machine excited only by the fundamental current, zero-current clamping tends to occur whenever the phase current crosses zero [CHO95], as shown in Fig. 5.4. Although it has been reported that the effect of zero-current clamping is the main contributor to carrier signal distortion in high-frequency signal injection based sensorless control [CHO07] [CHO08], zero-current clamping can not be observed when the high-frequency carrier signal is injected into the machine [GUE05], as shown in Fig. 5.5. The reason may be that the carrier voltage superimposed on the fundamental voltage results in multiple zero-crossings in the phase current when the fundament phase current is close to zero, hence the phase current hardly stays in zero region for a long time, eventually making zero-current clamping unclear. As a result, efforts for compensating

zero-current clamping effects in conventional compensation methods [CHO95] is not expected to suppress the carrier voltage distortion.

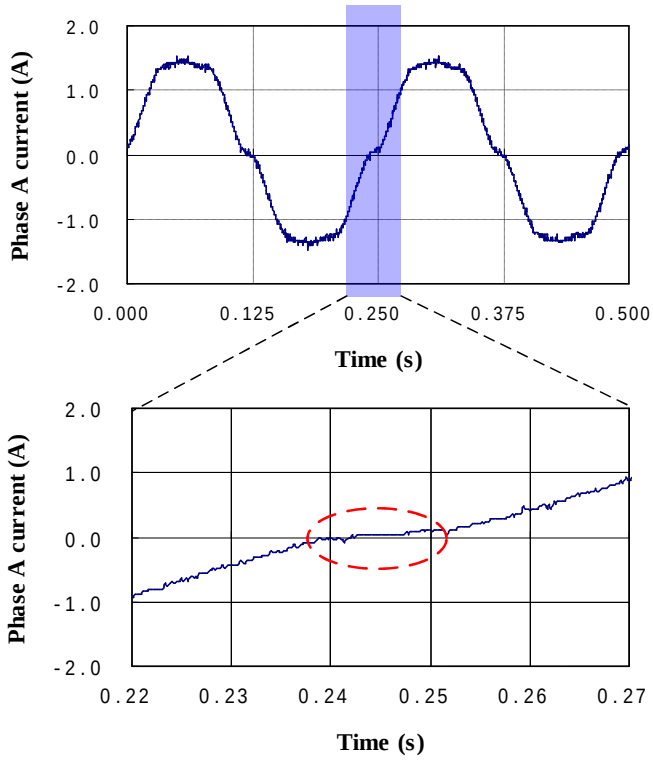

Fig. 5.4 Current zero-crossing (without injection)

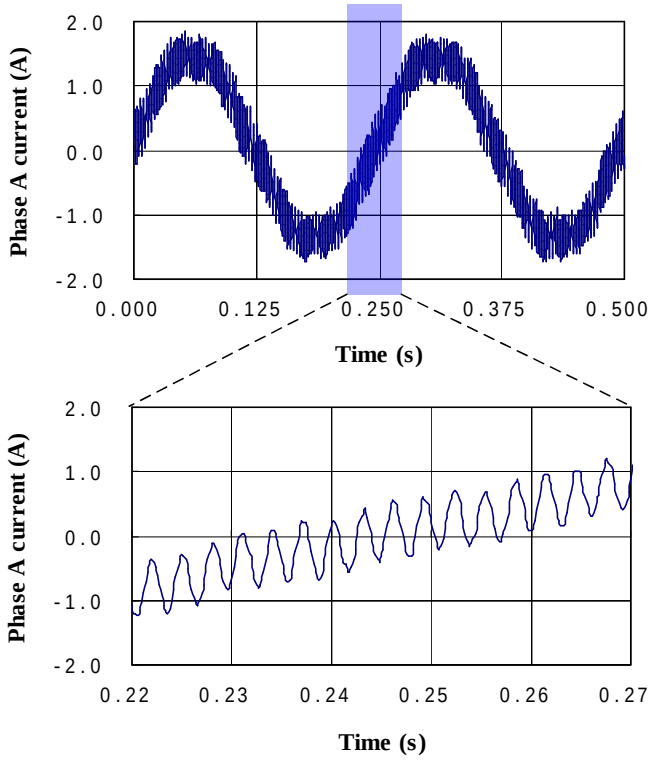

Fig. 5.5 Current zero-crossing (with injection)

5.2.6 Short pulse suppression

For PWM generation, the voltage pulse width becomes narrow with increasing voltage command. When the voltage pulse width is shorter than the deadtime, it would be suppressed to decrease the power devices switching loss. Since high-frequency carrier signal injection based sensorless control is only employed at lower speed ranges, where the command voltage is far away from the inverter voltage limits, short pulse suppression is not a problem in this case [GUE05].

5.2.7 Parasitic capacitance effects

The parasitic capacitance of power devices is shown in Fig. 5.6, in which the current flow path for positive current is indicated by the dashed line. When the current is transferred from the free-wheel diode to the IGBT, it can be accomplished immediately. The reason is that IGBTs are active switchers, whose turn-on can provide a low resistance path for immediate charging or discharging of parasitic capacitance. Consequently, the terminal voltage slope is fairly steep and almost independent on the current level, as shown by the rising edge in Fig. 5.7b and the falling edge in Fig. 5.8b. However, a different phenomenon can be observed in the current transferring from the IGBT to the free-wheel diode, which is initialized by the switching off of IGBT. The falling edge in Fig. 5.7b and the rising edge in Fig. 5.8b show the terminal voltage slope in this case. Due to the parasitic capacitance effect, the slope of the terminal voltage is significantly dependent on the current level [QIA95] [CHO95] [GUE05] [SAL11].

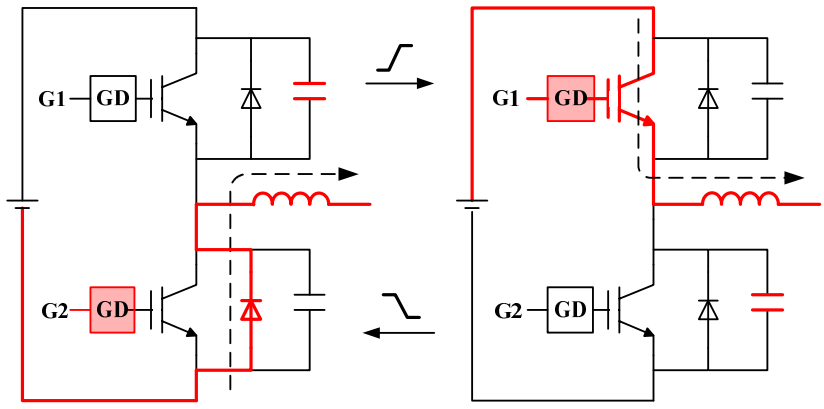

Fig. 5.6 Current flowing paths with consideration of parasitic capacitance ($i_s>0$).

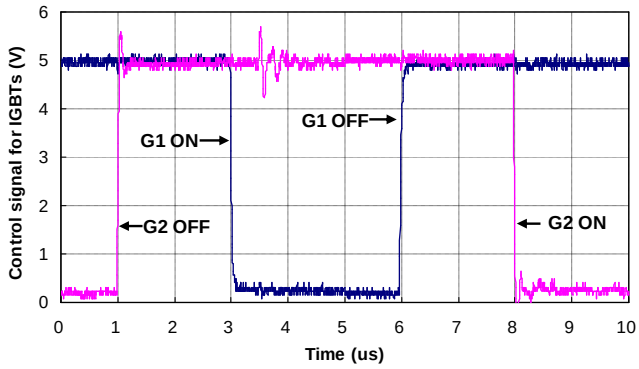

(a) Control signals for IGBTs

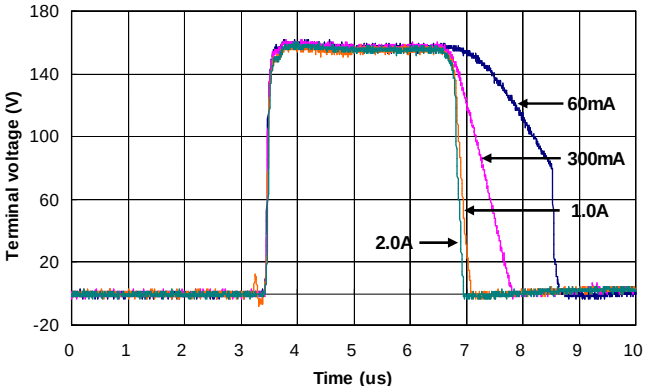

(b) Terminal voltage

Fig. 5.7 Measured terminal voltage (t_{dt}=2μs, i_s>0).

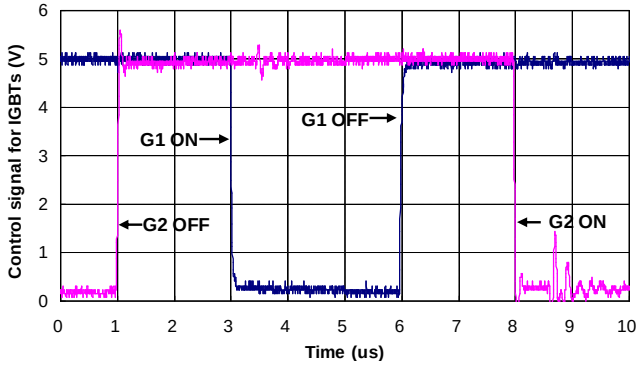

(a) Control signals for IGBTs

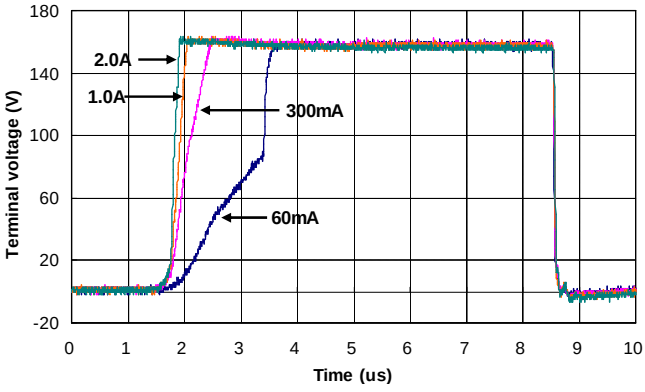

(b) Terminal voltage

Fig. 5.8 Measured terminal voltage (t_{dt}=2μs, i_s<0).

In order to obtain the relationship between terminal voltage error and phase current, the measured data under the condition of 2.0μs deadtime, 10kHz PWM switching frequency, and 150V DC bus voltage can be used to construct the curve, as indicated by the solid line in Fig. 5.9. It can be found that the terminal voltage error tends to saturation at higher current level, and the saturation value ΔU is about 2.6V for 2.0μs deadtime. The value of ΔU is determined by the deadtime for a given DC bus voltage and PWM frequency, and it would rise to 5.6V for 4.0μs deadtime for example. At lower phase current, however, the terminal voltage error is significantly dependent on the instantaneous current level, and the parasitic capacitance. The lower the parasitic capacitance, the steeper the slope of terminal voltage error. Without parasitic capacitors, the slope-change behavior of terminal voltage error at lower current level would become a step-change at the zero current point.

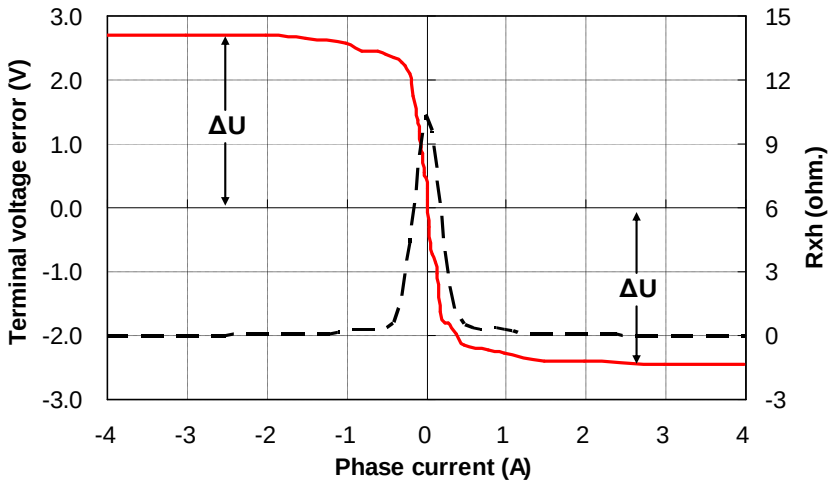

Fig. 5.9 Measured terminal voltage error (t_{dt}=2μs, V_{dc}=150V).

In carrier signal injection based sensorless techniques, the total current response consists of fundamental and carrier current components. Hence, the terminal voltage error can be expressed as:

$$\Delta u_{xo} = f(i_{xs}) = f(i_{xf} + i_{xh}) \tag{5. 4}$$

where, i_{xs} is the total phase current, i_{xf} is the fundamental current component, and i_{xh} is the carrier current components. When the carrier current is much smaller than the fundamental current, the above equation can be approximated as:

$$\Delta u_{xo} \approx f(i_{xf}) + f'(i_{xf}) \cdot i_{xh} \approx -sign(i_{xf}) \cdot \Delta U - R_{xh} \cdot i_{xh} \tag{5. 5}$$

where R_{xh} is designated as the equivalent HF resistance of the inverter,

$$R_{xh} = -f'(i_{xf}) \tag{5. 6}$$

Based on (5.6) R_{xh} for a deadtime of 2.0μs in the prototype machine drive system, is calculated and shown by the dashed line in Fig. 5.9. It can be concluded that the equivalent HF resistance of the inverter, determined by the characteristic of terminal voltage error, is an extremely nonlinear resistance. For the current higher than 0.5A, R_{xh} becomes nearly zero, which implies that the equivalent HF resistance of the inverter only exists near the zero-current region and reaches its maximum value at zero fundamental current.

5.3 Voltage Distortion Introduced by Inverter Nonlinearity Effects

5.3.1 Model of voltage distortion

In order to model the inverter nonlinearity, it is desirable to transfer the terminal voltage error to the phase voltage error. For a three-phase system with wye-connection, the terminal voltage can be expressed as:

$$\begin{cases} u_{ao}^* = u_{as}^* + u_{so}^* \\ u_{bo}^* = u_{bs}^* + u_{so}^* \\ u_{co}^* = u_{cs}^* + u_{so}^* \end{cases} \tag{5. 7}$$

Where u_{as}*, u_{bs}*, and u_{cs}* are the phase voltages, and u_{so}* is the machine neutral point voltage. For a balanced load without consideration of third harmonics, the phase voltages are constrained by,

$$u_{as}^* + u_{bs}^* + u_{cs}^* = 0 \tag{5. 8}$$

Then the machine neutral point voltage is therefore obtained as,

$$u_{so}^* = \frac{1}{3}(u_{ao}^* + u_{bo}^* + u_{co}^*) \tag{5. 9}$$

The combination of (5.7) and (5.9) gives,

$$\begin{cases} u_{as}^{*} = \dfrac{2u_{ao}^{*} - u_{bo}^{*} - u_{co}^{*}}{3} \\ u_{bs}^{*} = \dfrac{-u_{ao}^{*} + 2u_{bo}^{*} - u_{co}^{*}}{3} \\ u_{cs}^{*} = \dfrac{-u_{ao}^{*} - u_{bo}^{*} + 2u_{co}^{*}}{3} \end{cases} \tag{5.10}$$

Therefore, the phase voltage with consideration of terminal voltage error can be represented by,

$$\begin{cases} u_{as} = \dfrac{2u_{ao}^{*} - u_{bo}^{*} - u_{co}^{*}}{3} + \dfrac{2\Delta u_{ao} - \Delta u_{bo} - \Delta u_{co}}{3} \\ u_{bs} = \dfrac{-u_{ao}^{*} + 2u_{bo}^{*} - u_{co}^{*}}{3} + \dfrac{-\Delta u_{ao} + 2\Delta u_{bo} - \Delta u_{co}}{3} \\ u_{cs} = \dfrac{-u_{ao}^{*} - u_{bo}^{*} + 2u_{co}^{*}}{3} + \dfrac{-\Delta u_{ao} - \Delta u_{bo} + 2\Delta u_{co}}{3} \end{cases} \tag{5.11}$$

As a result, the phase voltage error can be obtained from measured terminal voltage error, given by,

$$\begin{cases} \Delta u_{as} = u_{as} - u_{as}^{*} = \dfrac{2\Delta u_{ao} - \Delta u_{bo} - \Delta u_{co}}{3} \\ \Delta u_{bs} = u_{bs} - u_{bs}^{*} = \dfrac{-\Delta u_{ao} + 2\Delta u_{bo} - \Delta u_{co}}{3} \\ \Delta u_{cs} = u_{cs} - u_{cs}^{*} = \dfrac{-\Delta u_{ao} - \Delta u_{bo} + 2\Delta u_{co}}{3} \end{cases} \tag{5.12}$$

Therefore, the terminal voltage error and phase voltage error can be calculated from (5.4) and (5.12) respectively, as depicted in Fig. 5.10, in which, the fundamental component is highlighted in red. It can be clearly seen that the voltage error consists of both fundamental and high-frequency components.

According to the definition of space vector, the disturbance voltage vector due to the inverter nonlinearity can be expressed as,

$$\begin{aligned} \Delta u &= \frac{2}{3}(\Delta u_{as} + \Delta u_{bs} \cdot e^{j2p/3} + \Delta u_{cs} \cdot e^{j4p/3}) \\ &= \frac{2}{3}(\Delta u_{ao} + \Delta u_{bo} \cdot e^{j2p/3} + \Delta u_{co} \cdot e^{j4p/3}) \\ &= \Delta u_{f} + \Delta u_{h} \end{aligned} \tag{5.13}$$

where Δu_f is the fundamental disturbance voltage component, and Δu_h is the high-frequency disturbance voltage component, as defined by,

$$\begin{cases} \Delta u_f = -\dfrac{2}{3}\Delta U[sign(i_{af}) + sign(i_{bf}) \cdot e^{j2p/3} + sign(i_{cf}) \cdot e^{j4p/3}] \\ \Delta u_h = -\dfrac{2}{3}[R_{ah} \cdot i_{ah} + R_{bh} \cdot i_{bh} \cdot e^{j2p/3} + R_{ch} \cdot i_{ch} \cdot e^{j4p/3}] \end{cases} \tag{5.14}$$

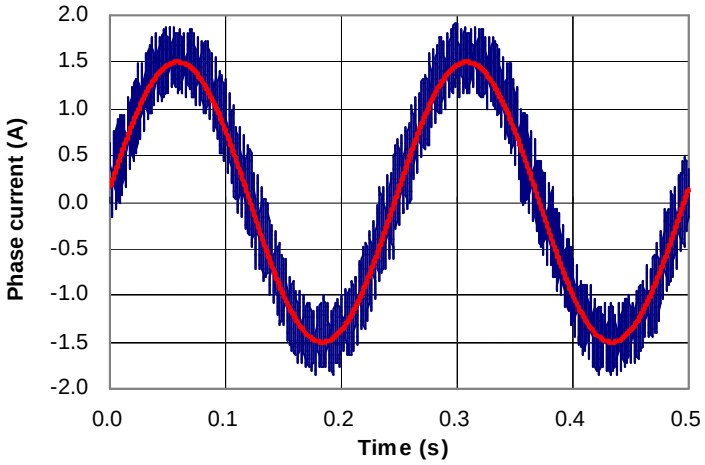

(a) Measured phase current

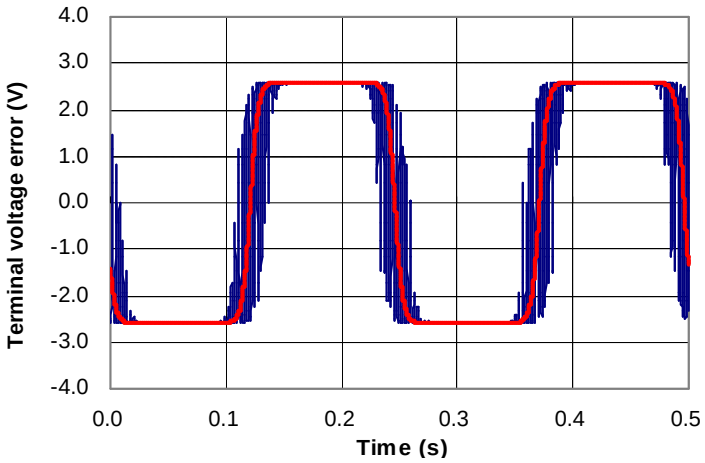

(b) Calculated terminal voltage error

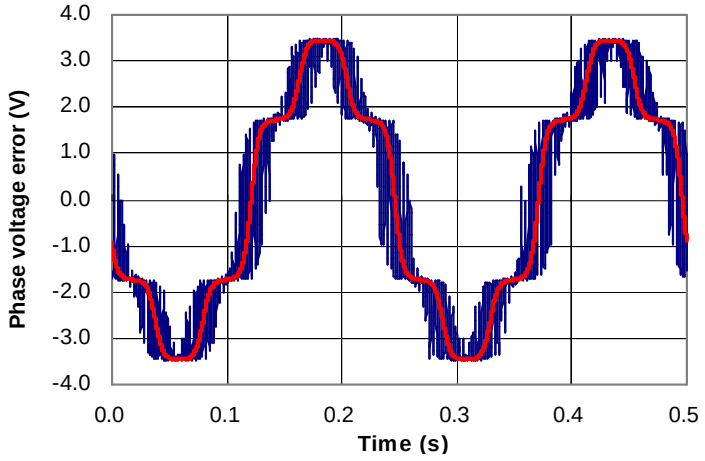

(c) Calculated phase voltage error

Fig. 5.10 Voltage distortion Introduced by inverter nonlinearity effects.

5.3.2 Fundamental voltage distortion

According to the definition of fundamental disturbance voltage vector, six fundamental disturbance voltage vectors, which have identical magnitude of ($4\Delta U/3$), can be plotted in the stationary reference frame, as shown in Fig. 5.11, in which, the whole α-β plane is separated into six regions, indicated as *S1~S6* [HOL94] [KIM03]. Dependent on the region where the fundamental current vector stays, the specific distortion voltage vector is introduced by inverter nonlinearity effects, as listed in Table 5.1.

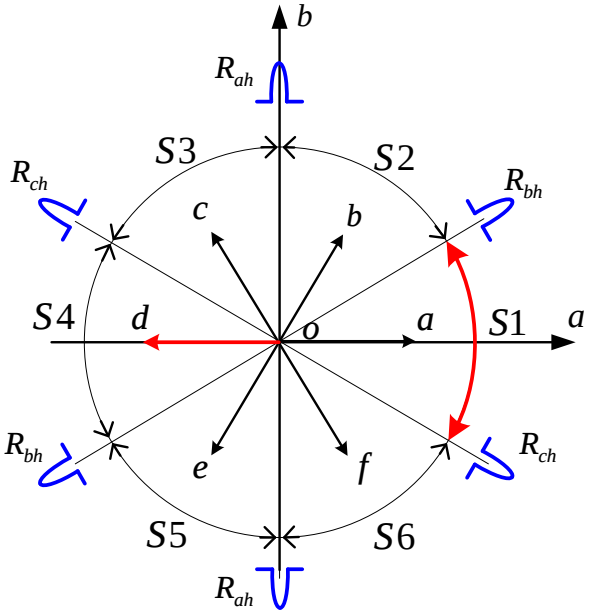

Fig. 5.11 Disturbance voltage due to inverter nonlinearity effects.

Table 5.1 Fundamental disturbance voltage vectors

Current sectors	Fundamental current vector position	Disturbance voltage vectors
S1	330° ~ 30°	od
S2	30° ~ 90°	oe
S3	90° ~ 150°	of
S4	150° ~ 210°	oa
S5	210° ~ 270°	ob
S6	270° ~ 330°	oc

The fundamental disturbance voltage vector exerts significant influences on the fundamental current. However, it has less impact on the carrier current distortion [GUE05].

5.3.3 Carrier frequency voltage distortion

The introduced carrier frequency disturbance voltage is a more important factor, which results in additional carrier current components. As suggested by (5.14), the carrier frequency voltage distortion is directly associated with the inverter equivalent HF resistance. If the three phase equivalent HF resistances of inverter are equal to each other, they act as normal stator resistance. Unfortunately, the foregoing analysis indicates that they are greatly nonlinear. When the fundamental phase current is in the vicinity of zero, the related HF resistance has a non-zero value, as depicted in Fig. 5.11. In other words, the equivalent HF resistances occur only when the fundamental current vector arrives close to the different sector boundaries, and disappear in the remaining areas. Additionally, the equivalent HF resistance reaches its peak value when the fundamental current vector is at the sector boundaries. With the same frequency as the carrier current, the HF disturbance voltage is the major contributor to carrier current distortion [GUE05]. The injected carrier voltage vector is affected six times in one fundamental cycle as there are six boundary-crossings. As a result, it gives rise to a visible perturbation on the carrier current response in the frequency domain, as shown in Fig. 5.12.

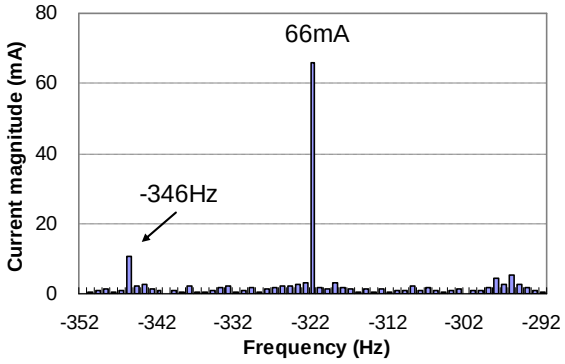

(a) Negative sequence (t_{dt}=2μs)

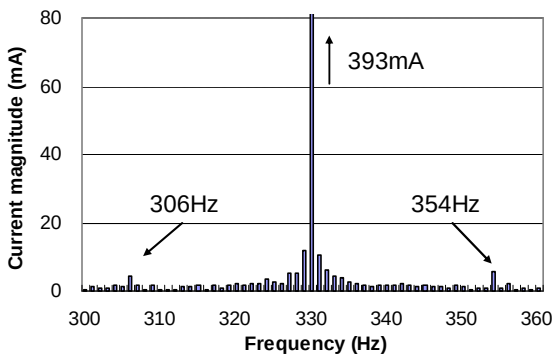

(b) Positive sequence (t_{dt}=2μs)

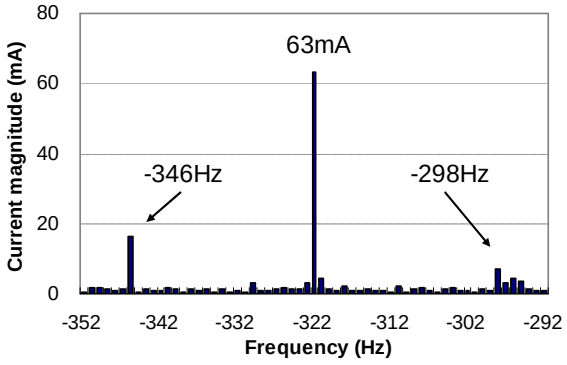

(c) Negative sequence (t_{dt}=4μs)

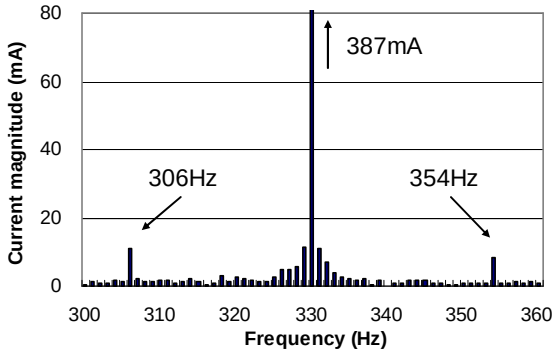

(d) Positive sequence (t_{dt}=4μs)

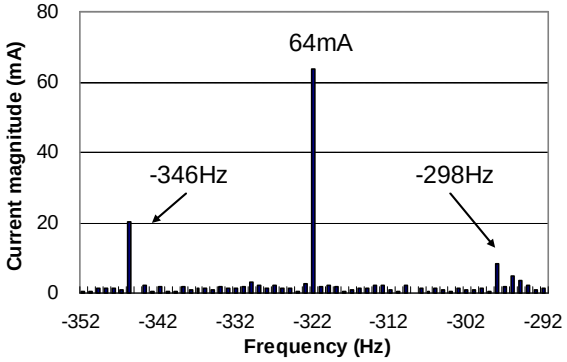

(e) Negative sequence (t_{dt}=6μs)

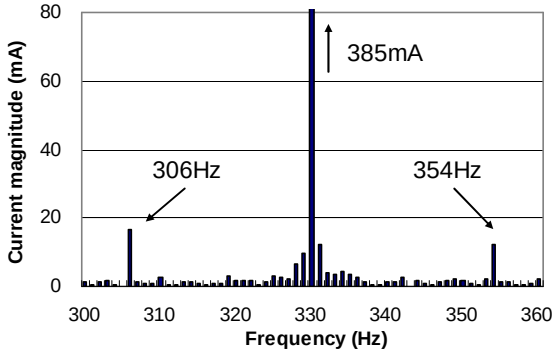

(f) Positive sequence (t_{dt}=6μs)

Fig. 5.12 Measured spectra of carrier current response (f=4Hz, f_c=330Hz).

5.4 Analysis of Carrier Current Distortion

For rotating carrier signal injection based sensorless control, although the positive sequence carrier current is dominant in the total carrier current response, it has no use in conventional sensorless methods. Only the negative sequence carrier current component, which contains position information of the phase angle, is utilized in the sensorless algorithm. However, the positive sequence carrier current response was proven to be useful for the compensation of inverter nonlinearity effects. Before describing the proposed compensation method, it is helpful to analyze the impacts of HF disturbance voltage on positive and negative sequence carrier current, respectively.

The HF carrier signal injection based method is often used at standstill and in the low speed range, in which the d-axis current is usually small or close to zero. Therefore, when the rotor stays at zero position (θ_r=0), the fundamental current space vector is located

close to the vicinity of positive or negative β-axis, and then R_{ah} has a non-zero value while $R_{bh}=R_{ch}=0$. In this case, the HF disturbance voltage vector defined by (5.14) can be simplified to:

$$\Delta u_h = -\frac{2}{3} R_{ah} \cdot i_{ah} \tag{5.15}$$

The real carrier current response becomes different from the ideal expression due to inverter nonlinearity effects. Considering its dominant contribution to the total carrier current response, the ideal carrier current can be substituted into the above equation,

$$\begin{aligned} \Delta u_h = &-\frac{1}{3} R_{ah} I_p e^{j(a-p/2)} - \frac{1}{3} R_{ah} I_n e^{j(a-2q_r-p/2)} \\ &-\frac{1}{3} R_{ah} I_p e^{j(-a+p/2)} - \frac{1}{3} R_{ah} I_n e^{j(-a+2q_r+p/2)} \end{aligned} \tag{5.16}$$

Equation (5.16) shows that the HF disturbance voltage introduced by the inverter nonlinearity effects consists of four terms. The first two terms are positive sequence vectors, while the last two terms are negative sequence vectors. Each voltage term generates corresponding positive and negative sequence carrier current, hence the resultant total carrier current response can be calculated and summarized in Table 5.2. For the relatively small amplitudes of I_n, the disturbance carrier current components with grey background in Table 5.2 can be neglected.

Table 5.2 Total carrier current components ($R_{ah} \neq 0$).

Voltage Term	Carrier Current I_{pos} (Positive sequence)	Carrier Current I_{neg} (Negative sequence)
$V_c e^{ja}$	$I_p e^{j(a-p/2)}$	$I_n e^{j(-a+2q_r+p/2)}$
$-\frac{R_{ah} I_p}{3} e^{j(a-p/2)}$	$-\frac{R_{ah} I_p^2}{3V_c} e^{j(a-p)}$	$-\frac{R_{ah} I_p I_n}{3V_c} e^{j(-a+2q_r+p)}$
$-\frac{R_{ah} I_n}{3} e^{j(a-2q_r-p/2)}$	$-\frac{R_{ah} I_p I_n}{3V_c} e^{j(a-2q_r-p)}$	$-\frac{R_{ah} I_n^2}{3V_c} e^{j(-a+4q_r+p)}$
$-\frac{R_{ah} I_p}{3} e^{j(-a+p/2)}$	$-\frac{R_{ah} I_p I_n}{3V_c} e^{j(a+2q_r-p)}$	$-\frac{R_{ah} I_p^2}{3V_c} e^{j(-a+p)}$
$-\frac{R_{ah} I_n}{3} e^{j(-a+2q_r+p/2)}$	$-\frac{R_{ah} I_n^2}{3V_c} e^{j(a-p)}$	$-\frac{R_{ah} I_p I_n}{3V_c} e^{j(-a+2q_r+p)}$

For conventional sensorless position detection, a parameter of ε constructed from negative sequence carrier current is used to estimate the position information, as given by,

$$e = -\sin(-a + 2q_r^e + \frac{p}{2})I_{neg\_a} + \cos(-a + 2q_r^e + \frac{p}{2})I_{neg\_b} \tag{5.17}$$

where I_{neg_α} is the α-axis component of total negative sequence carrier current and I_{neg_β} is the β-axis component of total negative sequence carrier current in the stationary reference frame. θ_r^e is the estimated rotor position.

When the additional carrier current components resulting from inverter nonlinearity effects, shown in Table 5.2, are considered, (5.17) can be re-written as,

$$e \approx I_n \sin(2\Delta q) - \frac{R_{ah} I_p^2}{3V_c}\cos(2q_r^e) - \frac{2R_{ah} I_p I_n}{3V_c}\cos(2\Delta q) \tag{5.18}$$

Furthermore, when the rotor position estimation error $\Delta\theta$ is sufficiently small, considering the real rotor position is close to zero in this case, (5.18) can be approximated to,

$$e \approx 2I_n \Delta q - \frac{R_{ah}}{3V_c}(I_p^2 + 2I_p I_n) \tag{5.19}$$

The same conclusion can be drawn for the cases of $R_{bh} \neq 0$ and $R_{ch} \neq 0$ (Appendix 6).

From (5.19), it can be seen that ε is associated with both estimated position error and inverter nonlinearity effects. Inevitably, the inverter nonlinearity effects are adverse to position estimation, which would give rise to a six harmonic on the estimated position information due to the nonlinear behavior of inverter equivalent HF resistance. The estimated position error generated by the inverter nonlinearity effects can be obtained from (5.19), as given by:

$$\Delta q \approx -\frac{R_{ah}(I_p^2 + 2I_p I_n)}{6V_c I_n} \tag{5.20}$$

To analyze the distortion of positive sequence carrier current, another important factor λ is introduced in this thesis, as given by,

$$l = -\sin(a - \frac{p}{2})I_{pos\_a} + \cos(a - \frac{p}{2})I_{pos\_b} \tag{5.21}$$

Substituting carrier current components shown in Table 5.2 into (5.21), it yields,

$$l \approx \frac{R_{ah}}{3V_c}(I_p^2 + 2I_p I_n) \tag{5.22}$$

Unlike ε, equation (5.22) shows that λ is independent of the position information, and only associated with the inverter nonlinear behavior.

5.5 Proposed Compensation Scheme

In conventional rotating injection based sensorless position detection, the parameter ε, constructed from negative sequence carrier current, is used to estimate the rotor position information. However, the inverter nonlinear behavior exerts adverse influences on it, as shown in (5.19). Due to the additional carrier current harmonic components induced by cross-saturation and multiple saliency effects located in the negative sequence domain [RAC08], the positive sequence carrier current component is only affected by the inverter nonlinearity effects. Therefore, it is practical to compensate for the inverter nonlinearity effects based on the distortion of positive sequence carrier current.

The comparison between (5.19) and (5.22) reveals that, without position estimation error ($\Delta\theta=0$), the signal ε has the opposite phase to that of λ. Hence, the combination of them gives

$$e + l \approx 2I_n \Delta q \tag{5.23}$$

It clearly shows that with the help of λ, the influence of inverter nonlinearity effects on ε can be compensated. The summation of ε and λ, i.e. ($\varepsilon+\lambda$), is only dependent on the estimated position error, hence it can be employed to estimate the position information accurately.

The complete system schematic diagram of the proposed compensation method is shown in Fig. 5.13, in which, ($\varepsilon+\lambda$) is utilized as the input signal to the position estimator, instead of ε as in the conventional approach. The commonly used synchronous reference frame filter (SRFF) technique is then used to separate the fundamental current, positive and negative sequence carrier current from the total current response. The isolated carrier current components (i_{pos} and i_{neg}) are used to estimate the rotor position information, while the fundamental current (i_f) is fedback to the current regulator. A PI controller and

an integrator are used as the position estimator. To compensate for the position estimation error resulting from cross-saturation effect, the compensation method proposed in [ZHU07] [KOC09] is employed.

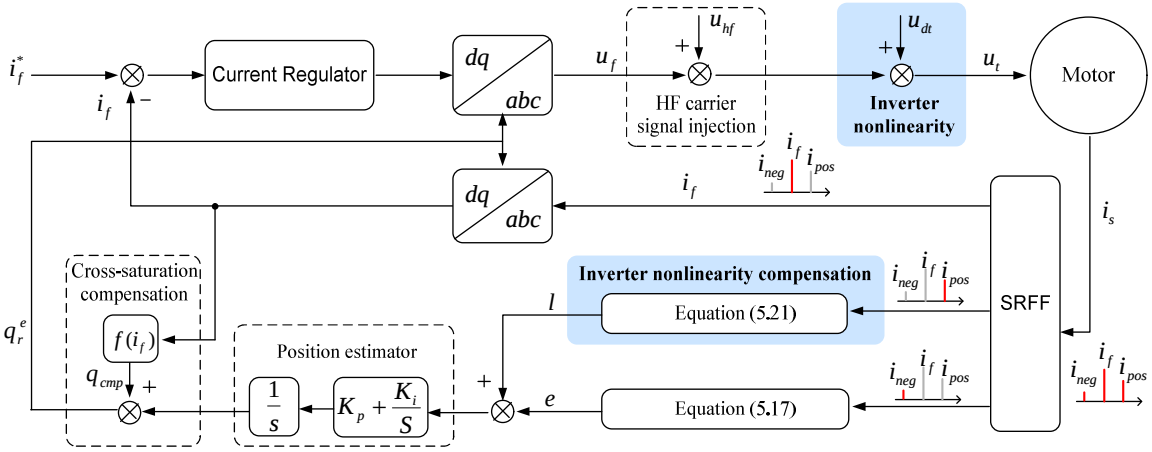

Fig. 5.13 Proposed compensation method for inverter nonlinearity effects.

In the proposed scheme, the value of ε and λ can be on-line obtained from (5.17) and (5.21) without any off-line commissioning process. By way of example, the on-line obtained ε, λ, and (ε+λ) in sensored operation mode ($\Delta\theta=0$) are shown in Fig. 5.14. From them, sixth harmonic ripple can be observed on both ε and λ, while their phases are opposite to each other, which is in good agreement with foregoing analysis. Although the ripple amplitude of ε and λ increase as deadtime increases, the ripple on (ε+λ) has been significantly suppressed. Consequently, sensorless operation performance is expected to be improved with the proposed compensation method. In Fig. 5.14, although the DC offsets in ε (due to cross-saturation effect and stator resistance [RAC08]) and λ (due to stator resistance [RAC08]) would cause additional constant estimation error for given load condition, the introduced estimation error can easily be compensated for together with cross-saturation compensation.

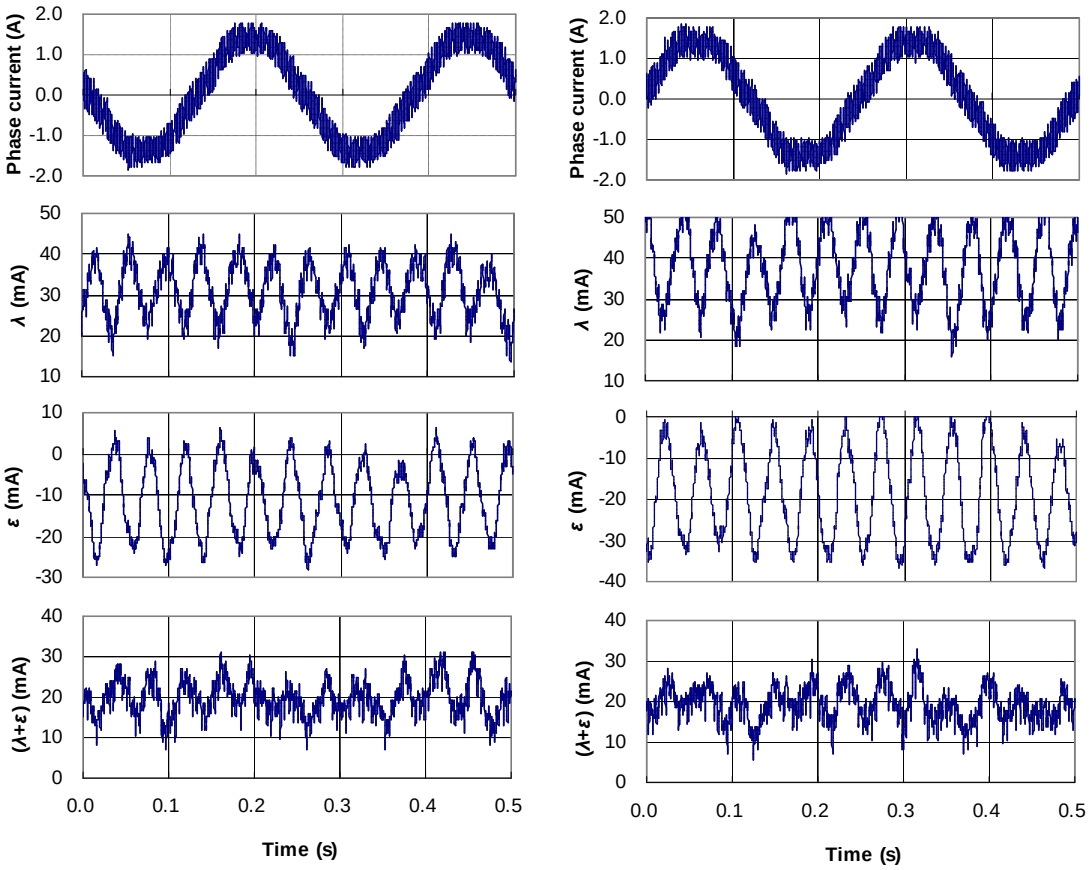

(a) t_{dt}=4μs (b) t_{dt}=6μs

Fig. 5.14 Calculated ε, λ, and (ε+λ) in sensored operation mode.

To evaluate the sensorless control performance of the proposed method, the pre-compensation method [INO09] [YUA09], as shown in Fig. 5.15, was also implemented for comparison purpose. Using the measured phase current, this method estimates the disturbance voltage due to inverter nonlinearity effects based on the inverter physical characteristics (Fig. 5.9), and then superimposes the estimated compensation voltage to the terminal voltage command. Although the principle of this method is straightforward, to obtain the inverter physical characteristics from experiments is a time-consuming task. Additionally, the measurement error of instantaneous current especially due to sampling delay makes it impossible to compensate for the disturbance voltage completely with a pre-compensation method.

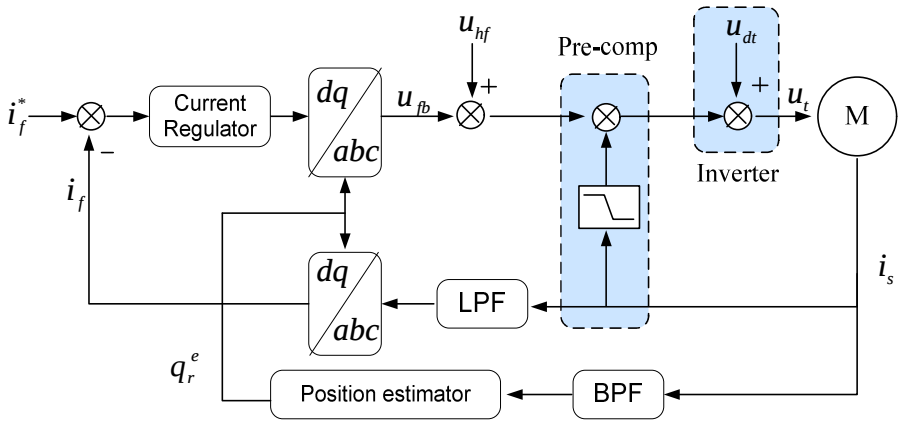

(a) Block diagram of pre-compensation method

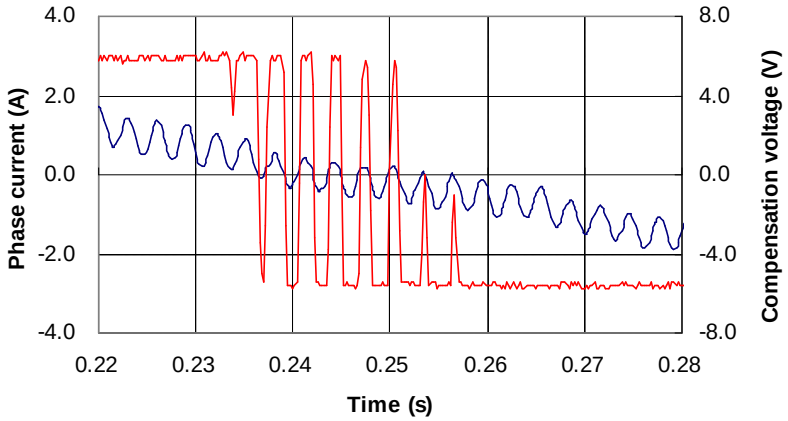

(b) Compensation voltage and measured phase current

Fig. 5.15 Pre-compensation method (t_{dt}=4μs, V_{dc}=150V)

The sensorless operation performances without compensation, with pre-compensation method and with proposed method are compared at different speed and load conditions, as shown in Fig. 5.16~Fig. 5.19. The DC bus voltage is 150V, and the deadtime is set to 4μs. For the prototype machine, a rotating carrier voltage with magnitude of 35V and frequency of 330Hz is determined for the purpose of sensorless effectiveness in the whole operating range. Inevitably, the injected carrier voltage and resultant carrier current response would causes additional losses, vibrations and unwanted audible noise. Consequently, the injection based sensorless method is only used at low speed range, where the back-EMF based sensorless method does not work well.

From the experimental results shown in Fig. 5.16-Fig. 5.19, the estimated position error without compensation scheme oscillates at six times the fundamental frequency, which results in much distortion on the current response. Although some improvement

can be observed with pre-compensation method, more improvement in the accuracy of estimated rotor position can be achieved when the proposed compensation scheme is employed. Furthermore, the fundamental current waveform is also improved with fewer harmonics due to more accurately estimated position information. As a result, the experimental results confirm the effectiveness and advantages of the proposed method.

5.6 Conclusions

HF disturbance voltage generated by the inverter nonlinearity effects is the key factor which distorts the carrier current response, and eventually deteriorates the accuracy of estimated rotor position information in sensorless control.

In rotating carrier signal injection based sensorless control method, although the positive sequence carrier current is dominant in the total carrier current response, it has no use in conventional sensorless methods. Only the negative sequence carrier current component, which contains position information in the phase angle, is utilized in the sensorless algorithm. However, the distortion of the negative sequence carrier current response due to inverter nonlinearity effects would give rise to significant position estimation error in sensorless control. To resolve this problem, this thesis develops a new post-compensation scheme, which utilizes the distortion of positive sequence carrier current to compensate the distortion of position-dependent negative sequence carrier current resulting from inverter nonlinearity.

The proposed compensation method is easy to implement on standard voltage source inverter without any additional hardware requirement or off-line commissioning process. Due to more accurate position information can be obtained with the proposed method, the fundamental current waveform can also be improved significantly with fewer harmonics. Compared with the pre-compensation methods, the proposed method does not directly compensate the disturbance voltage introduced by inverter nonlinearity effects using instantaneous carrier current. Consequently, this scheme is expected to be more robust to the carrier current measurement error. Experimental results demonstrate the effectiveness of proposed compensation method.

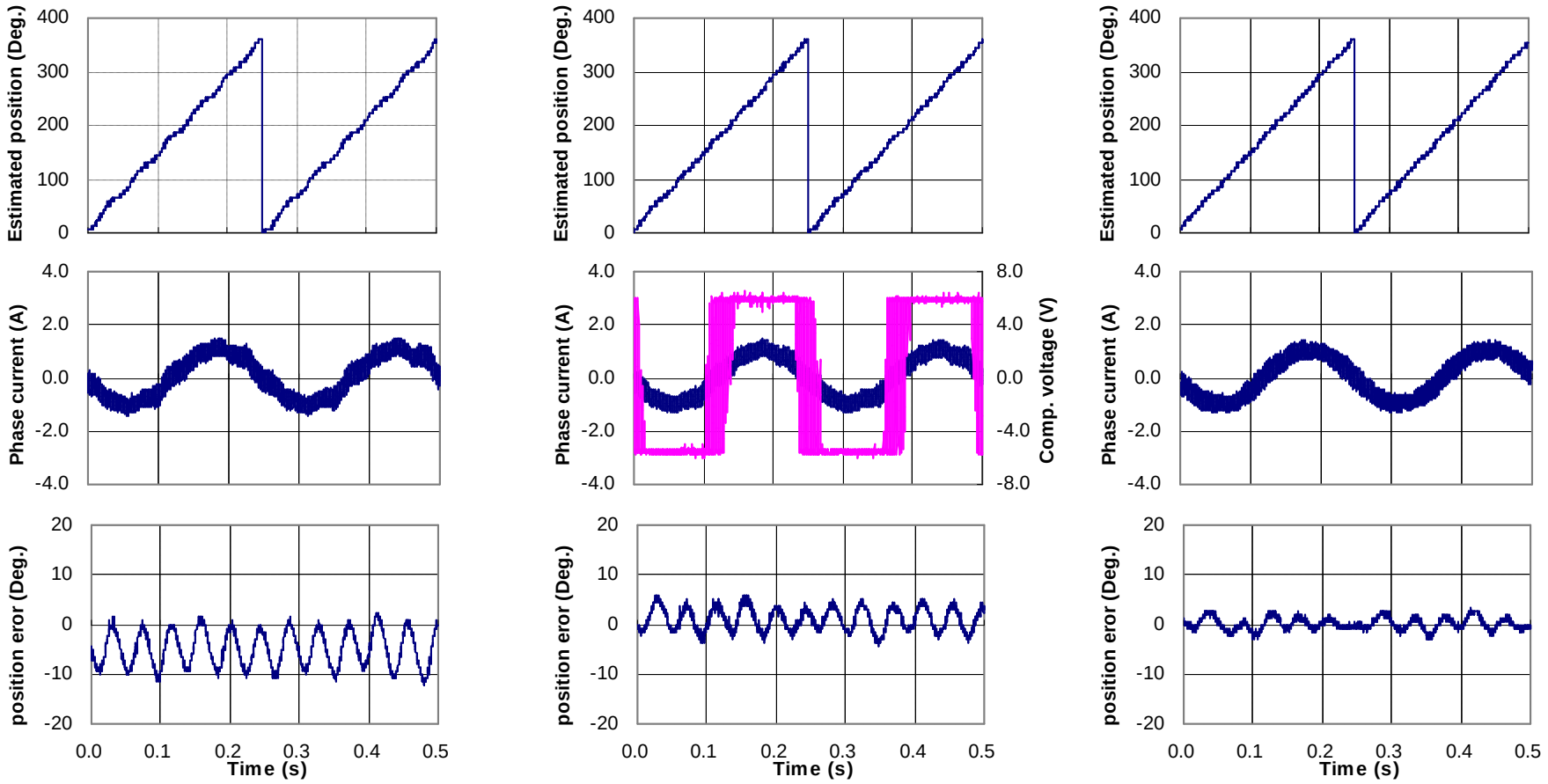

(a) Without compensation (b) Pre-compensation method (c) Proposed compensation method

Fig. 5.16 Comparison of sensorless operation performance (i_{df}=0A, i_{qf}=1A, f=4Hz, t_{dt}=4μs, V_{dc}=150V).

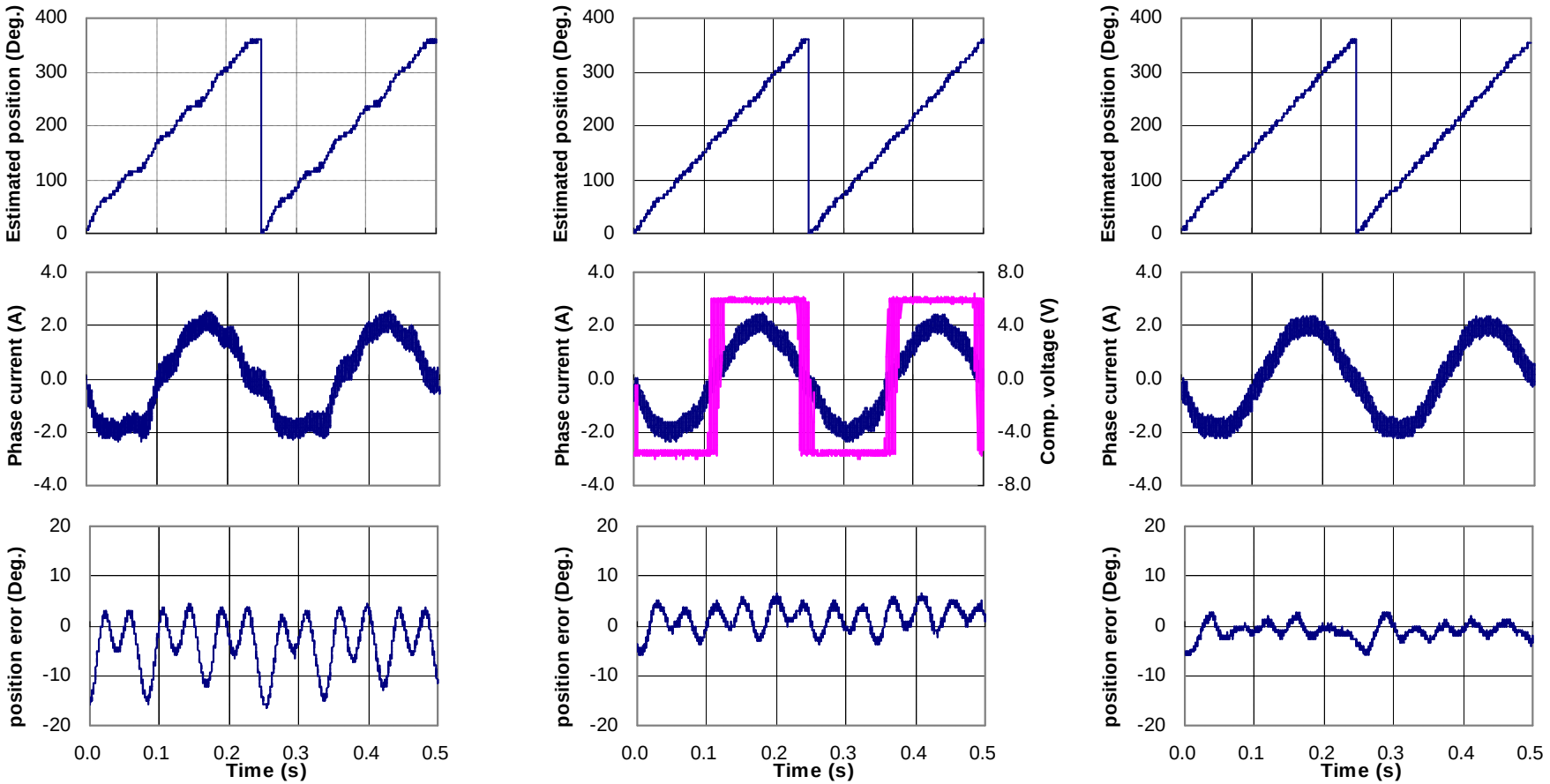

(a) Without compensation (b) Pre-compensation method (c) Proposed compensation method

Fig. 5.17 Comparison of sensorless operation performance (i_{df}=0A, i_{qf}=2A, f=4Hz, t_{dt}=4μs, V_{dc}=150V).

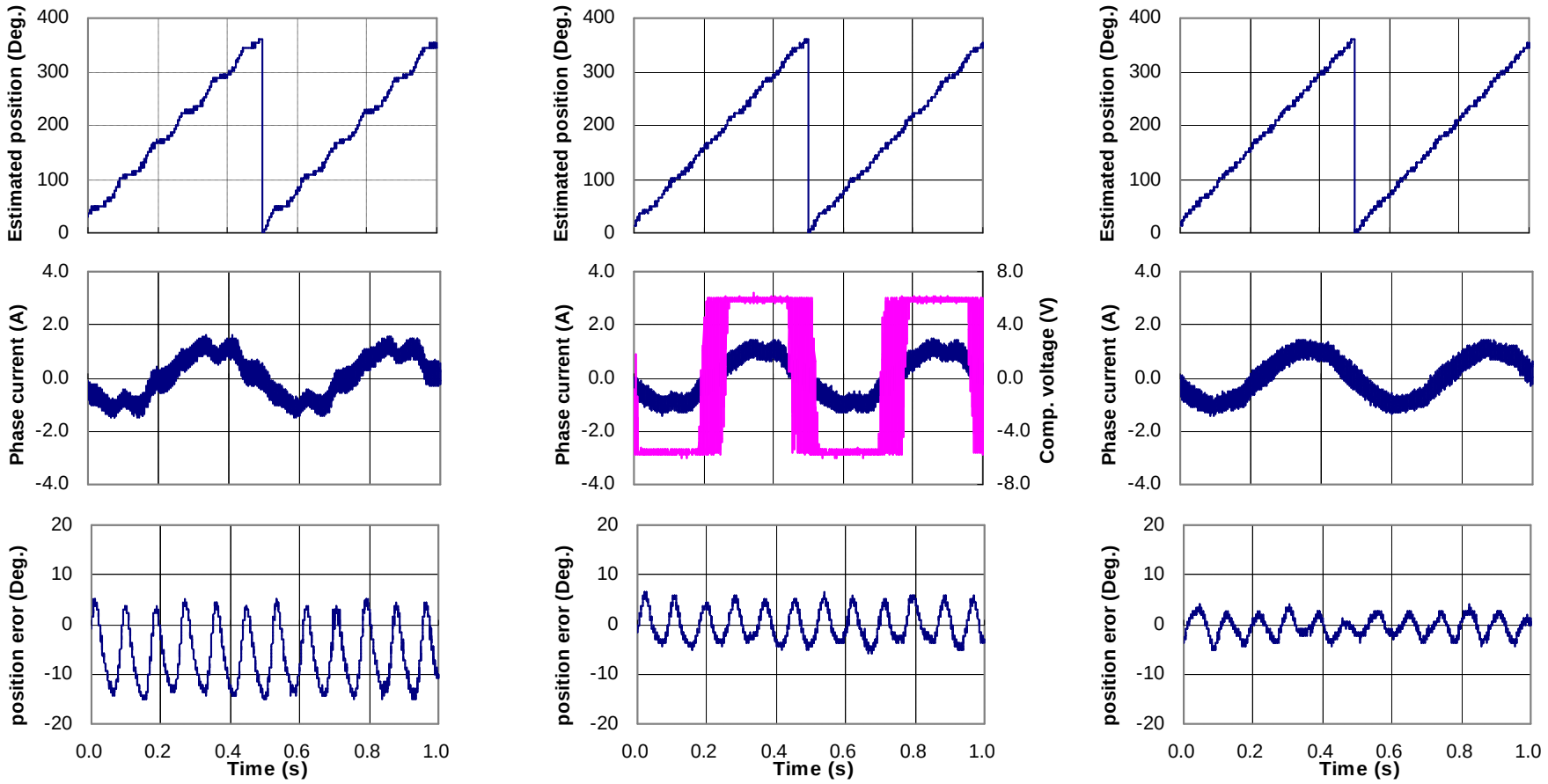

(a) Without compensation (b) Pre-compensation method (c) Proposed compensation method

Fig. 5.18 Comparison of sensorless operation performance (i_{df}=0A, i_{qf}=1A, f=2Hz, t_{dt}=4μs, V_{dc}=150V).

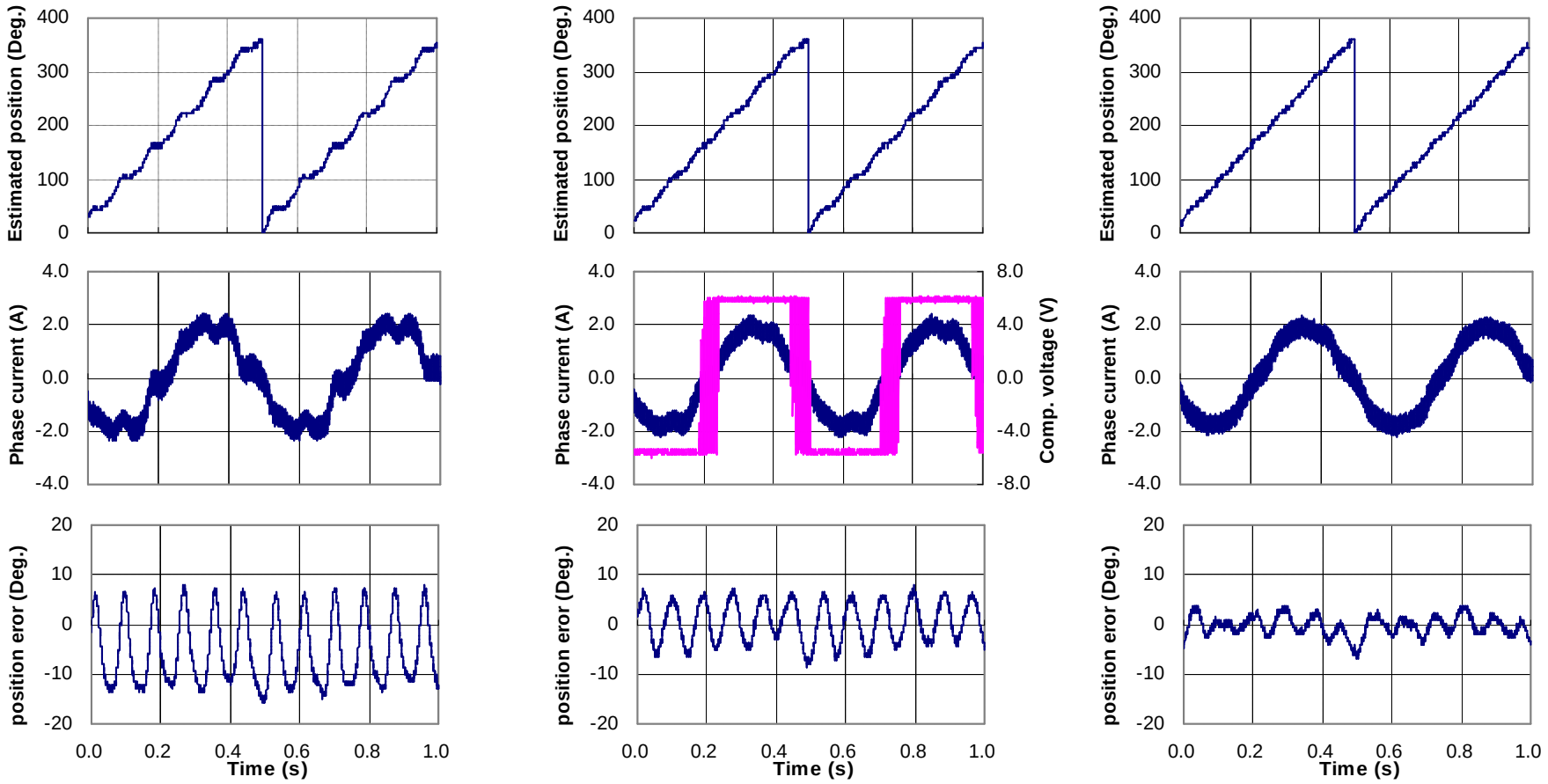

(a) Without compensation (b) Pre-compensation method (c) Proposed compensation method

Fig. 5.19 Comparison of sensorless operation performance (i_{df}=0A, i_{qf}=2A, f=2Hz, t_{dt}=4μs, V_{dc}=150V).

CHAPTER 6

IMPROVED SENSORLESS OPERATION BASED ON ONLINE OPTIMAL EFFICIENCY CONTROL

6.1 Introduction

No matter what kind of sensorless method is employed for PM BLAC machines, the accuracy of estimated position information is usually a critical concern in sensorless operation. However, nonlinear behavior in machines, such as saturation and cross-saturation effects, as well as inverter nonlinearities, exerts adverse influences on the position estimation. The resultant estimation error may cause the current response to deviate from the desired reference, thus deteriorating the sensorless performance, such as lower output torque capacity and lower system efficiency etc. Although great efforts have been made on the compensation for the nonlinearity effects to improve the accuracy of position estimation, it is usually difficult to completely compensate for the non-idealities.

From the efficiency point of view, optimal efficiency of machines, instead of accurate position estimation, can be considered as an objective for sensorless operation. In this way, it does not need compensation techniques to improve the position estimation. To achieve optimal efficiency, loss model based schemes are widely used in industrial applications [MOR94] [MAD04] [CAV05] [JEO06] [ADA09] [LEE09]. Although good dynamic performance can be guaranteed with this approach, the acquisition of loss model parameters is a big challenge for the practical implementation. Furthermore, accurate rotor position information is essential for these methods. Hence, the loss model based approches are often used in sensored operation, rather than sensorless operation. Alternatively, on-line searching is another promising method for optimal efficiency control [CHA96] [VAE99] [HOF04]. The optimal efficient working point can be adaptively tracked by adjusting a control variable (normally i_d^*) until the power input to the machine reaches the minimal value. Compared with loss model based methods,

although the searching control methods are only applied to steady state operation, they can tolerate rotor position error. Therefore, on-line searching control is a good candidate to improve sensorless operation by tracking optimal efficiency.

In order to enhance the energy efficiency performance of sensorless control, which is attractive for an efficiency-critical applications such as cooling fans and water pumps, this chapter utilizes a continuous searching concept in sensorless control to on-line track the optimal efficiency of PM BLAC machines at steady-state. Due to its adaptive searching behavior, the developed method is independent of the machine parameters and tolerant to estimated position error in sensorless control. By on-line calculation of the active power input, it can be easily implemented on the standard voltage source inverter without any hardware modification. With the proposed method, experimental results confirm that it is not necessary to put effort on the non-linearity compensation to improve the accuracy of rotor position estimation, while the optimal efficiency can be adaptively realized in steady-state sensorless operation, even though the estimated position information may be not accurate.

6.2 Loss Model for Conventional Optimal Efficiency Control

The developed sensorless method is combined with optimal efficiency tracking and does not require the loss model. However, in order to ease further discussions, it will be useful to analyze the loss model of PM BLAC machines. It is well documented that the losses of PM BLAC machines consist of copper loss, iron loss, stray loss and mechanical loss, which are reviewed as follows.

6.2.1 Copper loss

Copper loss is resistive loss due to stator resistance, as given by [LEE09],

$$P_{cu} = 1.5R_a(I_d^2 + I_q^2) \tag{6. 1}$$

where R_a is the phase resistance, I_d and I_q are the dq-axis currents in synchronous reference frame. Copper loss directly relies on the phase resistance and stator current level, and corresponding temperature rise in the windings, but it has no relationship with flux level and rotor speed.

6.2.2 Iron loss

Iron loss consists of hysteresis and eddy current losses, which can be approximated as [BER01],

$$P_{fe} = K_h w_r y_s^2 + K_e w_r^2 y_s^2 \quad (6.2)$$

where K_h and K_e are the coefficients of hysteresis loss and eddy current loss, respectively. ω_r is the electrical angular speed of rotor, and ψ_s is the stator flux.

Furthermore, the iron loss can be rewritten as,

$$P_{fe} = 1.5 w_r^2 y_s^2 / R_c \quad (6.3)$$

where R_c denotes the equivalent resistance of iron loss, which is a function of fundamental frequency [BER01],

$$R_c = \frac{1.5}{K_e + K_h / w_r} \quad (6.4)$$

From above equation, it shows that iron loss is associated with the stator flux level and rotor speed.

6.2.3 Stray loss

Stray loss results from the winding space harmonics and slot harmonics, and it can be evaluated as [LEE09],

$$P_{str} = 1.5 C_{str} w_r^2 (I_d^2 + I_q^2) \quad (6.5)$$

where C_{str} is the stray loss coefficient. Stray loss can be considered as the equivalent copper loss, which has a speed-dependent resistance.

6.2.4 Mechanical loss

Mechanical loss includes friction and windage losses, and it is only determined by the rotor speed and mechanical system. Unlike the foregoing losses, the mechanical loss, which is independent of machine current and flux level, is uncontrollable for given torque and speed condition [MAD04], hence it is not considered in the following discussion.

6.3 Optimal Efficiency Control

According to foregoing discussion, the summation of controllable losses (copper loss, iron loss and stray loss) gives,

$$P_{tl} = P_{cu} + P_{fe} + P_{str} = 1.5(R_a + C_{str} w_r^2) I_s^2 + w_r^2 y_s^2 / R_c \tag{6.6}$$

For given torque and speed condition, the mechanical loss is constant, hence the optimal efficiency control is to find the optimal *d*- and *q*-axis reference current set (i_d^*, i_q^*) in *dq* plane for the minimum value of P_{tl}. Meanwhile, the constraint of current and voltage limitation should be satisfied, as given by (6.7). In other words, the optimal efficiency control can be considered as a constrained optimization problem [LEE09].

$$\begin{cases} i_d^2 + i_q^2 \le I_{\max}^2 \\ V_d^2 + V_q^2 \le V_{\max}^2 \end{cases} \tag{6.7}$$

For salient permanent magnet BLAC machines, such as the interior permanent magnet BLAC machine used in this paper, MTPA control is often employed in constant torque operation to make use of the reluctance torque. In MTPA control, the stator current level is controlled to be minimal at given torque condition for minimum copper loss in the stator windings. From (6.6), therefore, it can be concluded that the MTPA control method has the ability of minimizing the summation of copper loss and stray loss.

In addition to copper loss and stray loss, iron loss is also an important part in the total losses of BLAC machines. The definition of iron loss reveals that it is proportional to the stator flux level for given speed.

Fig. 6.1 shows the constant torque operation trajectories in *dq* plane for the prototype machine ($L_d i_{max} < \psi_m$), in which, the MTPA curve is highlighted in blue, while the current limitation locus is indicated by red dotted circle. For given torque condition *T*, the intersection point between constant torque curve and MTPA trajectory (point a) is the minimum copper loss (MCL) working point, whereas the intersection point between constant torque curve and current limitation circle is the minimum iron loss (MIL) working point (point c). Obviously, the minimum total loss (MTL), i.e., optimal efficiency working point should stay between MCL and MIL along the constant torque curve of *T*. The position of MTL working point (point b) is determined by the loss

distribution between copper loss and iron loss. When copper loss is dominant in the total losses, the MTL point should nearly overlap with the MCL point. As the ratio of iron loss over total losses increase, the MTL point would move toward the MIL point.

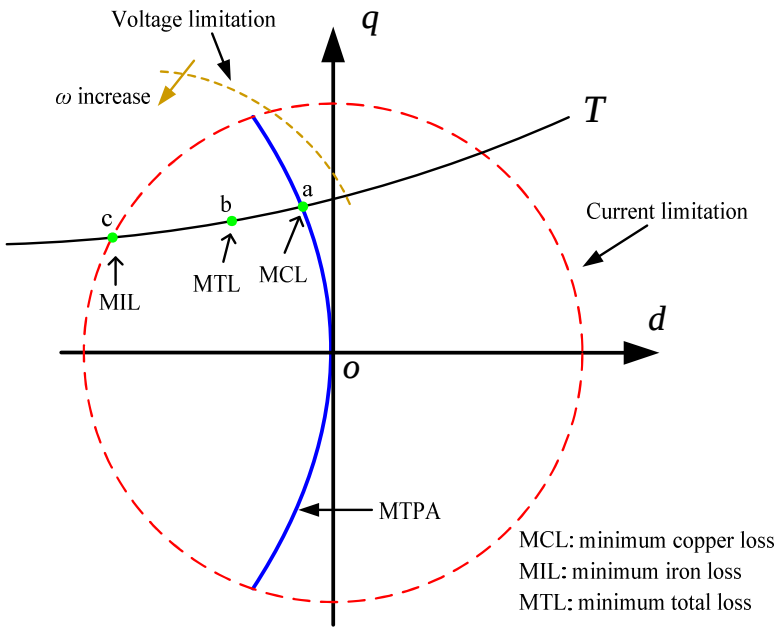

Fig. 6.1 Optimal efficiency working point in synchronous reference frame.

From the mathematical model, much effort has been made to resolve the constrained optimization problem, and achieve optimal efficiency tracking by using the calculated solution to construct a feed forward control [MOR94] [MAD04] [CAV05] [ADA09] [LEE09]. These methods track optimal efficiency without penalty on the dynamic performance in sensored operation. However, a variety of parameters of machine and loss model are required to find the optimal solution. Hence, the loss model-based methods are sensitive to parameters variation due to magnetic saturation and temperature change. Although an experimental method has been reported to measure the parameters of loss model [MAD04], it is time consuming to obtain the accurate loss model of PM BLAC machines. The other problem associated with loss model-based methods is the requirement of accurate rotor position information, which could not be guaranteed in conventional sensorless control. To overcome the foregoing limitation of loss model-based methods, the continuous searching concept is combined with sensorless control in this thesis to enhance the energy efficiency performance of sensorless control.

6.4 Instantaneous Active Power

For improved efficiency of sensorless control utilizing a continuous searching concept, the information of efficiency should be known for on-line tracking. However, the direct measurement of system efficiency requires additional transducers to measure the input and output power. At steady state (constant torque and speed), the minimum input active power operation can be interpreted as the optimal efficiency condition due to the constant output mechanical power. Meanwhile, the instantaneous power theory can be used to calculate the input active power to the inverter without any additional transducer for the DC link measurement.

The instantaneous power theory was first introduced in [AKA84]. For PM BLAC machines, the instantaneous active power input to the machine can be calculated in the stationary reference frame, as given by,

$$P_{ab} = 1.5(v_a i_a + v_b i_b) \tag{6. 8}$$

Normally, the measured current and reference command voltage are used to calculate the active power. When the high-frequency signal injection based sensorless method is used, it is preferable to make the power calculation in the estimated synchronous reference frame, where the fundamental component can be easily separated using a low pass filter,

$$P_{dq}^{e} = 1.5(v_d^e i_d^e + v_q^e i_q^e) = P_{ab} \tag{6. 9}$$

Although accurate rotor position is not available in sensorless control, the above equation shows that the calculated active power in the estimated synchronous reference frame is reliable, since it is independent of position estimation error.

Considering the loss components discussed in the foregoing section, the equivalent circuits of PM BLAC machines in steady-state are depicted in Fig. 6.2. According to the equivalent circuits, the active power input to the machine/drive system can be expressed as,

$$
\begin{aligned}
P_{dq} &= 1.5(v_d i_d + v_q i_q) \\
&= 1.5[(R_a + C_{str} w_r^2)(i_d^2 + i_q^2) + w_r (y_{\ d} i_q - y_{\ q} i_d)] \\
&= 1.5(R_a + C_{str} w_r^2) I_s^2 + 1.5 w_r (y_{\ d} i_{cq} - y_{\ q} i_{cd}) + 1.5 w_r (y_{\ d} i_{oq} - y_{\ q} i_{od}) \\
&= 1.5 R_a I_s^2 + 1.5 C_{str} w_r^2 I_s^2 + 1.5 w_r^2 y_{\ s}^{\ 2} / R_c + T w_m \\
&= P_{cu} + P_{str} + P_{fe} + P_o
\end{aligned}
\tag{6.10}
$$

For a given torque and speed condition, it shows that copper loss and stray loss are proportional to the stator current magnitude, while iron loss is proportional to the stator flux level. The calculated active power consists of total controllable losses and mechanical power output from the machine. From (6.10), it can be seen that the controllable losses (copper loss, stray loss and iron loss) can be controlled by adjusting the working point of machine. Consequently, it is possible to achieve the optimal efficiency control of PM BLAC machine by finding the minimal value of active power for improved sensorless operation.

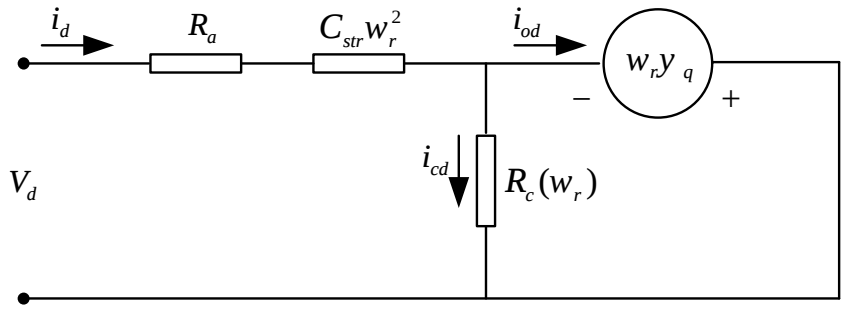

(a) d-axis circuit

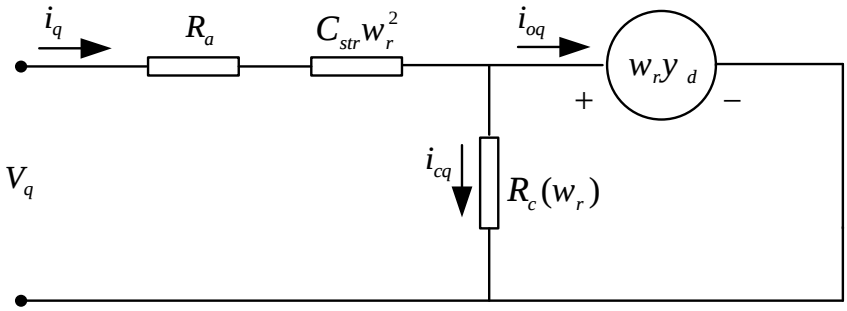

(b) q-axis circuit

Fig. 6.2 Equivalent circuits of PM BLAC machines [MOR94].

6.5 Improved Sensorless Operation Based on Optimal Efficiency Control

Due to the inherent limitation of loss model-based methods in sensorless operation, the on-line self searching algorithm is employed in this thesis to improve the sensorless performance in terms of optimal efficiency. In steady state, the machine output power and mechanical loss are constant due to constant torque and speed. However, the input power to the machine varies with the current reference set (i_d^*, i_q^*) in the *dq*-plane. Hence, the sensorless performance can be improved with optimal efficiency by on-line finding the optimal *d*- and *q*-axis current reference set (i_d^*, i_q^*) along the constant torque curve for achieving the minimal input power.

According to the adjustment type of control variable, the searching control can be categorized as continuous searching [CHA96] [VAE99] and numerical searching [HOF04]. The numerical searching is an iterative approach using quadratic polynomial interpolation. Fast convergence is claimed to be the major advantage of the numerical searching methods, however, the step-change of control variable (i_d^*) would give rise to torque variation for salient-pole BLAC machines and results in longer convergence time since waiting time is required to avoid the transient state after step change of i_d^*. Instead, the continuous searching scheme adjusts the control variable (i_d^*) continuously with pre-defined slope, hence the system would work more smoothly. In [CHA96] and [VAE99], with the help of additional DC link current sensor, the active power input to the drive is calculated from the DC bus voltage and current, and then the continuous searching method is used to track the optimal efficiency for sensored operation.

Based on the calculated active power from measured current and reference voltage command, this thesis utilizes the continuous searching concept in sensorless operation for on-line optimal efficiency control of PM BLAC machines. Therefore, much effort on the compensation of machine/drive non-ideal behavior for sensorless operation is not necessary. Since the power is calculated based on the instantaneous power theory, rather than from the DC link voltage and current, this method can be easily implemented on a standard voltage source inverter without any hardware modification. The block diagram

of on-line rotor position sensorless and optimal efficiency control is shown in Fig. 6.3 and detailed continuous searching algorithm is shown in Fig. 6.4 and Fig. 6.5.

The proposed improved sensorless method, which is independent of the machine parameters and tolerant to position error, could adaptively achieve minimum total loss, instead of minimum copper loss in MTPA control. However, the proposed approach is only valid at constant speed and constant torque condition. Therefore the steady state detection is necessary before activating the continuous searching process, Fig. 6.4.

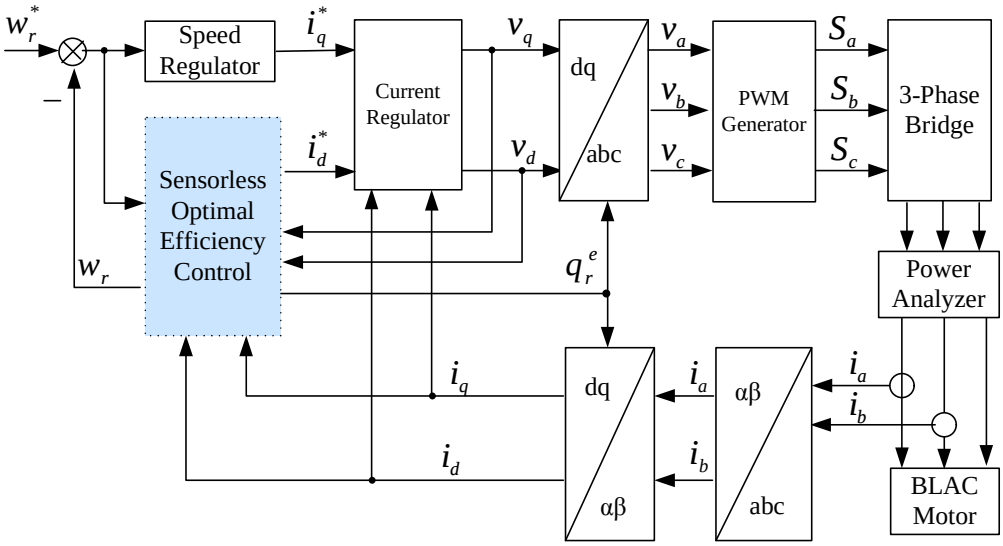

Fig. 6.3 Proposed improved sensorless control.

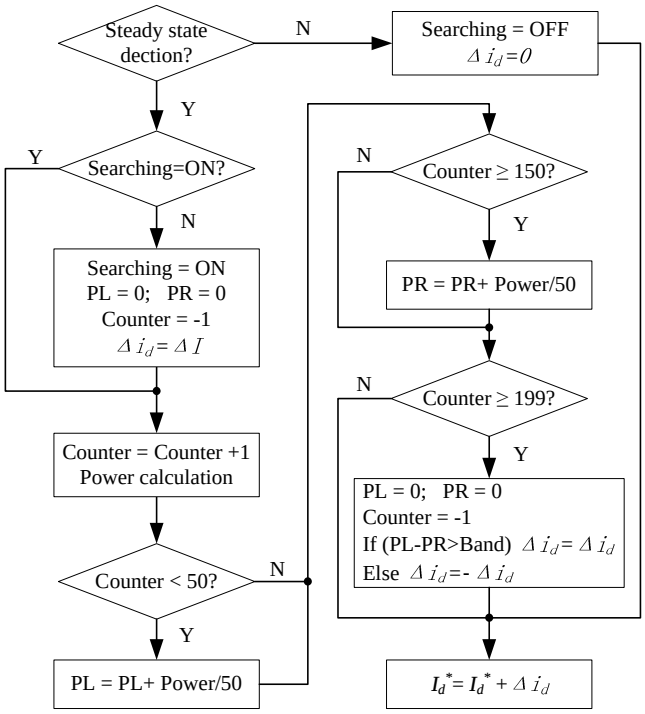

Fig. 6.4 Flow chart of searching algorithm for optimal efficiency control.

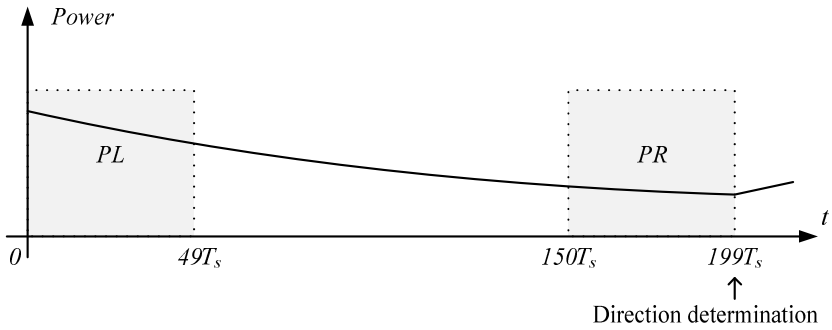

Fig. 6.5 Determination of searching direction.

6.6 Experimental Validation

6.6.1 Sensored operation

The prototype machine firstly operates under constant speed of 200RPM in sensored mode. Due to speed dependent load behavior of the DC machine load, the prototype machine actually operates at constant torque and speed condition. The loci of active power and estimated stator flux along the constant torque curve are shown in Fig. 6.6, in which the dotted red circle is the current limitation circle. Meanwhile, the measured active power input to the machine using power analyzer is indicated as a circle in Fig. 6.6(a). From Fig. 6.6(b), although the minimal iron loss occurs at i_d=*-3.7A* due to its proportional relationship with stator flux, the optimal efficiency point locates at nearly the same position as the MCL point, i.e., i_d=*-0,3A*. It reveals that the copper loss is dominant in this case. The minimal input active power is around 90W under this condition.

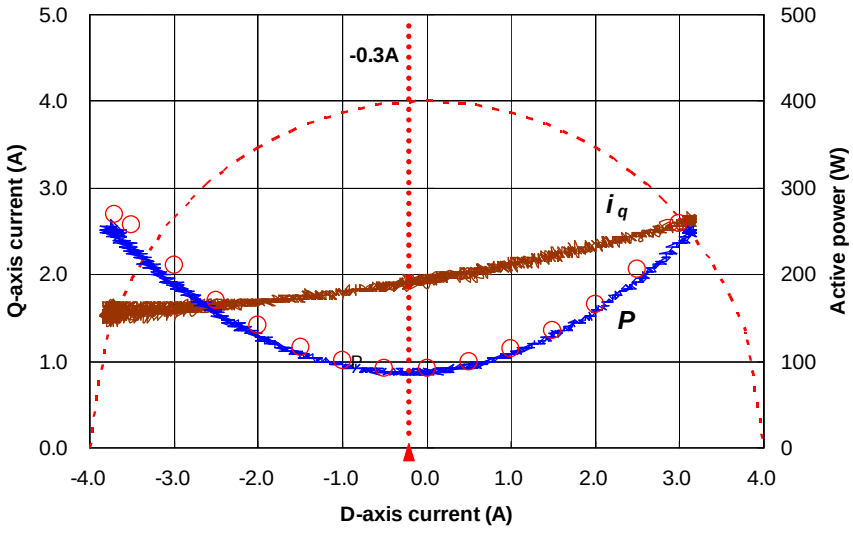

(a) Active power (*P*) input to the machine

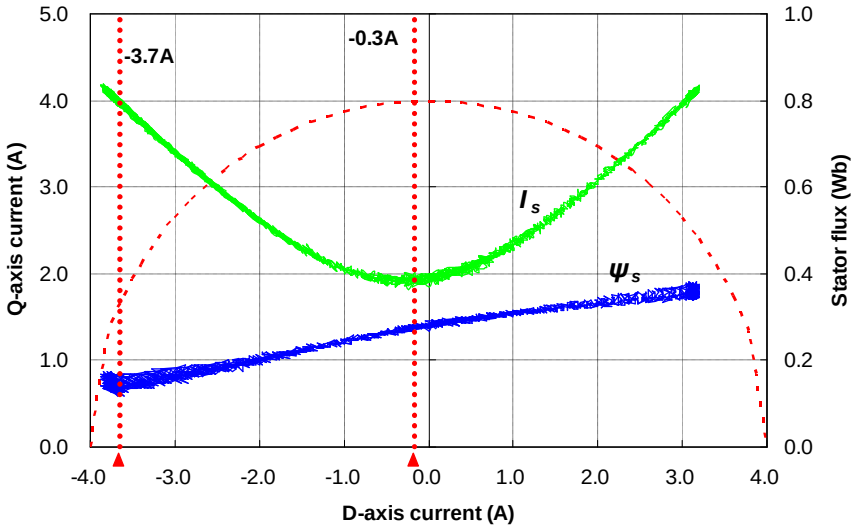

(b) Estimated stator flux (ψ_s)

Fig. 6.6 Loci of active power and stator flux along constant torque curve (200RPM).

Fig. 6.7 shows the optimal efficiency searching process under the same condition as before in sensored operation. When the searching algorithm is invoked at the time of 1.0s, the value of i_d^* smoothly changes from the initial value of *-3A*, meanwhile, the active power is gradually decreased from 190W. The searching direction of i_d^* is determined by the comparison between *PL* and *PR*. When the active power decreases to its minimal value (around 90W), the difference between *PL* and *PR* is less than pre-defined bandwidth, hence i_d^* changes its direction periodically, and the machine operates under optimal efficiency condition. Under the condition of optimal efficiency, the average value of i_d^* is around *-0.3A*, which is in a good agreement with experimental result shown in Fig. 6.6.

6.6.2 Sensorless operation

The performance of improved sensorless operation is validated also under the same torque and speed condition as sensored operation, as shown in Fig. 6.8 and Fig. 6.9. It is well known that the cross-saturation effect would introduce a load dependent position error on the position estimation in carrier signal injection based sensorless techniques. Although significant position error can be observed without cross-saturation compensation, Fig. 6.8 shows that the optimal efficiency still can be successfully tracked by the continuous searching algorithm. When the cross-saturation compensation method

is applied at the time of 33.0s, the estimated position error is decreased significantly, while the input active power is kept at the same level (around 90W). Under optimal efficiency conditions, although the current working points (i_d^*, i_q^*) with/without compensation are slightly different due to the position difference in Fig. 6.8, they are equal to each other in the accurate synchronous reference frame, viz. (*-0.3A, 1.8A*), as shown in Fig. 6.9, which is in a good agreement with the experimental results in sensored operation. Thus, it proves that with the proposed method, the sensorless performance could be improved with minimal input power without any compensation for nonlinear effects. Although only the carrier signal injection based sensorless technique is used for experimental validation, the proposed method also applies to model based sensorless technique due to its adaptive searching property.

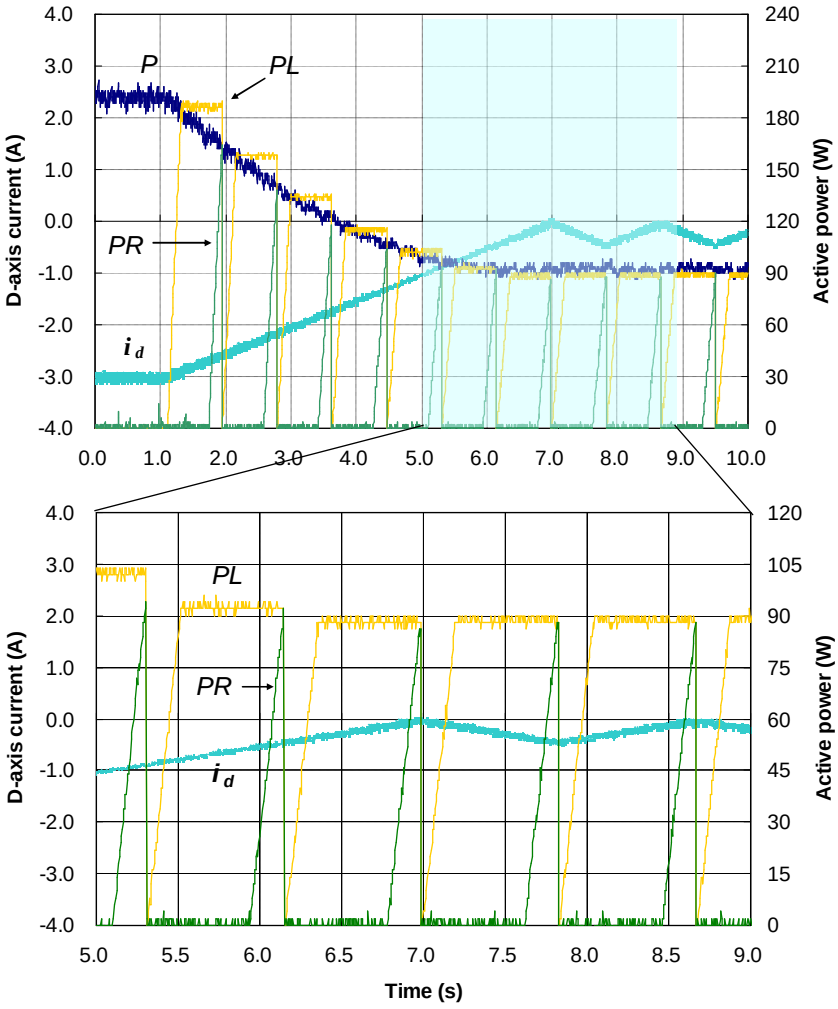

Fig. 6.7 Optimal efficiency tracking in sensored operation.

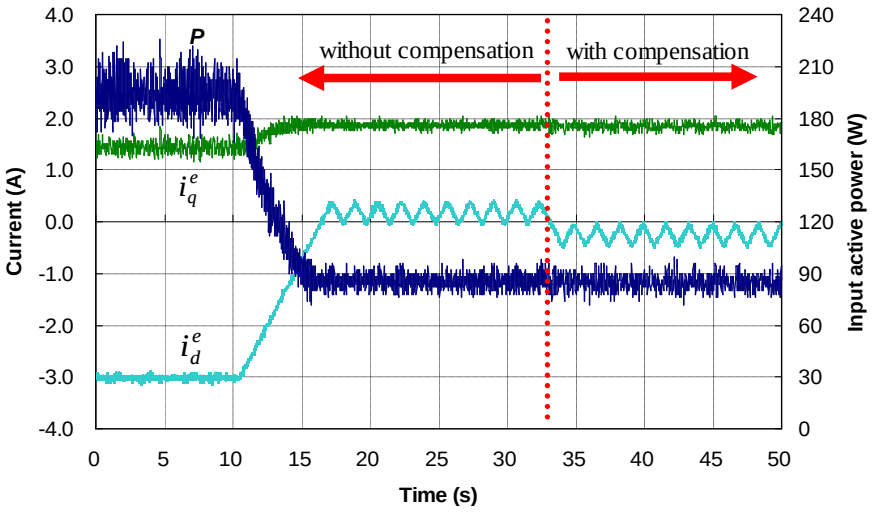

(a) Active power and *dq*-axis current in the estimated synchronous reference frame

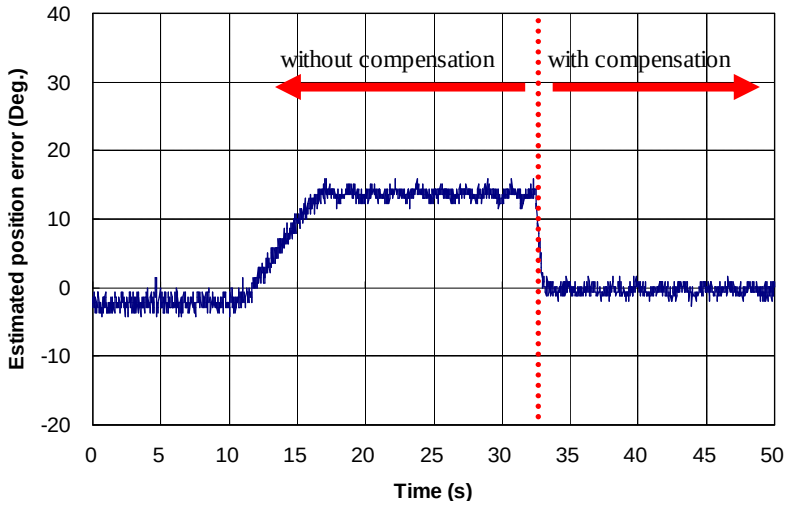

(b) Estimated position error

Fig. 6.8 Optimal efficiency tracking in sensorless operation with/without cross-saturation compensation.

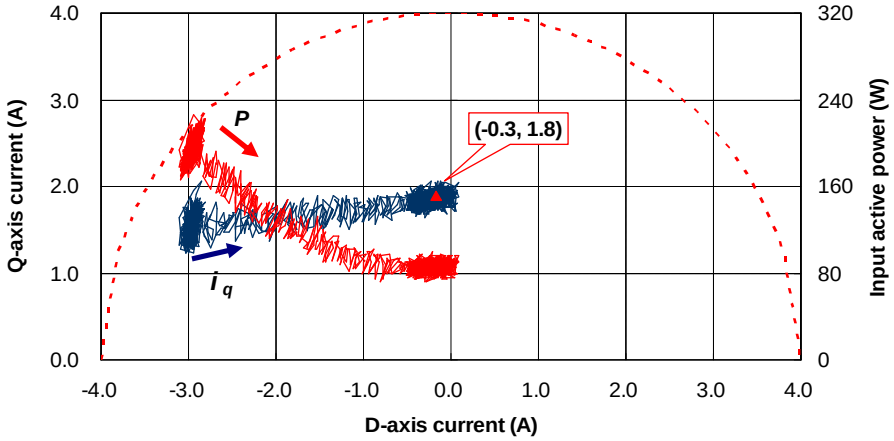

Fig. 6.9 Current and input active power loci in the accurate synchronous reference frame during the searching process.

6.7 Conclusions

In conventional sensorless control of PM BLAC machines, although much effort has been made on the compensation of non-linearity effects of machines and drives to improve the accuracy of position estimation, it is usually difficult to completely compensate for the non-ideal behaviors. From the efficiency point of view, in order to enhance the energy efficiency performance under sensorless control, which is attractive for the efficiency-critical applications such as cooling fans and water pumps, this thesis employs the continuous searching concept in sensorless control to on-line track the optimal efficiency in steady-state. In this way, the sensorless operation performance can be improved by the optimal efficiency tracking without any compensation of nonlinear effects. Although it is only applicable to steady state operation, the proposed method does not require any knowledge about the machine/drive, and can be easily implemented using a standard voltage source inverter without any hardware modification. Experimental results confirm that the energy efficiency with sensorless operation can be significantly improved with the proposed method, even though the estimated position information may be not accurate.

CHAPTER 7

GENERAL CONCLUSIONS AND DISCUSSIONS

This thesis is focused on the carrier signal injection based sensorless control of Permanent Magnet (PM) Brushless AC (BLAC) machines.

In order to investigate the machine saliency information, an experimental method is presented to measure machine saliency circle, which visually reveals the machine saliency information without any requirement of machine parameters. Based on the measurement results, Sensorless Safety Operation Area (SSOA) is introduced to investigate the effectiveness of sensorless operation for practical applications. Considering the absence of magnetic polarity information in the estimated rotor position from machine saliency property, a robust magnetic polarity detection scheme is proposed based on the magnetic saturation effect.

Inverter nonlinearity effects are studied from the respects of theoretical analysis and experimental measurement. Utilizing the distortion of positive sequence carrier current due to inverter nonlinearity effects, a novel on-line compensation scheme is developed for rotating carrier signal injection based sensorless methods. From the efficiency point of view, on-line continuous searching algorithm is employed in sensorless operation to improve the machine efficiency without any requirements of compensation methods on nonlinear effects.

7.1 Preliminary Knowledge for Saliency Based Sensorless Implementation

Machine saliency, resulting from machine geometrical anisotropy and magnetic saturation, is essential for saliency based sensorless control techniques. Although saliency based sensorless methods claim to be independent of machine parameters, the knowledge about machine saliency information could provide insight into the basic principle. FEA provides an option to predict machine saliency information, however, practical applications prefer to acquire the machine saliency information from experimental measurement. Based on other researcher's work, this thesis presents a simplified experimental procedure to measure the machine saliency information.

Although saliency based sensorless control methods estimate the position information from machine saliency behavior, they fulfill this task indirectly from measured carrier current response by injection of carrier voltage signal. Therefore, appropriate selection of injected carrier voltage signal (V_c/ω_c) is also important for sensorless development.

Considering the bandwidth of position observer and carrier signal demodulation, the higher the injected carrier voltage frequency, the better. However, it is upper limited by the PWM frequency. Normally, the carrier frequency is chosen as *1/50 ~ 1/10* PWM frequency. Regarding to amplitude of injected carrier voltage, it is a compromise between the utilization of DC bus voltage and SNR of the carrier current response. With an increase of the carrier voltage amplitude, the improved signal SNR is advantageous for sensorless estimation, while the available DC bus voltage for fundamental excitation would decrease. The carrier signal injection based sensorless methods are often employed for standstill and low speed operation, in which case, the required voltage for fundamental excitation is small, thus the amplitude selection for injected carrier voltage is unlikely a problem.

Accounting for the carrier current measurement error due to quantization error in the AD conversion, the Sensorless Safety Operation Area (SSOA) is defined in this thesis to investigate the feasibility of sensorless operation, which provides a practical criterion to determine the injected carrier voltage according to the machine saliency information, so that the machine can perform sensorless operation with guaranteed performance in steady state.

In summary, the preliminary work for the implementation of carrier signal injection based sensorless control can be illustrated in Fig. 7.1.

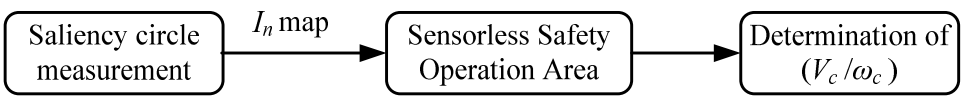

Fig. 7.1 Preliminary work for sensorless control implementation.

7.2 Non-ideal Attributions of Machines and Drives

For carrier signal injection based sensorless methods, the estimated position information from carrier current response is actually the machine saliency position. In the ideal case, the machine saliency position can be considered to be equal to the real rotor position. However, practical machines and drives exhibit non-ideal attributions, such as cross-saturation effects, multiple saliency effects, inverter nonlinearity effects, and so on. The non-ideal attributes introduce additional carrier current disturbance, eventually resulting in the deterioration of position estimation accuracy, degradation of dynamic performance and even stability problems. Consequently, it is desirable to develop associated compensation methods to suppress these negative effects on sensorless position estimation.

The cross-saturation effect generates the same spatial harmonic order as the primary saliency (overlapped spectrum), hence the introduced position estimation error is a critical concern. Fortunately, the load depend position estimation error is constant for given load condition, and it can be easily compensated utilizing the measured information by off-line commissioning process.

Unlike the cross-saturation effect, the multiple saliency effect generates harmonic components in the vicinity of primary saliency component (adjacent spectrum), which eventually introduces position dependent estimation error under sensorless control. Considering the load- and position-dependent property of multiple saliency effect, it is suggested to suppress the multiple saliency effect through appropriate machine design. Fortunately, the multiple saliency effect for the prototype machine is negligible.

Investigation and compensation of inverter nonlinearity effect is one of the major contributions of this thesis. As a disturbance voltage generator, inverter nonlinearity effects introduce unwanted carrier voltage distortion, thus resulting in significant position estimation error in carrier signal injection based sensorless control. To solve this problem, a novel on-line compensation scheme is developed for rotating carrier signal injection based sensorless methods in this thesis by utilizing the distortion of the positive sequence carrier current due to inverter nonlinearity effects. However, the proposed approach does

not apply to the commonly used *d*-axis pulsating carrier signal injection based sensorless technique.

Great efforts are required to compensate the nonlinear effects to improve the accuracy of estimated position information. Alternatively, optimal efficiency of machines, instead of accurate position estimation, is considered as the sensorless operation objective in this thesis. In this way, the sensorless operation performance can be improved by on-line optimal efficiency tracking without any compensation on nonlinear effects. Although it is only applicable to steady state operation (constant torque and constant speed), the proposed method does not require any knowledge about the motor and drive, and can be easily implemented using a standard voltage source inverter without any hardware modification.

7.3 Magnetic Polarity Identification

Since the machine primary saliency undergoes two cycles in single electrical period, the estimated position information from machine saliency behavior suffers from an angle ambiguity of π. Hence magnetic polarity identification is required for initial rotor position estimation. Based on magnetic saturation effect, this thesis identifies the magnetic polarity utilizing the monotonic variation of *d*-axis carrier current amplitude ($|i_{dh}|$) against *d*-axis fundamental current excitation (i_{df}). Although the convergence process of proposed method is not as quick as secondary harmonics based detection methods, it has higher SNR and reliable detection performance. Furthermore, the proposed method can be easily integrated with conventional carrier signal injection based sensorless estimation algorithm with slight increase of computation effort.

7.4 Future Work

7.4.1 Hybrid position estimation for wide speed range sensorless operation

Due to extra losses, addition current harmonics, torque ripple and noise resulting from carrier voltage injection, carrier signal injection based sensorless methods are only accepted for standstill and low speed operation, where fundamental model based sensorless methods fail to effectively estimate the rotor position information. PWM

excitation based sensorless methods could achieve wider speed range operation, however, the dedicated sensor for current derivative measurement is an obstacle to their practical applications. As a result, it is desirable to combine the injection and model based methods together. The combination should undertake smooth transition between different methods without penalty of dynamic performance.

7.4.2 Sensorless oriented machine design

This thesis is focused on saliency based sensorless control for PM BLAC machines. On the other hand, sensorless oriented machine design provides an attractive research field.

The nonlinear machine saliency property, involving magnetic saturation, cross-saturation, and multiple saliency effects, give rise to load dependent saliency level, shape and position, which is the major source of sensorless estimation trouble. Taking high quality saliency property as the machine design objective, it is expected that high performance sensorless position estimation could be achieved without complex compensation methods for nonlinear effects.

REFERENCES

[ACA06] P. P. Acarnley and J. F. Watson, "Review of position-sensorless operation of brushless permanent-magnet machines," *IEEE Trans. Industrial Electronics*, vol. 53, no. 2, pp. 352-362, 2006.

[ADA09] J.B. Adawey, S. Yamamoto, T. Kano, and T. Ara, "Maximum efficiency drives of interior permanent magnet synchronous motor considering iron loss and cross-magnetic saturation," *Proc. 2009 Int. Conf. on Electrical Machines and Systems*, 15-18 Nov. 2009, pp. 1-6.

[AIH99] T. Aihara, A. Toba, T. Yanase, A. Mashimo, and K. Endo, "Sensorless torque control of salient-pole synchronous motor at zero-speed operation," *IEEE Trans. Power Electronics*, vol. 14, no. 1, pp.202-208, January 1999.

[AKA84] H. Akagi, Y. Kanazawa, and A. Nabae, "Instantaneous reactive power compensators comprising switching devices without energy storage components," *IEEE Trans. Industry Applications*, vol. IA-20, no. 3, pp. 625–630, 1984.

[AND08] G. D. Andreescu, C. I. Pitic, F. Blaabjerg, and I. Boldea, "Combined flux observer with signal injection enhancement for wide speed range sensorless direct torque control of IPMSM drives," *IEEE Trans. Energy Conversion*, vol. 23, no. 2, pp. 393-402, 2008.

[ARI06] A. Arias, C.A. Silva, G.M Asher, J.C. Clare, and P.W. Wheeler, "Use of a matrix converter to enhance the sensorless control of a surface-mount permanent-magnet AC motor at zero and low frequency," *IEEE Trans. Industry Applications*, vol. 53, no. 2, pp. 440–449, 2006.

[BAE03] B.H. Bae, S.K. Sul, J.H. Kwon, and J.S. Byeon, "Implementation of sensorless vector control for super-high-speed PMSM of turbo-compressor," *IEEE Trans. Industry Applications*, vol. 39, no. 3, pp. 811-818, 2003.

[BER01] F.F. Bernal, A.G. Cerrada, and R. Faure, "Determination of parameters in interior permanent-magnet synchronous motors with iron losses without torque measurement," *IEEE Trans. Industry Applications*, vol. 37, no. 5, pp. 1265–1272, 2001

[BIA07a] N. Bianchi and S. Bolognami, "Influence of rotor geometry of an IPM motor on sensorless control feasibility," *IEEE Trans. Industry Applications*, vol. 43, no. 1, pp. 87–96, 2007.

[BIA07b] N. Bianchi, S. Bolognami, J.H. Jang, and S.K. Sul, “Comparison of PM motor structures and sensorless control techniques for zero-speed rotor position detection,” *IEEE Trans. Power Electronics*, vol. 22, no. 6, pp. 2466–2475, Nov. 2007.

[BLA98] V. Blasko, V. Kaura, and W. Niewiadomski, “Sampling of discontinuous voltage and current signals in electrical drives: a system approach,” *IEEE Trans. Industry Applications*, vol. 34, no. 5, pp. 1123-1130, 1998.

[BOL99] S. Bolognani, R. Oboe, and M. Zigliotto, “Sensorless full-digital PMSM drive with EKF estimation of speed and rotor position,” *IEEE Trans. Industrial Electronics*, vol. 46, no. 1, pp. 184-191, 1999.

[BOL09] I. Boldea, M. C. Paicu, G. D. Andreescu, and F. Blaabjerg, “Active flux DTFC-SVM sensorless control of IPMSM,” *IEEE Trans. Energy Conversion*, vol. 24, no. 2, pp. 314-322, 2009.

[BOL11] S. Bolognani, S. Calligaro, R. Petrella, and M. Sterpellone, “Sensorless control for IPMSM using PWM excitation: Analytical developments and implementation issues,” *Symposium on Sensorless Control for Electrical Drives*, 2011, pp. 64-73.

[BOU05] M. Boussak, “Implementation and experimental investigation of sensorless speed control with initial rotor position estimation for interior permanent magnet synchronous motor drive,” *IEEE Trans. Power Electronics*, vol. 20, no. 6, pp.1413–1422, 2005.

[BRI01] F. Briz, M.W. Degner, A. Diez, and R.D. Lorenz, “Measuring, modeling, and decoupling of saturation-injuced saliencies in carrier-signal injection-based sensorless AC drives,” *IEEE Transactions on Industry Applications*, vol.37, no.5, pp.1356-1364, 2001.

[BRI04] F. Briz, M. W. Degner, P. Garcia, and R. D. Lorenz, “Comparison of saliency-based sensorless control techniques for AC machines,” *IEEE Transactions on Industry Applications*, vol. 40, no. 4, pp. 1107-1115, 2004.

[CAV05] C. Cavallaro, A.O.D. Tommaso, R. Miceli, A. Raciti, G.R. Galluzzo, and M. Trapanese, “Efficiency enhancement of permanent-magnet synchronous motor drives by on-line loss minimization approaches,” *IEEE Trans. Industrial Electronics*, vol. 52, no. 4, pp. 1153–1160, 2005

[CHA96] C.C. Chan, and K.T. Chau, “An advanced permanent magnet motor drive system for battery-powered electric vehicles,” *IEEE Trans. Vehicular Technology*, vol. 45, no. 1, pp. 180–188, 1996

[CHE99] Y. S. Chen, “Motor topologies and control strategies for permanent magnet brushless AC drives”, PhD Thesis, University of Sheffield, 1999.

[CHE00] Z. Chen, M. Tomita, S. Ichikawa, S. Doki, and S. Okuma, “Sensorless control of interior permanent magnet synchronous motor by estimation of an extended electromotive force,” *Industry Applications Conference*, 2000, pp. 1814-1819 vol.3.

[CHE03] C. Zhiqian, M. Tomita, S. Doki, and S. Okuma, “An extended electromotive force model for sensorless control of interior permanent-magnet synchronous motors,” *IEEE Trans. Industrial Electronics*, vol. 50, no. 2, pp. 288-295, 2003.

[CHE10] J.L. Chen, T.H. Liu, and C.L. Chen, “Design and implementation of a novel high-performance sensorless control system for interior permanent magnet synchronous motors,” *IET Electric Power Applications*, vol. 4, no. 4, pp. 226-240, 2010.

[CHI09] C. Song, Z. Zheng, and X. Longya, “Sliding-mode sensorless control of direct-drive PM synchronous motors for washing machine applications,” *IEEE Trans. on Industry Applications*, vol. 45, no. 2, pp. 582-590, 2009.

[CHO95] J.W. Choi, and S.K. Sul, “A new compensation strategy reducing voltage current distortion in PWM VSI systems operating with low output voltages,” *IEEE Trans. Industry Applications*, vol. 31, no. 5, pp. 1001–1008, 1995.

[CHO96] J.W. Choi, and S.K. Sul, “Inverter output voltage synthesis using novel dead time compensation,” *IEEE Trans. Power Electronics*, vol. 11, no. 2, pp. 221–227, 1996.

[CHO07] C.H. Choi and J.K. Seouk, “Compensation of zero-current clamping effects for sensorless drives based on high-frequency signal injection,” *IEEE Trans. Industry Applications*, vol. 43, no. 5, pp. 1258–1265, 2007.

[CHO08] C.H. Choi and J.K. Seouk, “Pulsating signal injection-based axis switching sensorless control of surface-mounted permanent-magnet motors for minimal zero-current clamping effects,” *IEEE Trans. Industry Applications*, vol. 44, no. 6, pp. 1741–1748, 2008.

[COR98] M. J. Corley and R. D. Lorenz, “Rotor position and velocity estimation for a salient-pole permanent magnet synchronous machine at standstill and high speed,” *IEEE Trans. Industry Applications*, vol.34, no. 4, pp. 784–789, 1998.

[CUP10] F. Cupertino, P. Giangrande, L. Salvatore, and G. Pellegrino, “Model based design of a sensorless control scheme for permanent magnet motors

using signal injection," *IEEE Energy Conversion Congress and Exposition* (ECCE), 2010, pp. 3139-3146.

[DEG98] M.W Degner and R.D Lorenz, "Using multiple saliencies for the estimation of flux, position, and velocity in AC machines," *IEEE Trans. Industry Applications*, vol. 34, no. 5, pp. 1097–1104, 1998.

[FOO10] G. Foo and M. F. Rahman, "Sensorless direct torque and flux-controlled IPM synchronous motor drive at very low speed without signal Injection," *IEEE Trans. Industrial Electronics*, vol. 57, no. 1, pp. 395-403, 2010.

[FUE11] E. Fuentes and R. Kennel, "Sensorless-predictive torque control of the PMSM using a Reduced Order Extended Kalman Filter," *Symposium on Sensorless Control for Electrical Drives*, 2011, pp. 123-128.

[GAD10] S. M. Gadoue, D. Giaouris, and J. W. Finch, "MRAS sensorless vector control of an induction motor using new sliding-mode and fuzzy-logic adaptation mechanisms," *IEEE Trans. Energy Conversion*, vol. 25, no. 2, pp. 394-402, 2010.

[GAO07] Q. Gao, G. M. Asher, M. Sumner, and P. Makys, "Position estimation of AC machines over a wide frequency range based on space vector PWM excitation," *IEEE Trans. Industry Applications*, vol. 43, no. 4, pp. 1001-1011, 2007.

[GAR07a] P. Garcia, F. Briz, M.W. Degner, and D.D. Reigosa, "Accuracy, bandwidth, and stability limits of carrier-signal-injection-based sensorless control methods," *IEEE Trans. Industry Applications*, vol. 43, no. 4, pp. 990–1000, 2007.

[GAR07b] P. Garcia, F. Briz, D. Raca, and R.D. Lorenz, "Saliency-tracking-base Sensorless control of AC machines using structured neural networks," *IEEE Trans. Industry Applications*, vol. 43, no. 1, pp. 77–86, 2007.

[GUE05] J.M. Guerrero, M. Leetmaa, F. Briz, A. Zamarron, and R.D. Lorenz, "Inverter nonlinearity effects in high-frequency signal-injection-based sensorless control methods," *IEEE Trans. Industry Applications*, vol. 41, no. 2, pp. 618–626, 2005.

[GUG06] P. Guglielmi, M. Pastorelli, and A. Vagati, "Cross-saturation effects in IPM motors and related impact on sensorless control," *IEEE Trans. Industry Applications*, vol. 42, no 6, pp. 1516–1522, 2006.

[HA03] J.I. Ha, K. Ide, T. Sawa, and S.K. Sul, "Sensorless rotor position estimation of an interior permanent-magnet motor from initial states," *IEEE Trans. Industry Applications*, vol. 39, no. 3, pp. 761–767, 2003.

[HAM10] W. Hammel and R. M. Kennel, “Position sensorless control of PMSM by synchronous injection and demodulation of alternating carrier voltage,” *Symposium on Sensorless Control for Electrical Drives*, 2010, pp. 56-63.

[HAQ03] M.E. Haque, L. Zhong, M.F. Rahman, “A sensorless initial rotor position estimation scheme for a direct torque controlled interior permanent magnet synchronous motor drive,” *IEEE Trans. Power Electronics*, vol. 18, no. 6, pp.1376–1383, 2003.

[HAR00] L. Harnefors and H.P. Nee, “A general algorithm for speed and position estimation of AC motors,” *IEEE Trans. Industrial Electronics*, vol. 47, no. 1, pp. 77-83, 2000.

[HAR05] M.C. Harke, D. Raca, and R.D. Lorenz, “Implementation issues for fast initial position and magnet polarity identification of PM synchronous machines with near zero saliency,” *Conference on Power Electronics and Applications*, 2005, pp. 1–10.

[HAV98] A. M. Hava, R. J. Kerkman, and T. A. Lipo, “Carrier-based PWM-VSI overmodulation strategies: analysis, comparison, and design,” *IEEE Trans. Power Electronics*, vol. 13, no. 4, pp. 674-689, 1998.

[HOF04] H.F. Hofmann, S.R. Sanders, and A.E. Antably, “Stator-flux-oriented vector control of synchronous reluctance machines with maximized efficiency,” *IEEE Trans. Industrial Electronics*, vol. 51, no. 5, pp. 1066–1072, 2004.

[HOL94] J. Holtz, “Pulsewidth modulation for electronic power conversion,” *Proceedings of the IEEE*, vol. 82, no. 8, pp. 1194-1214, 1994.

[HOL98] J. Holtz, “Sensorless position control of induction motors – an emerging technology,” *IEEE Trans. Industrial Electronics*, Vol. 45, No. 6, pp. 840–852, 1998.

[HOL05] J. Holtz and J. Juliet, “Sensorless acquisition of the rotor position angle of induction motors with arbitrary stator windings,” *IEEE Trans. Industry Applications*, vol. 41, no. 6, pp. 1675-1682, 2005.

[HOL08] J. Holtz, “Acquisition of position error and magnet polarity for sensorless control of PM synchronous machines,” *IEEE Trans. Industry Applications*, vol. 44, no. 4, pp. 1172–1180, 2008.

[HOQ94] M.A. Hoque, and M.A. Rahman, “Speed and position sensorless permanent magnet synchronous motor drives,” *Proc. of Electrical and Computer engineering*, vol. 2, 1994, pp.689–692.

[HU98] J. Hu and B. Wu, "New integration algorithms for estimating motor flux over a wide speed range," *IEEE Trans. Power Electronics*, vol. 13, no. 5, pp. 969-977, 1998.

[HUA09] Y. Hua, "Sensorless control of surface mounted permanent magnet machine using fundamental PWM excitaiton", PhD Thesis, Department of Electrical and Electronic Engineering, University of Nottingham, 2009.

[HUA11] Y. Hua, M. Sumner, G. Asher, Q. Gao, and K. Saleh, "Improved sensorless control of a permanent magnet machine using fundamental pulse width modulation excitation," *IET Electric Power Applications*, vol. 5, no. 4, pp. 359-370, 2011.

[HWA10] S.H. Hwang and J.M. Kim, "Dead time compensation method for voltage-fed PWM inverter," *IEEE Trans. Energy Conversion*, vol. 25, no. 1, pp. 1-10, 2010.

[INO09] Y. Inoue, K. Yamada, S. Morimoto, and M. Sanada, "Effectiveness of voltage error compensation and parameter identification for model-based sensorless control of IPMSM," *IEEE Trans. Industry Applications*, vol. 45, no. 1, pp. 213–221, 2009.

[JAN95] P.L. Jansen and R.D. Lorenz, "Transducerless position and velocity estimation in induction and salient AC machines," *IEEE Trans. Industry Applications*, vol. 31, no. 2, pp. 240–247, 1995.

[JAN03a] J.H. Jang, S.K. Sul, J.I. Ha, K. Ide, and M. Sawamura, "Sensorless drive of surface-mounted permanent-magnet motor by high-frequency signal injection based on magnetic saliency," *IEEE Trans. Industry Applications*, vol. 39, no. 4, pp. 1031–1039, 2003.

[JAN03b] J.H. Jang, S.K. Sul, Y.C. Son, "Current measurement issues in sensorless control algorithm using high frequency signal injection method," *Conf. Rec. IEEE-IAS Annual Meeting*, 2003, pp. 1134–1141.

[JAN04] J.H. Jang, J.I. Ha, M. Ohto, K. Ide, and S.K. Sul,, "Analysis of permanent-magnet machine for sensorless control based on high-frequency signal injection," *IEEE Trans. Industry Applications*, vol. 40, pp. 1595-1604, Nov./Dec., 2004.

[JEO05] Y.S. Jeong, R.D. Lorenz, T.M. Jahns, and S.K. Sul, "Initial rotor position estimation of an interior permanent-magnet synchronous machine using carrier-frequency injection methods," *IEEE Trans. Industry Applications*, vol. 41, no. 1, pp. 38–45, 2005.

[JEO06] Y.S. Jeong, S.K. Sul, S. Hiti, and K.M. Rahman, "Online minimum-copper-loss control of an interior permanent-magnet

synchronous machine for automotive apllications," *IEEE Transactions on Industry Applications*, vol. 42, no. 5, pp. 1222–1229, 2006

[KAN10] J. Kang, "Sensorless control of permanent magnet motors," *Control Engineering*, vol. 57, no. 4, pp. 1-4, 2010.

[KEN10] R. Kennel, J. Rodriguez, J. Espinoza, and M. Trincado, "High performance speed control methods for electrical machines: An assessment," *in IEEE International Conference on Industrial Technology (ICIT)* 2010, pp. 1793-1799.

[KIM03] H. S, Kim, M. Hyung-Tae, and Y. Myung-Joong, "On-line dead-time compensation method using disturbance observer," *IEEE Trans. Power Electron.*, vol. 18, no. 6, pp. 1336-1345, 2003.

[KIM04a] H. Kim, K.K. Huh, and R.D. Lorenz, "A novel method for initial rotor position estimation for IPM synchronous machine drives," *IEEE Trans. Industry Applications*, vol. 40, no. 5, pp. 1369–1378, 2004.

[KIM04b] H. Kim and R.D. Lorenz, "Carrier signal injection based sensorless control methods for IPM synchronous machine drives," *IEEE Industry Applications Conference (IAS2004)*, 2004, pp. 977-984 vol.2.

[KOC09] H. W. De Kock, M. J. Kamper, and R. M. Kennel, "Anisotropy comparison of reluctance and PM synchronous machines for position sensorless control using HF carrier injection," *IEEE Trans. Power Electron.*, vol. 24, no. 8, pp. 1905-1913, 2009.

[LAN10] P. Landsmann, D. Paulus, P. Stolze, and R. Kennel, "Saliency based encoderless predictive torque control without signal injection," *in Power Electronics Conference (IPEC)* 2010, pp. 3029-3034.

[LEE09] J. Lee, k. Nam, S. Choi, and S. Kwon, "Loss-minimizing control of PMSM with the use of polynomial approximations," *IEEE Trans. Power Electronics*, vol. 24, no. 4, pp. 1071–1082, 2009

[LEI11] R. Leidhold, "Position sensorless control of PM synchronous motors based on zero-sequence carrier injection," *IEEE Trans. Industrial Electronics*, vol. 58, no. 12, pp. 5371-5379, 2011.

[LI07] Y. Li, Z. Q. Zhu, D. Howe, and C. M. Bingham, "Improved rotor position estimation in extended back-EMF based sensorless PM brushless AC drives with magnetic saliency accounting for cross-coupling magnetic saturation," *IEEE International Electric Machines and Drives Conference*, IEMDC 2007, May 3-5, 2007, Antalya, Turkey, pp.214-219.

[LI09a] Y. Li, “Sensorless control of permanent magnet brushless AC motors accouting for cross-coupling magnetic saturation”, PhD Thesis, Department of Electronic and Electrical Engineering, University of Sheffield, 2009.

[LI09b] Y. Li, Z.Q. Zhu, D. Howe, C.M. Bingham, and D. Stone, “Improved rotor position estimation by signal injection in brushless AC motors, accounting for cross-coupling magnetic saturation,” *IEEE Trans. Industry Applications*, vol.45, no.5, pp.1843-1849, 2009.

[LIN02] M. Linke, R. Kennel, and J. Holtz, “Sensorless position control of permanent magnet synchronous machines without limitation at zero speed,” *Industrial Electronics Society 28th Annual Conference (IECON 02)*, vol.1, pp. 674-679, 2002.

[LIN03] M. Linke, R. Kennel, and J. Holtz, “Sensorless speed and position control of synchronous machines using alternating carrier injection,” *Electric Machines and Drives Conference*, vol.2, pp. 1211-1217, 2003.

[LIU11] J. Liu, T. A. Nondahl, P. B. Schmidt, S. Royak, and M. Harbaugh, “Rotor position estimation for synchronous machines based on equivalent EMF,” *IEEE Trans. Industrial Applications*, vol. 47, no. 3, pp. 1310-1318, 2011.

[MAD95] A. Madani, J. P. Barbot, F. Colamartino, and C. Marchand, “Reduction of torque pulsations by inductance harmonics identification of a permanent-magnet synchronous machine,” *Proceedings of the 4th IEEE Conference on Control Applications*, 1995, pp. 787-792.

[MAD04] C. Mademlis, I. Kioskeridis, and N. Margaris, “Optimal efficiency control strategy for interior permanent-magnet synchronous motor drives,” *IEEE Trans. Energy Conversion*, vol. 19, no. 4, pp. 715–723, 2004

[MAT96] N. Matsui, “Sensorless PM brushless DC motor drives,” *IEEE Trans. Industrial Electronics*, vol. 43, no. 2, pp. 300-308, 1996.

[MON01] R. Monajemy, and R. Krishnan, “Control and dynamics of constant-power-loss-based operation of permanent-magnet synchronous motor drive system,” *IEEE Trans. Industrial Electronics*, vol. 48, no. 4, pp. 839–844, 2001.

[MOR94] S. Morimoto, Y.Tong, Y. Takeda, and T. Hirasa, “Loss minimization control of permanent magnet synchronous motor drives,” *IEEE Trans. Industrial Electronics*, vol. 41, no. 5, pp. 511–516, 1994.

[MOR96] J. C. Moreira, “Indirect sensing for rotor flux position of permanent magnet AC motors operating over a wide speed range,” *IEEE Trans. on Industry Applications*, vol. 32, no. 6, pp. 1394-1401, 1996.

[MOR02] S. Morimoto, K. Kawamoto, M. Sanada, and Y. Takeda, “Sensorless control strategy for salient-pole PMSM based on extended EMF in rotating reference frame,” *IEEE Trans. on Industry Applications*, vol. 38, no. 4, pp. 1054-1061, 2002.

[MOR07] R. Morales-Caporal and M. Pacas, “A predictive torque control for the synchronous reluctance machine taking into account the magnetic cross saturation,” *IEEE Trans. Industrial Electronics*, vol. 54, no. 2, pp. 1161-1167, 2007.

[NAI92] M. Naidu, and B.K. Bose, “Rotor position estimation scheme of a permanent magnet synchronous machine for high performance variable speed drive,” *Proc. of Industry Applications Society Annual Meeting*, vol. 1, 1992, pp. 48–53.

[NAK00] S. Nakashima, Y. Inagaki, and I. Miki, “Sensorless initial rotor position estimation of surface permanent-magnet synchronous motor,” *IEEE Trans. Industry Applications*, vol. 36, no. 6, pp. 1598–1603, 2000.

[NOG98] T. Noguchi, K. Yamada, S. Kondo, and I. Takahashi, “Initial rotor position estimation method of sensorless PM synchronous motor with no sensitivity to armature resistance,” *IEEE Trans. Industrial Electronics*, vol. 45, pp. 118–125, 1998.

[OGA98] S. Ogasawara, and H. Akagi, “Implementation and position control performance of a position-sensorless IPM motor drive system based on magnetic saliency,” *IEEE Trans. Industry Applications*, vol. 34, no. 4, pp. 806–812, July/August 1998.

[PAU11] D. Paulus, P. Landsmann, and R. Kennel, “Sensorless field-oriented control for permanent magnet synchronous machines with an arbitrary injection scheme and direct angle calculation,” *Symposium on Sensorless Control for Electrical Drives (SLED2011)*, pp. 41-46, 2011.

[PII08] A. Piippo, M. Hinkkanen, and J. Luomi, “Analysis of an Adaptive Observer for Sensorless Control of Interior Permanent Magnet Synchronous Motors,” *IEEE Trans. Industrial Electronics*, vol. 55, no. 2, pp. 570-576, 2008.

[QIA95] J. Qian, A. Khan, and I. batarseh, “Turn-off switching loss model and analysis of IGBT under different switching operation modes,” *Proc. of IEEE Industrial Electronics, Control, and Instrumentation* (IECON95), 1995, pp.240-245.

[RAC08a] D. Raca, P. Garcia, D. Reigosa, F. Briz, and R.D. Lorenz, “A comparative analysis of pulsating vs. rotating vector carrier signal injection-based

sensorless control," *Proc. of IEEE Applied Power Electronics Conference and Exposition* (APEC2008), Feb. 2008, pp. 879–885.

[RAC08b] D. Raca, M.C. Harke, and R.D. Lorenz, "Robust magnet polarity estimation for initialization of PM synchronous machines with near-zero saliency," *IEEE Trans. Industry Applications*, vol. 44, no. 4, pp. 1199-1209, 2008.

[RAC10] D. Raca, P. Garcia, D.D. Reigosa, F. Briz, and R.D. Lorenz, "Carrier-signal selection for sensorless control of PM synchronous machines at zero and very low speeds," *IEEE Trans. Industry Applications*, vol. 46, no. 1, pp. 167-178, 2010.

[RAU07] R. Raute, C. Caruana, J. Cilia, C. S. Staines, and M. Sumner, "A zero speed operation sensorless PMSM drive without additional test signal injection," *European Conference on Power Electronics and Applications*, pp. 1-10, 2007.

[RAU10] R. Raute, C. Caruana, C. S. Staines, J. Cilia, M. Sumner, and G. M. Asher, "Sensorless control of induction machines at low and zero speed by using PWM harmonics for rotor-bar slotting detection," *IEEE Trans. Industry Applications*, vol. 46, no. 5, pp. 1989-1998, 2010.

[REI08] D. Reigosa, P. Garcia, D. Raca, F. Briz, and R.D. Lorenz, "Measurement and adaptive decoupling of cross-saturation effects and secondary saliencies in sensorless-controlled IPM synchronous machines," *IEEE Trans. Industry Applications*, vol. 44, no. 6, pp. 1758–1767, 2008.

[ROB04] E. Robeischl and M. Schroedl, "Optimized INFORM measurement sequence for sensorless PM synchronous motor drives with respect to minimum current distortion," *IEEE Trans. Industry Applications*, vol. 40, no. 2, pp. 591–598, 2004.

[ROD11] J. Rodriguez, R. Kennel, J. Espinoza, M. Trincado, C. Silva, and C. Rojas, "High performance control strategies for electrical drives: an experimental assessment," *IEEE Trans. Industrial Electronics*, in press.

[SAL11] D. E. Salt, D. Drury, D. Holliday, A. Griffo, P. Sangha, and A. Dinu, "Compensation of inverter nonlinear distortion effects for signal-injection-based sensorless control," *IEEE Trans. Industry Applications*, vol. 47, no. 5, pp. 2084-2092, 2011.

[SCH96] M. Schroedl, "Sensorless control of AC machines at low speed and Standstill based on the 'INFORM' method," *Conf. Rec. IEEE-IAS Annual Meeting*, 1996, pp. 270–277.

[SEO06] J.K. Seok, J.K. Lee, and D.C. Lee, “Sensorless speed control of nonsalient permanent-magnet synchronous motor using rotor-position-tracking PI controller,” *IEEE Trans. Industrial Electronics*, vol. 53, no. 2, pp. 399-405, 2006.

[SHA98] S.M.A. Sharkh, and V. Barinberg, “A new approach to rotor position estimation for a PM brushless motor drive,” *9th Mediterranean Electrotechnical Conference* (MELECON 1998), pp. 1199-1203.

[SHE04] J.X. Shen, Z.Q. Zhu, and D. Howe, “Sensorless flux-weakening control of permanent-magnet brushless machines using third harmonic back EMF,” *IEEE Trans. Industry Applications*, vol. 40, no. 6, pp. 1629–1636, 2004.

[SIL06] C. Silva, G. M. Asher, and M. Sumner, “Hybrid rotor position observer for wide speed-range sensorless PM motor drives including zero speed,” *IEEE Trans. Industrial Electronics*, vol. 53, no. 2, pp. 373-378, 2006.

[STA06] C. S. Staines, C. Caruana, G. M. Asher, and M. Sumner, “Sensorless control of induction Machines at zero and low frequency using zero sequence currents,” *IEEE Trans. Industrial Electronics*, vol. 53, no. 1, pp. 195-206, 2006.

[STU03] B. Stumberger, G. Stumberger, D. Dolinar, A. Hamler, and M. Trlep, “Envaluation of saturation and cross-magnetization effects in interior permanent-magnet synchronous motor,” *IEEE Trans. Industry Applications*, vol. 39, no.5, pp. 1264–1271, Sep./Oct. 2003.

[SUK91] T. Sukegawa, K. Kamiyama, K. Mizuno, T. Matsui, and T. Okuyama, “Fully digital, vector-controlled PWM VSI-fed AC drives with an inverter dead-time compensation strategy,” *IEEE Trans. Power Electronics*, vol. 27, no. 3, pp. 552–559, 1991.

[TES00] N. Teske, G.M. Asher, M. Sumner, and K.J. Bradley, “Suppression of saturation saliency effects for the sensorless position control of induction motor drives under loaded conditions,” *IEEE Trans. Industrial Electronics*, vol. 47, pp. 1142-150, Oct. 2000.

[TES03] N. Teske, G.M. Asher, M. Sumner, K.J. Bradley, “Analysis and suppression of high-frequency inverter modulation in sensorless position-controlled induction machine drives,” *IEEE Trans. Industry Applications*, vol. 39, no. 1, pp. 10–18, 2003.

[VAE99] S. Vaez, and M.A. Rahman, “An online loss minimization controller for interior permanent magnet motor drives,” *IEEE Transactions on Energy Conversion*, vol. 14, no. 4, pp. 1435–1439, 1999.

[WAL06] O. Wallmark, “Control of permanent magnet synchronous machines in automotive applications,” PhD Thesis, Department of Energy and Environment, Charmers University of Technology, 2006.

[WAN10] H. Wang, M. Yang, L. Niu, and D. Xu, “Current-loop bandwidth expansion strategy for permanent magnet synchronous motor drives,” *the 5th IEEE Conference on Industrial Electronics and Applications (ICIEA2010)*, pp. 1340-1345, 2010.

[WIE09] K. Wiedmann, F. Wallrapp, and A. Mertens, “Analysis of inverter nonlinearity effects on sensorless control for permanent magnet machine drives based on high-frequency signal injection,” *13th European Conference on Power Electronics and Applications (EPE’09)*, 2009, pp. 1–10.

[YAN11] S.C. Yang, T. Suzuki, R.D. Lorenz, and T.M. Jahns, “Surface permanent magnet synchronous machine design for saliency tracking self-sensing position estimation at zero and low speeds,” *IEEE Trans. Industry Applications*, vol. 47, no. 5, pp. 2103-2116, 2011.

[YOO09a] A. Yoo and S.K. Sul, “Design of flux observer robust to interior permanent-magnet synchronous motor flux variation,” *IEEE Trans. Industry Applications*, vol. 45, no. 5, pp. 1670-1677, 2009.

[YOO09b] Y.D. Yoon, S.K. Sul, S. Morimoto and K. Ide, “High bandwidth sensorless algorithm for AC machines based on square-wave type voltage injection,” *Conf. Rec. IEEE ECCE*, 20-24 Sep. 2009, pp.2123-2130.

[YUA09] X. Yuan, I. Brown, R.D. Lorenz, and A. Qui, “Observed-based inverter disturbance compensation,” *Conf. Rec. IEEE ECCE*, 20-24 Sep. 2009, pp. 2520–2527.

[ZHU07] Z.Q. Zhu, Y. Li, D. Howe, and C.M. Bingham, “Compensation for rotor position estimation error due to cross-coupling magnetic saturation in signal injection based sensorless control of PM brushless AC motors,” *Proc. Int. Electric Machines and Drives Conference*, 3-5 May 2007, Antalya, Turkey, pp. 208–213.

APPENDICES

Appendix 1 Specification of prototype machine

Table A1.1 Specification and leading design parameters, dimensions of motors [CHE99]

	115 series motors
Rated voltage (peak)	158 V
Rated current (peak)	4.0 A
Rated power	0.6 kW
Rated speed	1000 rpm
Rated torque	4.0 Nm
Pole number	6
Slot number	18
Number of series connected conductors/pole/phase	152 turns
Wire diameter (2 wires stranded)	0.36 mm + 0.51 mm
Winding coil pitch	3 slots
Winding resistance per phase	6.0 Ω (20°C)
Skew	1 slot-pitch
Stator outer radius	53.30 mm
Stator inner radius	31.00 mm
Rotor outer radius	30.25 mm
Core length (stator)	32.00 mm
Core length (rotor)	30.00 mm
Shaft diameter	25.00 mm
Air gap length	0.75 mm
Magnet	UGIMAX 35HC1 (B_r=1.17* T, μ_r=1.07)
Stator Steel	Transil 310-50
Rotor Steel	Transil 310-50 (Surface-mounted PM motor) Transil 300-35 (Inset and interior PM motors)

* The remanence of UGIMAX35HC1 is about 1.23T at 20°C according to the data-sheet. However, the measured value is only 1.17T.

Appendix 2 Transformation of phase vector with harmonics

Assuming a phase vector $f(\delta)$ with harmonics can be expressed in stationary reference frame, as given by,

$$\begin{bmatrix} f_a(d) \\ f_b(d) \\ f_c(d) \end{bmatrix} = \begin{bmatrix} k_1 \cos d \\ k_1 \cos(d - \frac{2p}{3}) \\ k_1 \cos(d + \frac{2p}{3}) \end{bmatrix} + \begin{bmatrix} k_3 \cos 3d \\ k_3 \cos 3(d - \frac{2p}{3}) \\ k_3 \cos 3(d + \frac{2p}{3}) \end{bmatrix} + \begin{bmatrix} k_5 \cos 5d \\ k_5 \cos 5(d - \frac{2p}{3}) \\ k_5 \cos 5(d + \frac{2p}{3}) \end{bmatrix} + \begin{bmatrix} k_7 \cos 7d \\ k_7 \cos 7(d - \frac{2p}{3}) \\ k_7 \cos 7(d + \frac{2p}{3}) \end{bmatrix} + \mathbf{L} \quad \text{(A2. 1)}$$

It can be re-written as,

$$\begin{bmatrix} f_a(d) \\ f_b(d) \\ f_c(d) \end{bmatrix} = \begin{bmatrix} k_1 \cos d \\ k_1 \cos(d - \frac{2p}{3}) \\ k_1 \cos(d + \frac{2p}{3}) \end{bmatrix} + \begin{bmatrix} k_3 \cos 3d \\ k_3 \cos 3d \\ k_3 \cos 3d \end{bmatrix} + \begin{bmatrix} k_5 \cos 5d \\ k_5 \cos(5d + \frac{2p}{3}) \\ k_5 \cos(5d - \frac{2p}{3}) \end{bmatrix} + \begin{bmatrix} k_7 \cos 7d \\ k_7 \cos(7d - \frac{2p}{3}) \\ k_7 \cos(7d + \frac{2p}{3}) \end{bmatrix} + \mathbf{L} \quad \text{(A2. 2)}$$

With coordinate transformation, the phase vector $f(\delta)$ can be transformed to synchronous reference frame,

$$\begin{bmatrix} f_d \\ f_q \end{bmatrix} = \frac{2}{3} \begin{bmatrix} \cos q_r & \cos(q_r - 2p/3) & \cos(q_r + 2p/3) \\ -\sin q_r & -\sin(q_r - 2p/3) & -\sin(q_r - 2p/3) \end{bmatrix} \begin{bmatrix} f_a \\ f_b \\ f_c \end{bmatrix} \quad \text{(A2. 3)}$$

Performing this tedious calculation yields,

$$\begin{bmatrix} f_d \\ f_q \end{bmatrix} = \begin{bmatrix} k_1 \cos(q_r - d) \\ -k_1 \sin(q_r - d) \end{bmatrix} + \begin{bmatrix} k_5 \cos(q_r + 5d) \\ -k_5 \sin(q_r + 5d) \end{bmatrix} + \begin{bmatrix} k_7 \cos(q_r - 7d) \\ -k_7 \sin(q_r - 7d) \end{bmatrix} + \mathbf{L} \quad \text{(A2. 4)}$$

If the fundamental component of $f(\delta)$ is synchronous to the d-axis, i.e., $\delta=\theta_r+\varphi$, where φ is a constant phase shift. Then the above equation can be simplified to be,

$$\begin{bmatrix} f_d \\ f_q \end{bmatrix} = \begin{bmatrix} k_1 \cos j \\ k_1 \sin j \end{bmatrix} + \begin{bmatrix} (k_5 + k_7) \cos 6d \\ (-k_5 + k_7) \sin 6d \end{bmatrix} \cos j + \begin{bmatrix} (k_5 - k_7) \sin 6d \\ (k_5 + k_7) \cos 6d \end{bmatrix} \sin j + \mathbf{L} \quad \text{(A2. 5)}$$

It shows that only 6th, 12th… harmonics exist in the synchronous reference frame.

Appendix 3 Finite element calculated flux linkage of the prototype machine

Table A3.1 *d*-axis flux linkage at various *dq*-axis currents [LI09a].

ψ_d	i_d=4A	i_d=3A	i_d=2A	i_d=1A	i_d=0A	i_d=-1A	i_d=-2A	i_d=-3A	i_d=-4A
i_q=4A	0.2925	0.2776	0.2609	0.2415	0.2186	0.1923	0.1632	0.1321	0.1000
i_q=3A	0.2994	0.2849	0.2684	0.2487	0.2248	0.197	0.1662	0.1336	0.1002
i_q=2A	0.3049	0.2908	0.2747	0.2549	0.2301	0.2005	0.1678	0.1338	0.0995
i_q=1A	0.3085	0.2948	0.2792	0.2596	0.2342	0.2026	0.1681	0.1332	0.0984
i_q=0A	0.3097	0.2962	0.2809	0.2614	0.236	0.2032	0.1679	0.1327	0.0978
i_q=-1A	0.3085	0.2948	0.2792	0.2596	0.2342	0.2026	0.1681	0.1332	0.0984
i_q=-2A	0.3049	0.2908	0.2747	0.2549	0.2301	0.2005	0.1678	0.1338	0.0995
i_q=-3A	0.2994	0.2849	0.2684	0.2487	0.2248	0.197	0.1662	0.1336	0.1002
i_q=-4A	0.2925	0.2776	0.2609	0.2415	0.2186	0.1923	0.1632	0.1321	0.1000

Table A3.2 *q*-axis flux linkage at various *dq*-axis currents [LI09a].

Ψ_q	i_d=4A	i_d=3A	i_d=2A	i_d=1A	i_d=0A	i_d=-1A	i_d=-2A	i_d=-3A	i_d=-4A
i_q=4A	0.1348	0.1422	0.1502	0.158	0.1653	0.1714	0.1759	0.1789	0.1804
i_q=3A	0.1048	0.1112	0.1181	0.1252	0.1315	0.1366	0.1399	0.1416	0.142
i_q=2A	0.0719	0.0767	0.0821	0.0878	0.0931	0.0971	0.099	0.0993	0.0987
i_q=1A	0.0367	0.0392	0.0423	0.0458	0.0493	0.0518	0.0523	0.0518	0.0509
i_q=0A	0.0000	0.0001	0.0001	0.0001	0.0001	0.0001	0.0000	0.0000	0.0000
i_q=-1A	-0.0367	-0.0392	-0.0423	-0.0458	-0.0493	-0.0518	-0.0523	-0.0518	-0.0509
i_q=-2A	-0.0719	-0.0767	-0.0821	-0.0878	-0.0931	-0.0971	-0.099	-0.0993	-0.0987
i_q=-3A	-0.1048	-0.1112	-0.1181	-0.1252	-0.1315	-0.1366	-0.1399	-0.1416	-0.142
i_q=-4A	-0.1348	-0.1422	-0.1502	-0.158	-0.1653	-0.1714	-0.1759	-0.1789	-0.1804

Appendix 4 Measured incremental inductances of the prototype machine

Table A4.1 *d*-axis incremental inductance at various *dq*-axis currents [LI09a].

L_{dh}(mH)	i_d=-4A	i_d=-3A	i_d=-2A	i_d=-1A	i_d=0A	i_d=1A	i_d=2A	i_d=3A	i_d=4A
i_q=-4A	47.437	46.763	45.194	42.482	38.809	33.389	29.67	24.749	21.114
i_q=-3A	48.881	48.32	47.473	44.821	40.017	34.746	29.963	24.576	20.884
i_q=-2A	50.357	49.861	48.756	46.922	42.479	35.585	30.192	24.441	20.333
i_q=-1A	50.694	50.613	50.537	48.00	43.939	35.483	29.729	23.889	20.06
i_q=-0.5A	51.225	51.102	50.763	48.685	44.496	35.29	29.613	23.697	19.97
i_q=0.5A	50.283	50.249	50.185	47.752	42.556	34.464	27.745	22.983	20.644
i_q=1A	50.892	50.48	49.743	47.517	42.122	34.147	28.08	22.974	20.334
i_q=2A	50.374	49.754	48.48	45.355	40.521	34.142	28.092	23.235	19.713
i_q=3A	49.026	48.113	46.41	43.583	38.479	33.067	28.032	23.101	19.692
i_q=4A	47.793	46.749	44.338	40.717	36.197	31.978	27.25	23.296	20.172

Table A4.2 *q*-axis incremental inductance at various *dq*-axis currents [LI09a].

L_{qh}(mH)	i_d=-4A	i_d=-3A	i_d=-2A	i_d=-1A	i_d=0A	i_d=1A	i_d=2A	i_d=3A	i_d=4A
i_q=-4A	49.572	47.881	46.574	44.622	42.832	41.894	40.162	38.968	37.943
i_q=-3A	55.997	55.479	54.316	53.006	51.64	49.888	46.871	45.056	42.2
i_q=-2A	61.001	60.744	61.193	59.053	58.459	56.968	54.268	51.454	47.922
i_q=-1A	66.707	67.867	68.053	66.667	64.273	61.914	58.043	54.12	49.875
i_q=-0.5A	69.28	69.82	70.889	69.228	66.375	63.005	59.373	54.935	52.008
i_q=0.5A	70.296	70.349	69.041	67.83	64.759	62.76	57.634	54.323	49.491
i_q=1A	65.585	66.465	67.07	65.894	60.819	60.668	57.097	52.93	50.117
i_q=2A	62.923	61.235	59.931	58.761	56.844	55.598	52.672	49.339	44.733
i_q=3A	55.903	54.484	53.971	51.22	50.343	49.203	46.206	44.455	41.794
i_q=4A	51.267	47.684	46.401	43.189	41.822	41.188	39.732	37.656	35.576

Table A4.3 incremental mutual inductance at various *dq*-axis currents [LI09a].

L_{dqh}(mH)	i_d=-4A	i_d=-3A	i_d=-2A	i_d=-1A	i_d=0A	i_d=1A	i_d=2A	i_d=3A	i_d=4A
i_q=-4A	1.608	4.006	6.814	8.481	10.643	12.075	12.857	12.811	11.973
i_q=-3A	2.281	3.467	5.239	7.113	9.216	10.951	11.29	11.387	11.395
i_q=-2A	2.649	3.037	3.98	6.294	8.395	8.896	9.24	8.757	8.546
i_q=-1A	1.082	2.157	3.589	4.267	5.96	6.065	6.017	5.602	5.149
i_q=-0.5A	2.557	3.102	3.905	3.518	4.425	4.342	4.158	4.039	3.687
i_q=0.5A	3.721	3.251	2.756	2.035	0.231	-0.272	-0.871	-1.567	-2.183
i_q=1A	3.674	3.085	2.236	0.394	-1.289	-2.167	-2.942	-3.036	-3.166
i_q=2A	2.353	1.914	0.974	-1.229	-3.649	-5.482	-5.994	-6.526	-6.925
i_q=3A	1.894	0.989	-0.42	-3.353	-5.131	-7.076	-8.42	-8.97	-9.12
i_q=4A	1.935	-0.28	-2.836	-4.944	-7.459	-9.107	-10.484	-10.786	-10.862

Appendix 5 Fundamental voltage distortion due to inverter nonlinearity effects

According to (5.14), the fundamental voltage distortion due to inverter nonlinearity effects is,

$$\Delta u_f = -\frac{2}{3}\Delta U[sign(i_{af}) + sign(i_{bf})\cdot e^{j2p/3} + sign(i_{cf})\cdot e^{j4p/3}] \tag{A5. 1}$$

Taking Fourier series analysis, the fundamental phase voltage distortion with six step form can be derived as [HWA10],

$$\begin{cases} \Delta u_{as} = -\dfrac{4\Delta U}{p}[\cos d + \dfrac{1}{5}\cos 5d - \dfrac{1}{7}\cos 7d + \mathbf{L}] \\ \Delta u_{bs} = -\dfrac{4\Delta U}{p}[\cos(d - \dfrac{2p}{3}) + \dfrac{1}{5}\cos 5(d - \dfrac{2p}{3}) - \dfrac{1}{7}\cos 7(d - \dfrac{2p}{3}) + \mathbf{L}] \\ \Delta u_{cs} = -\dfrac{4\Delta U}{p}[\cos(d + \dfrac{2p}{3}) + \dfrac{1}{5}\cos 5(d + \dfrac{2p}{3}) - \dfrac{1}{7}\cos 7(d + \dfrac{2p}{3}) + \mathbf{L}] \end{cases} \tag{A5. 2}$$

where δ is the phase angle of fundamental current vector with respect to α-axis. With rotating transformation, the fundamental voltage distortion on the synchronous reference frame can be written as,

$$\begin{cases} \Delta u_d = -\dfrac{4\Delta U}{p}[\cos(d - q_r) + \dfrac{1}{5}\cos(5d + q_r) - \dfrac{1}{7}\cos(7d - q_r) + \mathbf{L}] \\ \Delta u_q = -\dfrac{4\Delta U}{p}[\sin(d - q_r) - \dfrac{1}{5}\sin(5d + q_r) - \dfrac{1}{7}\sin(7d - q_r) + \mathbf{L}] \end{cases} \tag{A5. 3}$$

Assuming that,

$$d = q_r + \frac{p}{2} + g \tag{A5. 4}$$

where γ is the phase shift between stator current vector and synchronous q-axis. In steady state operation, γ should be constant. Substituting (A5.3) to (A5.2), then it yields,

$$\begin{cases} \Delta u_d = \dfrac{4\Delta U}{p}[\sin g + \dfrac{1}{5}\sin(6q_r + 5g) + \dfrac{1}{7}\sin(6q_r + 7g) + \mathbf{L}] \\ \Delta u_q = \dfrac{4\Delta U}{p}[-\cos g + \dfrac{1}{5}\cos(6q_r + 5g) - \dfrac{1}{7}\cos(6q_r + 7g) + \mathbf{L}] \end{cases} \tag{A5. 5}$$

Only considering fundamental and 6th harmonic components, then it can be derived that,

$$\begin{bmatrix} \Delta u_d \\ \Delta u_q \end{bmatrix} \approx \frac{4\Delta U}{p}\cdot \begin{bmatrix} \cos g & -\sin g \\ \sin g & \cos g \end{bmatrix} \begin{bmatrix} \dfrac{12}{35}\sin 6(q_r + g) \\ -1 + \dfrac{2}{35}\cos 6(q_r + g) \end{bmatrix} \tag{A5. 6}$$

The above equation implies that the introduced voltage distortion in the synchronous reference frame is 6th harmonic with elliptic form, whose major axis length is six times to the minor axis length. The major axis of ellipse is always perpendicular to the fundamental current vector. When d-axis current is zero ($\gamma=0$), the major axis of ellipse is parallel with synchronous d-axis, otherwise, it would deviate with γ. In other words, as d-axis current increases along the negative d-axis, the voltage oscillation on q-axis would increase, while the voltage oscillation on d-axis would decrease. It should be noted that the distortion voltage ellipse is only dependent on the phase angle of fundamental current vector, instead of the current magnitude.

Appendix 6 Carrier current distortion due to inverter nonlinearity effects

With rotating injection, the carrier current response in stationary reference frame can be derived as,

$$v_{abh} = V_c \cdot e^{ja}, \qquad i_{abh} = I_p \cdot e^{j(a-p/2)} + I_n \cdot e^{j(-a+2q_r+q_m+p/2)} \tag{A6. 1}$$

where, $a = w_c t + j$.

According to (5.14), the carrier voltage distortion due to inverter nonlinearity is,

$$\Delta u_h = -\frac{2}{3}[R_{ah} \cdot i_{ah} + R_{bh} \cdot i_{bh} \cdot e^{j2p/3} + R_{ch} \cdot i_{ch} \cdot e^{j4p/3}] \tag{A6. 2}$$

Although the real carrier current response becomes different from the ideal expression (A6.1) due to inverter nonlinearity effects, (A6.1) is still valid for its dominant contribution in the total carrier current response. Consequently, the introduced carrier voltage distortion for the cases of $R_{ah} \neq 0$, $R_{bh} \neq 0$ and $R_{ch} \neq 0$ is derived respectively.

($R_{ah} \neq 0$, $R_{bh}=0$, $R_{ch}=0$)

$$\Delta u_h = -\frac{2}{3} R_{ah} \cdot i_{ah} = -\frac{2}{3} R_{ah} \cdot I_p \cos(a - p/2) - \frac{2}{3} R_{ah} \cdot I_n \cos(-a + 2q_r + p/2)$$
$$= -\frac{R_{ah} I_p}{3} e^{j(a-p/2)} - \frac{R_{ah} I_n}{3} e^{j(a-2q_r-p/2)} - \frac{R_{ah} I_p}{3} e^{j(-a+p/2)} - \frac{R_{ah} I_n}{3} e^{j(-a+2q_r+p/2)}$$

($R_{ah}=0$, $R_{bh} \neq 0$, $R_{ch}=0$)

$$\Delta u_h = -\frac{2}{3} R_{bh} i_{bh} \cdot e^{j2p/3} = -\frac{2}{3} R_{bh}[I_p \cos(a - 7p/6) + I_n \cos(-a + 2q_r - p/6)] \cdot e^{j2p/3}$$
$$= -\frac{R_{bh} I_p}{3} e^{j(a-p/2)} - \frac{R_{bh} I_n}{3} e^{j(a-2q_r+5p/6)} - \frac{R_{bh} I_p}{3} e^{j(-a-p/6)} - \frac{R_{bh} I_n}{3} e^{j(-a+2q_r+p/2)}$$

($R_{ah}=0$, $R_{bh}=0$, $R_{ch} \neq 0$)

$$\Delta u_h = -\frac{2}{3} R_{ch} i_{ch} \cdot e^{j4p/3} = -\frac{2}{3} R_{ch}[I_p \cos(a + p/6) + I_n \cos(-a + 2q_r + 7p/6)] \cdot e^{j4p/3}$$
$$= -\frac{R_{ch} I_p}{3} e^{j(a-p/2)} - \frac{R_{ch} I_n}{3} e^{j(a-2q_r+p/6)} - \frac{R_{ch} I_p}{3} e^{j(-a+7p/6)} - \frac{R_{ch} I_n}{3} e^{j(-a+2q_r+p/2)}$$

As a consequence, the total carrier current response with consideration of distortions resulting from inverter nonlinearity effects is summarized in Table A6.1 - A6.3.

Table A6.1 Total carrier current components ($\theta_r = 0$, $R_{ah} \neq 0$).

Voltage Term	Carrier Current I_{pos} (Positive sequence)	Carrier Current I_{neg} (Negative sequence)
$V_c e^{ja}$	$I_p e^{j(a-p/2)}$	$I_n e^{j(-a+2q_r+p/2)}$
$-\frac{R_{ah} I_p}{3} e^{j(a-p/2)}$	$-\frac{R_{ah} I_p^2}{3V_c} e^{j(a-p)}$	$-\frac{R_{ah} I_p I_n}{3V_c} e^{j(-a+2q_r+p)}$
$-\frac{R_{ah} I_n}{3} e^{j(a-2q_r-p/2)}$	$-\frac{R_{ah} I_p I_n}{3V_c} e^{j(a-2q_r-p)}$	$-\frac{R_{ah} I_n^2}{3V_c} e^{j(-a+4q_r+p)}$
$-\frac{R_{ah} I_p}{3} e^{j(-a+p/2)}$	$-\frac{R_{ah} I_p I_n}{3V_c} e^{j(a+2q_r-p)}$	$-\frac{R_{ah} I_p^2}{3V_c} e^{j(-a+p)}$
$-\frac{R_{ah} I_n}{3} e^{j(-a+2q_r+p/2)}$	$-\frac{R_{ah} I_n^2}{3V_c} e^{j(a-p)}$	$-\frac{R_{ah} I_p I_n}{3V_c} e^{j(-a+2q_r+p)}$

Table A6.2 Total carrier current components ($\theta_r = 2\pi/3$, $R_{bh} \neq 0$).

Voltage Term	Carrier Current I_{pos} (Positive sequence)	Carrier Current I_{neg} (Negative sequence)
$V_c e^{ja}$	$I_p e^{j(a-p/2)}$	$I_n e^{j(-a+2q_r+p/2)}$
$-\frac{R_{bh} I_p}{3}$	$-\frac{R_{bh} I_p^2}{3V_c} e^{j(a-p)}$	$-\frac{R_{bh} I_p I_n}{3V_c} e^{j(-a+2q_r+p)}$
$-\frac{R_{bh} I_n}{3} e^{j(a-2q_r+5p/6)}$	$-\frac{R_{bh} I_p I_n}{3V_c} e^{j(a-2q_r+p/3)}$	$-\frac{R_{bh} I_n^2}{3V_c} e^{j(-a+4q_r-p/3)}$
$-\frac{R_{bh} I_p}{3} e^{j(-a-p/6)}$	$-\frac{R_{bh} I_p I_n}{3V_c} e^{j(a+2q_r-p/3)}$	$-\frac{R_{bh} I_p^2}{3V_c} e^{j(-a+p/3)}$
$-\frac{R_{bh} I_n}{3} e^{j(-a+2q_r+p/2)}$	$-\frac{R_{bh} I_n^2}{3V_c} e^{j(a-p)}$	$-\frac{R_{bh} I_p I_n}{3V_c} e^{j(-a+2q_r+p)}$

Table A6.3 Total carrier current components ($\theta_r = \pi/3$, $R_{ch} \neq 0$).

Voltage Term	Carrier Current I_{pos} (Positive sequence)	Carrier Current I_{neg} (Negative sequence)
$V_c e^{ja}$	$I_p e^{j(a-p/2)}$	$I_n e^{j(-a+2q_r+p/2)}$
$-\frac{R_{ch} I_p}{3} e^{j(a-p/2)}$	$-\frac{R_{ch} I_p^2}{3V_c} e^{j(a-p)}$	$-\frac{R_{ch} I_p I_n}{3V_c} e^{j(-a+2q_r+p)}$
$-\frac{R_{ch} I_n}{3} e^{j(a-2q_r+p/6)}$	$-\frac{R_{ch} I_p I_n}{3V_c} e^{j(a-2q_r-p/3)}$	$-\frac{R_{ch} I_n^2}{3V_c} e^{j(-a+4q_r+p/3)}$
$-\frac{R_{ch} I_p}{3} e^{j(-a+7p/6)}$	$-\frac{R_{ch} I_p I_n}{3V_c} e^{j(a+2q_r+p/3)}$	$-\frac{R_{ch} I_p^2}{3V_c} e^{j(-a-p/3)}$
$-\frac{R_{ch} I_n}{3} e^{j(-a+2q_r+p/2)}$	$-\frac{R_{ch} I_n^2}{3V_c} e^{j(a-p)}$	$-\frac{R_{ch} I_p I_n}{3V_c} e^{j(-a+2q_r+p)}$

Appendix 7 Papers published during PhD study

Journal papers

1. L.M. Gong and Z.Q. Zhu, "A novel method for compensating inverter nonlinearity effects in carrier signal injection-based sensorless control from positive-sequence carrier current distortion," *IEEE Trans. Industry Applications*, vol. 47, no. 3, pp. 1283-1292, 2011.

2. Z.Q. Zhu and L.M. Gong, "Investigation of effectiveness of sensorless operation in carrier signal injection based sensorless control Methods," *IEEE Trans. Industrial Electronics*, vol. 58, no. 8, pp. 3431-3439, 2011.

Conference papers

1. L.M. Gong and Z.Q. Zhu, "Analysis and compensation of cross-saturation effect in rotating carrier signal injection based sensorless control methods for PM brushless AC motors," *Proceedings of the 16th International Conference on Automation & Computing*, Birmingham, UK, 11 September 2010, pp.54-59.

2. L.M. Gong and Z.Q. Zhu, "Modeling and compensation of inverter nonlinearity effects in carrier signal injection-based sensorless control methods from positive sequence carrier current distortion," *Energy Conversion Congress and Exposition* (ECCE), 2010, pp. 3434-3441.

3. Z.Q. Zhu and L.M. Gong, "Improved sensorless operation of permanent magnet brushless AC motors based on online optimal efficiency control," *IEEE International Electric Machines and Drives Conference* (IEMDC), 2011, pp. 1591-1596.

4. L.M. Gong and Z.Q. Zhu, “Improved rotating carrier signal injection method for sensorless control of PM brushless AC motors, accounting for cross-saturation effect,” *Power Electronics and ECCE Asia* (ICPE & ECCE), 2011, pp. 1132-1139.

5. L.M. Gong and Z.Q. Zhu, “Saliency investigation of PM brushless AC motors for high-frequency carrier signal injection-based sensorless control,” *Proceedings of the 17th International Conference on Automation and Computing*, Huddersfield, UK, 10 September 2011, pp.92-97.